Università degli Studi di Pavia
Dottorato di Ricerca in Fisica - XXXIV Ciclo

Study of the operation and trigger performance of GEM detectors in the CMS experiment

Simone Calzaferri

Tesi per il conseguimento del titolo

Università degli Studi di Pavia
Dipartimento di Fisica

Dottorato di Ricerca in Fisica - XXXIV Ciclo

Study of the operation and trigger performance of GEM detectors in the CMS experiment

Simone Calzaferri

Submitted to the Graduate School of Physics in partial fulfillment of the requirements for the degree of

DOTTORE DI RICERCA IN FISICA

DOCTOR OF PHILOSOPHY IN PHYSICS

at the

University of Pavia

University Supervisor: Prof. Paolo Vitulo

Cover: Tuscany hills wallpaper, URL: https://pixabay.com/photos/church-sunrise-fog-environment-6853164/.

Study of the operation and trigger performance of GEM detectors in the CMS experiment

Simone Calzaferri

Ph.D Thesis - University of Pavia

Pavia, Italy, February 14, 2022

The cruel faction in the long robe
Will come to hide under the sharp daggers:
The Duke to seize Florence and the diphthong place,
Its discovery by immature ones and sycophants.

(Nostradamus, Century X Quatrain 33)

List of Figures

1.1 Production cross section of several processes in proton-(anti)proton collisions as a function of center of mass collision energy [1]. . 6
1.2 Schematic representation of the LHC with the position of the main experiments [6]. 9
1.3 Leading order Feynman diagrams for Higgs boson production: (a) gluon-gluon fusion, (b) vector boson fusion, (c) Higgs-strahlung, (d) associated with a pair top of quarks [14]. 10
1.4 Production cross section of SUSY particles according to the Minimal Supersymmetric Standard Model, as a function of their mass [16]. 11
1.5 Cutaway representation of the CMS experiment, showing its main components and sub-detectors [18]. 12
1.6 Scheme of the CMS coordinate system [19]. 13
1.7 (a) The superconducting magnet (grey) inserted inside the iron yoke (red) before the installation of any detector in the spaces available inside the iron yoke [24]; (b) the magnetic field created by the superconducting magnet in a longitudinal view of the CMS detector, with the field intensity on the left and the field lines on the right of the figure [25]. 14
1.8 Cutaway representation of the CMS inner tracker, showing its main components [26]. 15
1.9 Cutaway representation of the pixel system of the CMS inner tracker, showing its endcap disks and barrel layers [26]. 15
1.10 ECAL structure, with its barrel, endcap and preshower systems [27]. 17
1.11 Structure of the preshower detector installed in front of ECAL [27]. 18
1.12 Scheme of CMS Hadron Calorimeter, with its main systems: the Hadron Barrel calorimeter (HB), Hadron Outer (HO), Hadron Endcap (HE) and Hadron Forward (HF) [29]. 18

1.13 View of a quadrant of the CMS Muon Spectrometer in the plane R-z at the end of Run-2 [32]. 19
1.14 View in x-y plane of the layout of CMS DT chambers in one of the wheels. The trajectory followed by a muon is also represented, bending in two different directions due to the different verse of the magnetic field inside the superconducting magnet and inside the return yoke [33]. 21
1.15 Layout of a Drift Tubes chamber in the $R-\phi$ plane: in the top and bottom part are represented the 2 SLs with wires parallel to the z-axis and in the middle is represented the central layer with wires orthogonal to the beampipe (a). The layout of a drift cell, with the electric field lines [32]. 22
1.16 (Left) view of ME2 CSC station: the inner ring is organised in 18 chambers, each covering 10° in $R-\phi$ plane, and the outer ring includes instead 36 ME2/2 10° chambers [33]; (Right) schematic view of a CSC chamber, showing the radial arrangement of cathode strips and the azimuthal organisation of anode wires [32]. 23
1.17 Schematic representation of a CMS double-gap RPC chamber [32]. 24
1.18 Schematic representation of the CMS trigger system [37]. . . . 25
1.19 Schematic representation of CMS L1 Trigger system during Run-2 [38]. 26
1.20 Scheme of the CMS DAQ system [40]. 29
1.21 Schedule of the LHC operations [42]. 30
1.22 Simulation of absorbed dose in CMS after an integrated luminosity of 3000 fb^{-1} [43]. 32
1.23 View of a quadrant of the CMS Muon Spectrometer in the plane R-z in Phase 2. In red are indicated the GEM stations GE1/1, GE2/1 and ME0 [46]. 34

2.1 Scheme of a cylindrical ionisation detector [48]. 38
2.2 Operation regions of single wire gaseous detector, with the pulse amplitude plotted for events releasing two different amounts of energy in the gas medium [49]. 39
2.3 (a) Scheme of a Multi-Wire Proportional Chamber: the typical parameters are $S = 2\,\mathrm{mm}$ as wire pitch and the distance of wires from the cathode plane l around 3-4 times larger than S; (b) Representation of electric field lines and equipotential surfaces in the plane orthogonal to the plane of the wires in an MWPC [50]. 40
2.4 Rate capability of MWPC and MSGC in different configurations [51]. 41

2.5 (a) Representation of a MSGC in the plane orthogonal to the strips, including a scheme of the electric field and equipotential lines; (b) representation of a MSGC with the electrodes sizes and mutual distances [52] [53]. 42

2.6 MSGC strips damaged by discharges occurring in the gas medium [52]. 43

2.7 (a) Representation of the structure and operating scheme of a MICROMEGAS detector; (b) representation of the electric field and equipotential lines in the plane orthogonal to the micromesh [52] [55]. 44

2.8 Current detected in a MICROMEGAS, for different particle fluxes [52]. 45

2.9 (a)(b) Top view of a GEM foil from an electron microscope picture and in a scheme illustrating the pitch of the holes $P = 140\,\mu$m. (c)(d) Lateral section of a GEM hole in an electron microscope picture and in a scheme, showing the thickness of the copper cladding $t = 5\,\mu$m, the Kapton foil thickness $T = 50\,\mu$m and the inner and outer diameters of the hole $d = 50\,\mu$m and $D = 70\,\mu$m. It can be noted that the shape of the hole is biconical [56] [57]. 46

2.10 Electric field in a GEM detector, showing the field lines and the equipotential surfaces in the plane orthogonal to the foil [56]. 47

2.11 Schematic representation of a single GEM detector [57]. 47

2.12 Single GEM operated in Ar/CO_2 (70/30%) (a) Collection efficiency as a function of the drift electric field E_D, measured with different methods: integral current and pulse with two different amplifier shaping times. (b) Current measured on different electrodes: I_D is the current on the drift cathode electrode, I_T and I_B are respectively the currents on the top and bottom copper clads of the GEM foil, I_S the current registered on the readout strips, I_{TOT} is given by the sum $I_{TOT} = I_S + I_B$ and represents the real GEM gain [57]. 48

2.13 Current flowing on the electrodes of a double GEM detector as a function of the transfer electric field E_T. The detector operates with gas mixture Ar/CO_2 (70/30%), drift E_D and induction E_I fields are fixed at $5\,$kV/cm and the potential differences on the foils are set to $\Delta V_{GEM\,1} = 500\,$V and $\Delta V_{GEM\,2} = 350\,$V. The currents represented are: the current flowing on the drift electrode I_D, on the top and bottom layer of the first GEM foil I_{T1} and I_{B1}, on the top and bottom layer of the second GEM foil I_{T2} and I_{B2}, and the current induced on the readout strips I_S [57]. 51

2.14 Gain and discharge probability as a function of the voltage applied to each GEM foil in single, double and triple GEM configuration. The solid line refers to the effective gain data, while the dashed one refers to the discharge probability. [56]. . 52
2.15 Design adopted by CMS for a GE1/1 triple-GEM detector. In figure the electric fields of each region, together with their thickness are illustrated: E_D and g_D for the drift region, E_{T1} and g_{T1} for the first transfer region, E_{T2} and g_{T2} for the second transfer region, E_I and g_I for the induction region [60]. 54
2.16 Scanning Electron Microscope (SEM) picture of a GEM foil after one single discharge with an energy of 2 mJ [62]. 56
2.17 Discharge event registered on a 10 cm $\times$ 10 cm triple-GEM detector. The voltage on the single electrodes are measured with a high voltage probe with an attenuation factor 1000. To trigger the acquisition of the discharge event an antenna is used [62]. 57
2.18 Discharge event registered on a GE1/1 long triple-GEM detector. The voltage on the single electrodes are measured with a high voltage probe with an attenuation factor 1000. To trigger the acquisition of the discharge event an antenna is used. It can be noted a much more complex behaviour in the discharge evolution than what observed in a 10 cm $\times$ 10 cm triple-GEM detector [62]. 58
2.19 Thanks to the distance among a GE1/1 and a ME1/1 station, the possibility to measure the $\Delta\phi$ bending angle formed by a muon trajectory crossing these two stations is offered [64]. . . 59
2.20 Level 1 muon trigger rate as a function of the L1 muon p_T threshold at an LHC luminosity of $2 \cdot 10^{34}\,\mathrm{cm}^{-2}\mathrm{s}^{-1}$, in blue without the GE1/1 station and in purple with the station installed [64]. 60
2.21 Magnetic field in GE1/1 installation region (dashed rectangle): on the left the intensity of the magnetic field in the plane $z-r$ is shown, on the right the angle formed between the magnetic field vector and the z-axis [64]. 61
2.22 Representation of the GE1/1 station with all its Super-Chambers: on the left a Super-Chamber is represented, in the middle the arrangement of Super-Chambers in the GE1/1 ring and on the right the GE1/1 station installed in the so-called nose of the CMS detector. In blue and magenta respectively the long and short Super-Chambers [64]. 62
2.23 Segmentation of the foil in sectors, 40 for short and 47 for long chambers. The colour represents the η sector of the readout plane facing the corresponding part of the GEM foil, red and blue respectively for the 1st and the 8th sectors [65]. 63

2.24 Exploded representation of a fully equipped GE1/1 detector [65]. 64

2.25 Patch panel of a single GE1/1 chamber [65]. 64

2.26 Mapping of the GE1/1 HV system. 65

2.27 Mapping of the GE1/1 LV system. 66

2.28 Scheme of a VFAT3 ASIC installed on GE1/1 chambers. The acronyms in the figure mean in order: Constant Fraction Discriminator (CFD), Analogue to Digital Converter (ADC) and Static Random Access Memory (SRAM) [64]. 70

2.29 GE1/1 single chamber equipped with the GEB, the 24 VFATs and the OptoHybrid board, on the stand deputed to perform the electronics quality control [65]. 71

2.30 Mapping of VFATs on the covered readout sectors [65]. 72

2.31 The OptoHybrid board installed on a GE1/1 chamber, with its main components highlighted [65]. 73

2.32 Reconstruction efficiency, as a function of η, of the local trigger primitive object, called *stub*, in a scenario with $PU = 140$ and $\sqrt{s} = 14\,\text{TeV}$. In red the performance offered by the detectors installed in CMS till the end of Run 2, while in blue the improvements offered by the installation of the GE2/1 station [46]. 75

2.33 Scheme of the readout plane of GE21: the 4 radial sectors are labelled as M1-M4, and each of them is divided in 12 sectors with 128 strips each [75]. 76

2.34 Estimation of the background hit rate provided by neutrons, photons, electrons and positrons on the three GEM stations planned to be installed in CMS. [46]. 77

2.35 Reconstruction efficiency of ME0 muons. In blue are represented the Tight ME0Muons, selected requiring the presence of a ME0 segment with $\Delta\phi < 0.15$ with respect to the direction of the tracker track, while in red the Loose ME0Muons ($\Delta\phi < 0.50$) [43]. 78

2.36 $H \to ZZ^* \to 4\mu$ channel: η distribution of the highest-$|\eta|$ muon among the 4 produced in the decay. The events represented in the distribution are given by a selection that was produced using a CMS geometry with tracking, calorimeter and muon systems extended to $|\eta| = 4.0$. The signal events $H \to ZZ^* \to 4\mu$ and the irreducible background events $ZZ \to 4\mu$ are respectively indicated with empty and solid red. The dashed lines correspond to the acceptance of CMS at the end of Run 1 [76]. 79

3.1 Schedule for the production of a GE1/1 Super-Chamber, from the material inspection to the final validation: the components and the GEM foils are firstly inspected at CERN and then shipped to the production sites, to ensure they use good quality components in the production. At the production sites, as well as at CERN, quality controls up to QC5 are performed, before shipping the detectors back to CERN, where the last quality controls are performed [77]. 82

3.2 Scheme of a GEM foil, with defects and deposits which could increase its leakage current [19]. 84

3.3 Scheme of the resistive divider used during the QC tests. On the right are indicated the channels corresponding to each connection: D for Drift, 1T, 2T and 3T for the top face of the three foils, 1B, 2B, 3B for the bottom face [19]. 87

3.4 Scheme of the setup used for the noise rate measurement in QC4 [19]. 88

3.5 Scheme of the setup used for the effective gas gain measurement in QC5 [19]. 89

3.6 (a) Anodic current I_a and photon interaction rate R; (b) effective gas gain as a function of the HV equivalent divider current $I_{divider}$, corrected by a normalisation factor, which contains the pressure and temperature of the production site P and T where QC5 has been performed, and the mean values of pressure and temperature present in the CMS experimental cavern P_0 and T_0. This provides a common reference for chambers tested in different production sites, with different environmental condition [78]. 90

3.7 Scheme of the HV circuit used to power each GEM foil in a GE1/1 detector [80]. 91

3.8 Equivalent circuit of a GEM foil with an HV sector with a short in a GE1/1 detector. 91

3.9 GE1/1 chamber on the QC7 stand, equipped only with the electronics. The evacuation of the heat from FEASTs and the OptoHybrid is granted by heat sinks and a fan placed above the chamber [81]. 93

3.10 Scheme of the response efficiency of a VFAT channel to an input charge signal in presence of noise. In blue is represented the s-curve response, given by the step response smeared by the white noise and in green the charge threshold value of the response (50% efficiency). In red is represented the noise with its standard deviation, the ENC. 96

3.11 S-curve of chamber GE+1/1/09 of the positive endcap in the CMS experiment. This chamber shows dead channels in VFAT 23 (vertical white lines) and channels with a low ENC (too narrow colour change with respect to the other channels), for example near channel 17 or 128. 97

3.12 S-curves of VFAT 16 of chamber GE11-X-L-CERN-0007, equipped with the cooling plate and the chimney. On the left the s-curve taken at $CFG\_THR\_ARM = 100$, while on the right that taken after applying the 100 Hz noise threshold value [82]. . . 98

3.13 S-bit rate curves: (a) curve taken for VFAT 16 of chamber GE11-X-L-CERN-0007, already equipped with the cooling plate and the chimney [82]; (b) broken s-bit curve for VFAT 5 of chamber GE11-X-S-FIT-0004. This chamber was already installed in the CMS experiment and was re-extracted and sent back to QC7 to fix this issue. The broken s-bit line in this chamber has been fixed by re-plugging the OptoHybrid board and the VFAT [83]. 99

3.14 Summary plots for VFATs in chamber GE11-X-L-CERN-0007: (a) the box plot of the charge threshold values of all the channels of the VFAT; (b) the ENC values [82]. The summary is made using a standard box plot, including in the yellow box a fraction of values from the first quartile to the third quartile (25%-75%); the median is represented by the central box horizontal line and the distribution mean with a small circle [84]. 100

3.15 VFAT DAC threshold scan for VFAT 12 of chamber GE11-X-L-CERN-0043. The low threshold for channels in the right part of the plot is given by the partial unplugging of the VFAT: the absence of connection among the chip and the strips reduces the capacitance of the readout channel and in this way its collection of noise signals, resulting in a very low and unrealistic DAC threshold for the unplugged channels [85]. 101

3.16 Current plot showing the current drained by the power supply at 8 V during the operation on the QC7 stand. [81]. 102

3.17 Structure of the QC8 stand with the naming conventions adopted to identify the chambers and the labels of the electronic modules connected to the corresponding positions [65]. 103

3.18 Picture of the QC8 cosmic stand at the GEM lab in the 904 building at CERN [86]. 104

3.19 Current drained by the HV power supply on channel G3Top of chamber in position 2-2-Top in the QC8 stand from 2019-06-25-00:00:01 UTC to 2019-06-27-00:00:01 UTC. 111

3.20 Voltage provided by the HV power supply on channel G3Top of chamber in position 2-2-Top in the QC8 stand from 2019-06-25-00:00:01 UTC to 2019-06-27-00:00:01 UTC. 112

3.21 Status of HV G3Top channel of the chamber in position 2-2-Top in the QC8 stand from 2019-06-25-00:00:01 UTC to 2019-06-27-00:00:01 UTC. 113

3.22 Current values for the G3Top channel of the chamber in position 2-2-Top: zoom on the time region when the trip occurred. The positive current which triggered the trip of the channel (02:04 UTC), the negative current of the ramp down and the positive current corresponding to the new channel ramp up (04:04 UTC) can be observed. 114

3.23 Detailed evolution of the status of channel G3Top for chamber in position 2-2-Top in the QC8 stand during the trip occurred at 2019-06-25 02:04. In the table are reported the Time Stamp (TS) of a status value, the status in decimal and binary format and its complete meaning. 115

3.24 LV current drained by the A3016 board during the operation in the QC8 stand by chamber in position 4-2-Bot. 115

3.25 Panel of the online HV monitor: in the top-left corner of the browser the desired Super-Chamber can be selected by a tab, while in each tab is created a 7×3 grid, with on each line three plots for each HV channel of the Super-Chamber. In each line, from left to right there are current, voltage and status code plots. 116

3.26 (a) Super-Chamber GE+1/1/36 operated in GEM mode: here all the electrodes are operated in concert and the ramp-up occurs in sequence ($\text{ramp} - \text{up} = 3\,\text{V/s}$). (b) Super-Chamber GE+1/1/30 operated in FREE mode: here the three foils trip, they are turned off and then recovered, while all the other electrodes stay stable. 118

3.27 Six consecutive recoveries on the HV of chamber GE-1/1/01. In this case, when the chamber started the ramp of the last electrode the chamber tripped, the channels are all turned off and the recovery procedure restarts from scratch. When the limit of six recoveries is reached, the channels are left off. . . . 119

3.28 Transition from READY FOR PHYSICS mode ($700\,\mu\text{A}$) to STANDBY mode ($580\,\mu\text{A}$) interrupted from the occurrence of a trip and its recovery, while the transition procedure was being executed. (a) The interruption of the transition in Super-Chamber GE-1/1/02; (b) the trip in Super-Chamber GE+1/1/09 which triggered the interruption. 121

3.29 LV current for both layers of Super-Chamber GE+1/1/26, operated at 8 V. The main levels present also in QC7 operation can be spotted: the STANDBY mode at the power up (1.75 A), the run mode (2.8 A) and the scan mode (with a mean current level over 3.3 A). Layer 1 was excluded from the scan in this case. 122
3.30 Trip on Super-Chamber GE+1/1/30: (a) the voltage plot, (b) the current plot. During this event a discharge propagated to the readout plane and damaged the front-end electronics. . . . 123
3.31 LV current plot of Super-Chamber GE+1/1/30: since the occurrence of a trip in the HV system at 2021-07-18 18:06:20 UTC, a distancing of the current levels shows up. This is symptom of damage created in the front-end electronics. 124
3.32 S-curves of Layer 1 of Super-Chamber GE+1/1/30 for VFAT 16: on the left the s-curve collected at the end of June 2021, while on the right that collected on 22 July 2021. The first s-curve was collected applying the $THR\_ARM\_DAC = 100$ threshold, while the second was collected at a higher value because of an issue in the VFAT calibration. It can be noticed anyway as after the trip occurrence, 8 new dead channels appeared on VFAT 16. 125
3.33 Example of valid and non valid trips: the first trip is not counted since happens when the ramp is ongoing and the stability of the last electrode has not yet been reached, the second trip is counted, since it happened with all the electrodes active and stable. 126
3.34 Weekly trip report for Super-Chamber GE+1/1/03 from week 18 to week 39 of 2021 (3rd May - 3rd October): in the top plot is reported the trip rate per day for this chamber, given by the ratio between the number of trips counted during the week (mid plot) and the operation time with all the electrodes active and stable (bottom plot). 132
3.35 Trip report for all Super-Chambers from week 18 to week 39 of 2021 (3rd May - 3rd October): in the top plot is reported the trip rate per day per Super-Chamber, given by the ratio between the number of trips counted during the week (mid plot) and the operation time with all the electrodes active and stable (bottom plot). It can be noticed that the outlier Super-Chambers in the trip rate plot correspond to those with a lower operation time. 133
3.36 Operation of the CMS magnetic field from 7th to 16th October 2021. 134
3.37 Short in the GE-1/1/31 Super-Chamber ($I_{G3Top} = 42.1\,\mu$A, at $\Delta V_{G3Top} = 430.2$ V). This short has been identified to be on the 3rd foil in Layer 2. 134

3.38 Super-Chamber GE-1/1/31: first occurrence of a linear increase of the current of channel G3Top, during a recovery ramp. This happens after a trip involving G1Top and G2Top (12:53 UTC) and in particular after the trip on G3Top (12:55 UTC). From left to right are reported respectively the HV current and voltage plots. 135

3.39 Trip rate calculated during the READY FOR PHYSICS mode, using 580 μA and 620 μA equivalent divider current voltages for the STANDBY mode, for each Super-Chamber. 135

3.40 Trip rate calculated for the transitions from STANDBY to READY FOR PHYSICS mode, using 580 μA and 620 μA equivalent divider current voltages for the STANDBY mode, for each Super-Chamber. 136

3.41 Trip rate calculated for trips occurring in the STANDBY mode, using 580 μA and 620 μA equivalent divider current voltages for the STANDBY mode, for each Super-Chamber. 136

3.42 Trip rate calculated for the transitions from READY FOR PHYSICS to STANDBY mode, using 580 μA and 620 μA equivalent divider current voltages for the STANDBY mode, for each Super-Chamber. 137

3.43 Summary of the mean trip rate for the 72 GE1/1 Super-Chambers, occurring in the STANDBY (SB) and READY FOR PHYSICS (RD) modes and during the transitions between these two states: $SB \rightarrow RD$ and $RD \rightarrow SB$. Two different sets of equivalent divider current voltages have been used for the STANDBY mode, 580 μA and 620 μA, while in the READY FOR PHYSICS mode the Super-Chambers were always set to 700 μA equivalent divider current voltages. The trip rate relative to the trips occurring during the READY FOR PHYSICS and STANDBY mode is normalised over the days of operation. On the other hand, for trips occurring during the transitions, the rate is normalised over the number of transitions performed. 137

3.44 Scheme of the HV circuit which powers one GEM foil. The foil top face is segmented into sectors (40 for short chambers and 47 for the long ones), while the bottom face is not segmented. 138

3.45 (a) Scheme of the equivalent circuit given by the creation of a short circuit in two HV sectors of the same foil in the same Super-Chamber layer. (b) Scheme of the equivalent circuit given by the creation of a short circuit in two HV sectors of the same foil type but in distinct Super-Chamber layers. . . . 139

3.46 (a) Resistance of short circuits per each Super-Chamber involved; (b) distribution of resistance values 140

3.47 (a) Foil with the short circuit; (b) context when the short circuit manifested for the first time. The labels on the external side of the pie chart are the frequency percentages. 141

4.1 Example diagram of the decay of τ in three muons in the final state, with neutrino oscillation [91]. 143

4.2 (a) η distribution of generated tau leptons; (b) p_t distribution of generated tau leptons. 147

4.3 (a) η distribution of generated muons coming from the decay of tau leptons; (b) p_t distribution of generated muons coming from the decay of tau leptons. In blue, green and red are respectively shown the distributions corresponding to the trailing, medium and leading-p_t muons. 148

4.4 (a) η distribution of generated tau leptons (GEN_PARTICLES [99]) which decayed into muons with a high enough p_t to produce a global muon in the reconstruction: the cuts applied to the muons GEN_PARTICLES are $p_t > 3.5\,\text{GeV}$ in the barrel ($|\eta| < 1.2$) and $p_t > 2.0\,\text{GeV}$ in the endcap ($|\eta| > 1.2$); (b) η distribution of TkMuons. Both plots have been produced using the PU0 signal sample. 149

4.5 (a) $\Delta\eta$ mutual distance among generated muons produced by the τ decay; (b) $\Delta\phi$ mutual distance among generated muons produced by the τ decay. In blue are represented the distribution of mutual distances between the trailing and the medium-p_t muons, in green between the trailing and leading ones, and in red between the medium and leading ones. 150

4.6 (a) ΔR radius calculated for the three generated muons produced by the $\tau \to 3\mu$ decay. This parameter is the radius of the smallest circle containing the triangle built using the three muon pairs ΔR as sides; (b) illustration of the three different triangles which can be obtained in the triangle construction: acute on the middle top, rectangle on the left bottom and obtuse on the right bottom. 151

4.7 (a) distribution of $\Delta\phi$ bending angle for different p_t positive muons in the positive endcap of CMS; (b) cumulative distribution of $\Delta\phi$ bending angle for different p_t positive muons in the positive endcap of CMS. 152

4.8 (a) Number of RecHits used to build ME0 segments in signal and background samples; (b) ME0 segments η position in signal and background samples. 153

4.9 Maximum $\Delta\eta - \Delta\phi$ separation among ME0 segments matched with $\tau \to 3\mu$ muons. The events plotted are those where all the three muons lied within the ME0 acceptance. In (a) and (b), the separations built looking to the ME0 segments points in the 1st and 6th layer are respectively represented. 154
4.10 Maximum $\Delta\eta - \Delta\phi$ separation for each triplet of ME0 segments for background events. The angular separations are determined looking to the η and ϕ positions of ME0 segments points in the 1st (a) and 6th ME0 layers (b). 155
4.11 (a) ΔR radius distribution for ME0 segments matched with muons produced by the $\tau \to 3\mu$ decay. (b) ΔR radius distribution for each triplet of ME0 segments for signal and background events. 157
4.12 $|\Delta\phi|$ bending angle calculated for ME1/1 (a) and ME2/1 (b) CSCCorrelatedLCTs. The tails at high bending angles comes from an erroneous assignment of the GEM pad by the reconstruction algorithm. 158
4.13 (a) quality of CSCCorrelatedLCTs from ME1/1 station; (b) η position of CSCCorrelatedLCTs from ME2/1 station. 159
4.14 Maximum $\Delta\eta - \Delta\phi$ separation among ME1/1 (a) and ME2/1 (b) CSCCorrelatedLCTs matched with $\tau \to 3\mu$ muons. The events plotted are those where all the three muons lied in the stations acceptance. The angular separations are determined looking to the η and ϕ positions of points given by the intersection of key LCT strips and wires in the 3rd CSC layer. . . . 161
4.15 Maximum $\Delta\eta - \Delta\phi$ separation for each triplet of ME1/1 (a) and ME2/1 (b) CSCCorrelatedLCTs for background events. The angular separations are determined looking to the η and ϕ positions of points given by the intersection of key LCT strips and wires in the 3rd CSC layer. 163
4.16 ΔR radius distribution for ME1/1 (a) and ME2/1 (b) LCTs matched with muons produced by the tau decay. 163
4.17 ΔR radius distribution for each triplet of ME1/1 (a) and ME2/1 (b) LCTs for signal and background events. 164
4.18 (a) p_t distribution of EMTF tracks; (b) Charge distribution of EMTF tracks. 164
4.19 (a) Quality of EMTF tracks for signal and background events; (b) ΔR radius distribution for EMTF tracks matched with muons produced by the tau decay. 166
4.20 ΔR radius distribution for each triplet of EMTF tracks for signal and background events. 167
4.21 (a) p_t distribution of TkMuons; (b) Reduced χ^2 distribution of TkMuons. 169

4.22 (a) Distribution of POCA z coordinate for TkMuons; (b) ΔR radius distribution for TkMuons matched with muons produced by the τ decay. 171
4.23 ΔR radius distribution for each triplet of TkMuons for signal and background events. 172
4.24 TkMuon invariant mass obtained from signal and background TkMuon triplets, zooming on the τ mass range (a) and looking the whole mass range (b). As can be noticed, in the background distribution, the peak typical of the $\tau \to 3\mu$ decay is absent and the distribution is well separated from it. The shape of the background is determined by the combinatorics of TkMuon objects. 173
4.25 Trigger rate and efficiency obtained for selections using 3 TkMuons at $PU = 200$. Each point represents the trigger rate and efficiency for a different selection. 174
4.26 Triple EMTF selections with fixed ΔR radius flag *DeltaR2*, and different p_t, quality and charge cuts. On the x-axis is reported an index which corresponds to a particular combination of p_t cuts, explained in Tab. A.1. 175
4.27 Maximum number of triggerable signal events (a) for selections with a trigger rate $R < 10\,\text{kHz}$. Their corresponding trigger rate is reported in the plot (b). The total integrated luminosity considered is $\int \mathcal{L}\,dt = 3000\,\text{fb}^{-1}$, and the pileup condition is $PU = 200$. In the plots the results for different values of the *diffDR* parameter are shown. This parameter does not act on the categories where it was not implemented: tripleME0, tripleTK, tripleEMTF, doubleEMTFsingleME0 and singleEMTFdoubleME0. 183
4.28 Maximum number of triggerable signal events (a) for selections with a trigger rate $R < 10\,\text{kHz}$. Their corresponding trigger rate is reported in plot (b). The total integrated luminosity considered is $\int \mathcal{L}\,dt = 3000\,\text{fb}^{-1}$, and the *diffDR* parameter is set to 0.001. In the plots the pileup condition are $PU = 140$ and $PU = 200$. 184
4.29 Category *singleEMTFdoubleME0*: maximum signal efficiency (a) and number of triggerable signal events (b) in each 500 Hz slice for rate $R < 10\,\text{kHz}$. The total integrated luminosity considered is $\int \mathcal{L}\,dt = 3000\,\text{fb}^{-1}$. The details on each point are reported in Tab. A.2 for $PU = 140$ and in Tab. A.3 for $PU = 200$. 185
4.30 Category *doubleEMTFsingleME0*: maximum signal efficiency (a) and number of triggerable signal events (b) in each 500 Hz slice for rate $R < 10\,\text{kHz}$. The total integrated luminosity considered is $\int \mathcal{L}\,dt = 3000\,\text{fb}^{-1}$. The details on each point are reported in Tab. A.4 for $PU = 140$ and in Tab. A.5 for $PU = 200$. 185

4.31 Category *tripleTK*: maximum signal efficiency (a) and number of triggerable signal events (b) in each 500 Hz slice for rate $R <$ 10 kHz. The total integrated luminosity considered is $\int \mathcal{L}\, dt =$ 3000 fb^{-1}. The details on each point are reported in Tab. A.6 for $PU = 140$ and in Tab. A.7 for $PU = 200$. 186
4.32 (a) Category *tripleME0*: comparison between the maximum number of triggerable events per 500 Hz slice offered by the cuts on ΔR radius and on $\Delta\eta - \Delta\phi$ separation (identified with the flags *DeltaR* and *Chi*); (b) Category *tripleME21*: comparison between the maximum number of triggerable events per 500 Hz slice offered by the cuts on ΔR radius and on $\Delta\eta - \Delta\phi$ separation with *diffDR* parameter set to 0.001, (indicated in the top right part of the plot). The same result has been obtained also for the other *diffDR* investigated values (0.01, 0.04, 0.07 and 0.10). In this case, only for the *Chi*-flagged cuts results were found in the rate region $R < 10$ kHz. In both figures, both $PU = 140$ and $PU = 200$ pileup scenarios are reported. 187
4.33 Category *tripleTK*: comparison between the maximum number of triggerable events offered by the cuts on ΔR radius and on the invariant mass of the TkMuon triplet (identified respectively with the flags *DeltaR* and *Mass*). 188
4.34 Summary of results obtained performing a logical OR between the most proficient trigger paths for $PU = 140$ (reported in Tab. A.4, Tab. A.2 and Tab. A.6) and for $PU = 200$ (reported in Tab. A.5, Tab. A.3 and Tab. A.7). On the left is reported the signal efficiency, while on the right the number of triggerable events, for a total integrated luminosity of 3000 fb^{-1}. 188

List of Tables

2.1 Example of electric fields normalised to the maximum one, $E_{GEM\,1}$. These data refer to the CMS GE-1/1/01 Super-Chamber. GE1/1 chambers adopt a design 3/1/2/1 mm for the gap spacing. 55

3.1 Estimated time for each main step in the production of a GE1/1 Super-Chamber. 83
3.2 Meaning of the status bits in the HV 12-bit status code for a CAEN A1515TG board. 106
3.3 Meaning of the status bits in the LV 16-bit status code for a CAEN A3015/A3015HP board. 107

4.1 Channels contributing to the production of tau leptons at the LHC. The charge conjugate states are included in the estimation [91] 144
4.2 $\Delta\phi$ threshold values designed to select 95% of muons with a fixed p_t. 150
4.3 $\Delta\eta$ coverage of each ME0 η-partition. 154
4.4 Bi-gaussian fit parameters for $\Delta\eta - \Delta\phi$ segments separations seen in the 1st and 6th ME0 layer. 155
4.5 Features of the Q values which define the concentration ellipses, with the relative fraction of events enclosed inside of the ellipses for bi-gaussian distributed random variables. 156
4.6 ΔR radius cuts for the ME0 segments. The *DeltaR0* flag indicates the setting where the ΔR radius cut is not applied. . . . 157
4.7 $\Delta\phi$ bending thresholds set for ME1/1 and ME2/1 CSCCorrelatedLCTs. 159
4.8 Quality thresholds adopted for ME1/1 and ME2/1 CSCCorrelatedLCTs. *Quality0* is the flag when no quality cut is applied. *Quality1* gives only a minimal contribution, but it has been defined anyway to try to keep the highest possible fraction of signal events. The specific description of the meaning of the different quality codes is reported in [102]. 160

4.9 Cuts applied on LCT η position: the table reports the values which are rejected by each selection. The *Veto0* is the flag when no selection is applied. 160
4.10 Bi-gaussian fit parameters for $\Delta\eta - \Delta\phi$ LCTs separations seen in the ME1/1 and ME2/1 stations. 160
4.11 ΔR radius cuts for the ME11 LCTs. The *DeltaR0* flag indicates the setting where the ΔR radius cut is not applied. 162
4.12 ΔR radius cuts for the ME21 LCTs. The *DeltaR0* flag indicates the setting where the ΔR radius cut is not applied. 162
4.13 Features of quality cuts used for EMTF tracks. The *Quality0* flag indicates the setting where the quality cut is not applied. 166
4.14 ΔR radius cuts for the EMTF tracks. The *DeltaR0* flag indicates the setting where the ΔR radius cut is not applied. . . . 167
4.15 Categories involving EMTF tracks. All of them require three input objects and their description is provided in the second column. 168
4.16 Reduced χ^2 cuts used for the TkMuons. The *Quality0* flag indicates the setting where the reduced χ^2 cut is not applied. In the last column, the fraction of TkMuons included in the selection range is reported. 169
4.17 Features of cuts on curvature $1/r$ used for TkMuons. The *Charge0* flag indicates the setting where the cut is not applied. 170
4.18 Cuts on the z-coordinate of POCA of TkMuons. To be used, a TkMuon has to present a POCA with $|z|$ higher than the threshold illustrated in the second column ($|z_{POCA}| > z_{threshold}$). 170
4.19 ΔR radius cuts used for the TkMuons. The *DeltaR0* flag indicates the setting where the ΔR radius cut is not applied. . . . 171
4.20 Invariant mass $m_{\mu\mu\mu}$ cuts used for the TkMuons. The *Mass0* flag indicates the setting where the cut is not applied. 172
4.21 Summary of highest efficiency results obtained by categories *singleEMTFdoubleME0*, *doubleEMTFsingleME0* and *tripleTK* and by their logical OR, in the rate region $R < 10\,\text{kHz}$. In the table are reported the trigger efficiency (ϵ), the trigger rate (R) and the number of triggerable events (N) referred to $3000\,\text{fb}^{-1}$ integrated luminosity. 181
4.22 Summary of highest efficiency results obtained by categories *singleEMTFdoubleME0*, *doubleEMTFsingleME0* and *tripleTK* and by their logical OR, in the rate region $R < 1\,\text{kHz}$. In the table are reported the trigger efficiency (ϵ), the trigger rate (R) and the number of triggerable events (N) referred to $3000\,\text{fb}^{-1}$ integrated luminosity. 181

A.1 Meaning of each p_t index for triple selections with a cut on p_t. 194

A.2 Category *singleEMTFdoubleME0*: details on the selections that, in $PU = 140$ conditions, achieved the maximum efficiency in 500 Hz slices with trigger rate $R < 10$ kHz. Inside the square brackets, the description of the p_t cut is reported, with the last number indicating the p_t threshold for the EMTF track involved in the selection, and the first and second numbers indicating the p_t ($\Delta\phi$ bending) threshold required on the ME0 segments pair. The first flag is applied to the segment with the highest bending in the pair (lowest p_t), while the second flag is applied to the segment with the lowest bending in the pair (highest p_t). The details on ME0 $\Delta\phi$ thresholds are provided in section 4.5.1.1. In the last three columns the signal efficiency, the trigger rate and the number of triggerable events in an integrated luminosity of 3000 fb^{-1} are reported. 196

A.3 Category *singleEMTFdoubleME0*: details on the selections that, in $PU = 200$ conditions, achieved the maximum efficiency in 500 Hz slices with trigger rate $R < 10$ kHz. Inside the square brackets, the description of the p_t cut is reported, with the last number indicating the p_t threshold for the EMTF track involved in the selection, and the first and second numbers indicating the p_t ($\Delta\phi$ bending) threshold required on the ME0 segments pair. The first flag is applied to the segment with the highest bending in the pair (lowest p_t), while the second flag is applied to the segment with the lowest bending in the pair (highest p_t). The details on ME0 $\Delta\phi$ thresholds are provided in section 4.5.1.1. In the last three columns the signal efficiency, the trigger rate and the number of triggerable events in an integrated luminosity of 3000 fb^{-1} are reported. 197

A.4 Category *doubleEMTFsingleME0*: details on the selections that, in $PU = 140$ conditions, achieved the maximum efficiency in 500 Hz slices with trigger rate $R < 10$ kHz. Inside the square brackets the description of the p_t cut is reported, with the first and second numbers indicating the p_t threshold applied respectively on the trailing and leading p_t tracks in the pair of EMTF tracks involved in the selection, and the last number indicating the p_t ($\Delta\phi$ bending) threshold required on the ME0 segment. The details on ME0 $\Delta\phi$ thresholds are provided in section 4.5.1.1. In the last three columns the signal efficiency, the trigger rate and the number of triggerable events in an integrated luminosity of 3000 fb^{-1} are reported. 198

A.5 Category *doubleEMTFsingleME0*: details on the selections that, in $PU = 200$ conditions, achieved the maximum efficiency in 500 Hz slices with trigger rate $R < 10$ kHz. Inside the square brackets the description of the p_t cut is reported, with the first and second numbers indicating the p_t threshold applied respectively on the trailing and leading p_t tracks in the pair of EMTF tracks involved in the selection, and the last number indicating the p_t ($\Delta\phi$ bending) threshold required on the ME0 segment. The details on ME0 $\Delta\phi$ thresholds are provided in section 4.5.1.1. In the last three columns the signal efficiency, the trigger rate and the number of triggerable events in an integrated luminosity of 3000 fb^{-1} are reported. 199

A.6 Category *tripleTK*: details on the selections that, in $PU = 140$ conditions, achieved the maximum efficiency in 500 Hz slices with trigger rate $R < 10$ kHz. Inside the square brackets the description of the p_t cut is reported, with the first, second and third number indicating the p_t threshold applied respectively on the trailing, medium and leading p_t tracks in the triplet of TkMuons involved in the selection. In the last three columns the signal efficiency, the trigger rate and the number of triggerable events in an integrated luminosity of 3000 fb^{-1} are reported. 200

A.7 Category *tripleTK*: details on the selections that, in $PU = 200$ conditions, achieved the maximum efficiency in 500 Hz slices with trigger rate $R < 10$ kHz. Inside the square brackets the description of the p_t cut is reported, with the first, second and third number indicating the p_t threshold applied respectively on the trailing, medium and leading p_t tracks in the triplet of TkMuons involved in the selection. In the last three columns the signal efficiency, the trigger rate and the number of triggerable events in an integrated luminosity of 3000 fb^{-1} are reported. 201

A.8 Details on trigger path OR for $PU = 140$, performed using the most proficient trigger paths indicated in Tab. A.2, Tab. A.4 and Tab. A.6. In the path description, Q stands for *Quality*, C for *Charge*, V for *VtxZ*, DR for *DeltaR* and M for *Mass*. In the right columns are reported in order the signal efficiency ϵ, the trigger rate R and the number of triggerable events N, for a total integrated luminosity of 3000 fb^{-1}. 202

A.9 Details on trigger path OR for $PU = 200$, performed using the most proficient trigger paths indicated in Tab. A.3, Tab. A.5 and Tab. A.7. In the path description, Q stands for *Quality*, C for *Charge*, V for *VtxZ*, DR for *DeltaR* and M for *Mass*. In the right columns are reported in order the signal efficiency ϵ, the trigger rate R and the number of triggerable events N, for a total integrated luminosity of 3000 fb^{-1}. 203

Contents

List of Figures i

List of Tables xvi

Introduction 1

1 The LHC accelerator and the CMS experiment 5
- 1.1 The Large Hadron Collider . . . 5
  - 1.1.1 Luminosity . . . 7
  - 1.1.2 The LHC experiments . . . 8
- 1.2 Particle physics at the LHC . . . 8
  - 1.2.1 The Higgs boson . . . 9
- 1.3 The CMS experiment . . . 11
  - 1.3.1 General design . . . 12
  - 1.3.2 The superconducting magnet . . . 13
  - 1.3.3 Inner Tracker . . . 14
  - 1.3.4 Calorimeters . . . 16
  - 1.3.5 Muon system . . . 17
  - 1.3.6 Trigger system . . . 25
    - 1.3.6.1 Level-1 Trigger . . . 26
    - 1.3.6.2 High Level Trigger . . . 28
- 1.4 The CMS and LHC upgrades . . . 28
  - 1.4.1 Overview . . . 28
  - 1.4.2 CMS challenges for HL-LHC . . . 30
    - 1.4.2.1 High pileup . . . 30
    - 1.4.2.2 High radiation dose . . . 31
    - 1.4.2.3 Summary of CMS upgrades for HL-LHC . . . 32

2 The CMS GEM upgrade 37
- 2.1 History and evolution of gaseous detectors . . . 37
  - 2.1.1 First gas detectors . . . 37
  - 2.1.2 The Multi-Wire Proportional Chamber (MWPC) . . . 39

2.1.3 The Micro Strip Gas Chamber (MSGC) . . . 41
2.1.4 The MIcro MEsh GAseous Structure (MICROMEGAS) 43
2.1.5 The Gas Electron Multiplier (GEM) . . . 44
2.1.5.1 GEM foil manufacturing . . . 45
2.1.5.2 Single GEM detector . . . 46
2.1.5.3 Double GEM detector . . . 50
2.1.5.4 Triple GEM detector . . . 52
2.2 The GE1/1 station . . . 58
2.2.1 Design of a single chamber . . . 60
2.2.2 Services of GE1/1 chambers . . . 64
2.2.2.1 HV system . . . 65
2.2.2.2 The LV system . . . 65
2.2.2.3 The gas system . . . 66
2.2.2.4 The cooling system . . . 67
2.2.2.5 The Detector Control System (DCS) . . . 67
2.2.2.6 The Detector Safety System (DSS) . . . 68
2.2.2.7 The back-end electronics . . . 68
2.2.2.8 The front-end electronics . . . 69
2.3 The GE2/1 station . . . 73
2.4 The ME0 station . . . 74
2.4.1 Impact on physics in the forward region . . . 76

3 GE1/1 quality control and commissioning 81
3.1 Production and quality control of GE1/1 chambers . . . 81
3.1.1 QC1: the material inspection . . . 83
3.1.2 QC2: the leakage current test . . . 84
3.1.3 The assembly . . . 85
3.1.4 QC3: the gas leak test . . . 86
3.1.5 QC4: HV test in CO_2 . . . 86
3.1.6 QC5: Gas gain and uniformity response measurement . 87
3.1.6.1 Effective gas gain measurement . . . 87
3.1.6.2 Gas gain uniformity . . . 88
3.1.7 QC6: HV stability test . . . 89
3.1.8 QC7: electronics test . . . 92
3.1.8.1 Two chamber equipment phases in QC7 . . . 93
3.1.8.2 Procedure in QC7 . . . 93
3.1.9 Chamber coupling . . . 100
3.1.10 QC8: cosmic test . . . 100
3.1.10.1 The experimental setup of the QC8 cosmic stand 101
3.1.10.2 Procedure in QC8 . . . 107
3.1.10.3 Monitoring of HV and LV . . . 108
3.2 Operation of chambers at P5 . . . 111
3.2.1 HV on-line monitor . . . 114
3.2.2 HV and LV off-line monitor . . . 116

3.2.2.1 Main features of the HV monitoring 117
3.2.2.2 LV monitoring 120
3.2.2.3 Study of HV trip rates 123
3.2.2.4 Operation during the CMS magnet commissioning. 125
3.2.2.5 Conclusion 131

4 A trigger study on $\tau \to 3\mu$ channel for the Phase 2 upgrade 143
4.1 The $\tau \to 3\mu$ decay 143
4.2 Production at the LHC 144
4.3 Simulation environment 145
4.3.1 Used samples 146
4.4 Features of the signal sample 147
4.5 Objects used in the study 148
4.5.1 ME0 segments 149
4.5.1.1 Cut on the $\Delta\phi$ bending angle 149
4.5.1.2 Cut on quality 152
4.5.1.3 Cut on η position 153
4.5.1.4 Cut on $\Delta\eta - \Delta\phi$ separation 153
4.5.1.5 Cut on ΔR radius 156
4.5.2 CSCCorrelatedLCT of ME1/1 and ME2/1 157
4.5.2.1 Cut on the $\Delta\phi$ bending angle 158
4.5.2.2 Cut on quality 159
4.5.2.3 Cut on η position 159
4.5.2.4 Cut on $\Delta\eta - \Delta\phi$ separation 160
4.5.2.5 Cut on ΔR radius 161
4.5.2.6 Cut on diffDR 161
4.5.3 EMTF tracks 163
4.5.3.1 Cut on p_t 163
4.5.3.2 Cut on charge 165
4.5.3.3 Cut on quality 166
4.5.3.4 Cut on ΔR radius 166
4.5.3.5 Selection categories involving EMTF tracks . 167
4.5.4 TkMuons 168
4.5.4.1 Cut on p_t 168
4.5.4.2 Cut on reduced χ^2 169
4.5.4.3 Cut on charge 169
4.5.4.4 Cut on POCA (Point Of Closest Approach) position 170
4.5.4.5 Cut on ΔR radius 170
4.5.4.6 Cut on invariant mass 171
4.6 Efficiency and rate results 173
4.6.1 Visualization of results 174
4.6.2 Summary of results for each category 176

4.6.3 Summary of results for three most profitable categories 177
4.6.4 Comparison between similar cuts 178
4.6.5 Logical OR among the three best categories 179
4.6.6 Conclusion and future outlook 180

5 Conclusion **189**

Appendices **191**

A Additional information about the trigger study **193**
A.1 Samples used in the trigger study 193
A.2 Main labels of p_t cuts 194
A.3 Details on trigger best categories 195
A.3.1 Details on singleEMTFdoubleME0 category 195
A.3.2 Details on doubleEMTFsingleME0 category 195
A.3.3 Details on tripleTK category 195
A.4 Details on trigger OR results 195

Bibliography **204**

Introduction

Since the end of 2018, the CERN Large Hadron Collider (LHC) accelerator started an upgrade campaign with the objective of increasing the proton-proton collisions center of mass energy to $\sqrt{s} = 14\,\text{TeV}$ and running at instantaneous luminosity around $5{-}7{\cdot}10^{34}\,\text{cm}^{-2}\text{s}^{-1}$, with the final goal of delivering a $3000\,\text{fb}^{-1}$ integrated luminosity. In this context the LHC experiments started as well an upgrade campaign, to cope with the future experimental conditions, in terms of background radiation and events pileup.

The CMS experiment, in particular, started, among others, an upgrade of the muon system, programming the installation of three new stations based on the GEM (Gas Electron Multiplier) technology, called GE1/1, GE2/1 and ME0. These new stations will increase the redundancy of the muon system, help to keep under control the trigger rate and improve the muon p_t measurement. In addition, the ME0 station is supposed to increase also the coverage of the muon system up to $|\eta| < 2.8$. These detectors are characterised by a high radiation hardness, to ensure they survive in the high radiation environment foreseen during the High Luminosity LHC phase.

This thesis work took place in the context of the production, installation and commissioning of the GE1/1 system. In the first and second chapters, the GEM upgrade is introduced, focusing in particular on the GE1/1 station. In the third chapter, the discussion moves then to the description of the production and validation protocols of the chambers, illustrating all the steps and quality controls that a detector has to overcome to be installed in the CMS experiment.

In the second part of this chapter, all the activities performed during the detectors commissioning are illustrated, focusing on the tools I developed for the monitoring of the GE1/1 power systems and on the role of HV trips in the detectors' operation, in particular during the CMS magnet commissioning and the early LHC collisions performed at the end of LS2 (end of October 2021).

Finally, in the fourth chapter, a trigger study for Phase 2 dedicated to the $\tau \to 3\mu$ decay channel is presented: this decay is a case study since it is a Lepton Flavour Violating decay with a very suppressed branching ratio in the standard model. A higher branching ratio is foreseen by some Beyond Stan-

dard Model models, opening the possibility to observe a statistically significant signature. This possibility led to the development of trigger algorithms dedicated to this channel.

In this chapter I will show how the study exploits the upgrades programmed for CMS in Phase 2, looking in particular at the possibilities introduced by the new muon GEM stations.

Since this channel involves many muons in the final state, with low p_t and mainly reconstructed in the experiment endcap region, where the background plays an important role in the signal selection, decays with similar features could benefit from the study performed on this particular channel as well.

Chapter 1

The LHC accelerator and the CMS experiment

1.1 The Large Hadron Collider

The Large Hadron Collider (LHC) is the biggest and most powerful particle accelerator in the world. Its construction was approved in 1994 by the European Organization for Nuclear Research and took around 10 years of work, from 1998 to 2008, when the first beams of protons have been delivered in the accelerator. The LHC is located in an underground circular tunnel, 26.7 km long and from 45 m to 170 m below the surface. The tunnel was built between 1984 and 1989 to host up to the year 2000 the Large Electron Positron (LEP) collider, a machine used to make precision Standard Model measurements, colliding electron and positron bunches up to a center of mass energy of 209 GeV. The LHC accelerates and collides bunches of protons, up to a center of mass energy of 13 TeV. The choice of protons is of primary importance for the discovery of new physics processes, for two main reasons:

- the higher mass of the protons with respect to electrons allows to increase the energy of bunches, since the emission of synchrotron radiation scales as m^{-4}, where m is the mass of the accelerated particle;
- the hadronic nature of protons allows to explore a wider range of energies since in hard collisions interaction of quarks and gluons occurs, that carry only a fraction of the proton momentum.

This increase in the center of mass energy collision is significant for the discovery of high mass particles which were not accessible in the energy range of previous accelerators, or to increase the production cross section of particles, like the Higgs boson, whose production cross section increases with the energy.

The LHC is the last and most powerful of a large complex of accelerators, used to increase the energy of proton bunches in several steps. Until 2020, the

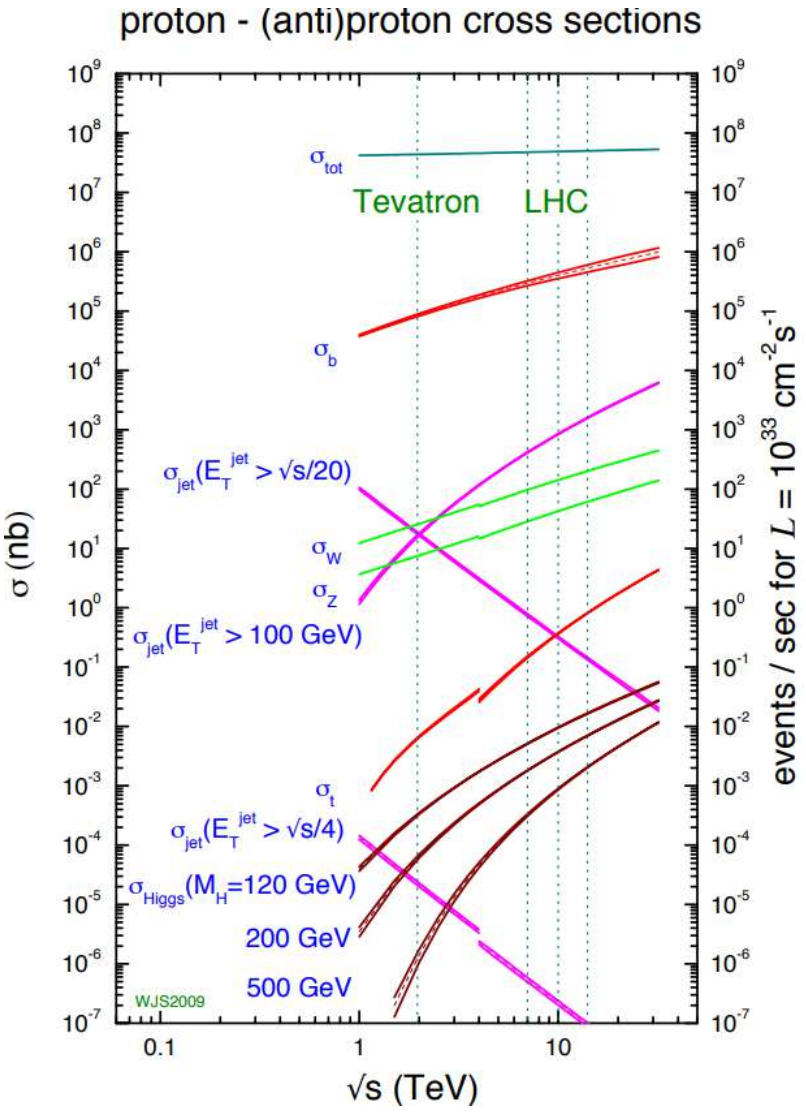

Figure 1.1: Production cross section of several processes in proton-(anti)proton collisions as a function of center of mass collision energy [1].

first step consisted in producing a bunch of protons ionising a volume of hydrogen, which was then introduced in the linear accelerator Linac2, bringing the energy of protons up to 50 MeV and injecting this in the Proton Synchrotron Booster (PSB). In 2020, Linac2 has been replaced by Linac4, which accelerates a bunch of negative hydrogen ions H^- up to 160 MeV; immediately before the injection in PSB the electrons are stripped from the hydrogen ions, leaving only protons.

In PSB protons are accelerated up to an energy of 2 GeV and then PSB feeds the Proton Synchrotron (PS), a 628.3 m accelerator which brings the energy of protons up to 28 GeV. The PS splits the PSB bunches in smaller ones, hosting up to 72 bunches in one cycle, and spaces them of 25 ns, the same

spacing of the LHC. The accelerator fed by PS is the 6.9 km long Super Proton Synchrotron (SPS), which accelerates the proton bunches up to 450 GeV. In 2016, looking to the increase in luminosity of the accelerators in the following decade, a new beam production scheme called Batch Compression Merging and Splitting (BCMS) was introduced, fixing to 144 the maximum number of bunches hosted by SPS per cycle. After a bunch has been fully accelerated by SPS, it is introduced in the LHC which accelerates it to 6.5 TeV, the maximum available energy up to now for the beams. In particular, during the filling of the LHC, the bunches are divided among the two rings of the LHC, which circulate the beams in opposite directions and host a maximum of 2556 bunches per ring. In this way when the two bunches collide the energy in the center of mass will be 13 TeV.

Furthermore, the LHC can be used also as a heavy ion accelerator, when instead of protons it is filled with lead ion $^{208}Pb^{82+}$ bunches. These ions are initially accelerated by the linear accelerator Linac3 up to 4.2 MeV, then accumulated in the Low-Energy Ion Ring accelerator and their energy is increased to 72 MeV. After this they are delivered to PS, SPS and finally to the LHC, reaching the final energy of 2.76 TeV per nucleon. In this case, the energy available in the center of mass for a lead-lead ions collision is 1.15 PeV.

The LHC manages to keep so energetic beams on the right curvature thanks to 1632 superconducting magnets placed all over its 27 km ring, capable of creating a $8.3\,T$ magnetic field. To achieve this result the magnets are cooled down with liquid helium to 1.9 K, a temperature at which helium is a super-fluid, maximizing its cooling power. The particular design of the LHC magnets has made possible to host both the LHC pipes inside the same cryostat, providing opposite sign magnetic fields for the protons/ions circulating in opposite directions in the two pipes, reducing by a significant amount the cost of doing the same job with two separated magnets.

1.1.1 Luminosity

In addition to the center of mass energy $\sqrt{s}$, another important parameter to describe the collider properties is its instantaneous luminosity $\mathcal{L}$, basically the number of collisions happening per unit of time and per unit of cross-sectional area of the intersecting beams. $\mathcal{L}$ depends on:

- the number of particles contained in the two beams, respectively n_1 and n_2;
- the collision frequency f_{coll};
- the rms of transversal widths of bunches with respect to the direction of collision σ_x^* and σ_y^*;
- a geometric factor $\mathcal{F}$ ($\mathcal{F} \leq 1$) which considers, for example, the finite bunch length and the intersection angle of bunches.

$$\mathcal{L} = f_{coll} \frac{n_1 n_2}{4\pi \sigma_x^* \sigma_y^*} \mathcal{F} \tag{1.1}$$

Knowing the collider luminosity and the interaction cross section of colliding particles σ_{int}, the number of interaction N in a time interval can be calculated

$$N = \sigma_{int} \int \mathcal{L}\, dt = \sigma_{int}\, L_{INTEGRATED}, \tag{1.2}$$

where $\int \mathcal{L}\, dt = L_{INTEGRATED}$ is called integrated luminosity and is usually measured in fb^{-1}. Up to now, the LHC has experienced different data-taking periods, increasing gradually its luminosity up to $2 \cdot 10^{34}\,\mathrm{cm}^{-2}\mathrm{s}^{-1}$, two times the original design luminosity of the LHC, reaching an integrated luminosity of $189.3\,\mathrm{fb}^{-1}$.

1.1.2 The LHC experiments

Along the LHC circumference, four points for the collision of beams have been designed, called Interaction Points (IP) and in these positions caverns to host experimental sites have been dug. The experiments hosted in these caverns are ATLAS (A Toroidal LHC ApparatuS) [2], placed at IP1, CMS (Compact Muon Solenoid) [3] at IP5, ALICE (A Large Ion Collision Experiment) [4] at IP2 and LHCb (Large Hadron Collider beauty experiment) [5] at IP8. When the construction of the LHC was approved, it was decided to build two experiments with the purpose of investigating in detail the Standard Model physics and searching for physics Beyond the Standard Model (BSM): ATLAS and CMS. Having two experiments concentrated on the same search and studying mainly events of the same type (proton-proton collisions at the same center-of-mass energy) is fundamental in order to have a measurement confirmation by two independent collaborations, for example, to confirm the discovery of the Higgs boson. The ALICE experiment is concentrated on the research on quark-gluon plasma, studying the collisions of lead-ions. Finally, the LHCb experiment is focused on bottom-quark physics, to investigate phenomena involving CP violation and to shed light on the matter-antimatter asymmetry in the universe.

1.2 Particle physics at the LHC

The LHC is designed to investigate unexplored fields of particle physics, thanks to its high energy, which unlocks high mass particle production, and luminosity, which increases the statistics available to study rare processes predicted by the Standard Model or to understand with higher precision already observed phenomena.

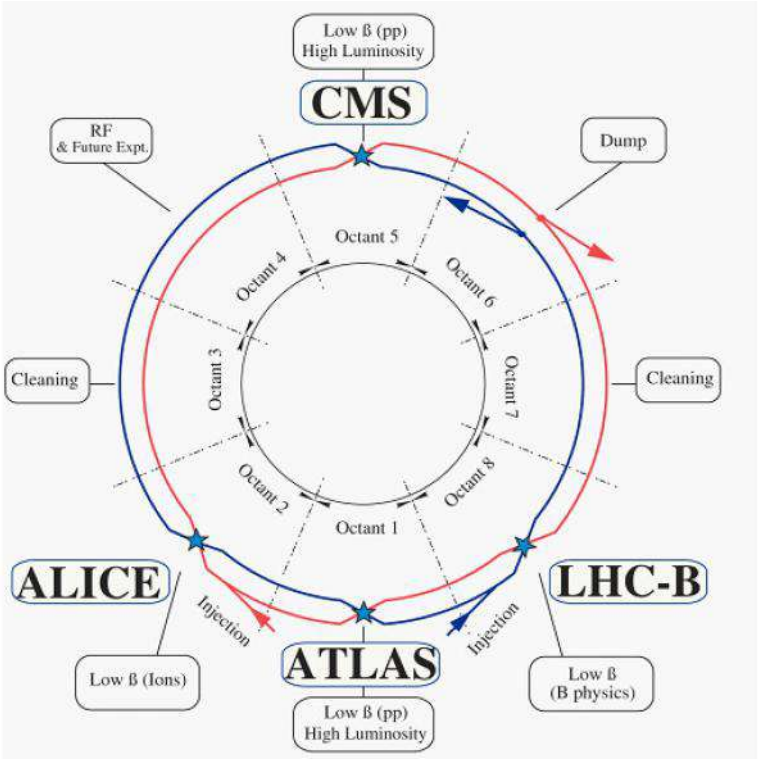

Figure 1.2: Schematic representation of the LHC with the position of the main experiments [6].

1.2.1 The Higgs boson

The most important and famous result obtained during the LHC years of operation is the discovery in 2012 by the ATLAS and CMS collaborations [7] [8] of a particle with a mass of $\sim$ 125GeV, which has been identified as the Higgs boson. This discovery has started a campaign of studies to understand if the properties of this "new" particle were in agreement with those predicted by the Standard Model for the Higgs boson.

The Higgs boson plays a particular game in the Standard Model: it allows the presence of massive particles in the Standard Model. In the Standard Model indeed the presence of massive particles breaks the symmetry $SU(3) \times SU(2) \times U(1)$ on which the model is built. The introduction of a neutral scalar boson with spin 0, allows maintaining the gauge symmetry through a mechanism called Brout-Englert-Higgs (BHE).

As shown in Fig. 1.1 at the LHC the Higgs boson production is pretty rare with respect to the production for example of beauty quarks, with a cross section several orders of magnitude smaller. Its production can happen through different channels and 4 main ones are illustrated for the LHC at $\sqrt{s} = 14\,\text{TeV}$ in the following list:

- the gluon-gluon fusion (Figure 1.3a) which is the dominant process at

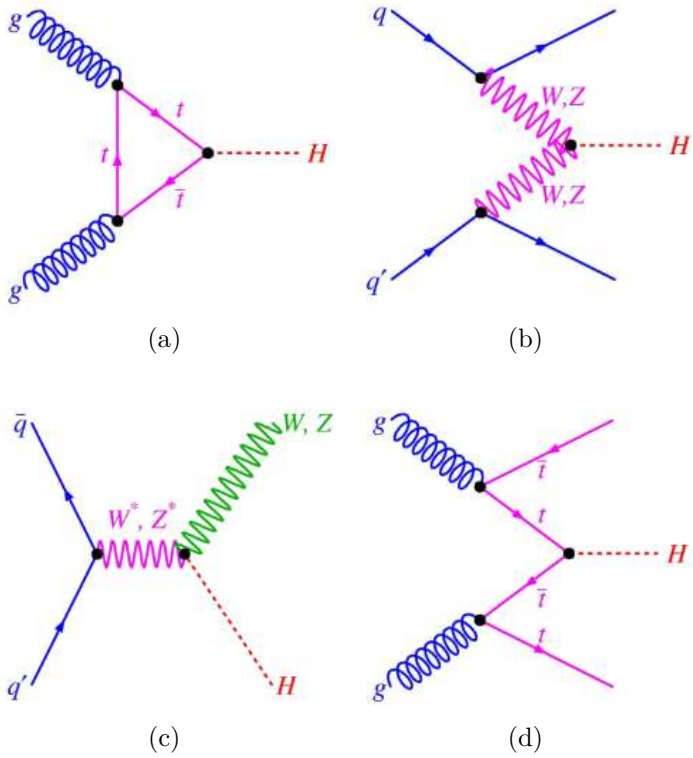

Figure 1.3: Leading order Feynman diagrams for Higgs boson production: (a) gluon-gluon fusion, (b) vector boson fusion, (c) Higgs-strahlung, (d) associated with a pair top of quarks [14].

the LHC (87% of the total production at $\sqrt{s} = 14\,\text{TeV}$ for a $125\,\text{GeV}$ Higgs boson);

- the vector boson fusion (Figure 1.3b) is the second most important for the production, and it consists in the emission of quarks, which will hadronise in jets, and one Higgs boson;
- the so-called Higgs-strahlung (Figure 1.3c), a process where a virtual vector boson decays in a real $W^{\pm}$ or Z boson emitting a Higgs boson;
- the production associated with a pair of top quarks (Figure 1.3d), which offers the possibility of studying the coupling of the Higgs boson to the top quark.

The Higgs boson was observed for the first time by the ATLAS and CMS experiments in 2012, analyzing the channels $\gamma\gamma$, ZZ, W^+W^-, $\tau^+\tau^-$, bb and $\mu^+\mu^-$. The highest contribution came from the channels $\gamma\gamma$ and $ZZ \to 4l$. In the following years, analysing data from various run periods, at different center of mass energies, integrated luminosities and investigating different

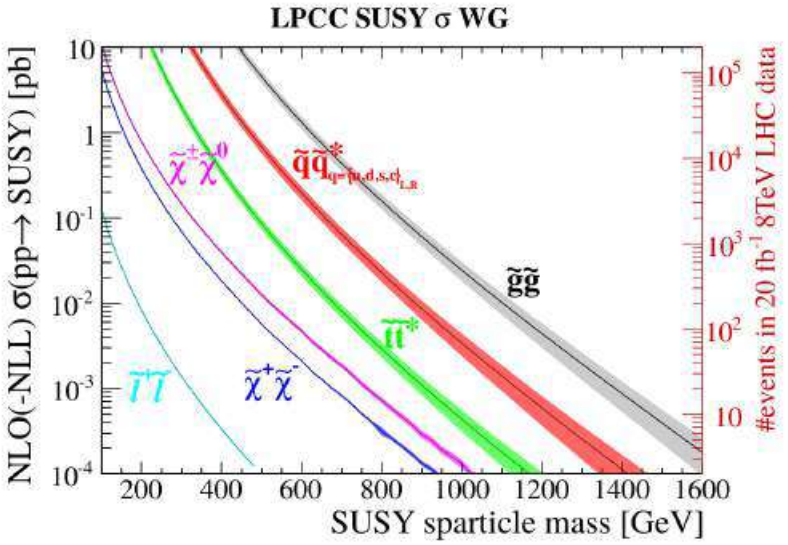

Figure 1.4: Production cross section of SUSY particles according to the Minimal Supersymmetric Standard Model, as a function of their mass [16].

channels, the measurements of the Higgs boson mass improved and the CMS experiment measured a mass of the Higgs boson of 125.35 GeV with a precision of 0.15 GeV [7], while the ATLAS experiment of 124.97 GeV with a precision of 0.24 GeV [8].

1.3 The CMS experiment

The CMS experiment is one of the four main experiments installed on the LHC ring, in particular, hosted in an underground cavern dug at the Interaction Point 5 (IP5) of the LHC. The main reasons that pushed the scientists to place the experiments in underground caverns are the practical limitations of installing a such large accelerator on surface in an inhabited area, and, furthermore, to contain in the cavern the radiations produced by the particle interactions, and to limit the flux of cosmic radiations on the detector, to have a lower source of noise on detectors. CMS has been designed with multiple goals, among which there are the discovery of the Higgs boson and the study of its properties, a deeper study of already known Standard Model processes and the study of physics Beyond the Standard Model (BSM) at the TeV energy scale. The high luminosity provided by the LHC is of primary importance for the study of rare processes, such as the production of supersymmetric particles (SUSY), which are supposed to have a production cross section of the order of $\sigma \sim$ pb (Fig. 1.4).

1.3.1 General design

The CMS detector is designed to provide a 4π coverage for the detection of particles and consists of a cylindrical barrel closed by two endcap disks on the bases of the cylinder. The detector is $\sim$ 21 m long, 15 m high (diameter of the cylinder) and with a weight of $\sim$ 14000 tons. A schematic representation can be found in Figure 1.5, where the main components and sub-detectors are represented.

Moving from the innermost to the outer part of the detector, the closest system to the interaction point (IP), where collisions take place, is the tracking detector, followed by the electromagnetic and hadronic calorimeters (ECAL and HCAL respectively). These detectors are enclosed in the bore of the superconducting magnet, followed in turn by the steel yoke and the Muon Spectrometer, which covers the outermost part of the detector and so the most extended surface.

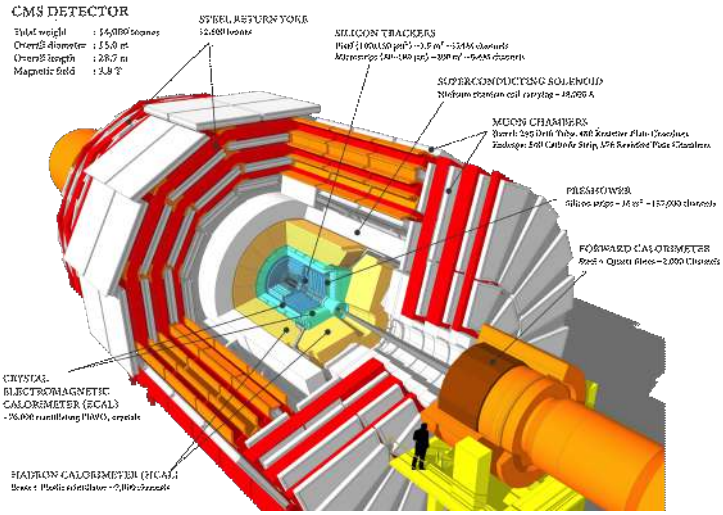

Figure 1.5: Cutaway representation of the CMS experiment, showing its main components and sub-detectors [18].

The coordinate system used in CMS consists of a x-axis pointing toward the center of the LHC ring, a y-axis pointing toward the surface and a z-axis parallel to the beam pipe and directed towards the Jura mountains; its origin position is placed in the IP. Another useful system is the spherical coordinates system, which uses the transverse distance from IP $R = \sqrt{x^2 + y^2}$, the azimuthal angle ϕ and the polar angle θ. The emission of particles is very dis-homogeneous with a lot more particles produced in the region covered by the endcaps and a lower number in the barrel, so to have a more uniform picture of particle directions, instead of θ, it is a practice to use the so-called *pseudorapidity* η, defined as

$$\eta = -\ln\left(\tan\frac{\theta}{2}\right). \tag{1.3}$$

A visual representation of these coordinate systems is shown in Fig. 1.6.

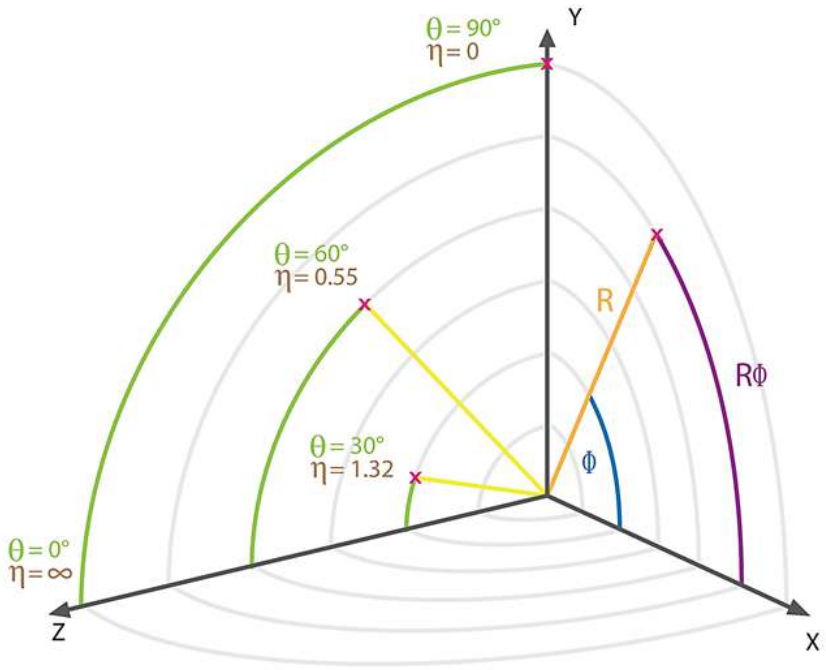

Figure 1.6: Scheme of the CMS coordinate system [19].

1.3.2 The superconducting magnet

In a particle physics experiment, the magnet is of primary importance since the magnetic field allows to determine the momentum and charge of the particles from the bending of their trajectory.

One peculiar feature of CMS is its compact design, made possible by the use of a superconducting solenoid, which provides a 3.8 T magnetic field parallel to the beampipe in the barrel region. In a solenoid indeed the bending of a track starts from $R = 0$, while in a toroid the magnetic field is present only inside the torus, so the bending of the trajectory starts only from the inner surface of the torus, requiring bigger dimensions for the apparatus [23].

The majority of CMS weight is given by the superconducting magnet, $\sim$ 300 tons, and the steel yoke, $\sim$ 12000 tons, used to contain the high magnetic field (3.8 T) produced by the superconducting magnet. The magnet is 12.5 m long and has an inner diameter of 5.9 m; the magnetic field is created using an impressive intense current of 19.14 kA, which can be sustained by cooling down the magnet to 4.5 K with a liquid helium cryogenic system, cooled itself with a liquid nitrogen cryogenic system.

A representation of the generated magnetic field is given in Figure 1.7b,

showing the uniformity of the magnetic field inside the solenoid and the distribution of the magnetic field "trapped" inside the steel return yoke.

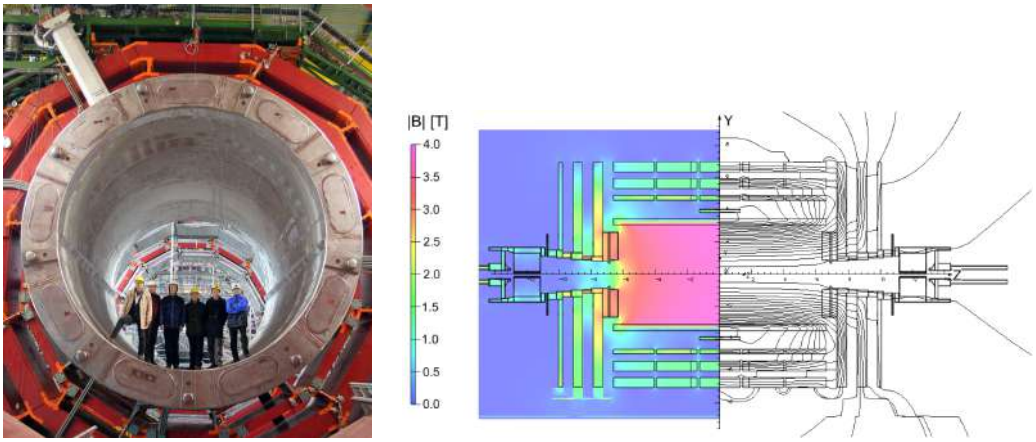

(a) (b)

Figure 1.7: (a) The superconducting magnet (grey) inserted inside the iron yoke (red) before the installation of any detector in the spaces available inside the iron yoke [24]; (b) the magnetic field created by the superconducting magnet in a longitudinal view of the CMS detector, with the field intensity on the left and the field lines on the right of the figure [25].

1.3.3 Inner Tracker

The CMS inner tracker is the sub-detector closest to the beampipe, bathed in a 3.8 T magnetic field, and it is designed to reconstruct charged particles in the region $|\eta| < 2.5$ with high efficiency and momentum resolution. In addition, its fast response enables this system to assign the reconstructed particles to the correct bunch crossing, fundamental for a correct collection of data. A fundamental task performed by the tracker is the reconstruction and distinction of both vertices produced by multiple interactions in the same bunch crossing, and displaced vertices generated by the weak decay of particles.

The tracker installed now in CMS has been designed to operate at the LHC design luminosity of $10^{34}\,\mathrm{cm}^{-2}\mathrm{s}^{-1}$, which produces a flux of ~ 1000 particles, with an average number of 20 pileup interactions per proton-proton collision event.

A cutaway representation of the inner tracker is reported in Figure 1.8. The overall shape is a cylinder 5.4 m long and with a diameter of 2.4 m, while in detail the system can be divided into two main parts: the inner part, made of pixel detectors, and the outer part, composed of microstrip detectors.

The pixel detector (Figure 1.9) is composed of three layers in the central part, installed at radii between 4.4 cm to 10.2 cm from the beampipe, and of two disks on each side of the cylinder, installed at $z = \pm 34.5$ cm and

$z = \pm 46.5\,\text{cm}$. These layers are segmented in 66 million rectangular pixels, providing to the pixel tracker a global spatial resolution of $15 - 20\,\mu\text{m}$ and coverage in the range $|\eta| < 2.5$.

On the other hand, the outer part of the inner tracker consists of silicon microstrip sensors, distributed in barrel layers and endcap disks, creating a structure similar to that of the pixel tracker. In particular, respectively 4 and 6 silicon microstrip layers compose the Tracker Inner Barrel (TIB) and the Tracker Outer Barrel (TOB), while 3 and 9 disks compose the Tracker Inner Disks (TID) and the Tracker Endcaps (TEC), as can be observed in detail in Figure 1.8.

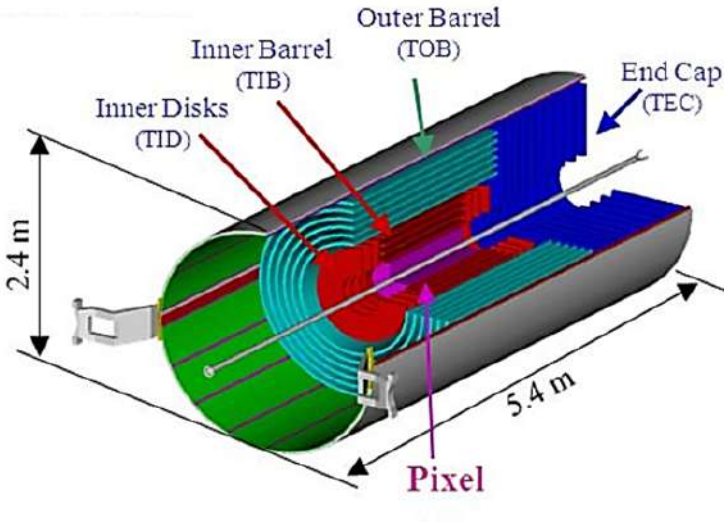

Figure 1.8: Cutaway representation of the CMS inner tracker, showing its main components [26].

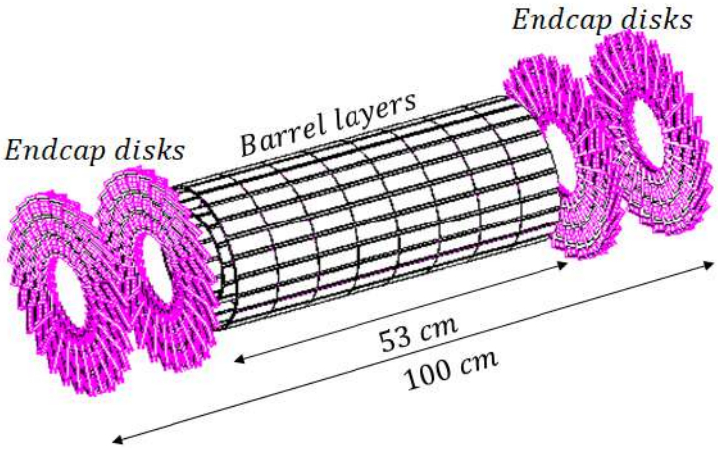

Figure 1.9: Cutaway representation of the pixel system of the CMS inner tracker, showing its endcap disks and barrel layers [26].

1.3.4 Calorimeters

CMS relies on two calorimeters for the measurement of particles energies, the electromagnetic calorimeter (ECAL) and the hadronic calorimeter (HCAL). The first provides an energy measurement of charged particles and photons, while the latter measures the energy of hadrons, providing a measurement of the overall energy of the jets generated by hadronization processes.

ECAL

ECAL is the innermost of the two calorimeters. Its design has been decided looking to the challenge of observing the Higgs boson in its decay channels $H \to \gamma\gamma$, $H \to ZZ^{(*)}$ and $H \to WW$, by detecting photons, electrons and positrons produced by the decay of the vector bosons. ECAL is in this way fundamental for the reconstruction of the Standard Model and new physics processes involving a leptonic decay: for example a decay involving gluinos and squarks, where the leptonic decay of these particles allows the measurement of their mass.

This calorimeter provides coverage in the pseudorapidity range $|\eta| < 3.0$. It is a homogeneous calorimeter and its basic building blocks are lead tungstate crystals ($PbWO_4$). This material has a radiation lenght $X_0 = 8.9\,\text{mm}$ and a Molière radius of 21.9 mm. The ECAL crystals are trapezoidal with a front square side, and their size is designed to exploit at best the properties of this material. The detector is composed, similarly to all the detectors in CMS, of a barrel and an endcap calorimeter (Fig. 1.10). The barrel calorimeter is composed of crystals with length of 230 mm (25.8 X_0), while the endcap crystals are 220 mm long (24.7 X_0). On the other hand, the size of the square side is adapted to the Molière radius, with $20 \times 20\,\text{mm}^2$ barrel crystals and $30 \times 30\,\text{mm}^2$ endcap crystals.

An additional system of ECAL is a preshower detector, installed in front of the crystals, providing coverage in the range $1.65 < |\eta| < 2.61$. Its main purpose is to provide a separation between photons and neutral pions. This detector is composed of layers of lead, $3X_0$ thick, and two layers of a silicon strip detector and layers of moderator, to moderate the flux of neutrons, as can be seen in Figure 1.11.

HCAL

The main purpose of the CMS hadron calorimeter is the measurement of the energy of jets produced by processes involving the hadronization of quarks and gluons, but also to suggest the presence of particles that do not interact into the detector measuring the missing transverse energy, such as neutrinos or supersymmetric particles.

HCAL is a sampling calorimeter divided into 4 systems: Hadron Barrel (HB), which covers the region $|\eta| < 1.39$, Hadron Endcap (HE), covering

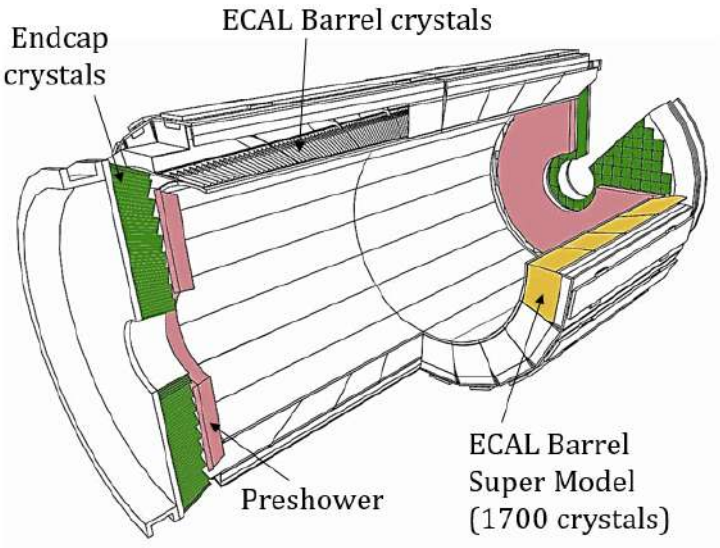

Figure 1.10: ECAL structure, with its barrel, endcap and preshower systems [27].

$1.30 < |\eta| < 3.00$, Hadron Outer (HO), covering $|\eta| < 1.26$ and Hadron Forward (HF), positioned at a longitudinal distance of 11.15 m from the origin of the CMS coordinate system. In particular, HB and HE are placed inside the superconducting magnet, while HO is placed immediately outside. Due to the limited space available inside the solenoid magnet, the depth of HB provides only 5.82 interaction lengths (λ_I) in its central region and $10.6\,\lambda_I$ at $|\eta| = 1.3$. To compensate for this limited depth at low η, it has been decided to introduce an additional layer outside the solenoid, called HO, increasing the depth to a minimum of $11.8\,\lambda_I$ in the central region.

The active part of the detector consists of plastic scintillator tiles, read out by wavelength-shifting plastic fibers; since the central systems of HCAL are placed inside the CMS superconducting magnet or immediately outside, the materials composing the detector experience the 3.8 T magnetic field and therefore the absorber material of the calorimeter must be a non-magnetic one. Accordingly, the absorber material is brass for the internal HCAL layers and stainless steel for the front and back HCAL sides. Stainless steel is used both for its non-magnetic properties, but also to increase the mechanical strength of the detector.

The detailed structure of HCAL is shown in Figure 1.12

1.3.5 Muon system

A powerful method for the identification of signatures of interesting processes over the high background rate of events expected at the LHC, and even more in the High Luminosity phase of the LHC, is muon detection. The most

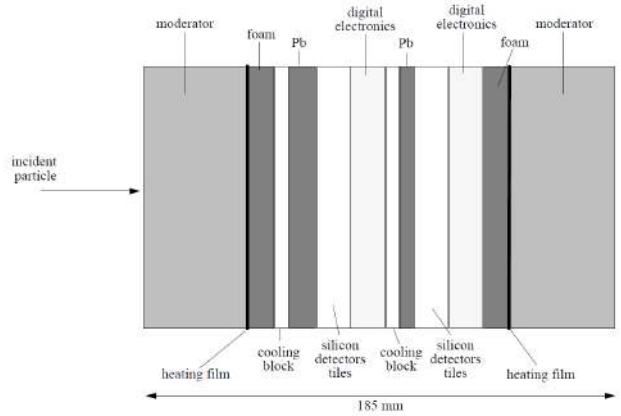

Figure 1.11: Structure of the preshower detector installed in front of ECAL [27].

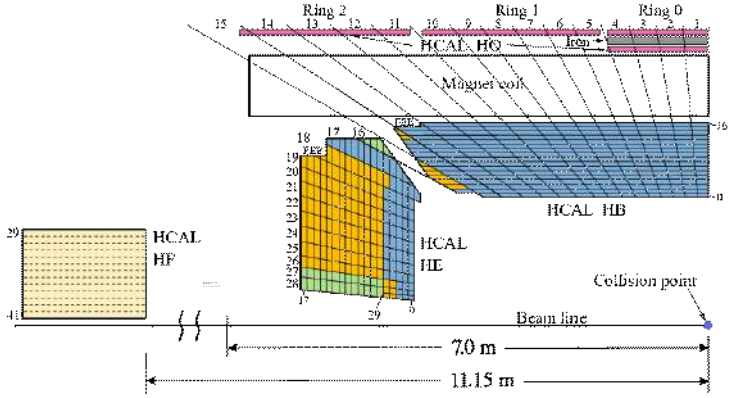

Figure 1.12: Scheme of CMS Hadron Calorimeter, with its main systems: the Hadron Barrel calorimeter (HB), Hadron Outer (HO), Hadron Endcap (HE) and Hadron Forward (HF) [29].

obvious example of channels with muons in their final state is the decay of the Higgs boson in ZZ or ZZ^*, decaying in turn into 4 leptons.

For this channel, the maximum mass resolution is achieved if all the leptons are muons, because the radiative loss of muons in the tracker material is lower than that experienced by electrons. The role played by the muon spectrometer is fundamental to provide a good p_T resolution to the reconstructed standalone muons, that goes as $\sim 1/L^2$, where L is the length of the reconstructed track. This information is useful in particular for the CMS L1 trigger and High Level Trigger systems to select the most interesting bunch crossing events. In addition the muon system starts to play an important role also in offline p_T measurement for very high p_T muons ($\sim 1\,\text{TeV}$). This particular example and others predicted by SUSY models show the discovery potential of muon final states and the necessity to equip CMS with a powerful muon detection system, with wide angular coverage.

Its main purposes are muon identification, momentum measurement and triggering. The good muon momentum resolution and trigger capability are provided by the solenoidal magnet and its flux-return yoke. The muon detection is moreover improved by the absorption of hadrons performed by the return yoke.

The muon system is composed of a barrel and two endcap sections and consists of a total detection surface of 25000 m^2. To cover a so wide area muon detectors must be inexpensive, reliable and robust. Its design is addressed to the momentum and charge measurement over the entire kinematic range of the LHC and up to Run 2 consisted of three different kinds of gaseous detectors: Drift Tubes (DT), Resistive Plate Chambers (RPC) and Cathode Strip Chambers (CSC). In 2019 the installation of the first station of Gas Electron Multiplier (GEM) detectors has started, which will increase the redundancy in the muon reconstruction and will help to keep under control the trigger rate in the High Luminosity phase of the LHC.

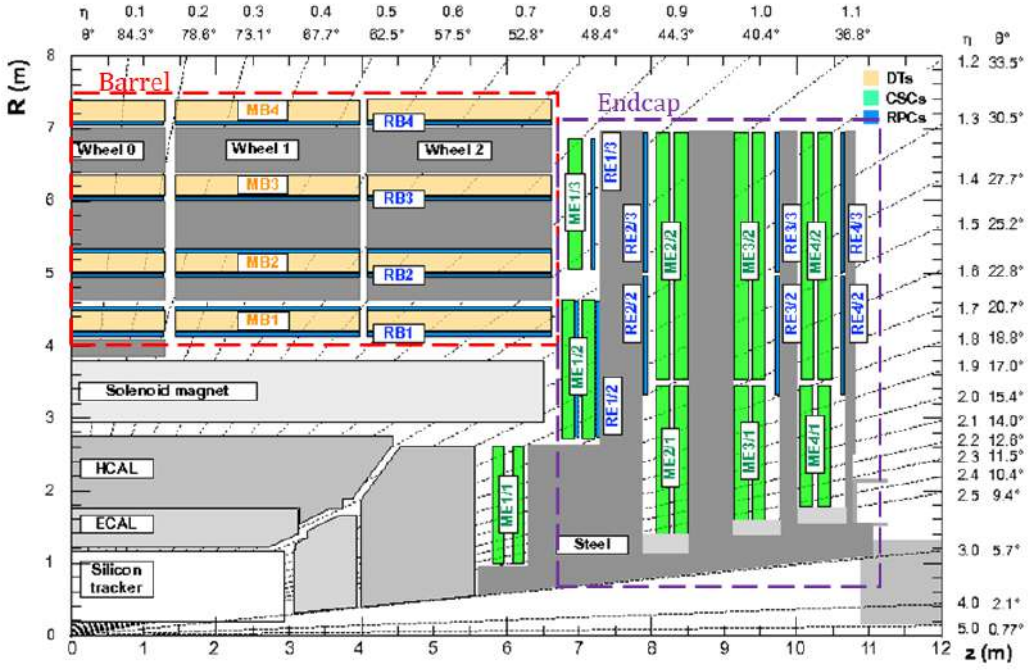

Figure 1.13: View of a quadrant of the CMS Muon Spectrometer in the plane R-z at the end of Run-2 [32].

As shown in Figure 1.13, the detectors used in the barrel region are Drift Tube chambers, that will operate in a region with a small neutron-induced background, with a muon rate smaller than that expected in the endcaps and with a uniform magnetic field mostly contained in the steel yoke. DT chambers cover the pseudorapidity range $|\eta| < 1.2$ and are organised in 4 different concentric stations MB1, MB2, MB3 and MB4. In the endcaps, where the muon rate and the background level are higher and the magnetic field is lower

and non-uniform, a different technology must be used. In these conditions high temporal and spatial resolution and high radiation hardness are required: these requirements are met by Cathode Strip Chambers. CSCs are organised in 4 stations, ME1, ME2, ME3 and ME4, positioned at increasing z values and cover the angular range $0.9 < |\eta| < 2.4$ and with the detector planes oriented in the direction perpendicular to the beampipe. Finally, both the 2 endcaps and the barrel are instrumented with Resistive Plate Chambers, covering the angular range $|\eta| < 1.9$ and organised in stations RB1, RB2, RB3 and RB4 in the barrel and RE1, RE2, RE3 and RE4 in the endcaps. Because of their fast response time, RPCs are used to assign unambiguously the reconstructed muons to the correct bunch crossing.

Drift Tubes (DT)

The barrel region is characterised by a pretty uniform magnetic field, mostly contained in the flux-return yoke, by a small neutron-induced background and by a small muon rate, which traduces in weaker requirements in terms of occupancy and radiation hardness for the detectors that will operate in this region. Drift Tubes chambers meet these requirements and are organised in 5 longitudinal wheels (Wheels 0, ±1, ±2), each divided into 4 concentric stations (from MB1 to MB4), as shown in Figure 1.14. A total of 250 DT chambers are installed in the CMS muon spectrometer.

As shown in Figure 1.15a, a DT chamber is composed of 3 (or 2 for MB4 chambers) super-layers (SL), each of them made of 4 layers of rectangular drift cells. The drift cells of one layer are staggered with respect to the cells of the layer nearby, to maximize the angular coverage offered by the detector and to solve the left-right ambiguity in the muon trajectory reconstruction. From a single-hit in a drift tube is indeed impossible to know which side of the wire, placed at the center of the tube, was crossed by the particle. In addition, this design allows to measure the track crossing time, applying a "mean-timer" algorithm, which requires at least 3 hits per super-layer.

The drift cell ($42\,\text{mm} \times 13\,\text{mm}$) is the basic component of each chamber and its layout is illustrated in Figure 1.15b. The cell is rectangular and its frame consists of two parallel aluminium planes and two "I"-shaped aluminium beams. The aluminium frame is at ground potential. Inside each cell are installed:

- two cathode strips installed on the I-beams and set to $-1200\,\text{V}$,
- two electrode strips applied to the aluminium parallel plates and set to $+1800\,\text{V}$,
- a $50\,\mu\text{m}$ wide and from 2 m to 4 m long stainless steel anode wire (respectively for smallest and largest chambers), placed at the center of the cell, set to $+3600\,\text{V}$.

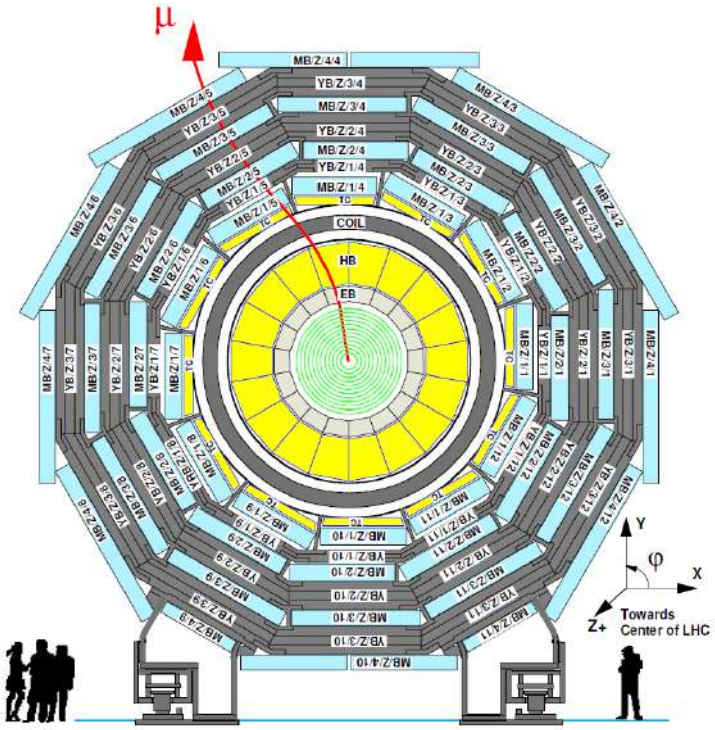

Figure 1.14: View in x-y plane of the layout of CMS DT chambers in one of the wheels. The trajectory followed by a muon is also represented, bending in two different directions due to the different verse of the magnetic field inside the superconducting magnet and inside the return yoke [33].

In particular, Figure 1.15a shows that in the external SLs the wires are oriented parallel to the beampipe, and in the central SL the wires are perpendicular to the beampipe direction. In this way, the external layers are appointed to measure the $R-\phi$ coordinates of ionisations left by a particle passing through the chamber, while the central layer measures the $r-z$ coordinates. The central layer is missing in the outermost DT station (MB4).

As all the detectors installed in the muon spectrometer, DTs are gaseous detectors and, in particular, use a gas mixture Ar/CO_2 (85/15). When a charged particle passes through the detector volume, an ionisation is produced inside the gaseous medium and the ions and electrons drift respectively towards the cathode and the anode of the drift cell. The muon crossing distance from the single wire is determined by a dedicated algorithm which derives it from the signal time of arrival, respect to the bunch crossing time, and from the electrons drift velocity in the gas mixture.

The achieved spatial resolution is $\sim 170\,\mu$m , while the time resolution is of few nanoseconds offline and of 25 ns at the L1 trigger level, much lower than the maximum drift time (~ 400 ns) [32].

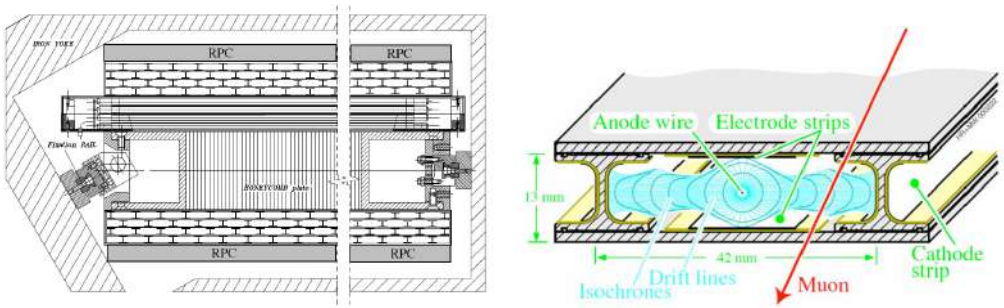

(a) (b)

Figure 1.15: Layout of a Drift Tubes chamber in the $R-\phi$ plane: in the top and bottom part are represented the 2 SLs with wires parallel to the z-axis and in the middle is represented the central layer with wires orthogonal to the beampipe (a). The layout of a drift cell, with the electric field lines [32].

Cathode Strip Chambers (CSC)

The endcap region is characterised by a non-uniform magnetic field and high hit rate, that requires good radiation hardness and low occupancy for the detector technology that has to operate in that region. CSCs are gaseous detectors, with cathode strips running radially, to measure the ϕ coordinate, and anode wires arranged perpendicularly to the strips, to measure the η coordinate.

A total of 540 chambers are installed, covering the range $0.9 < |\eta| < 2.4$, and are organised in 4 stations (ME1, ME2, ME3, ME4) at different z positions as shown in Fig. 1.13. The chamber planes are perpendicular to the beampipe and stations are organised in 2 or 3 concentric rings. The station closest to the interaction point is ME1, which is organised in 3 rings: ME1/1, ME1/2 and ME1/3. ME1/1 is closer than ME1/2 and ME1/3 to the interaction point. The other three disks (ME2, ME3 and ME4) have only 2 rings. The single rings are organised in 18 or 36 chambers, covering respectively 20° or 10° in the $R-\phi$ plane, and, in each ring, the chambers are arranged to have a small overlap to maximize the hermeticity in ϕ. Fig. 1.16a shows the station ME2, with the inner ring ME2/1 composed of 18 chambers, and the outer ME2/2 ring with 36 chambers.

The CSCs are multiwire proportional gaseous detectors. They are composed of 6 anode wire planes enclosed inside 7 stacked trapezoidal cathode panels, forming 6 gaps for muon detection. On one cathode panel for each gaseous gap strips have been milled, with a radial arrangement and at a constant $\Delta\phi$ pitch, varying from 8.4 mm for the chambers installed in the rings closer to the beampipe, to 16 mm for the chambers placed in the outer rings. On the other hand, the anodic wires are arranged in the azimuthal direction, orthogonal to the strips and their mutual distance varies in the range $2.5 - 3.16$ mm. During the detector operation, the anode wires are set to a

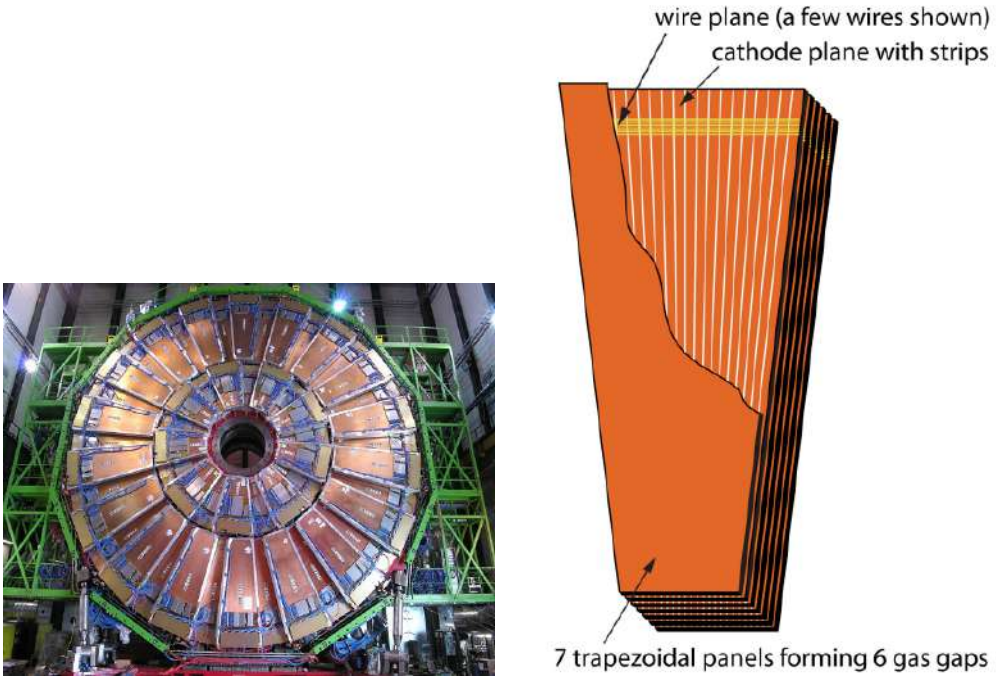

(a) (b)

Figure 1.16: (Left) view of ME2 CSC station: the inner ring is organised in 18 chambers, each covering 10° in $R-\phi$ plane, and the outer ring includes instead 36 ME2/2 10° chambers [33]; (Right) schematic view of a CSC chamber, showing the radial arrangement of cathode strips and the azimuthal organisation of anode wires [32].

potential between 2.9 kV and 3.6 kV and the detector gaps are filled with a gaseous mixture $Ar/CO_2/CF_4$ (40/50/10). When a particle crosses the detector, the ionisation produced inside the gaseous medium starts an avalanche of ions and electrons, which induce a signal on several nearby strips. Averaging the signal induced on the wires and strips of each layer, a spatial resolution of around 50 μm is achieved [32].

Resistive Plate Chambers (RPC)

Resistive Plate Chambers (RPCs) are an additional technology used in CMS for the detection of muons and used in particular for their fast time response, similar to that of a scintillator, providing good spatial and temporal resolution for particle tracking. They are installed both in CMS barrel and endcap regions, reaching a coverage up to $|\eta| < 1.9$, as shown in Figure 1.13.

In the barrel region, RPCs are installed in the 5 barrel wheels together with DT chambers, organised in concentric structures called "rolls". For each of the 2 outer DT rolls, one layer of RPC chambers is installed on the inner side of each DT chamber, while for the 2 inner DT rolls an additional RPC

layer is installed on the outer side.

In the endcap regions, RPCs are installed adjacent to CSC stations, organised in concentric structures called "rings". As shown in Figure 1.13, there is an RPC station adjacent to each CSC station, except for stations ME1/1, ME2/1, ME3/1 and ME4/1, the closest ones to the beampipe.

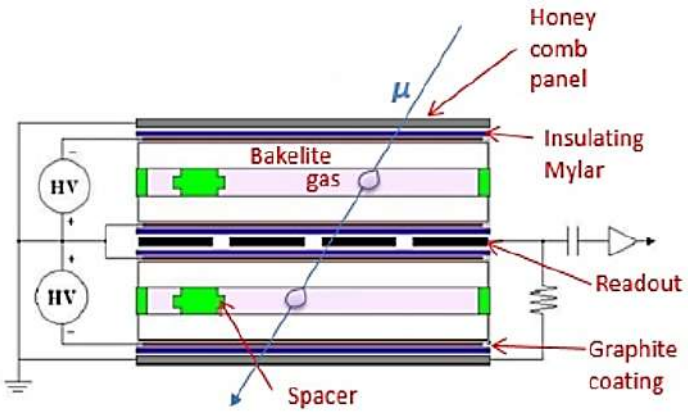

Figure 1.17: Schematic representation of a CMS double-gap RPC chamber [32].

The structure of each RPC chamber installed in CMS is illustrated in Fig. 1.17. It is composed of two gaps containing the gas mixture $C_2H_2F_4/i-C_4H_{10}/SF_6$ (95.2%/4.5%/0.3%), where a crossing muon will produce an ionisation, allowing its detection. Each of the gaps is delimited by two layers of HPL (High Pressure Laminate), externally coated with graphite, which will act as the electrode where the voltage needed to operate the detector is applied. In the central part of the detector, a plane of read-out strips is positioned, placed between two graphite electrodes and two mylar insulating planes. In particular, the pitch of the strips increases with the distance of the detector from the beampipe, from 1.5 cm for the innermost detectors to 4 cm for the outermost ones. The spatial resolution is so dictated by the strip pitch of the station considered, while the intrinsic time resolution offered by RPCs is of few nanoseconds.

The two central electrodes are set to $-9.6\,\mathrm{kV}$, to operate the detector in avalanche mode. Usually, RPC detectors are operated in streamer mode, but the high charge produced in this process allows to sustain only a rate of $\sim 100\,\mathrm{Hz/cm^2}$, too low for operating in the LHC conditions. For this reason, the detectors are operated in avalanche mode, increasing of about one order of magnitude their rate capability, but producing also a smaller collected charge per each crossing muon, which requires improved amplification electronics on the detector front-end. To increase the charge induced on the read-out strips, the double-gap design was adopted, collecting on the strips the charge induced from both gaps.

1.3.6 Trigger system

Depending on the LHC operative configuration a variable number of collision events happen in CMS. In the LHC design configuration, a bunch collision takes place every 25 ns and with a luminosity of $10^{34}\,\mathrm{cm}^{-2}\mathrm{s}^{-1}$, producing a mean number of 17 collisions per bunch crossing. Since the size of a proton-proton collision event in CMS is of the order of 1 MB and the event production rate is 40 MHz, it is technically impossible up to now to save every event produced in CMS, since it would mean to save ~ 40 TB/s. The most reasonable way to proceed is to select only the events that are judged potentially interesting for the ongoing physics search. The trigger system operates this selection. In Run 2 in particular it reduced the rate of selected events from 40 MHz to about 1 kHz. It operates in two steps: the Level-1 step and the High Level Trigger step, shortly called L1 and HLT respectively. A schematic representation of the CMS trigger system is shown in Fig. 1.18.

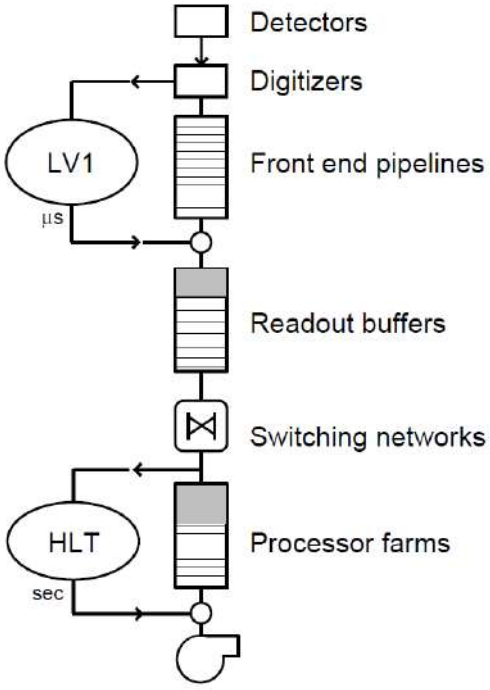

Figure 1.18: Schematic representation of the CMS trigger system [37].

The Level-1 system operates the first event selection in CMS after the front-end electronics and reduces the event data rate from 40 MHz to 100 kHz. The system up to now receives data from the muon system and from the calorimeters and is based on custom designed electronics, such as Application Specific Integrated Circuits (ASICs), and largely programmable electronics, such as Field Programmable Gate Arrays (FPGAs). It was chosen to use these technologies for their flexibility and for the decision speed required at this level.

The High Level Trigger system receives the events accepted by the L1 trigger and is designed to perform a rate reduction from 100 kHz to 1 kHz. The system consists of a computing farm with about 26000 cores of high-performance commercial processors.

1.3.6.1 Level-1 Trigger

The Level-1 Trigger system operates at the level immediately after the detectors front-end electronics and decides if an event has to be accepted or ignored, depending on the data coming from the detectors. This decision must be taken in a time window shorter than 4 μs, because this is the time in which detector data stay stored in the buffer electronics. After this time the buffer is overwritten and those data can no longer be retrieved.

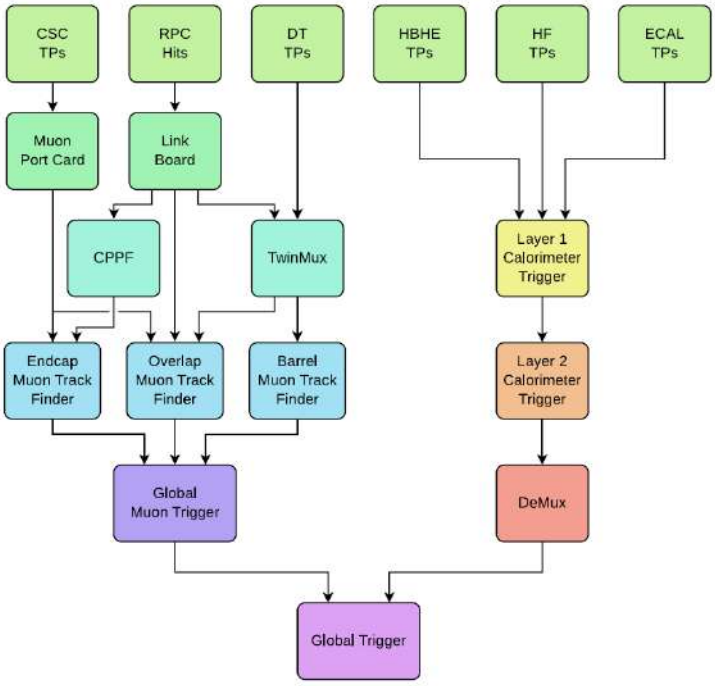

Figure 1.19: Schematic representation of CMS L1 Trigger system during Run-2 [38].

The Level-1 Trigger itself is composed of many levels (Fig. 1.19) and involves the muon system sub-detectors (DT, CSC, RPC) and the calorimeters (ECAL, HCAL, HF).

Calorimeter trigger. The first layer in the calorimeter trigger involves the collection of Trigger Primitives coming from HCAL and ECAL, which consist of energy deposits of a group of read-out channels. This group of channels, called trigger tower, has dimensions $\Delta\eta \times \Delta\phi = 0.087 \times 0.087$ in the barrel region and 0.17×0.17 in the endcaps. Once collected, the energy deposits are

calibrated, sorted and finally delivered to the second layer of the Calorimeter Trigger.

The second layer performs the task of providing candidates for electrons, photons, τ leptons, jets, energy sums and information relevant for muons (MIP bits).

Finally, a demultiplexer (DeMux) board sorts, serializes and formats events for the Global Trigger processing, which will take the decision to accept or ignore the event.

Muon trigger. The first elements along the processing chain of the muon trigger system are the Local Triggers of muon sub-detectors: RPC, CSC and DT. These detectors provide data in different formats: track segments and hit patterns for DTs, 3-dimensional segments for CSCs, while RPCs provide information in form of hits. In addition, all these three sub-detectors provide an identification of the bunch crossing which generated the track candidates.

Objects produced by DTs and CSCs are also called Trigger Primitives (TPs): these objects, together with RPC hits are delivered to the regional Track Finders, to perform the muon tracking. In CMS three regional Track Finders are defined:

- Barrel Muon Track Finder (BMTF), covering $|\eta| < 0.8$ and using information from DTs and barrel RPCs,
- Overlap Muon Track Finder (OMTF), covering $0.8 < |\eta| < 1.2$ and using information from DTs, CSCs and RPCs installed in this η range,
- Endcap Muon Track Finder (EMTF), covering $1.2 < |\eta| < 2.4$ and using information from CSCs and endcap RPCs.

The process of combination of RPC hits information with Trigger Primitives depends on the regional Track Finder considered: regarding the barrel region, DT Trigger Primitives and RPC hits are correlated before the information is sent to the BMTF, in the TwinMux; on the other hand, in OMTF and EMTF the RPC hits are treated alongside TPs inside the Track Finder processors.

In the Track Finders, the information coming from different muon stations are correlated, following different approaches [38], to form muon track candidates, whose physical parameters (p_T, charge, η, ϕ and a quality score) are estimated and assigned to it.

Finally, the tracks are delivered to the Global Muon Trigger which improves the trigger efficiency and reduces the trigger rates, using the complementarity and redundancy of the three muon sub-detectors. The Global Muon Trigger receives up to 36 muon candidates for each bunch crossing and selects the best eight muon candidates, choosing the best on the basis of candidates parameters (p_t, charge, η, ϕ and a quality score). These 8 muon candidates are transmitted to the L1 Global Trigger.

Global Trigger and Trigger Control System. The Global Trigger is the final step in the L1 Trigger architecture. It receives particle candidates and calorimeter objects from Global Muon Trigger and Global Calorimeter Trigger and runs in parallel many algorithms, that determine if the event is physically interesting. The decision to accept the event is taken together with the Trigger Control System, which informs the Global Trigger on the readiness of sub-detectors readout systems and of the Data AcQuisition system (DAQ), and in case of readiness allows the Global Trigger to deliver the L1 Accept signal (L1A). Once the event has been accepted, it is acquired and delivered to the HLT farm for further processing.

1.3.6.2 High Level Trigger

Traditionally, in a particle physics experiment after the L1 trigger there are two other trigger levels: Level-2, which performs a rate reduction, and Level-3 which uses more complex algorithms to accept or reject an event. In CMS, these properties are both integrated into the HLT farm, also called Event Filter Farm.

When an L1 Accept signal is sent by the Level-1 Trigger, the data coming from all the CMS sub-detectors are collected in Readout Units (RU), forming fragments of one event (Fig 1.20). The Readout Builder Network switches these fragments to many Builder Units (BU), which merge the fragments to form a complete event. This product can now be analysed with complex algorithms by the Filter Units (FU). The algorithms running in parallel on the different Filter units show if an event must be accepted or not. Once it has been decided that the event must be accepted, it's finally delivered to the storage site Tier-0.

1.4 The CMS and LHC upgrades

1.4.1 Overview

The LHC operation periods are divided into Runs and Long Shutdown periods (Fig. 1.21). During the writing of this thesis, the LHC is approaching the end of the Long Shutdown 2, preparing itself and the experiments for Run-3, which will show an increase in the proton beam energy to 6.8 TeV and with an instantaneous luminosity up to $2 \cdot 10^{34}\,\mathrm{cm}^{-2}\mathrm{s}^{-1}$, two times the design luminosity of the LHC. Run-3 will start in 2022 and it will last till 2025, collecting an integrated luminosity of about $350\,\mathrm{fb}^{-1}$.

At the end of this period, the High-Luminosity LHC (HL-LHC) programme, also called Phase 2, will start. This will consist in operating the LHC to have a center of mass energy in proton-proton collisions of $\sqrt{s} = 14\,\mathrm{TeV}$ and in a major upgrade in the instantaneous luminosity, up to $5 - 7 \cdot 10^{34}$, with the goal of delivering an integrated luminosity around $3000\,\mathrm{fb}^{-1}$.

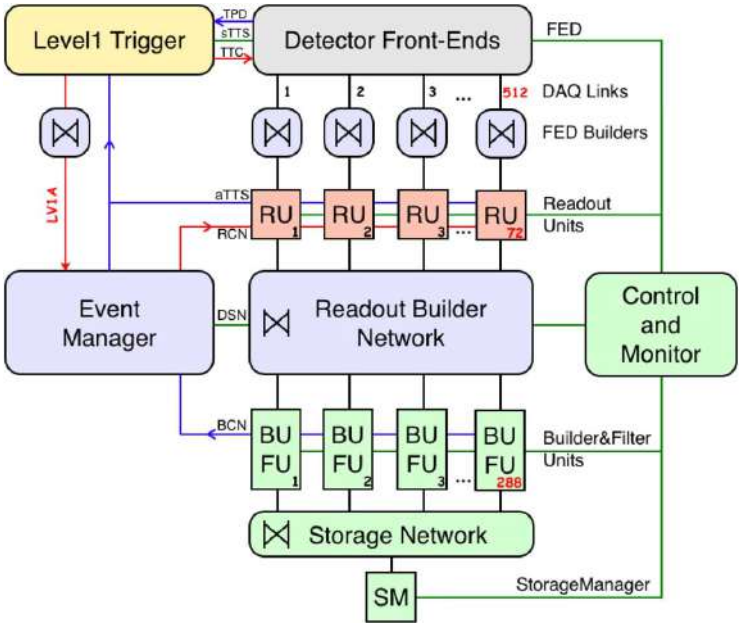

Figure 1.20: Scheme of the CMS DAQ system [40].

The higher luminosity will provide higher statistics, allowing to put tighter limits on phenomena such as the Higgs boson self-coupling, the existence of supersymmetric particles or to shed light on new physics not yet observed. Last but not least, the higher statistics will allow improving the precision of electroweak measurements, top-quark and already observed physics phenomena.

However, there are also drawbacks. The luminosity increase represents a major technological challenge for the experiments in terms of event complexity and radiation damage.

In HL-LHC the higher number of protons concentrated in each bunch will indeed increase the number of $p - p$ interactions per each bunch crossing (BX), which are called "pileup" interactions (PU). At the beginning of Run-2, the average number of pileup interactions was $\sim$ 25. In Phase-2 this value will increase to an average value of 140, producing events with a far higher number of particles to detect, reconstruct and analyse.

Furthermore, the higher flux of particles produced by the higher number of interactions per event translates into a higher dose delivered to the detector components. The dose delivered per year in Phase-2 will be compatible with that delivered in the whole operation period from 2011 to 2018. This means that many detectors may suffer radiation damage and need a technological upgrade.

To sustain these challenging operation conditions, the LHC experiments have started a wide upgrade campaign, to maintain or improve their performance in terms of background rejection, detection efficiency, resolution and radiation hardness. In particular, the CMS experiment has programmed the

Figure 1.21: Schedule of the LHC operations [42].

replacement of the inner tracker with a new one with an extended η coverage, the replacement of the endcap calorimeters with a new design High Granularity Calorimeter (HGCal), the installation of new muon stations and a major upgrade of the trigger system during the LS-3.

1.4.2 CMS challenges for HL-LHC

As already said, the main factors degrading the CMS performance in HL-LHC are the higher number of pileup interactions, provided by the higher instantaneous luminosity, and the higher radiation doses delivered to the detectors, consequence of the high integrated luminosity.

1.4.2.1 High pileup

The average number of pileup $p-p$ interactions predicted in CMS for HL-LHC is 140, for an instantaneous luminosity of $5 \cdot 10^{34}\,\mathrm{cm}^{-2}\mathrm{s}^{-1}$. The new focusing and crossing scheme of beams at the interaction point will allow to potentially deliver a luminosity of $2 \cdot 10^{35}\,\mathrm{cm}^{-2}\mathrm{s}^{-1}$, but this would result in an unsustainable collision pileup, for the detectors and for the trigger systems. For this reason, the plan is to operate at a lower luminosity ($5 \cdot 10^{34}\,\mathrm{cm}^{-2}\mathrm{s}^{-1}$), tuning it through a process called luminosity levelling, that regulates the beam focus and crossing profile, all along the beam fill process.

The $p-p$ interactions occurring per each bunch crossing can be classified as *soft* or *hard*. The hard collisions are the minority of the interactions and represent the potentially most interesting ones: these are characterised by an amount of exchanged energy of the order of 0.1-few TeV and for this reason,

are interesting for the discovery of new physics. On the other hand, the soft interactions are the majority and consist of a process with a smaller amount of energy exchanged.

A high number of interactions per bunch crossing (high PU) means a high number of particle produced, each of them creating an energy deposit in the detectors crossed (hits). The increase in the number of hits to correlate will enhance the complexity that trigger and reconstruction algorithms have to face: this could result indeed in erroneous assignment of hits to a track, degrading the measurement of physical parameters of the crossing particle.

Additional complexity is given by contaminations from events produced in the following or preceding bunch crossings: this process is called *out-of-time pileup*. This effect is created by the detectors time resolution: if the time assignment is higher than the time interval between a bunch crossing and the following one, 25 ns, the detector data could be collected and assigned to the wrong bunch crossing. On the other hand, the pileup interactions occurring in the same bunch crossing of the triggered event are labelled as *in-time pileup*.

Furthermore, the increase of the beam luminosity could increase the background contribution given by the interaction of beam particles with the pipe material (*beam halo*), the production of secondary particles from the interaction of beam particles with residual gas molecules in the vacuum pipe (*beam-gas interactions*) or signals produced by the decay of radionuclides generated by the activation of detector components (*residual radiation*).

1.4.2.2 High radiation dose

In CMS different kinds of particles cross the detectors and each of them undergoes interaction which can start a shower of secondary particles. The most relevant contributions are represented by

- charged particles which interact with the detector and create a shower of hadrons;
- photons and electrons, which create electromagnetic showers;
- neutrons, which can travel long distances inside the detector, producing damages also far away from their generation point, in particular low energy neutrons, which lose energy mainly by elastic scattering. In addition, interacting neutrons can produce electrons and photons, which could initiate the production of other secondary particles.

A high flux of particles crossing a detector can alter its operation, since the radiations, in particular low energy neutrons, can modify the crystalline structure of the active material or create discharges that could damage the front-end electronics.

The effect of radiation damage is well shown in the inner tracker detector, which requires reaching the full depletion condition to ensure the detection

of crossing particles. The radiation damage modifies the silicon crystalline structure, increasing noise and requiring a higher bias voltage to reach the full depletion condition.

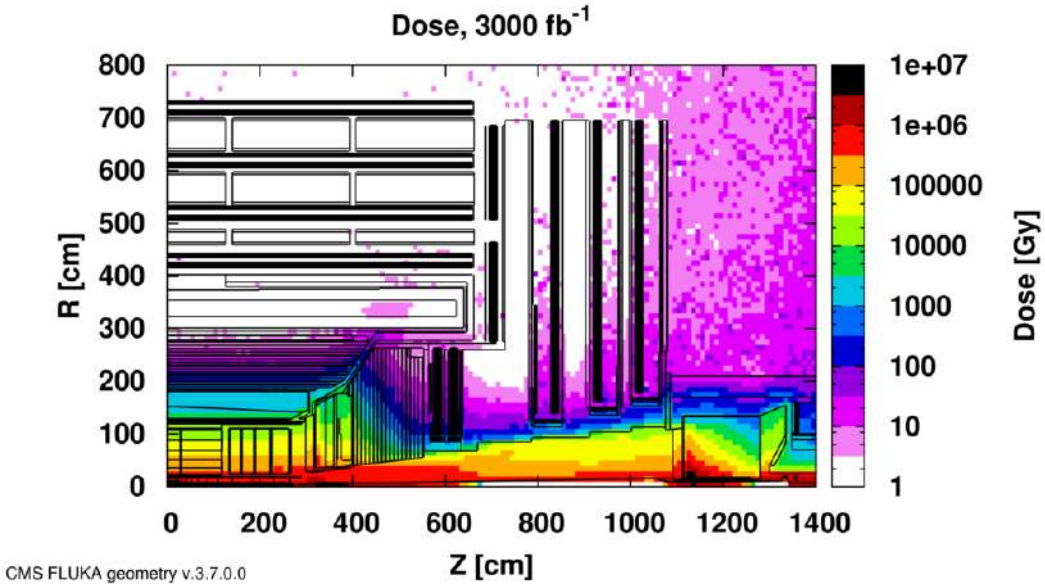

Figure 1.22: Simulation of absorbed dose in CMS after an integrated luminosity of 3000 fb^{-1} [43].

In Fig. 1.22 the simulation of the distribution of the dose absorbed by CMS after an integrated luminosity of 3000 fb^{-1} in the plane R-z is represented, showing as the majority of the dose concentrates in the region near the beampipe, inside the tracker and in the endcaps high η region.

1.4.2.3 Summary of CMS upgrades for HL-LHC

To face the challenging operation conditions foreseen in the HL-LHC era, the CMS experiment has scheduled a wide upgrade campaign. Almost all the CMS subsystems will be involved and also new detector stations will be installed to help the detector to maintain its performance in detection efficiency, resolution and background rejection. For the sake of brevity, I will mention only a part of them.

Inner tracker and calorimeters One way to sustain a higher flux of particles keeping a low occupancy of the detector is the increase of the number of sensor units in each detector. For this reason, the upgrade of the inner tracker and of the endcap calorimeter will consist mainly in an increase of their granularity. For the inner tracker, the granularity will be increased by a factor of 4, while for the endcap calorimeter a new design calorimeter will be installed in LS3, called High Granularity Calorimeter (HGCal).

This detector will consist of an electromagnetic and a hadronic section, with overall radiation and interaction lengths of $110.9\,X_0$ and $10.7\,\lambda$ respectively [45]. In particular, the electromagnetic and hadronic sections will be both longitudinally than transversally segmented. Its high granularity, around 6 million readout channels, will enable to provide a 3D energy deposition profile of the showers, together with very fast timing capabilities. This upgrade will result in an improvement in particle identification, energy resolution and pileup rejection in the endcap region, characterised by high rates of particles and high radiation doses.

Its development and installation will be challenging from many points of view, due to the huge number of readout channels to handle: for front-end electronics, trigger systems, software and computing, but also from an engineering point of view, since it requires the routing of thousands of power and signal cables in a very limited space.

L1 Trigger The LHC increase in luminosity will be reflected in an unacceptable increase in the trigger rate. To profit in statistics from the increased LHC luminosity, a sufficient rate reduction should be accomplished, avoiding at the same time an excessive loss in efficiency for the studied physics channels. To accomplish this task a tracking procedure will be implemented already at the L1 Trigger level: in order to do so, the L1 electronics will also be upgraded, making it possible to run more complex algorithms, and the L1 Trigger latency will increase from $4\,\mu$s to $12.5\,\mu$s. To cope with these new operation conditions, an upgrade in the front-end electronics and an increase in the acceptable trigger rate will also be necessary, in particular, to keep under control algorithms involving photons and hadrons, more influenced by the pileup increase with respect to other kinds of algorithms.

Upgrades in the muon system To maintain its discovery potential in the HL-LHC, the muon spectrometer will be upgraded, improving the already installed muon detectors and installing also new ones, based on different technologies. The main muon system properties to maintain are the muon identification and reconstruction capabilities and the momentum resolution reached in the past Runs. In particular, maintaining and possibly improving these capabilities will be fundamental for the integration of a new Track Trigger, which will match candidate tracks in the tracker with L1 trigger muons, exploiting in particular their p_T information.

These last features will be achieved thanks to the installation of new muon stations: this will indeed increase the redundancy, making possible to solve tracking ambiguities already at the trigger level, and keeping in this way the trigger rate under control without increasing the p_T threshold, which could lead to the loss of new physics events, containing low p_T muons. In addition, the installation of new muon stations is important for the standalone triggering of long-lived BSM particles, decaying outside of the CMS inner tracker.

The muon detector technologies at the end of Run-2 were CSCs, DTs and RPCs. CSCs will undergo an upgrade involving mainly their electronics, to sustain the higher L1 trigger latency programmed for HL-LHC. This upgrade will imply a higher power consumption by this subsystem, making necessary also an upgrade of the LV system. On the other hand, also the HV power system will be upgraded, to cope with the higher background rates and provide better monitoring of the detector currents.

The second system is represented by DTs, which will be upgraded in their front-end electronics components, to ensure its survival in the higher radiation environment and to improve its trigger rate capability: this will be made possible by transferring to the USC counting room the Minicrates which host the logics deputed to the time digitization and the L1 trigger primitives generation. In addition, this upgrade also aims at providing improved objects at the L1 trigger level (segments).

Finally, the RPCs system will install new RPC detectors in the region $|\eta| > 1.6$, stations RE3/1 and RE4/1 (Fig. 1.23), increasing the redundancy in the endcap. The new RPCs will have thinner electrodes and gaps in order to cope with the rate present in this η region. The back-end electronics of the whole RPC system will also be upgraded, in order to improve time resolution.

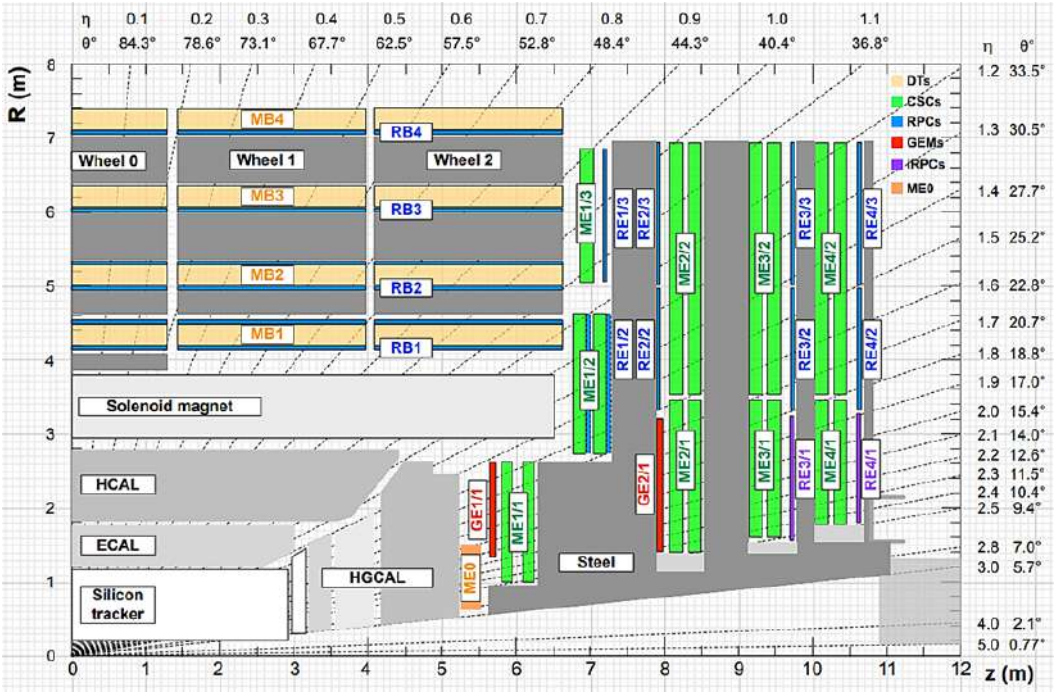

Figure 1.23: View of a quadrant of the CMS Muon Spectrometer in the plane R-z in Phase 2. In red are indicated the GEM stations GE1/1, GE2/1 and ME0 [46].

In the region $|\eta| > 1.6$ the redundancy will be increased not only with RPCs detectors but three additional stations will be installed close to the

existing CSC station: GE1/1, GE2/1 and ME0 (Fig. 1.23). These stations will be based on the so-called *Gas Electron Multiplier* technology (GEM). GEM is a technology characterised by a high radiation hardness and high rate capability. These detectors are gaseous detectors operating with a mixture of Ar/CO_2 (70%/30%): they show a stable gas gain for rates $\sim$ MHz/cm^2. Given their high rate capability, they are suitable to operate in the η region of the endcap where a rate up to 150 MHz/cm^2 is expected. In addition, these detectors have a spatial resolution $\sim 100\,\mu$m.

In LS2 the GE1/1 station has been installed in CMS and its commissioning is ongoing (2021), while the stations GE2/1 and ME0 will be installed during the Run-3 End of Year Technical Stop (EYTS) and the LS3 (Fig. 1.21). In particular, GE1/1 and GE2/1 will be installed in the region $1.6 < |\eta| < 2.4$ and increase the redundancy by adding more detection layers to the η region already instrumented with CSCs and RPCs. On the other hand, the ME0 station will increase the muon spectrometer detection coverage, since it will be installed in the region $2.0 < |\eta| < 2.8$. The increased coverage of the pixel tracker for Phase-2, near $\eta \sim 4$, and the replacement of the endcap calorimeters with the newly designed HGCal, driven the possibility to leave enough room behind the calorimeter to install a muon station. The hostility of the environment determined that also ME0 should use GEM technology.

Chapter 2

The CMS GEM upgrade

In this chapter the evolution of gas detectors will be illustrated, arriving to explain the design of GEM (Gas Electron Multiplier) detectors. The discussion will move then to the description of the GEM stations already installed (GE1/1) and programmed for a future installation in the CMS experiment (GE2/1 and ME0).

2.1 History and evolution of gaseous detectors

2.1.1 First gas detectors

The history of gaseous detectors starts at the beginning of the 20th century, with the development of the first devices for radiation detection: the ionisation chambers, the proportional counter and the Geiger-Müller counter. These detectors have all the same design but different names from their different operating conditions. The design is a simple cylinder filled with a gas medium and with a thin wire placed at the center of the tube, as illustrated in Fig 2.1. During its operation, a radial electric field is created inside the tube, described by the law

$$E = \frac{1}{r} \frac{V_0}{\ln(b/a)} \tag{2.1}$$

where V_0 is the voltage applied to the anode wire, b and a are respectively the inner radius of the cylinder and the outer radius of the anode wire and r the radial distance from the cylinder axis. When an ionising particle enters the gas medium, releases part of its energy, which ionises the gas and creates a cloud of ions and electrons. The mean number of ion-electron pairs created in the ionisation process is proportional to the energy released in the gas medium. By the effect of the electric field, the electrons are accelerated towards the

anode wire, while the ions towards the cathode, where they are collected. Custom electronics finally reads the signal produced on the anode wire.

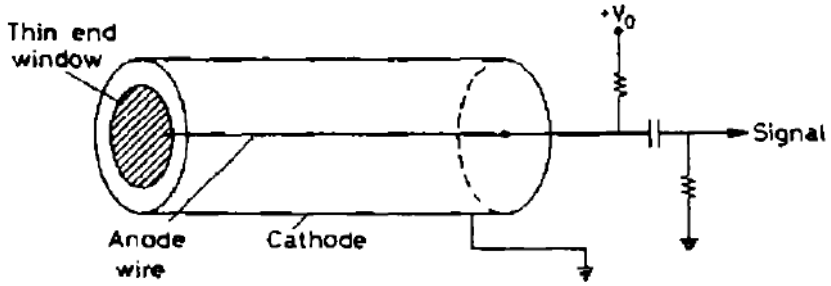

Figure 2.1: Scheme of a cylindrical ionisation detector [48].

The detector can be classified as an ionisation chamber, a proportional counter or a Geiger-Müller counter, depending on the applied voltage V_0. This voltage indeed defines what happens to the freed ion-electron pairs once created, defining different operation regions, as shown in Fig. 2.2. The first region is the *recombination region*, where the detector operates when the applied voltage is not enough to collect all the electron-ion pairs produced in the ionisation process before they recombine. The second region is the *ionisation region*, represented by the first plateau on the left and obtained applying a V_0 value high enough to obtain a complete collection of ion-electron pairs produced in the ionisation process: a gas detector operating in this region is called *ionisation chamber*.

When the voltage is further increased, the detector enters the so-called *proportional region*. In this case, the electrons produced in the primary ionisation and accelerated by the electric field, acquire a high enough energy to ionise other gas molecules and produce a so-called *avalanche* multiplication. This avalanche is created mainly near the anode wire, where the electric field has a higher intensity. In particular, the number of ion-electron pairs produced is proportional to the number of electrons produced in the primary ionisation, resulting in a proportional current signal detected on the anode wire. From this, a detector operating in this region is called a *proportional chamber*. It is important to notice that the majority of the signal detected on the anode wire is induced by the movement of the ions created in the gas: these indeed take a longer time to reach the cathode, with respect to the time taken by electrons to reach the anode, as illustrated in detail in Section 6.5.1 of [48].

If the voltage is increased still further, non-linear effects start to arise. The ions created in the medium indeed take a very long time to drift towards the cathode: if in the meantime too many ions are created they accumulate in the detector, creating a space charge and altering the detector electric field. In this way, the avalanche multiplication still occurs, but no longer proportionally to the number of primary electrons. This region is called the *limited proportionality region*.

Finally, a further increase in the operation voltage pushes the detector in the so-called *Geiger-Müller region*, where the space charge created becomes so abundant to self limit the multiplication, saturating the output current. In this operation region indeed many avalanches are created and develop along the entire length of the anode wire, instead of a single and localised avalanche. The saturation of the current implies that the output current does not give an indication of the number of primary electrons or on the energy deposited by the ionising particle which triggered the avalanche process.

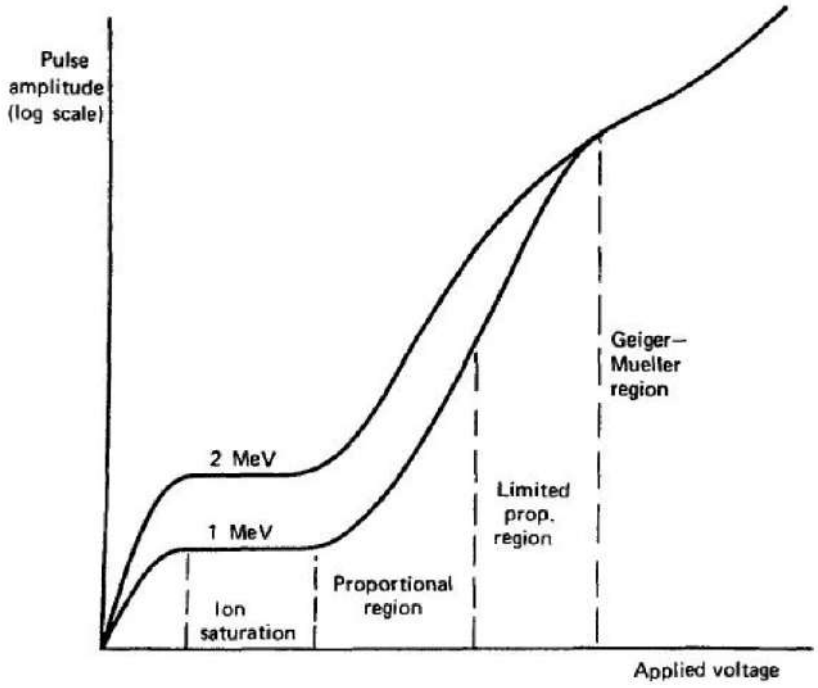

Figure 2.2: Operation regions of single wire gaseous detector, with the pulse amplitude plotted for events releasing two different amounts of energy in the gas medium [49].

2.1.2 The Multi-Wire Proportional Chamber (MWPC)

The first idea to cover large detection areas using proportional counters was to create an array of these detectors, placed next to each other, but this is a solution not very attractive from the mechanical point of view. In addition, this does not provide a satisfying space resolution, due to the space occupied by each detector, resulting in a low granularity.

In 1968 Charpak and his team built the first working Multi-Wire Proportional Chamber, made of a set of parallel wires closely spaced and enclosed between two parallel planes. The two planes are the detector cathode and are set to a negative potential, while all the wires are grounded, so set at the same potential. A scheme of the design is illustrated in Fig 2.3a. The innovative

discovery made by Charpak and his collaborators was to recognise that in this configuration each wire operates as an independent counter. Variations in the original MWPC design has been made over the years and one example are the CSC chambers installed in CMS [32].

The spatial resolution σ of an MWPC is determined by the wire mutual distance S as $\sigma = S/\sqrt{12}$. So for a typical spacing $S = 2\,\text{mm}$, a resolution of $\sim 0.5\,\text{mm}$ is obtained. This resolution can be improved by stacking many layers of chambers, with different wire orientations and segmenting the cathode planes. On the other hand, the time resolution of an MWPC is usually $\sim 20\,\text{ns}$, when operated with an Ar/CO_2 (70/30%) gas mixture.

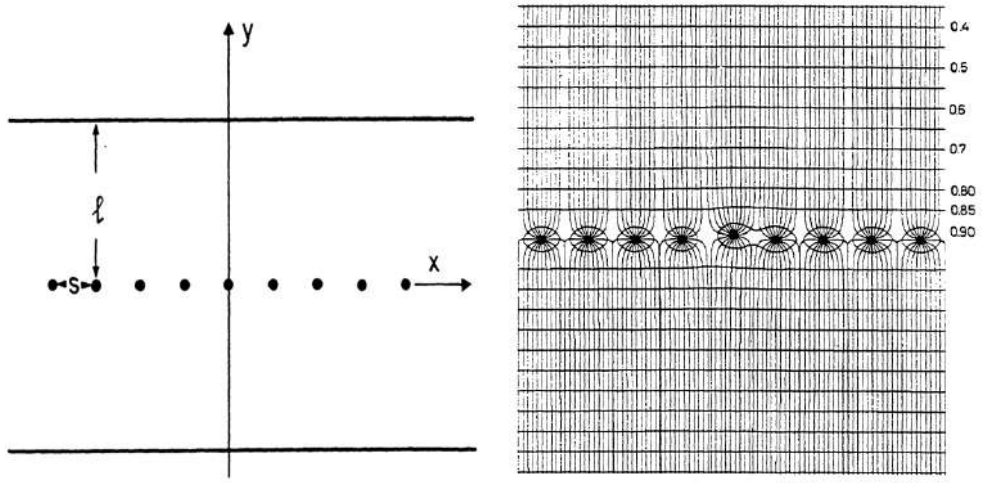

(a) (b)

Figure 2.3: (a) Scheme of a Multi-Wire Proportional Chamber: the typical parameters are $S = 2\,\text{mm}$ as wire pitch and the distance of wires from the cathode plane l around 3-4 times larger than S; (b) Representation of electric field lines and equipotential surfaces in the plane orthogonal to the plane of the wires in an MWPC [50].

The MWPC presents anyway some limitations, first of all in the arrangement of the anode wires. During the chamber operation indeed a high electric field is created between the wires, that can be displaced in the direction perpendicular to the anode wire and alter the electric field in the chamber and its operation. This results in practice in a maximum spatial resolution of the order of 1 mm for an MWPC.

Furthermore, the limited drift velocity of the space charge created during each ionisation limits the rate capability of the detector. Each time a space charge is created, the electric field around the wires suffers from a screening phenomenon. A too high flux of particles could be in this way underestimated since the gas gain becomes lower as the accumulated space charge increases. Such a decrease in performance is illustrated in Fig. 2.4.

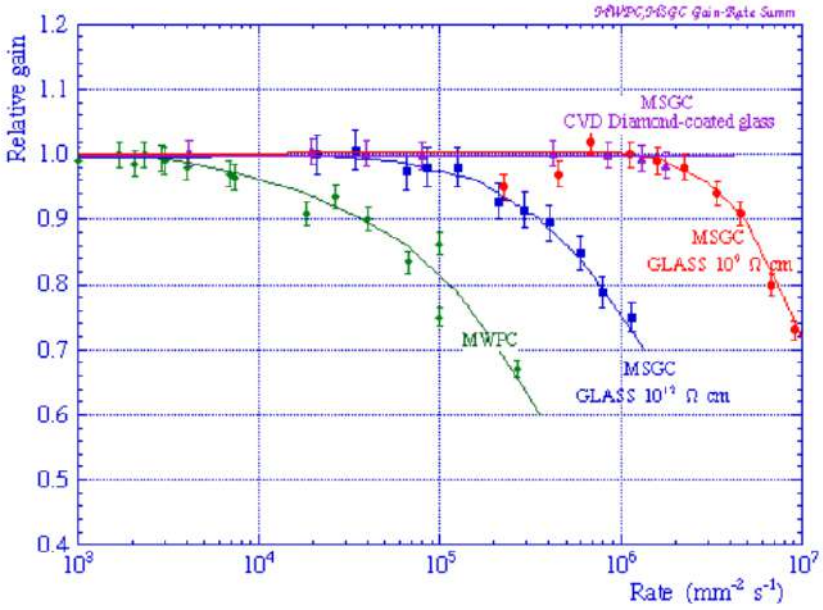

Figure 2.4: Rate capability of MWPC and MSGC in different configurations [51].

Finally, also *aging* can affect the MWPCs operations. This effect derives from the interaction of ionising particles with the case medium: when a particle crosses the gas medium and produces an ionisation the gas molecules can break and their remnants can deposit on the wires, screening the electric field given by the bare wire and modifying the gas gain uniformity of the chamber.

2.1.3 The Micro Strip Gas Chamber (MSGC)

To overcome the limitations of a design including wires, a new generation of gaseous detectors has been introduced, called Micro Pattern Gaseous Detectors. One first example of MPGDs is the Micro Strip Gas Chamber (MSGC). The basic design of this detector is illustrated in Fig. 2.5.

The innovative idea of this detector design was to place the anode and cathode electrodes on the same insulating plane, removing the problem of repulsion among the wires and the following distortion in the electric field. This possibility was offered by the application of photolithographic techniques to build the electrodes. As shown in Fig. 2.5b, the anode strips are the narrower ones; this strip arrangement, united to the effect given by an additional cathode electrode placed on the top of the detector, the *drift electrode*, creates the peculiar field illustrated in Fig. 2.5a. Below the insulating substrate an additional electrode, called *back-plane* is placed, segmented in strips perpendicular to the anode and cathode strips. The segmentation of the backplane provides in this way an additional spatial coordinate, enabling a 2D localisation of the

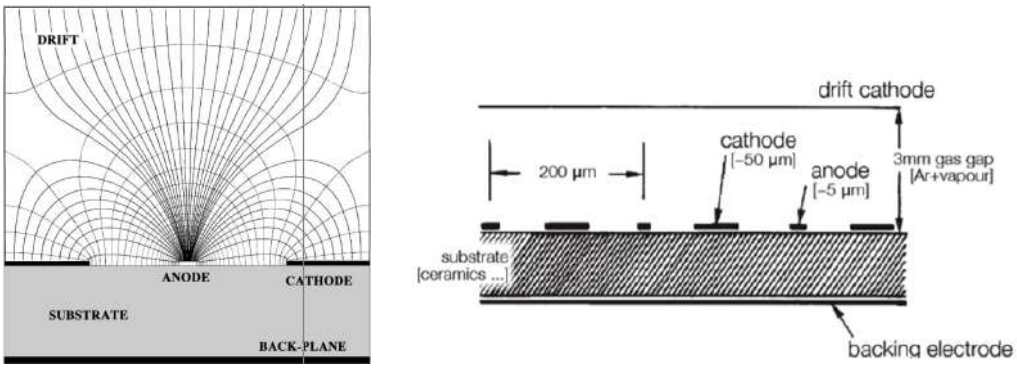

(a) (b)

Figure 2.5: (a) Representation of a MSGC in the plane orthogonal to the strips, including a scheme of the electric field and equipotential lines; (b) representation of a MSGC with the electrodes sizes and mutual distances [52] [53].

ionising particle.

In this configuration, when an ionising particle crosses the gas medium creates ion-electron pairs, with the ions collected by the cathode strips, while the electrons will drift towards the anode strips, where the stronger electric field makes possible their multiplication. This design in particular solves the limitations given by the MWPCs in terms of rate capability (Fig 2.4) and space resolution, from $O(mm)$ (MWPC) to $O(100\,\mu\text{m})$ (MSGC).

Even if reduced, the aging effect still verifies for MSGCs, due to the formation of polymers in the avalanche process. The aging effect is limited by choosing a different gas mixture to operate the detector, which increased the operation time of the detector up to an integrated charge of at least 120 mC/cm (equivalent to 10 years of operation at the LHC in its design configuration).

Two other problems arise in this MSGC design configuration: the charging-up of the insulator substrate and the occurrence of discharges between near strips, triggered for example by a crossing heavily ionising particle, such as a neutron or a nuclear fragment. The first effect involves the substrate free region between two strips and consists of the accumulation of ions generated in the avalanche process. This accumulation leads to a distortion of the design electric field but can be solved by producing the detector with a slightly conductive substrate, increasing the rate sustained by the detector to about $1\,\text{MHz/mm}^2$, without a significant loss in the gas gain uniformity, as shown by the red data set in Fig. 2.4.

The discharge problem is the most serious one: the discharges occurring between two electrodes lead sometimes to damage in the strips (shown in Fig. 2.6), creating short circuits and making areas of the detector inoperable. These discharges represent a major obstacle for the operation of MSGCs in the high luminosity LHC conditions, where a high flux of heavily ionising

particles is foreseen.

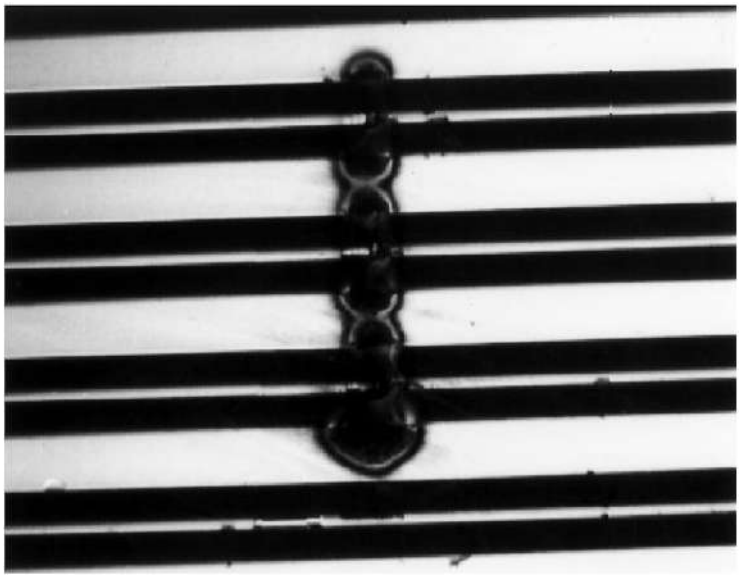

Figure 2.6: MSGC strips damaged by discharges occurring in the gas medium [52].

2.1.4 The MIcro MEsh GAseous Structure (MICROMEGAS)

The limitations shown by MSGCs have clarified that a further R&D in gaseous detectors was needed to match the requirements of the new High Energy Physics experimental conditions. This has led to the development of many MPGDs and one of them is the MIcro MEsh GAseous Structure (MICROMEGAS).

This detector is composed of

- a plane of anode readout strips deposited on a PCB,
- a drift cathode electrode on the top of the detector,
- a micromesh between the strips and the drift electrode, dividing the gas into two regions.

The micromesh creates two different electric field regions: the conversion region (3 mm), with a moderate electric field $\sim 100\,\mathrm{V/cm}$, and the amplification region ($100\,\mu\mathrm{m}$), with a stronger electric field $\sim 50\,\mathrm{kV/cm}$, as illustrated in Fig. 2.7.

The high electric field in the amplification region and its small size ($100\,\mu\mathrm{m}$) allow that most of the positive ions are collected on the mesh and don't accumulate in the amplification gap. This provides a high rate capability to the MICROMEGAS, allowing it to operate in high particle fluxes, as illustrated in Fig. 2.8.

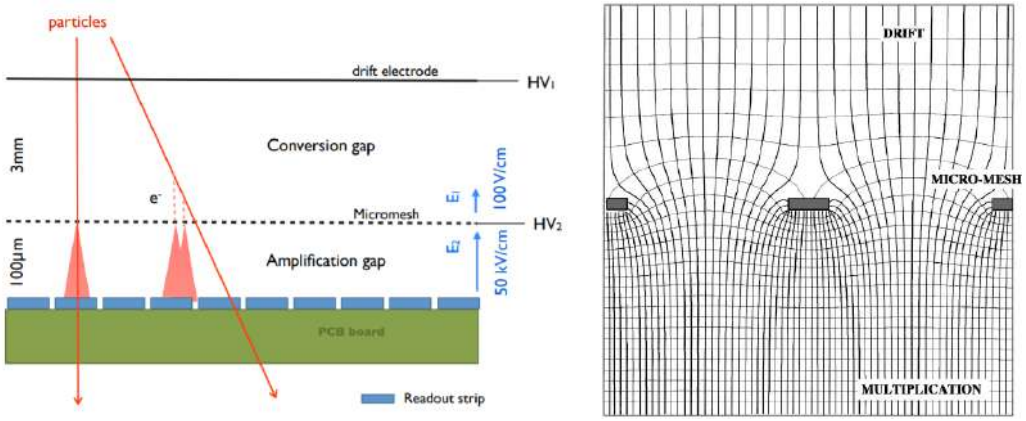

(a) (b)

Figure 2.7: (a) Representation of the structure and operating scheme of a MICROMEGAS detector; (b) representation of the electric field and equipotential lines in the plane orthogonal to the micromesh [52] [55].

The defect of this design is represented by the fact that a high electric field is generated in the amplification gas, which translates in the possibilities of discharges on the readout strips. This as for MSGCs represents a serious issue, since the discharges could create short circuits among the readout strips, making inoperable regions of the detector.

2.1.5 The Gas Electron Multiplier (GEM)

In 1997 Fabio Sauli invented a new detector technology, called the Gas Electron Multiplier (GEM). First of all, he understood that it was better to have the multiplication of the signal not directly in the gas medium close to the readout strips, but possibly inside the layer separating the gas in regions: for this, he designed a special layer, called *GEM foil*. Then Sauli understood that the multiplication of the signal could be achieved in successive multiplications, instead of just in one stage. We'll come back in the next sections on this second point, for the moment let's focus on the function process of a GEM foil. A GEM foil consists of a polyimide foil cladded on both sides with copper; on the foil, a series of holes are made by chemical etching, as illustrated in Fig. 2.9.

The particular design allows creating a modest electric field in the gas region surrounding the foil and an intense electric field inside the holes. This field is created applying an electric tension between the two copper clads of the GEM foil; applying a voltage difference of $300 - 500\,\mathrm{V}$ the field created inside the holes is ($\sim 100\,\mathrm{kV/cm}$). Thanks to a so intense field the electrons can accelerate enough to trigger an avalanche multiplication. A schematic representation of the electric field in the chamber is shown in Fig. 2.10.

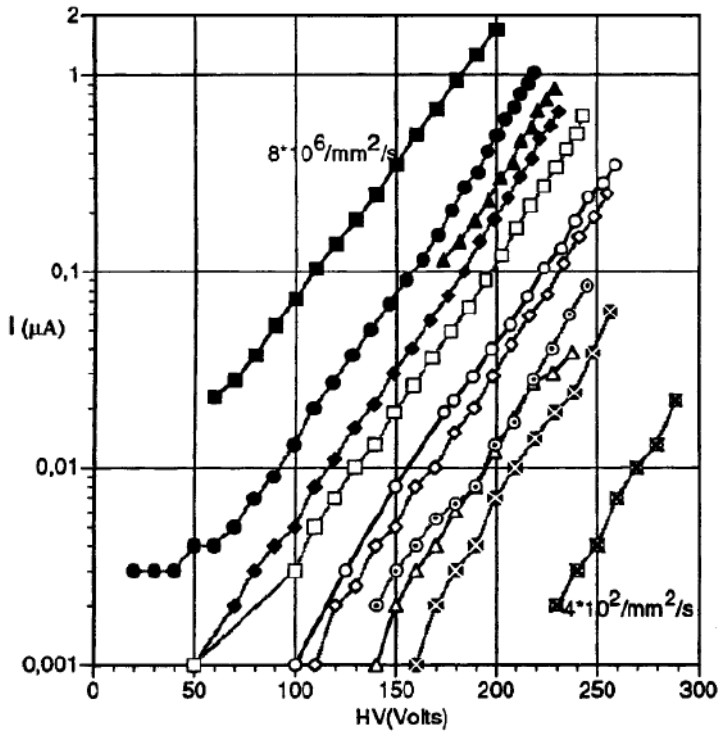

Figure 2.8: Current detected in a MICROMEGAS, for different particle fluxes [52].

Using two or more GEM foils in cascade allows reaching a total higher gain, with lower operating voltage in a single foil. Using a lower voltage is fundamental to prevent the formation of discharges, which could create damages in the detector or even in the electronics, in case of propagation. The most common design, also adopted by the CMS GEM project, consists of three stacked GEM foils.

2.1.5.1 GEM foil manufacturing

Three main parameters have to be considered in the GEM foil manufacturing:

- hole diameter,
- hole pitch,
- hole shape.

The configuration adopted by the CMS GEM project is a biconical hole, with pitch $P = 140\,\mu$m and with the diameter of the top and bottom faces respectively $D_{top} = 70\,\mu$m and $D_{bot} = 85\,\mu$m. This asymmetric configuration has been chosen, since it optimises the foil electron collection and extraction efficiencies, respectively called ϵ_{coll} and f_{extr}. These last two quantities will be presented in the next section.

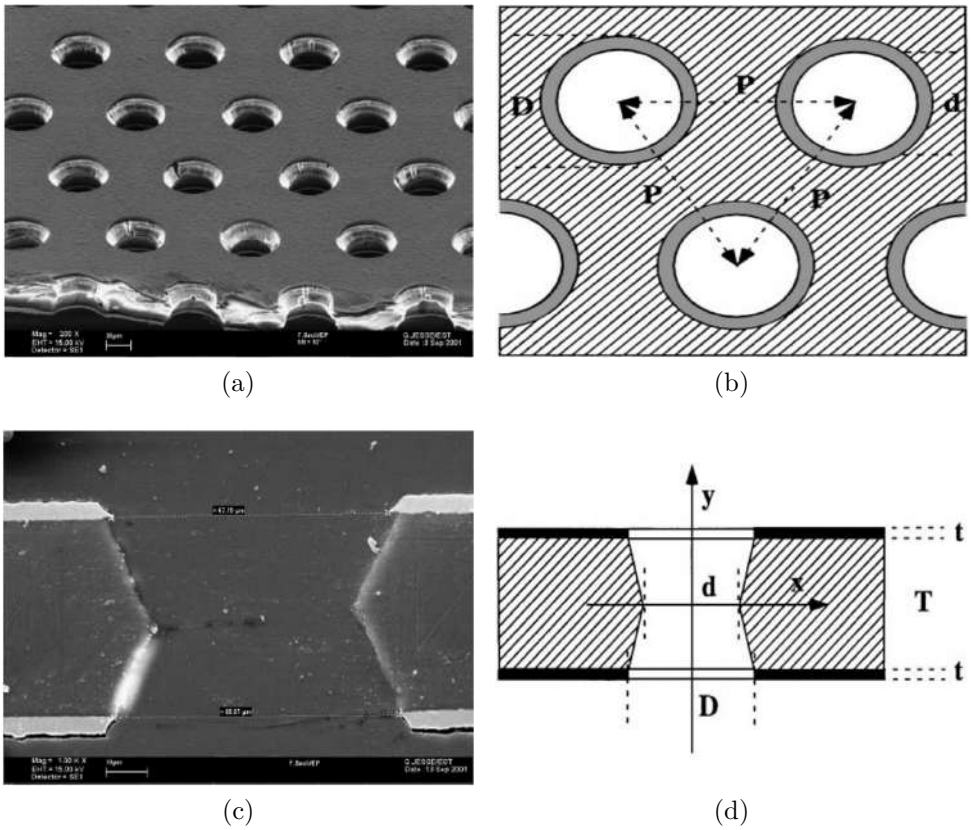

(a) (b)

(c) (d)

Figure 2.9: (a)(b) Top view of a GEM foil from an electron microscope picture and in a scheme illustrating the pitch of the holes $P = 140\,\mu$m. (c)(d) Lateral section of a GEM hole in an electron microscope picture and in a scheme, showing the thickness of the copper cladding $t = 5\,\mu$m, the Kapton foil thickness $T = 50\,\mu$m and the inner and outer diameters of the hole $d = 50\,\mu$m and $D = 70\,\mu$m. It can be noted that the shape of the hole is biconical [56] [57].

2.1.5.2 Single GEM detector

The simplest design for a GEM detector is composed of a single GEM foil, a cathode electrode on the top and a patterned anode at the bottom to collect the signal, as illustrated in Fig. 2.11.

In this detector design the only mechanical parameters, apart from the GEM foil model, are the distance of the foil from the cathode and anode electrodes. The region between the GEM foil and the cathode is called *drift gap,* while the region between the foil and the anode is the *induction gap.* These two distances are indicated respectively as h_D and h_I.

During the detector operation, the detector is filled with a proper gas mixture, such as Ar/CO_2 (70/30%), and three electric fields are created inside the detector: the drift and induction electric fields E_D and E_I in the corresponding gap regions, and the amplification electric field E_A inside of the

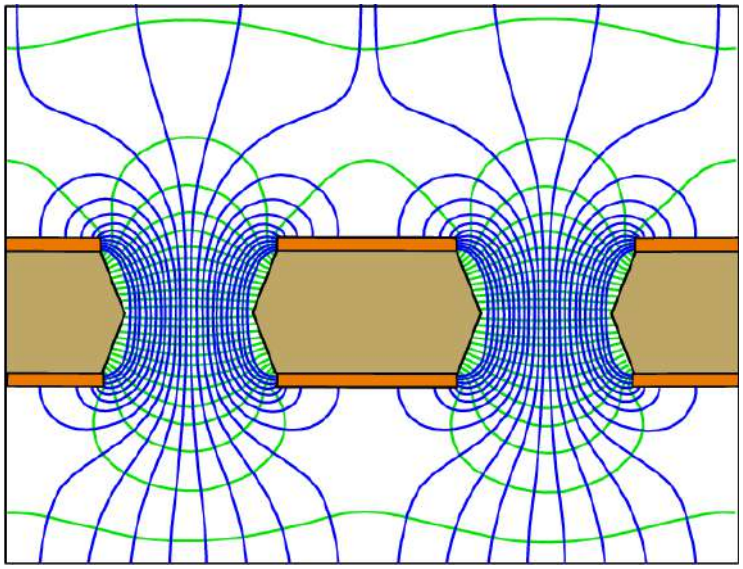

Figure 2.10: Electric field in a GEM detector, showing the field lines and the equipotential surfaces in the plane orthogonal to the foil [56].

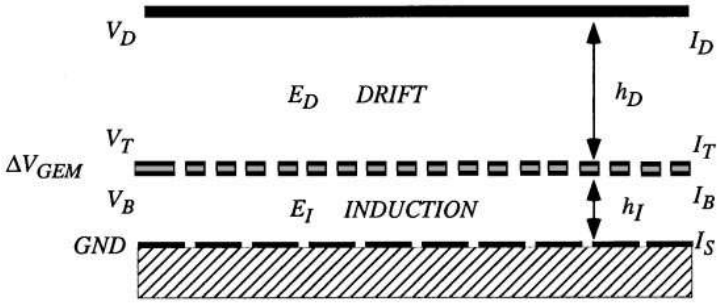

Figure 2.11: Schematic representation of a single GEM detector [57].

GEM holes.

When an ionising particle crosses the detector and creates an ionisation in the drift gap, primary ion-electron pairs are created inside the gas medium and, following the electric field lines, the positive ions start to drift towards the cathode while the electrons move towards the top layer of the gem foil. Inside the holes, the electrons are multiplied, producing in this way a corresponding number of positive ions.

Since some of the field lines terminate on the foil (Fig. 2.10), the majority of the ions produced in the multiplication will be collected on the top copper clad of the GEM foil. On the other hand, the multiplication electrons cross the hole, with a part of them collected on the bottom copper clad and the others starting crossing the induction gap, proceeding towards the readout strips.

In this way, the majority of the signal will be induced by the electrons moving in the induction region and also faster. This is innovative with respect

to the other gaseous detectors, where the signal is induced by the ions, that due to their low mobility gave a longer signal in time.

Drift and induction electric fields. The drift (E_D) and induction (E_I) electric fields are involved in two different ways in the readout signal formation.

E_D is involved in the collection of the primary electrons produced in an ionisation process above the GEM foil, routing them inside a GEM hole. The quantity defined to understand the quality of the electron collection is called *collection efficiency:*

$$\epsilon_{coll} = \frac{electrons\ collected\ in\ the\ holes}{electrons\ produced\ above\ the\ holes}. \tag{2.2}$$

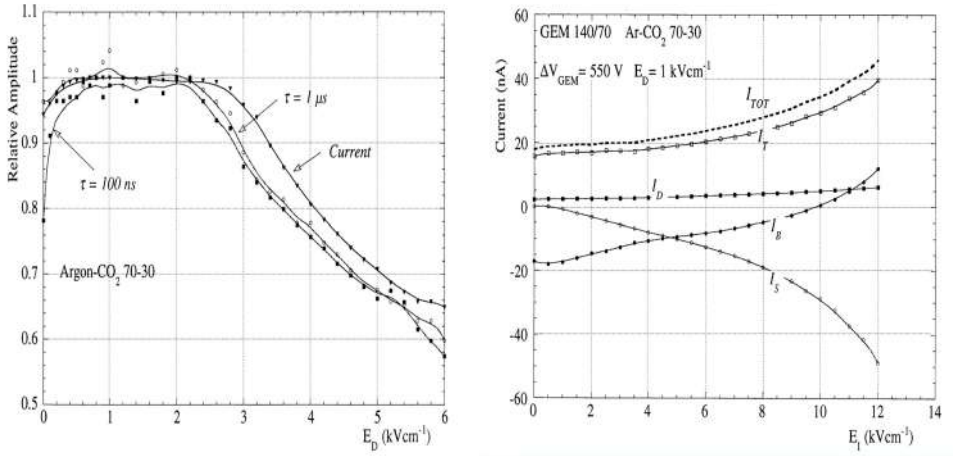

(a) (b)

Figure 2.12: Single GEM operated in Ar/CO_2 (70/30%) (a) Collection efficiency as a function of the drift electric field E_D, measured with different methods: integral current and pulse with two different amplifier shaping times. (b) Current measured on different electrodes: I_D is the current on the drift cathode electrode, I_T and I_B are respectively the currents on the top and bottom copper clads of the GEM foil, I_S the current registered on the readout strips, I_{TOT} is given by the sum $I_{TOT} = I_S + I_B$ and represents the real GEM gain [57].

Fig 2.12a shows how a small drift field $E_D < 0.5\,\mathrm{kV/cm}$ gives a small collection efficiency. This effect is given by the recombination of the electrons (significant for electronegative gas mixtures) and by their too small drift velocity to form a fast enough signal (in Fig. 2.12a shaping times of $1\,\mu$s and 100 ns have been considered). On the other hand, ϵ_{coll} is small also for an intense field ($E_D > 3\,\mathrm{kV/cm}$). In this case, a big fraction of electrons is collected on the top surface of the GEM foil, since the number of lines of the electric field closing on the top surface of the GEM foil increases.

For intermediate field values $E_D \sim 1 - 3\,\mathrm{kV/cm}$, ϵ_{coll} reaches a constant maximum value and, for this reason, the operation electric field is chosen in this region. Usually, for a Ar/CO_2 (70/30%) gas mixture, $E_D \sim 2\,\mathrm{kV/cm}$ is used.

The induction electric field E_I is instead involved in the extraction of multiplied electrons from the hole and their transfer to the anode readout electrode, and this is evaluated by the extraction efficiency f_{extr}, defined as

$$f_{extr} = \frac{electrons\ extracted\ from\ the\ holes}{electrons\ produced\ inside\ the\ holes}. \tag{2.3}$$

In this case, the multiplication electrons are produced inside the hole and pushed out of it thanks to the electric field inside the hole, but for a too low E_I value, they cannot reach the anode electrode to produce the readout signal. The electrons in this case are indeed attracted and collected on the bottom layer of the foil. This behaviour is illustrated in Fig 2.12b, where I_S is the current induced on the readout strips and I_B is the current measured on the bottom copper clad of the GEM foil. For an intense induction electric field $E_I > 8\,\mathrm{kV/cm}$, a large electric field is created on the edge of the anode strips and trigger a discharge. In order to minimize discharges and have a good extraction efficiency, a compromise choice is $E_I \sim 5\,\mathrm{kV/cm}$, which allows to route $\sim 50\%$ of the multiplication electrons on the readout strips.

Drift and induction gap thickness. The thickness of the drift gap has to ensure at the same time a good intrinsic detection efficiency and maintain the rate specifications. The 3 mm thickness is wide enough to ensure the production of a number of clusters for a full detection of minimum ionising particles in a High Energy Physics experiment like CMS. A wider gap on the other hand would not affect the detection efficiency, but it would affect the rate capability since the charges will have a wider volume to cross before being collected.

The induction gap thickness has to ensure a good extraction efficiency from the holes and at the same time minimize the formation of discharges. With a sub-millimetric gap, the electrons would have a small region to cross, but the adoption of such a design would require a high mechanical tolerance, since imperfections in the design would trigger discharges on the readout plane and could lead also to non-uniformities in the gain. For this reason, an easier to handle thickness of $1 - 2\,\mathrm{mm}$ is usually chosen.

GEM foil voltage. The role of the voltage applied to the two copper clads of the GEM foil, indicated with ΔV_{GEM} (Fig. 2.11), is to fix the amplification factor inside the GEM holes. The gain describing the amplification in an avalanche process is described by the typical relationship

$$dn = n \cdot \alpha(x) \cdot dx, \tag{2.4}$$

where n is the number of electrons at a certain position x, α is the first Townsend coefficient, representing the number of ion-electron pairs created per unit length and dn the variation of the electron number in a path dx. The Townsend coefficient depends in particular on the temperature, pressure and electric field present in the gas.

The intrinsic gain obtained integrating over the electron path $[x_1, x_2]$ is

$$G_{in} = e^{\int_{x_1}^{x_2} \alpha(x)\, dx}. \tag{2.5}$$

Getting an average value α of the Townsend coefficient over the path and making explicit the dependence by the voltage difference V_{GEM}, the relationship can be rewritten as

$$G_{in} \propto \cdot e^{\alpha V_{GEM}}. \tag{2.6}$$

The intrinsic gas gain of a single GEM detector is $O(10^3)$, but due to the configuration of the drift and induction electric fields, the effective gas gain is generally lower than 10^3. E_D and E_I determine indeed the collection and extraction efficiencies, ϵ_{coll} and f_{extr}, which contribute to the effective gas gain in the following way

$$G_{eff} = G_{in} \cdot \epsilon_{coll} \cdot f_{extr} = G_{in} \cdot T, \tag{2.7}$$

where $T = \epsilon_{coll} \cdot f_{extr}$ is called *electron transparency*.

The strategy to obtain a higher effective gas gain, up to $O(10^4 - 10^5)$, is to use a detector including more than one GEM foil.

2.1.5.3 Double GEM detector

In a double GEM detector an additional player is added to the design, the transfer region. As for the drift and induction gaps, the electric field and the thickness of this region has to be determined. Since in CMS triple-GEM detectors are installed, the transfer gap thickness will be analysed only for those detectors, while the transfer electric field will be illustrated in the double GEM configuration, for an easier understanding.

Transfer electric field The transfer gap can be seen in two different ways: as induction region of the previous GEM foil, or as drift region for the following one. For this reason, the transfer electric field has to optimize both the extraction efficiency f_{extr} from the previous GEM foil and the collection efficiency ϵ_{coll} for the next GEM foil.

In Fig. 2.13 the currents flowing on the different electrodes for a double GEM detector operating with a gas mixture of Ar/CO_2 (70/30%) are represented, as a function of the transfer electric field E_T. The drift and induction fields have been fixed both at 5 kV/cm, while the potential difference on the GEM foils has been set respectively to $\Delta V_{GEM\,1} = 500$ V and $\Delta V_{GEM\,2} = 350$ V.

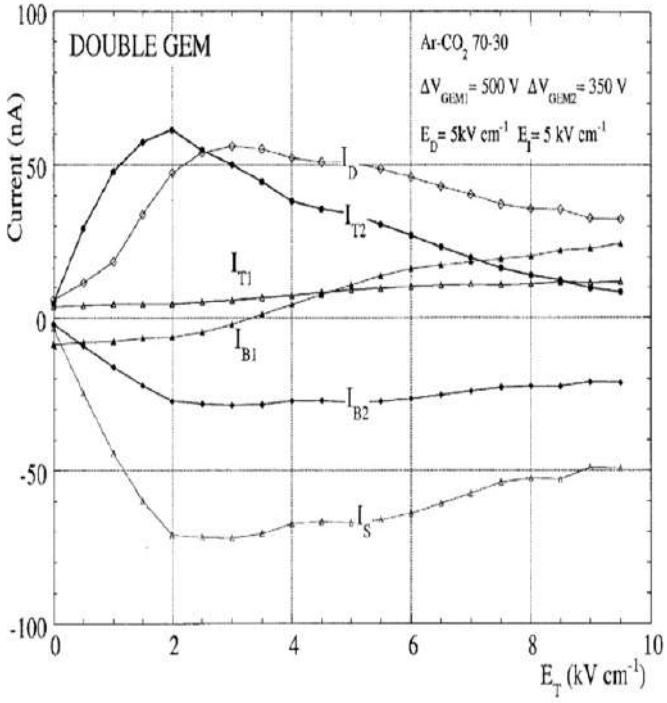

Figure 2.13: Current flowing on the electrodes of a double GEM detector as a function of the transfer electric field E_T. The detector operates with gas mixture Ar/CO_2 (70/30%), drift E_D and induction E_I fields are fixed at 5 kV/cm and the potential differences on the foils are set to $\Delta V_{GEM\,1} = 500\,\mathrm{V}$ and $\Delta V_{GEM\,2} = 350\,\mathrm{V}$. The currents represented are: the current flowing on the drift electrode I_D, on the top and bottom layer of the first GEM foil I_{T1} and I_{B1}, on the top and bottom layer of the second GEM foil I_{T2} and I_{B2}, and the current induced on the readout strips I_S [57].

It can be observed from the current values that for a transfer field $E_T < 2\,\mathrm{kV/cm}$ the electrons are correctly collected and multiplied by the first GEM foil, but then they are mainly collected on the bottom copper clad of the first GEM foil. This is due to the field lines closing on the foil, minimizing the extraction efficiency, and can be well understood looking at the current flowing on the bottom layer of the first GEM foil (I_{B1}), which reaches its maximum negative value for $E_T \to 0$. Due to this effect, the current observed on the bottom clad of the second GEM foil I_{B2} and that induced on the readout strips I_S goes to 0.

On the other hand, for a transfer field $E_T > 6\,\mathrm{kV/cm}$ the electrons are mainly collected on the top of the second GEM foil and not by its holes, reducing its collection efficiency. This can be understood by pointing out the decreasing trend of the current flowing on the top copper clad of the second GEM foil I_{T2}.

To minimize both these effects, E_T is usually chosen in the range $E_T \sim$

$3-5\,\mathrm{kV/cm}$ and these considerations are valid also for a triple GEM detector.

2.1.5.4 Triple GEM detector

The triple GEM design allows performing the amplification in three stages. This allows achieving a higher gas gain, with a moderate potential difference on the GEM foils and with a lower discharge probability, as illustrated in Fig 2.14.

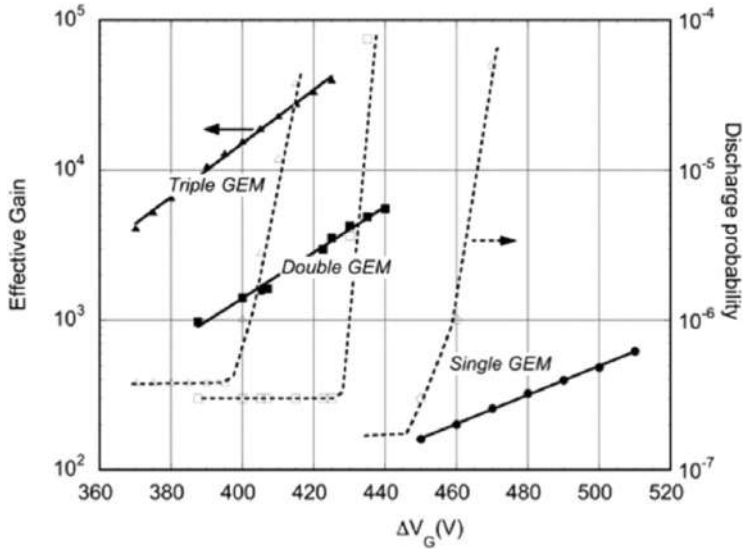

Figure 2.14: Gain and discharge probability as a function of the voltage applied to each GEM foil in single, double and triple GEM configuration. The solid line refers to the effective gain data, while the dashed one refers to the discharge probability. [56].

As for double-GEM configuration, transfer gaps are introduced in the detector. They basically play the role to feed the next GEM foil with the multiplication electrons of the previous one. An electric field similar to that adopted for double-GEM detectors ($E_T \sim 3-5\,\mathrm{kV/cm}$) can be adopted in both of them, while a deeper description is needed about the thickness of the two transfer gaps.

First transfer region thickness. When a particle crosses the detector gas medium, it can produce ionisation in any of the gaps, undergoing a number of multiplications as the number of the GEM foils following the region where the ionisation occurred. Obviously, the signal has to be intense enough to be discriminated by the front-end electronics. So a particle producing the first ionisation in the second transfer gap or in the induction gap will produce a not enough intense signal to be accepted by the front-end electronics. On the other hand, a particle ionising for the first time in the first transfer gap (2 next multiplication stages) could produce a usable signal, thanks to the local

fluctuations in the gas gain, and be detected in the same way as a particle which ionised in the drift region (3 multiplication stages). This effect produces a broadening in the time resolution of the detector since a signal originating in the first transfer region will reach the readout electrode in a smaller time than one born in the drift region. This time depends on the thickness of the transfer gap g_{T1} and on the drift velocity inside this region (determined by the electric field in this region and by the gas mixture used) and is of the order of $\Delta t = g_{T1}/v_{drift_{T1}}$. One solution to minimize this effect, called the *bi-GEM effect*, is to offer to the particle a smaller transfer region where to ionise, or, in other words, make the first transfer gap narrower (1 mm).

Second transfer region thickness. Unlike the first transfer gap, the second transfer region cannot contribute to the bi-GEM effect, due to the insufficient multiplication achieved by only one multiplication stage. On the other hand, this transfer region plays an important role in the formation of discharges: the high density of multiplication electrons in a single GEM hole could indeed overcome the Raether limit (maximum gain $G < 10^8$) and push the detector in the streamer mode, triggering the production of a discharge. There are two main solutions to limit this:

- add a quencher to the gas mixture,
- allow a wider electron diffusion in the gap.

The quencher limits the discharge problem, absorbing the photons emitted by the de-excitation of molecules which could trigger secondary avalanches and ultimately a discharge. However, the quencher usage is limited by the development of ageing phenomena which contribute to the detector operation degradation.

The most convenient solution is so represented by making the electrons spread on more than one hole and this can be done by manufacturing a thicker transfer gap, taking advantage of the electron cloud diffusion phenomenon. The solution adopted by the CMS GEM project is a second transfer gap 2 mm thick, as a compromise between the minimization of the discharge probability and the space requirements imposed by the experiment installation region. In particular, in Fig. 2.15 the 3/1/2/1 design adopted by CMS for the GE1/1 station is illustrated.

Gain of a triple-GEM detector. Since the multiplication of the signal occurs in cascade stages, the intrinsic gain can be roughly determined as the product of Eq. 2.6 for the three gem foils, becoming

$$G_{in} \propto \prod_{k=1}^{k=3} e^{<\alpha> \cdot V_{GEM\,k}} \propto e^{<\alpha> \sum_{k=1}^{k=3} \Delta V_{GEM\,k}}, \tag{2.8}$$

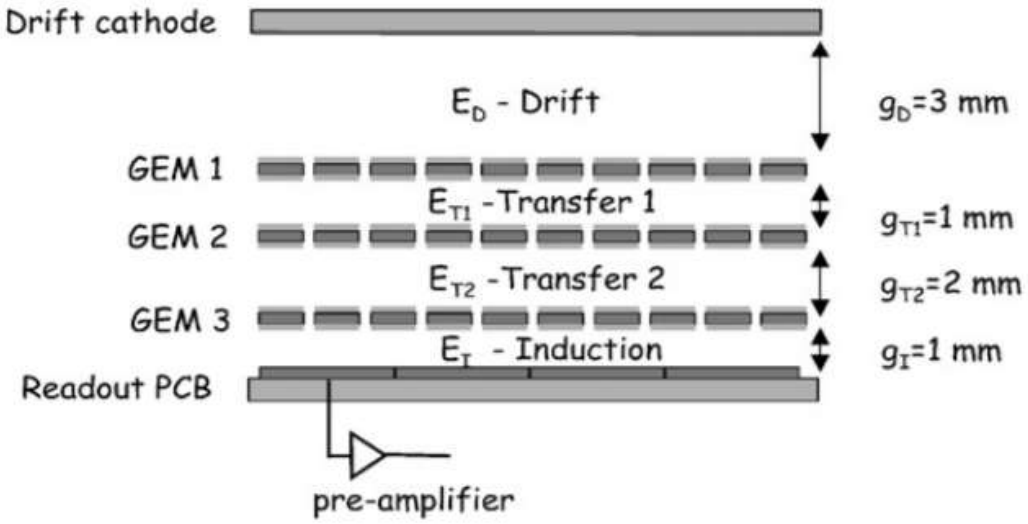

Figure 2.15: Design adopted by CMS for a GE1/1 triple-GEM detector. In figure the electric fields of each region, together with their thickness are illustrated: E_D and g_D for the drift region, E_{T1} and g_{T1} for the first transfer region, E_{T2} and g_{T2} for the second transfer region, E_I and g_I for the induction region [60].

where $< \alpha >$ is the average first Townsend coefficient across the holes and $\Delta V_{GEM\,k}$ is the voltage applied to the single GEM foil.

As for the single GEM detector, for each foil, there are factors ϵ_{coll} and f_{extr} that reduce the intrinsic gain. Similarly to Eq. 2.7, the effective gas gain can be expressed as the product of an intrinsic gain G_{in} and of a transparency T_{tot} :

$$G_{eff} = G_{in} \cdot T_{tot} = \prod_{k=1}^{k=3} e^{<\alpha> \cdot \Delta V_{GEM\,k}} \cdot T_k = e^{<\alpha> \cdot \sum_{k=1}^{k=3} V_{GEM\,k}} \cdot \prod_{k=1}^{k=3} \epsilon_{coll\,k} \cdot f_{extr\,k}, \tag{2.9}$$

where the sum of the voltages applied on the single foils can also be labelled as $\Delta V_{GEM}^{tot} = \sum_{k=1}^{k=3} \Delta V_{GEM\,k}$. To have a fixed gain, as suggested by Eq. 2.9, the potential differences applied to the single GEM foils can also be different from each other, and only their sum ΔV_{GEM}^{tot} has to be maintained constant.

In particular, making $\Delta V_{GEM\,1}$ the highest one and $\Delta V_{GEM\,3}$ the lowest one is a solution that allows:

- to limit the bi-gem effect, since the primary electrons created in the first transfer region will undergo a lower multiplication, reducing the probability to produce a final signal high enough to be discriminated by the front-end electronics;

- to limit the discharge occurrence, since the charge reaching the third foil will be higher, but the amplification inside the hole is lower and

Channel	E/E_{max}
Drift gap	0,040
GEM foil 1	1
Transfer gap 1	0,047
GEM foil 2	0,982
Transfer gap 2	0,047
GEM foil 3	0,937
Induction gap	0,067

Table 2.1: Example of electric fields normalised to the maximum one, $E_{GEM\,1}$. These data refer to the CMS GE-1/1/01 Super-Chamber. GE1/1 chambers adopt a design 3/1/2/1 mm for the gap spacing.

the electron cloud is also distributed among many holes by the diffusion effect.

To have an idea of how much the electric fields differ from each other, I have reported in Tab. 2.1 an example, referring to a GE1/1 chamber installed in CMS.

Discharges. A discharge in a GEM detector is triggered when the Reather limit is overcome inside a hole, due to the high number of charges produced in the avalanche multiplication. In the case of a triple GEM the second transfer gap is one of the major players in the discharge creation.

A discharge is usually created between the top and bottom side of a GEM foil and it manifests as a fast drop in the voltage difference applied to the foil and at the same time induces a signal on the nearby electrodes. When a discharge is created inside a foil two main things may happen:

- the discharge does not propagate to the other foils or layers which don't lay on the same foil which summoned the discharge. In this case, the voltage on the foil is recovered in a time scale of the order of a few milliseconds.
- the discharge propagates to other distant layers.

There are two different hypotheses at the basis of the propagation of a discharge that crosses a gas gap:

- a photon emitted during the original discharge extracts charges from the gas medium and/or from the metallic electrodes,
- the original discharge heats the copper rim of the hole, partially melting the copper and changing the hole shape (Fig 2.16). The heating of the hole enables the extraction of electrons from copper by thermionic emission and the electric field present in the area drives them away from the extraction point.

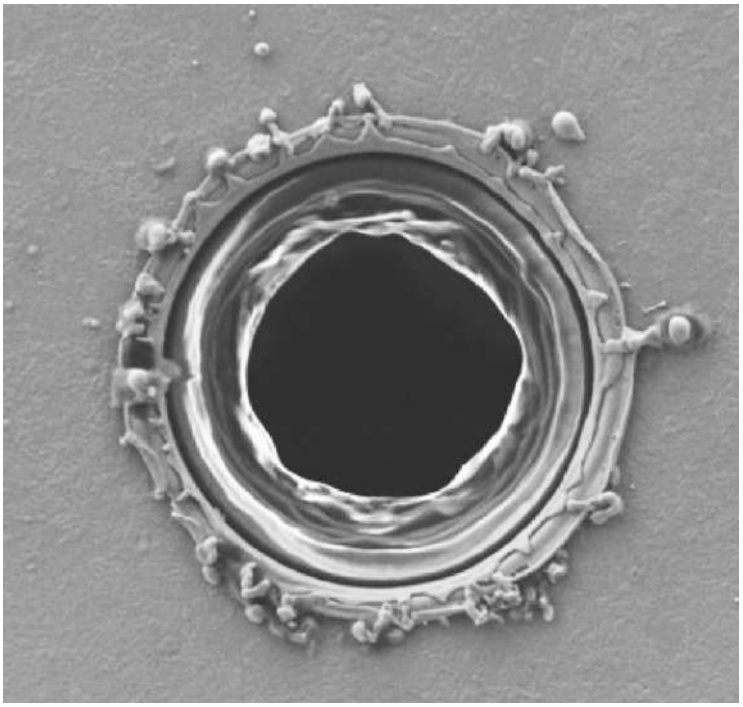

Figure 2.16: Scanning Electron Microscope (SEM) picture of a GEM foil after one single discharge with an energy of 2 mJ [62].

Given the complexity introduced by the propagation in the detector, to study the dynamics of a discharge is necessary to monitor the voltage of each HV electrode in the detector. For this purpose, high voltage probes are used to measure the voltage on each HV electrode and an antenna electrode is used to identify the beginning of the discharge event and trigger the acquisition.

Fig. 2.17 shows an example of the behaviour of the electrodes of a 10 cm $\times$ 10 cm triple-GEM detector in a discharge event. In particular, are represented the electrodes of the third GEM foil, the bottom and the top one respectively labelled G3Bot and G3Top.

At time 0 the original discharge is created and after $\sim 14\,\mu$s it propagates to the readout plane, creating a conductive channel in the gas. The consequence of this is a drop to zero of the voltage of both the electrodes of the foil (*G3Top* and *G3Bot*), draining the charge accumulated on the foil. It can be also observed that after a relatively short time the system tries to restore the voltage, but another discharge propagates on the readout. The drain of the charge from the foil is of fundamental importance to understand how much damage a discharge could carry: during a discharge indeed the GEM foil behave as a huge plane capacitor, with a lot of charge accumulated on, and in a propagated discharge all this charge can flow on the readout plane.

The dimension of the copper plane from which the charge can be drained during a discharge plays so a fundamental role in defining the amount of its energy: to limit this, foils with a segmented top copper layer started to

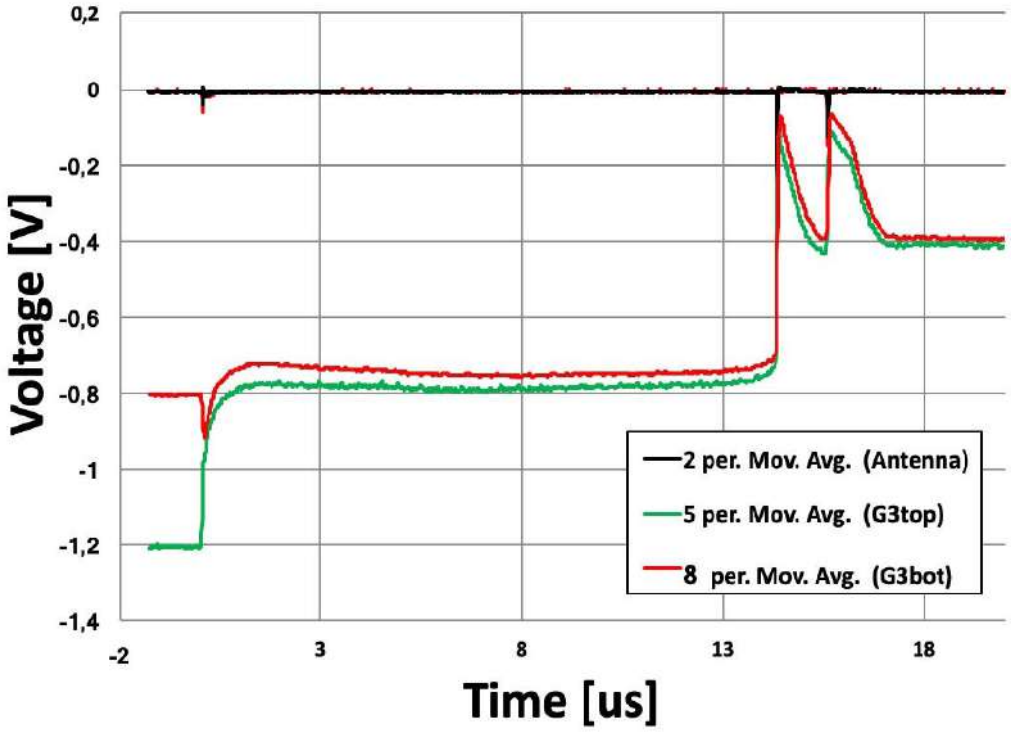

Figure 2.17: Discharge event registered on a 10 cm × 10 cm triple-GEM detector. The voltage on the single electrodes are measured with a high voltage probe with an attenuation factor 1000. To trigger the acquisition of the discharge event an antenna is used [62].

be used. Furthermore, each of the segmentation sectors of a copper layer is decoupled with a resistor of $1 - 10\,\mathrm{M}\Omega$, but this is not enough to prevent discharge occurrence and consequent damages. The event that reignited the interest in the investigation of discharge propagation was the slice test of GE1/1 CMS GEM detectors, where propagated discharges were identified as responsible for the loss of electronics readout channels. The situation for these detectors is particularly important since the bottom plane of the foils is made of a single unsegmented copper foil and so all the charge stored on the copper layer can feed the propagated discharge. The studies performed by the CMS GEM group concluded that to have a safe detector operation, a segmentation of both sides of the GEM foils is needed, with each sector decoupled with a $0.1 - 10\,\mathrm{M}\Omega$ resistor [63].

However, this segmentation approach could not be used to protect GE1/1 detectors, since their production was already concluded. On the other hand, the values of decoupling resistors, between the power supply and the foils, have been increased and a so-called *drain resistor* has been introduced on the readout plane. The role of this resistor is particularly interesting: once a propagated discharge reached the readout plane a conductive path is created inside the gas medium, and the charge of the foils flows towards the ground.

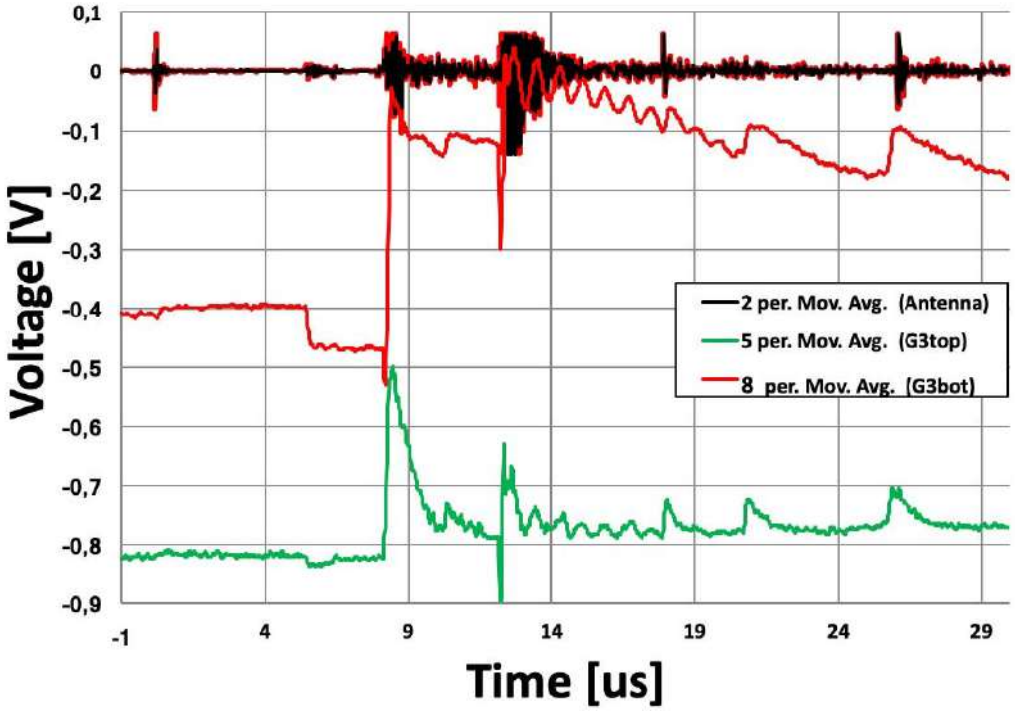

Figure 2.18: Discharge event registered on a GE1/1 long triple-GEM detector. The voltage on the single electrodes are measured with a high voltage probe with an attenuation factor 1000. To trigger the acquisition of the discharge event an antenna is used. It can be noted a much more complex behaviour in the discharge evolution than what observed in a 10 cm $\times$ 10 cm triple-GEM detector [62].

If a resistor is introduced on this path, part of the potential difference, which sustains the electric field in the last gap, falls on the resistor, decreasing in this way the electric field in the gap and discouraging the reignition of a discharge.

The segmentation solution will be instead implemented in GE2/1 and ME0 CMS GEM stations, with a protection resistor connected to each sector. The only layer that will not undergo a segmentation will be anyway the G3Bot, since its segmentation would introduce a cross-talk effect between the strips, creating an induced signal also on the strips not involved in the avalanche collection.

2.2 The GE1/1 station

The GE1/1 station is the first CMS subsystem based on triple-GEM technology. Its installation in the CMS detector started in July 2019 and its commissioning is ongoing (at the time this thesis is written), in preparation for the incoming Run-3 data-taking period. The purpose of this detector is to co-operate with the CSC station ME1/1 in the production of L1 trigger

primitives, adding 2 hits to the reconstruction of each track. This increase in redundancy is particularly important for the L1 trigger, allowing to use a lower p_t threshold for the reconstructed muons. Fig. 2.19 shows how the co-operation of GE1/1 and ME1/1 stations will allow measuring the $\Delta\phi$ bending angle of a muon in the $R-\phi$ plane. Thanks to this, a better momentum resolution and a lower number of fake candidates can be achieved, resulting in a lower L1 trigger rate without increasing the p_T threshold, as illustrated in Fig. 2.20.

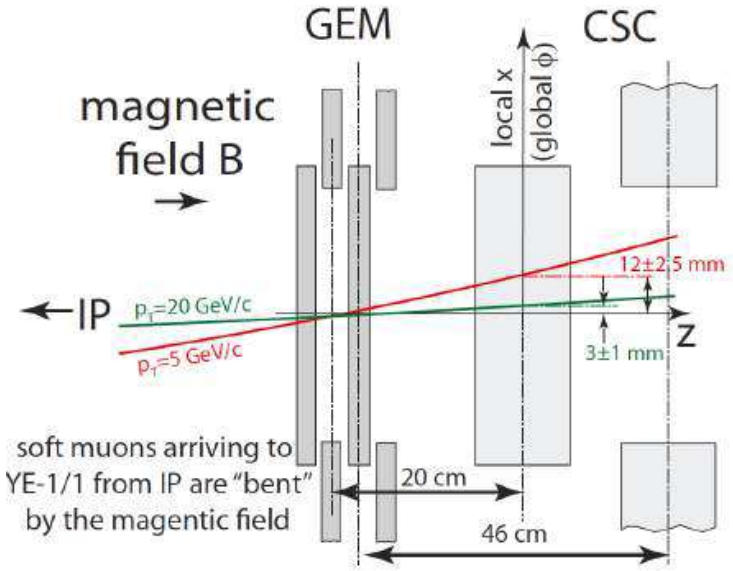

Figure 2.19: Thanks to the distance among a GE1/1 and a ME1/1 station, the possibility to measure the $\Delta\phi$ bending angle formed by a muon trajectory crossing these two stations is offered [64].

Up to Run-2 in the slot for the installation of GE1/1 no detector was installed. In the region indeed RPCs cannot be used, due to their insufficient rate capability. This condition can instead be sustained by GE1/1 since its detectors have a rate capability higher than $10\,\mathrm{kHz/cm^2}$. Furthermore, the GE1/1 station can also sustain an integrated charge of $200\,\mathrm{mC/cm^2}$ without showing any loss in gain, coping with the harsh radiation environment where has to operate.

As shown in Fig. 1.23, the GE1/1 station is installed in the region of the endcap closest to the interaction point, 130.2 cm radially distant from the beampipe and covers the pseudo-rapidity range $1.55 < |\eta| < 2.18$. In this position, it is the first muon detector encountered by a particle coming from the interaction point. The magnetic field in this region is $\sim 3\,\mathrm{T}$, but is not uniform in the chamber (Fig 2.21) and such a configuration makes it harder to assign to a crossing particle the correct p_T from its bending angle in the ϕ plane.

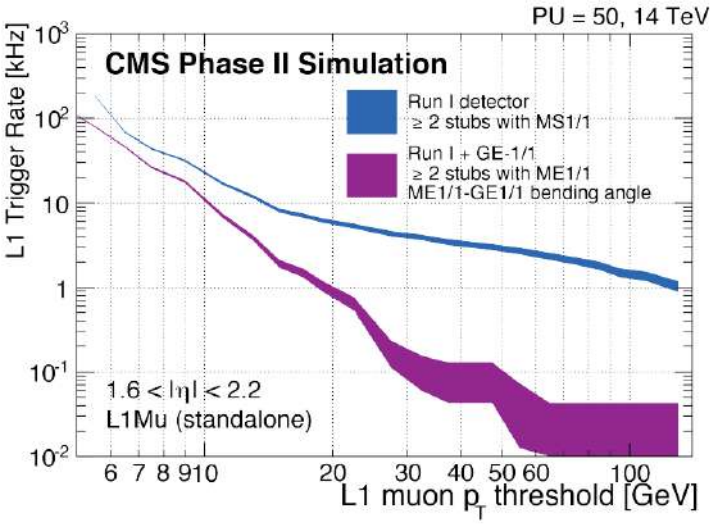

Figure 2.20: Level 1 muon trigger rate as a function of the L1 muon p_T threshold at an LHC luminosity of $2 \cdot 10^{34}\,\mathrm{cm}^{-2}\mathrm{s}^{-1}$, in blue without the GE1/1 station and in purple with the station installed [64].

In each endcap, the station is composed of 36 modules, called *Super Chambers,* with a radial angular coverage of 10.15°. These modules are staggered to achieve an overlapping in the ϕ plane, achieving a full coverage: for this reason, the modules are of two types, a short and a long Super-Chamber, as is illustrated in Fig. 2.22. The long Super-Chambers cover the pseudo-rapidity range $1.55 < |\eta| < 2.18$, while the short ones cover $1.61 < |\eta| < 2.18$.

A Super-Chamber is composed of two triple-GEM *single chambers,* called *layers.* The layer closer to the interaction point is labelled *Layer 1 (L1)*, while the other is *Layer 2 (L2).*

Once mounted in CMS, the two layers are powered by a common HV line. This design was chosen to reduce by a factor 2 the number of boards required to power the whole station and in this way also the budget required. This puts a strong requirement on the choice of chambers paired in a Super-Chamber: they should have a similar gas-gain. In this way when an HV configuration is chosen, this will be the same for both layers and both of them should show similar behaviour in terms of gain.

2.2.1 Design of a single chamber

Every single GE1/1 chamber is a triple-GEM detector, manufactured with a gap spacing scheme 3/1/2/1 mm, as illustrated in Fig. 2.15. Each GEM foil used in the manufacturing shows a segmentation on the top copper clad (facing towards the drift electrode), while it consists of a unique copper layer on the bottom copper clad (facing towards the readout electrode). The segmentation of the top layer is illustrated in Fig. 2.23 and consists of the division of the

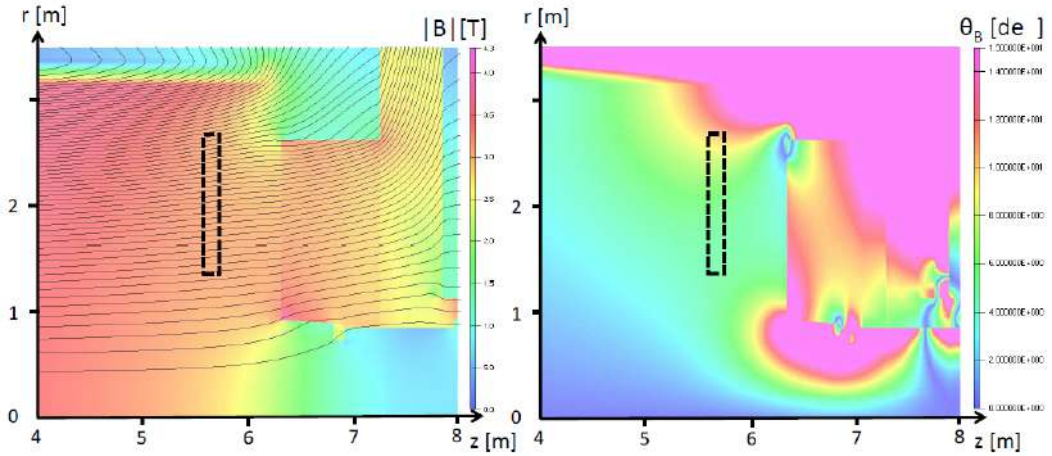

Figure 2.21: Magnetic field in GE1/1 installation region (dashed rectangle): on the left the intensity of the magnetic field in the plane $z - r$ is shown, on the right the angle formed between the magnetic field vector and the z-axis [64].

copper layer in sectors orthogonal to the long side of the chamber, 40 for short and 47 for long chambers. This design was considered for two main reasons:

- to minimize the amount of charge which can be drained from the foil during a discharge event: this led also to the installation of 10 MΩ protection resistors in each sector of the top copper layer, while on the bottom one no protection resistor is applied. The role of the resistor is to quench the discharge;
- to minimize the area of the detector that becomes inoperable or changes its operation in terms of gas gain if a short circuit is created in the sector.

As in all triple-GEM detectors, the readout plane is situated on the anode below the induction gap. The anode plane is segmented in two directions.

- Along the η direction in 8 sectors (Fig. 2.23).
- Along the ϕ direction in strips with a mutual pitch of 461 μrad, for a total of 384 strips in a single η partition. The pitch in mm depends on the strip position in the chamber and on the chamber type, short or long.

The total number of strips in a GE1/1 detector is then $8 \cdot 384 = 3072$.

The design of the electronics foresees that the strips in a single η partition are not readout all together by a single device, but divided into 3 groups of 128 strips and readout by three corresponding devices, the *VFAT* chips.

The drift plane, the GEM foils and the readout plane are fixed mechanically to a plastic frame, forming a bare detector, not equipped with any of

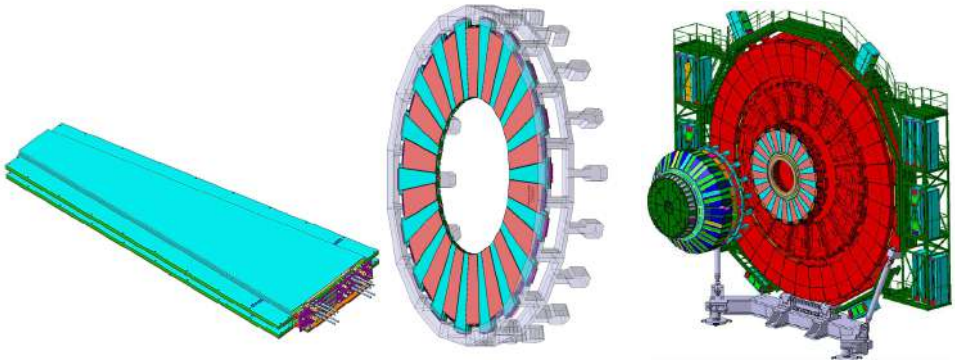

(a) (b)

Figure 2.22: Representation of the GE1/1 station with all its Super-Chambers: on the left a Super-Chamber is represented, in the middle the arrangement of Super-Chambers in the GE1/1 ring and on the right the GE1/1 station installed in the so-called nose of the CMS detector. In blue and magenta respectively the long and short Super-Chambers [64].

the services. The assembly procedure is performed without using glue, to avoid any ageing process caused by the outgassing of materials inside of the detector.

Once the bare chamber has been closed, it has to be equipped with the electronics and all the services that allow its operation, as illustrated in the exploded representation of a single chamber in Fig. 2.24. On the top of the readout board, the electronics and the cooling plate are installed and, on one side of the chamber, the patch panel.

This interface, illustrated in Fig. 2.25, hosts the connectors for the services (the gas pipes, the HV and LV power cables and the electronics optical fibers) and the connection to the ground of the CMS endcap. The ground reference is distributed to all the electronics components, to the HV and LV inputs and to the external structure of the chamber.

To complete the chamber two other components need to be installed:

- an external aluminium frame, enclosing the internal plastic one;
- an aluminium cover, called *chimney*, with a Kapton foil applied to its inner side, to avoid an ohmic contact between the chimney and the cooling plate below.

Together with a copper coating applied on the external side of the drift board, they form a Faraday cage, fundamental to insulate the electronics from any electromagnetic noise present in the CMS cavern during the detector operation. The electric contact among these components is ensured by the screws fixing the chimney to the aluminium frame and by thin cables attached to the patch panel, connected in turn to the CMS endcap ground.

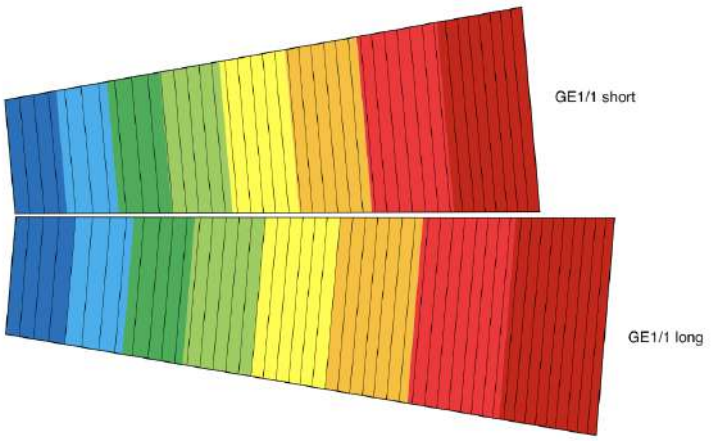

Figure 2.23: Segmentation of the foil in sectors, 40 for short and 47 for long chambers. The colour represents the η sector of the readout plane facing the corresponding part of the GEM foil, red and blue respectively for the 1st and the 8th sectors [65].

The cooling plate. The cooling plate consists of a copper layer with a copper pipe attached to it and routed outside of the chamber, on the patch panel side. Its custom shape ensures contact with all the electronic components installed on the chamber, which need to be cooled during their operation. The input and output pipes are coated with Kapton tape, to ensure the electrical insulation between the cooling plate and the patch panel, and so the external side of the chamber which acts as a Faraday cage. When 2 single chambers are coupled in a Super-Chamber, a plastic U-pipe is applied to connect the cooling plates of the two chambers to supply both of them with only one cooling line.

The fluid used to cool the detector during its operation is water with a temperature of $16\,°C$.

The HV filter. As illustrated in Fig. 2.25 a tiny box is present on the patch panel of each chamber, whose purpose is to reduce as much as possible the noise introduced inside of the chamber by the HV cables. This task is performed by 7 T-filter circuits, one for each of the 7 HV fed electrodes, consisting of:

- a $10\,\mathrm{k}\Omega$ resistor connected to the GEM electrode considered;
- a $2.2\,\mathrm{nF}$ capacitor connected to the ground;
- a $320\,\mathrm{k}\Omega$ resistor, connected on the side facing to the power supply board.

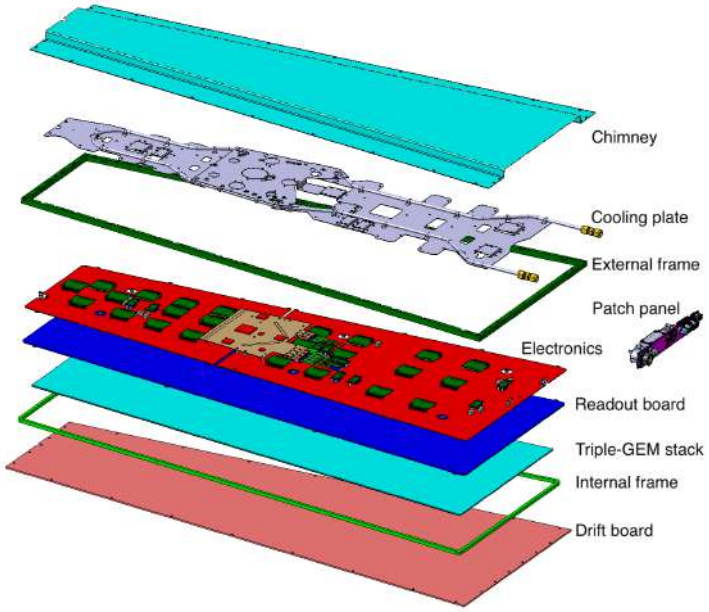

Figure 2.24: Exploded representation of a fully equipped GE1/1 detector [65].

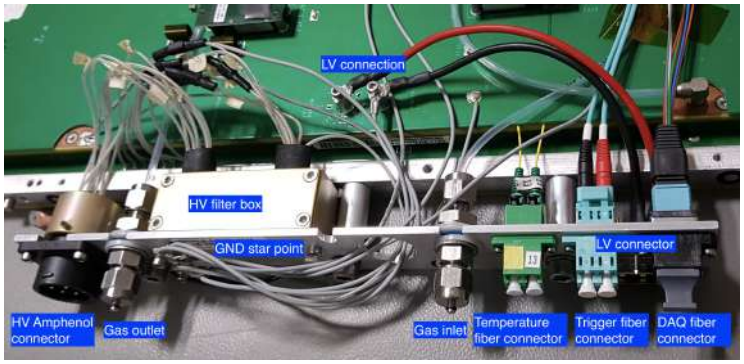

Figure 2.25: Patch panel of a single GE1/1 chamber [65].

2.2.2 Services of GE1/1 chambers

To operate correctly GE1/1 chambers the station has to be equipped with several services, each one controlled by a dedicated system, described shortly in the following sections. To enable a single operator to have everything under control at the same time during his shift, such a variety of systems needs to be centrally controlled by a unique node and this is ensured by the Detector Control System (DCS). At the same time, the safe operation of the detector has to be granted and the Detector Safety System (DSS) is the apparatus deputed to this task.

2.2.2.1 HV system

The HV power system consist of four CAEN-SY4527 mainframes located in CMS service cavern (USC), each of them hosting 9 HV boards CAEN-A1515TG. This power board has been specifically designed to power triple-GEM detectors: it powers 14 HV pins, creating a multichannel power supply system. This offers wider flexibility in the voltage settings: for example, it allows to power one channel alone and so investigating the detector behaviour with only one active gap.

The channels of a board are used to power two adjacent Super-Chambers, as illustrated in the HV mapping in Fig. 2.26. Both the layers of a Super-Chamber, required to have a similar gas-gain, are powered by the same group of 7 HV channels. The sharing of one channel among two equivalent electrodes of the two layers is achieved through a Y-splitter patch panel located in the HV racks.

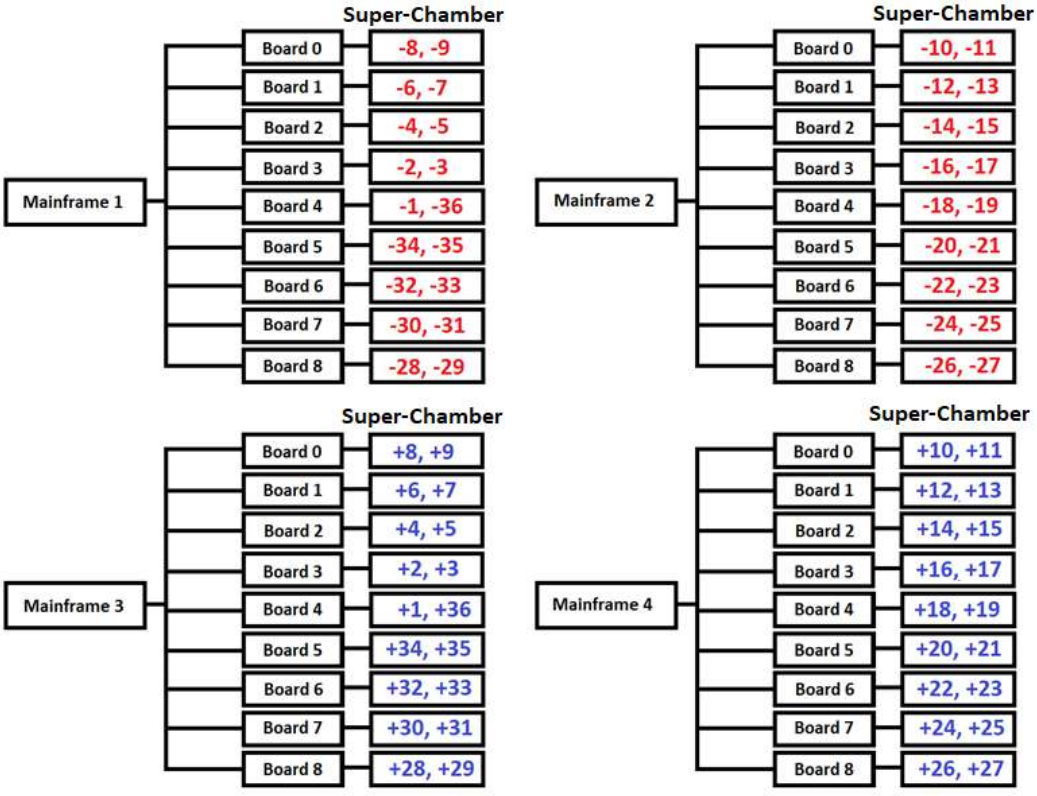

Figure 2.26: Mapping of the GE1/1 HV system.

2.2.2.2 The LV system

The LV power system is composed of a part placed in the Underground Service Cavern (USC) and one in the Underground Experimental Cavern (UXC). The

starting point of the system is located in the service cavern and consists of 4 branch controllers CAEN-A1676A. As illustrated in Fig. 2.27, each branch controller sends commands to a pair of crates Easy3000, placed in UXC.

Each crate hosts up to five boards CAEN-A3016HP and their power is provided by the CAEN-A3486 power supply, called *MAO*. In turn, each board feeds up to 6 single chambers, corresponding to 3 Super-Chambers. Each layer in a Super-Chamber indeed has its dedicated LV supply line, requiring a voltage up to 8 V. This offers a flexible and independent operation of the electronics of the two layers of a Super-Chamber.

Since the cable going from the board to the detector is tens of meters long, some of the supplied voltage ($O(0.1\,\mathrm{V})$) is dispersed along the cable. For this reason, two sense wires measure the actual voltage applied to the chamber and this information is used to tell the board how much the delivered voltage has to be increased to have the desired one on the chamber.

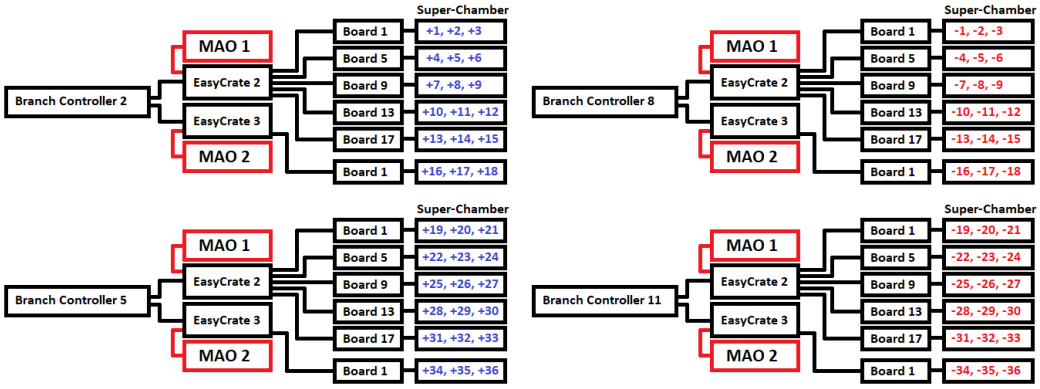

Figure 2.27: Mapping of the GE1/1 LV system.

2.2.2.3 The gas system

The design of the gas system of CMS articulates in a main and a spare line for each endcap, split into 12 lines, each of them feeding 6 adjacent single chambers and belonging to Layer 1 or Layer 2 of adjacent Super-Chambers. On each line are present two flowcells, to check the input and output flux. The gas mixture enters and exits from the chamber through input and output nozzles (Fig. 2.25). The flux at the moment is set to 18 l/h per gas line.

At the start of the main supply line a gas mixer combines the Ar and CO_2 in the desired percentages. The standard mixture used for the chamber operation is Ar/CO_2 (70/30%).

The system is designed to flux the chambers both in Ar/CO_2 and in pure CO_2. This is particularly useful when the chambers remain inactive for a long period (for example after the technical stops). In this case, the procedure states to perform training of the HV electrodes first in pure CO_2 and then in the standard mixture, to clean the electrodes from any dust accumulated

on the foil, which could cause a discharge. The training usually consists in keeping a single foil to a fixed voltage for many hours ($\sim 12\,hours$), before turning it off and moving to the next foil.

2.2.2.4 The cooling system

The cooling system is designed to refrigerate the on-detector electronics during its operation. To perform this task, cool water at a temperature of $16\,°C$ and with a pressure of $9\,bar$ is pumped into the system. Both layers of a Super-Chamber are cooled by the same cooling supply line since they are connected together by a plastic U-pipe. The strength of this connection is checked when each Super-Chamber is assembled, to be sure not to have a detachment of the pipe in the CMS cavern with a consequent leak of water.

2.2.2.5 The Detector Control System (DCS)

To simplify the operation of the detector, the HV, LV and gas systems are controlled by a single system: the Detector Control System (DCS). From this node, the operator can deliver the commands to these three systems, which will answer executing the desired command (for example setting a voltage value on an HV channel of a Super-Chamber) and storing the measured values of HV, LV and gas parameters in a dedicated database.

One additional functionality provided by the DCS is to enable the operator to deliver simple commands to the whole system. Furthermore, more complex scripts can be inserted to perform predefined procedures instead of executing them manually, with the possibility of an error by the operator.

If during the operation of any of the systems, one of the parameters overcomes a fixed threshold, the DCS raises an alarm and can take action to ensure the detector safety, depending on the entity of the event. For example, if the current of a fixed HV channel overcomes its operation threshold I_0, the board A1515 sends a kill command to the interested channel and, at the same time, the DCS raises an alarm for the operator. The boards indeed are programmed to switch off if a too high current flows in a channel, to ensure a safe operation of the detector.

Furthermore, through the DCS the systems are connected to dedicated databases, where the quantities of interest in terms of detector operation and monitoring, for example, the monitored voltage or the current threshold can be saved. In addition, when an action is taken on a channel of these systems, a status flag is also set and saved in the database, available for any needed future investigation.

The GEM DCS also monitors the gas system, but, in this case, it can only monitor the gas mixing parameters and it is not enabled to change them. In case of any problem in the mixing, it raises an alarm to the *CMS gas group.*

In addition, the GEM DCS is integrated into the CMS Central DCS, which is designed to operate all together every CMS subsystem from a single node

and gather the corresponding alarms. There are two operation modes of the subsystems: *local* and *global*.

When a subsystem is in *local mode*, its control is in the hands of the subsystem detector expert, which has the power to change its operating parameters depending on the operation needs, with complete autonomy from the other subsystems.

When the control of the subsystem is released to the Central DCS, the subsystem is in *central mode* and it can be operated only by the CMS Technical Shifter. This operator has a limited action on the subsystem and can basically switch it on or off, but not change the operating parameters.

If any change in the operating parameters is needed the CMS Technical Shifter has to release the control, putting the subsystem in local and enabling the detector expert to operate.

2.2.2.6 The Detector Safety System (DSS)

The DSS is the system that, together with the DCS, ensures the safety of the detector. This system is designed to react to major safety threats and take action to save the detector from damages, for example in case of fire, leaks or any other threat which could undermine the detector operation.

Regarding the GEM subsystem, DSS has its own sensors installed on the HV and LV racks and can take action on the rack, for example turning off the entire rack or activating a fire extinguishing valve.

The DSS is enabled to execute automatically only some actions, while for others it only raises an alarm, to make the CMS Technical Shifter and Shift Leader aware of a possible threat. In case of a major threat alarm these operators could decide to take action on the main DSS panel, placed in the CMS control room, for example, switch off instantaneously a subsystem (bypassing the DCS switch off procedure), or execute a protected action, such as switching off the entire CMS experiment.

2.2.2.7 The back-end electronics

The back-end electronics is the part of the electronics installed in the Underground Service Cavern (USC), connected with the detectors in the Underground Experimental Cavern (UXC) by optical fibres tens of metres long. This system is composed of two μTCA crates (also called shelves), each of them hosting:

- a MicroTCA Carrier Hub (MCH), responsible for providing services to every card hosted in the shelf;
- six custom made AMCs (Advanced Mezzanine Card), called *Calorimeter Trigger Processor cards* (CTP7);
- an AMC13;

The CTP7 boards are the first element of the back-end electronics to receive the data stream from the front-end electronics. This custom made AMC was formerly designed for the upgrade of the calorimeter trigger system, but its ability to handle a gigabit stream of input and output data and its flexibility suited well with the DAQ requirements for the GE1/1 chambers. Each of these modules handles the data stream coming from 12 single chambers (6 Super-Chambers).

The AMC13 performs three tasks:

- distributes the 40 MHz CMS clock to the electronics, to synchronize the cards hosted in the shelf and their command executions;
- reads the status of the front-end electronics and communicate it to the central CMS control system, the Timing and Control Distribution System or TCDS;
- gathers the stream of data collected by the CTP7 boards and sends it to the CMS central DAQ.

2.2.2.8 The front-end electronics

The front-end electronics is the part of the readout electronics located on the chamber and is composed of 4 main components:

- the GEM Electronics Board or *GEB*,
- the FEAST voltage converter,
- the VFAT3 ASIC;
- the OptoHybrid board.

The GEB. The GEB is a passive PCB module designed to route the LV power from the patch panel to the single active components installed on the chamber. In addition, it also routes the signals induced on the strips towards the readout VFAT3 chips. Finally, other paths connect the VFATs with the OptoHybrid board, attached to the GEB with a SAMTEC connector.

The FEAST. On every single chamber, 9 *FEASTMP-CLP DC-DC voltage converters* (FEAST) provide a customized voltage to the electronic components. Each of these modules is a DC-DC converter, transforming the 8 V provided by the LV supply cable attached to the patch panel, in a voltage in the range $1 - 2.55$ V. The heat produced in the conversion is evacuated on the top of the FEAST, through the cooling plate, thermally in contact by a drop of non-conductive thermal paste applied on the top of each FEAST.

The VFAT3 ASIC. The VFAT3 ASIC (Very Forward Atlas and Totem ASIC) has been designed starting from the radiation tolerant module originally designed for detectors installed in the TOTEM experiment. In each GE1/1 single chamber, there are 24 VFAT3 ASICs and their scheme is illustrated in Fig. 2.28, while a picture of the single chamber assembled with the GEB, the 24 VFATs and the OptoHybrid board is given in Fig. 2.29. In this last picture, the OpthoHybrid board is the large dark green board installed in the middle of the chamber, while the 24 VFATs are the light green square elements placed all over the chamber. The VFATs are labelled from 0 to 23 and each of them covers a readout sector corresponding to a fixed $i\phi$ and $i\eta$ sector, as shown in Fig. 2.30.

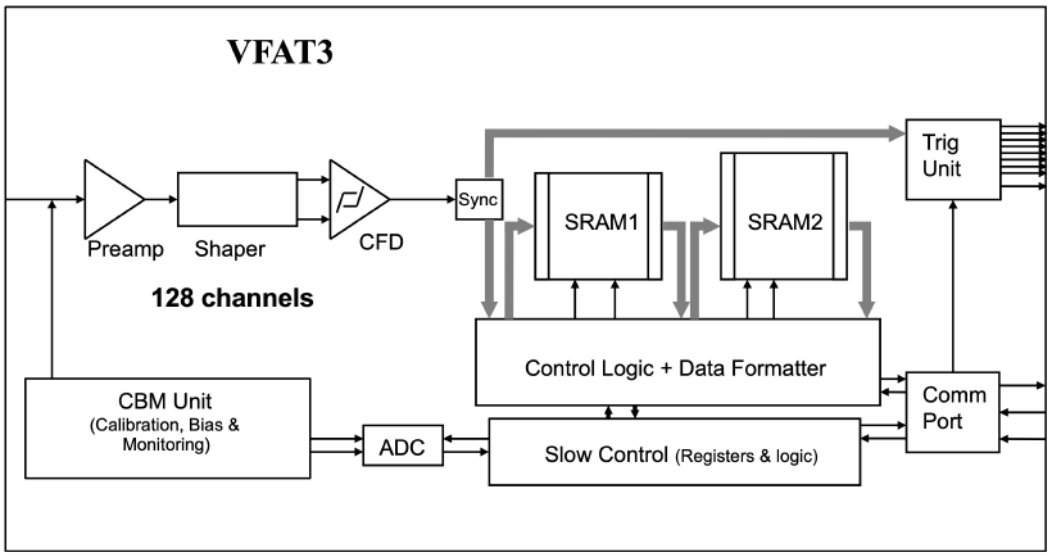

Figure 2.28: Scheme of a VFAT3 ASIC installed on GE1/1 chambers. The acronyms in the figure mean in order: Constant Fraction Discriminator (CFD), Analogue to Digital Converter (ADC) and Static Random Access Memory (SRAM) [64].

Each VFAT is equipped with 128 input channels, collecting the signal from the readout strips of the corresponding readout sector. It can be programmed to read both positive than negative input signals, that for each input channel are elaborated by the circuit sketched in Fig. 2.28, starting with a preamplifier, a shaper and a Constant Fraction Discriminator (CFD) in cascade. In this last component, two main operations are performed:

- the identification of the arrival time of the signal, by a Zero Crossing Comparator (ZCC);
- the comparison of the input signal with a threshold value (the threshold is given by the sum of a global value and a per-channel adjustable value).

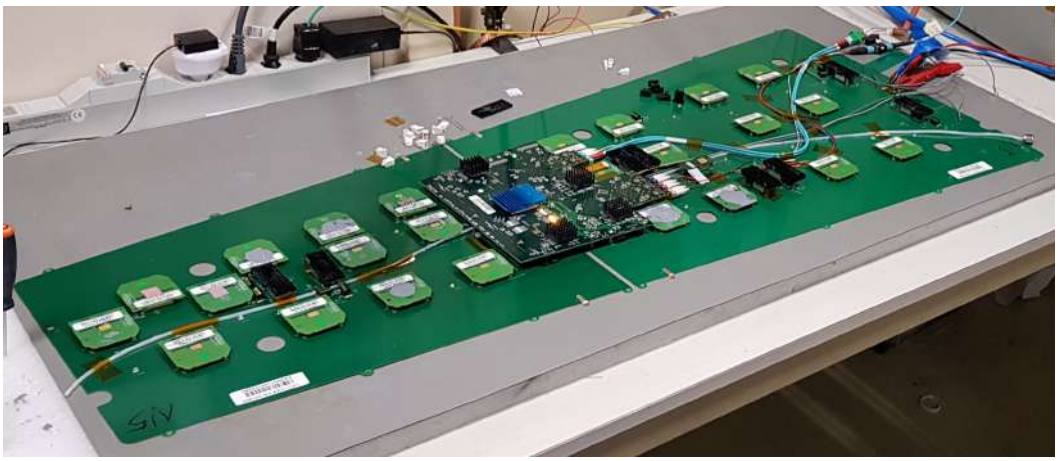

Figure 2.29: GE1/1 single chamber equipped with the GEB, the 24 VFATs and the OptoHybrid board, on the stand deputed to perform the electronics quality control [65].

If a signal results higher than the set threshold, it is synchronised with the 40 MHz clock and a boolean is set to true, authorising the acquisition of the digitised signal.

After this operation, the digital signal is routed in two different paths: the data path and the trigger path. The first thing to mention is that they have a different granularity: the data path exploits the whole granularity provided by the strip segmentation, while the trigger path uses half of the whole granularity.

In this path indeed a logical OR between neighbour strips is performed producing output information consisting of 64 bits (1 bit per pair of strips), called also *s-bit*. These s-bits are transferred every bunch-crossing, synchronised with the LHC clock. The logical OR of two neighbouring strips is also called *pad*.

In the data path, exploiting the whole detector granularity, the digitised signals are stored in a buffer (SRAM1). In this buffer a fixed BX signal can be hosted for a time corresponding to 1024 BXs, corresponding to 25.6 μs, and then overwritten with new data. In case an L1A trigger signal (L1 Accept) arrives in this time range, the data are transferred to the next memory unit SRAM2. In this operation, a timestamp is attached to the data.

The SRAM2 acts as a FIFO, storing the data waiting for the construction of a package to deliver them off the chip to the next unit in the DAQ, the OptoHybrid board.

In addition to these components, there are two additional units:

- the Slow Control Unit, enabling the communication to read and write in a register the parameters to configure the chip;
- the CBM (Calibration, Bias and Monitoring) unit, involved in setting

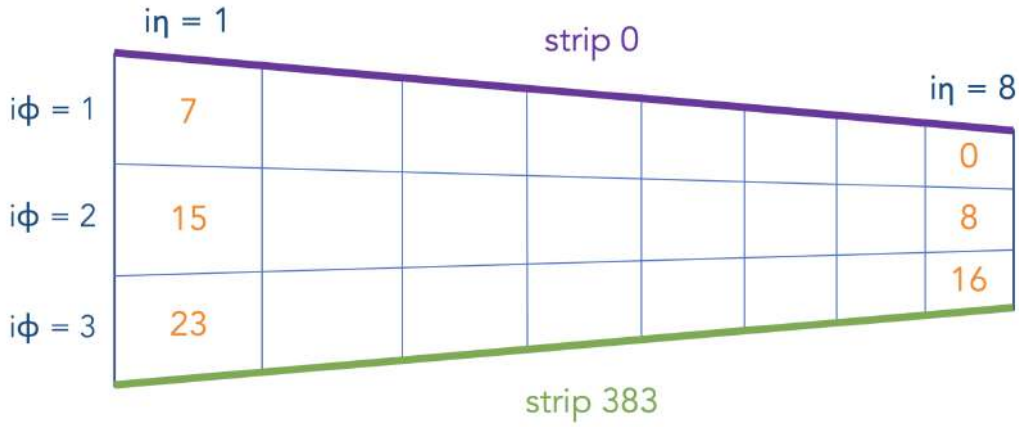

Figure 2.30: Mapping of VFATs on the covered readout sectors [65].

and fetching the setting parameters.

These VFAT setting parameters are stored in registers and are used to define the threshold required on each channel, transforming the register value saved in a bias voltage or in a current.

The CMB module is particularly important also to test the response of the VFAT channels. This is done using an incorporated calibration module that can send a voltage or current pulse, producing a signal similar to the input one given by the readout strips.

Finally, in addition to the elements illustrated in the VFAT scheme, it can be pointed out that two other important components are present on each VFAT3 chip:

- a 470 Ω resistor on each channel, to quench possible discharges reaching the readout plane, protecting the channel from possible damages;
- a gold heat exchanger rectangle, placed on the top of the chip, to evacuate the heat produced during the chip operation. This heat exchanger is thermally coupled with the cooling plate using the same non-conductive thermal paste used to thermally couple the FEASTs.

The Optohybrid board. Fig. 2.31 shows the OptoHybrid board OHv3c. This component is the heart of the front-end electronics and performs two main tasks:

- analyses and delivers the trigger hits to the GEM backend and to the CSC Trigger Mother Board (TMB);
- transfers the data from the 24 VFATs to the GEM backend.

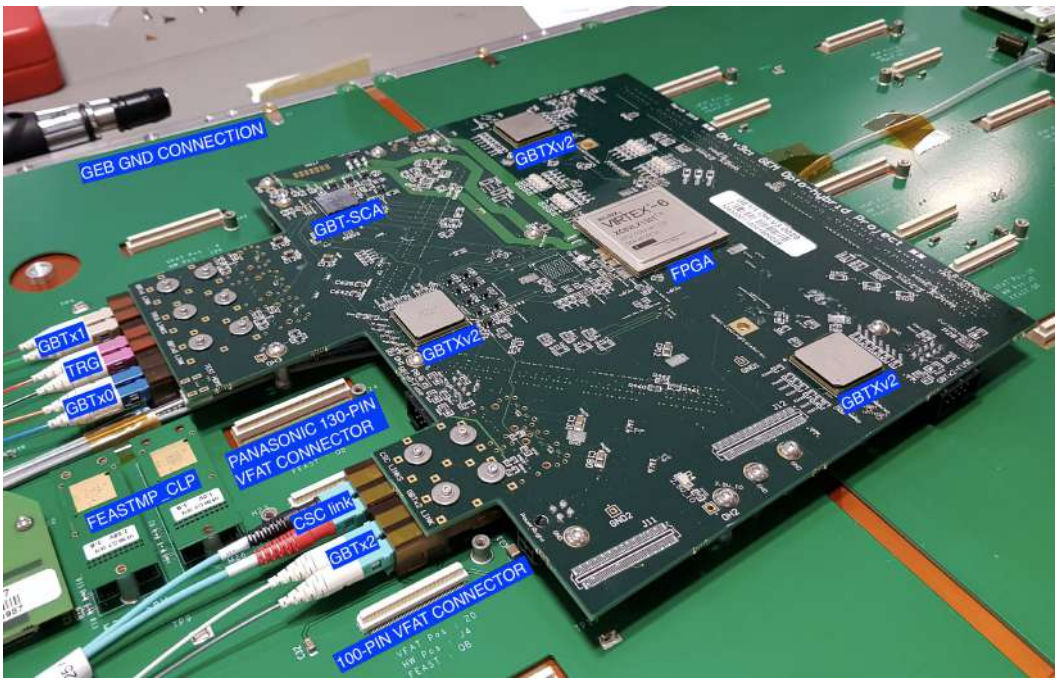

Figure 2.31: The OptoHybrid board installed on a GE1/1 chamber, with its main components highlighted [65].

In Fig. 2.31 five components on the board are highlighted:

- one FPGA Xilinx Virtex-6, responsible for processing the trigger hits and transferring them to the back-end;
- three GBTXv2 ASICs gigabit transceivers, responsible for transferring the data from the VFATs to the backend. In addition, one of them is also in charge of programming the FPGA and of the communication with the slow control unit;
- the Giga-Bit Transceiver - Slow Control Adapter (GBT-SCA), responsible for the slow control commands.

As for the other heating elements in the front-end electronics, these last three components are thermally coupled with the cooling plate using a non-conductive thermal paste, applied on the top of each of them.

2.3 The GE2/1 station

The GE2/1 station will be the second GEM station to be installed in CMS. At the end of LS2, the installation of the first demonstrator chambers has taken place, while the complete installation of the station is foreseen during the Run 3 technical stops.

The station will be placed in the second layer of detectors of the muon system, starting from the interaction point, and in the first ring seen from the beampipe. The covered pseudo-rapidity range will be $1.6 < |\eta| < 2.4$, as shown in Fig. 1.23. The structure of the station will be similar to that of GE1/1, consisting of Super-Chambers with 2 detection layers each. The main differences are:

- the angular coverage in ϕ of 20° per Super-Chamber (18 Super-Chambers per endcap, 72 single chambers in total);
- the area covered by each chamber will be 1.45 m^2, while the total area will cover 105 m^2, becoming the largest GEM station installed in CMS.

Similarly to GE1/1, the GE2/1 station will increase the redundancy in the endcap muon system, providing two additional reconstructed hits and bringing to 8 the total number of hits in the region covered also by GE1/1. This is particularly important, since a higher number of hits along a muon trajectory, allows to:

- improve the local trigger primitive object (*stub*) reconstruction efficiency, as illustrated in Fig. 2.32;
- lower the L1 trigger rate in the region;
- lower the number of muons with a wrong p_t estimation.

This improvement in the p_t estimation is supported by the possibility of measuring the $\Delta\phi$ bending angle formed by a muon crossing the stations GE2/1 and ME2/1, similarly to what was done through the cooperation of GE1/1 and ME1/1.

Furthermore, an important role in the p_t estimation process is played also by the lack of iron between the GEM and the CSC station, which reduces the multiple scattering contribution and leads to a reduction in the number of soft muons misidentified as harder muons, supporting a consequent reduction in the L1 trigger rate.

Turning to the design of the chamber, as for GE1/1 chambers the 3/1/2/1 mm spacing has been adopted. The readout plane employs strips with a variable pitch, from 0.5 mm (closer to the beampipe) to 1.2 mm (farther from the beampipe). As for GE1/1, the strips are read in groups of 128, but in this case by 12 VFATs per each sector, as illustrated in Fig. 2.33. The signals elaborated by the VFATs are then routed and processed by an OptoHybrid board per each of the 4 main sectors.

2.4 The ME0 station

ME0 will be the third GEM station to be installed in CMS (foreseen during LS3) and it will be installed in the space left empty behind HGCAL, after

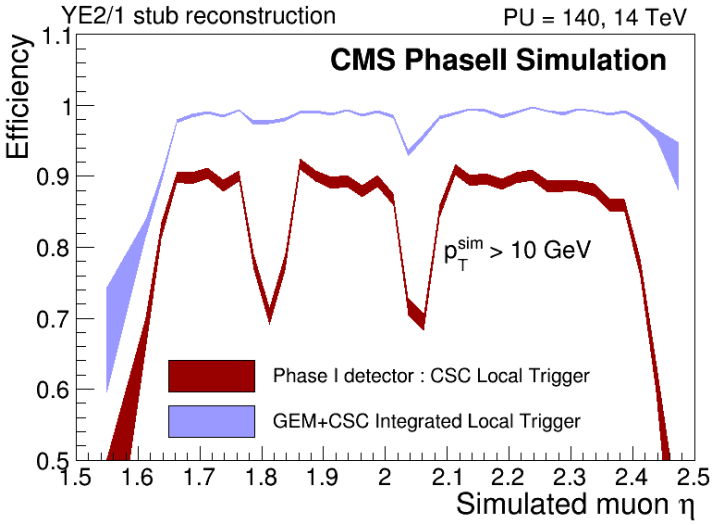

Figure 2.32: Reconstruction efficiency, as a function of η, of the local trigger primitive object, called *stub,* in a scenario with $PU = 140$ and $\sqrt{s} = 14\,\text{TeV}$. In red the performance offered by the detectors installed in CMS till the end of Run 2, while in blue the improvements offered by the installation of the GE2/1 station [46].

the installation of this new version of the endcap hadron calorimeter. It will cover the pseudorapidity range $2.0 < |\eta| < 2.8$ and will consist of 18 modules per endcap with a ϕ coverage of 20° per module. Each module will consist of 6 GEM detector layers.

As for the other GEM stations, the readout plane is segmented into sectors with 128 strips, read by a dedicated front-end electronics component. The ME0 design consists of 8 partitions in the longitudinal side of the chamber (also called *η-partitions*), and 3 in the ϕ direction, for a total number of 24 readout sectors per chamber.

As for the other GEM stations, the ME0 station will allow to increase the number of hits per track and to improve the p_t estimation, but will also increase the coverage of the muon system making possible to perform a better investigation of channels with many muons in the final state, exploiting also the forward ones.

The advantages and innovations introduced by the installation of the ME0 station are:

- the introduction of 6 additional hits useful for the reconstruction of a muon, reducing the L1 trigger rate for muons reconstructed also by other stations of the muon system;

- part of the η range of ME0 does not overlap with that of GE1/1 ($2.18 < |\eta| < 2.40$) and in this region ME0 performs the second measurement of the muon bending (the first one in this η region is that performed by

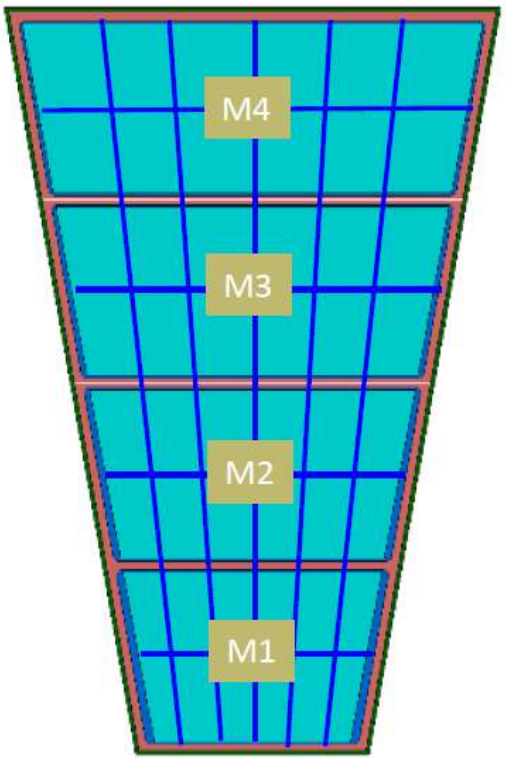

Figure 2.33: Scheme of the readout plane of GE21: the 4 radial sectors are labelled as M1-M4, and each of them is divided in 12 sectors with 128 strips each [75].

the cooperation of GE2/1 and ME2/1 stations). The six GEM layers of ME0 allow indeed to build a segment laying entirely in this station, not requiring cooperation with a nearby station.

- ME0 will increase the coverage of the muon system from $\eta = 2.4$ to $\eta = 2.8$, providing a muon station covering part of the upgraded tracker.

One of the main challenges for the ME0 station is the high background radiation in the region, requiring a deeper R & D in terms of radiation hardness and rate capability of the detector. As illustrated in Fig. 2.34, it is much higher than the background sustained by the other 2 GEM stations. This high background can affect also the production of the ME0 segments, since a background hit could be used in its building process, assigning a softer p_t to a high p_t muon. This effect worsens with the increase of η, as illustrated in Fig. 2.35.

2.4.1 Impact on physics in the forward region

The strongest motivation leading to the installation of the ME0 station, as well as the other GEM stations, is the impact on the detection of physics channels

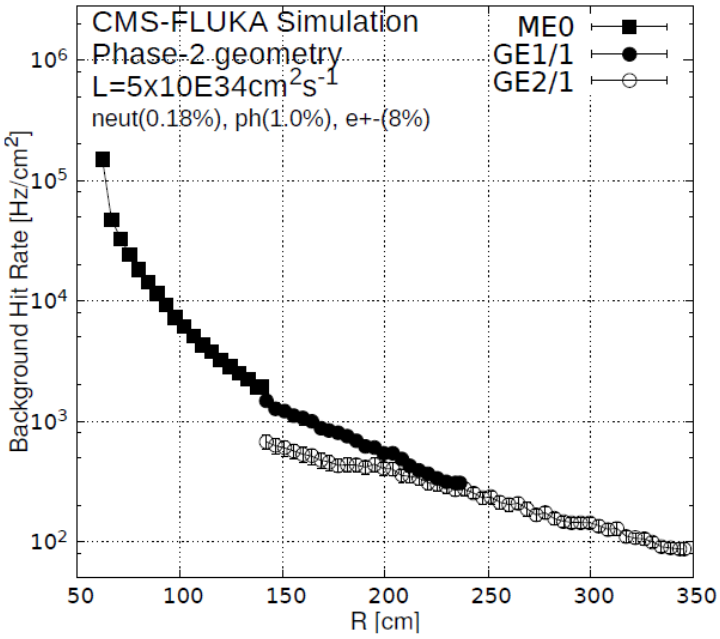

Figure 2.34: Estimation of the background hit rate provided by neutrons, photons, electrons and positrons on the three GEM stations planned to be installed in CMS. [46].

with multi-muon production in the forward region. The ME0 station alone would indeed lead to an increase in the muon acceptance of 10-20%.

In this context, two main channels were investigated:

- the $H \to ZZ^* \to 4\mu$ decay,
- the $\tau \to 3\mu$ decay.

The $H \to ZZ^* \to 4\mu$ decay. Fig. 2.36 shows the distribution of signal events ($H \to ZZ^* \to 4\mu$) and irreducible background events ($ZZ \to 4\mu$) using a CMS geometry with the tracking, calorimetry and muon systems extended up to $|\eta| = 4.0$. It can be noticed in particular that a great part of the signal events lay outside of the CMS acceptance at the end of Run 1 (vertical dashed lines).

More recent studies focused on the ME0 station highlighted that 15% of the signal muons lay in its acceptance, with an 8% fraction falling in the region $2.4 < |\eta| < 2.8$. In addition, the signal muons in this region are characterised by a low p_t, and this makes challenging to distinguish the signal muons from the pileup ones.

The $\tau \to 3\mu$ decay. The second process considered is the $\tau \to 3\mu$ decay channel: this channel is one of the cleanest decays involving the Lepton

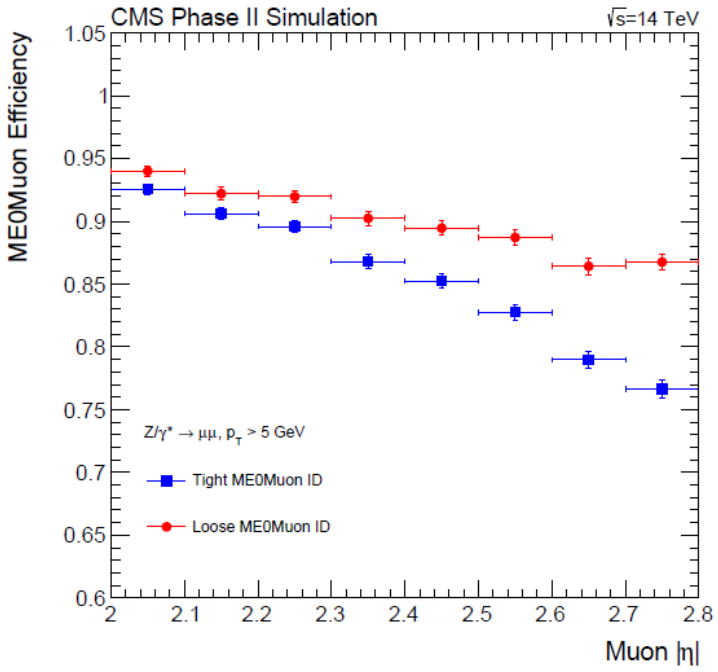

Figure 2.35: Reconstruction efficiency of ME0 muons. In blue are represented the Tight ME0Muons, selected requiring the presence of a ME0 segment with $\Delta\phi < 0.15$ with respect to the direction of the tracker track, while in red the Loose ME0Muons ($\Delta\phi < 0.50$) [43].

Flavour Violation (LFV) and is characterised by an extremely low branching ratio predicted by the Standard Model ($\mathcal{B}(\tau \to 3\mu) \sim 10^{-40}$). Some models involving physics Beyond the Standard Model (BSM), raise this branching ratio of many orders of magnitude ($\mathcal{B}(\tau \to 3\mu) \sim 10^{-11}$-$10^{-8}$), reaching a potentially accessible event statistic. The muons composing this signal are in particular characterised by a soft p_t and most of the reconstructable muons are found in a forward collimated cone, having challenges in signal-background discrimination similar to those of the $H \to ZZ^* \to 4\mu$ channel. Recent studies pointed out that an increase in the acceptance of the muon system up to $|\eta| \sim 3$ would lead to an increase of its signal acceptance by a factor of 2.9. The $\tau \to 3\mu$ decay will be in particular described more in detail in the last chapter of this thesis, with the description of a dedicated trigger study.

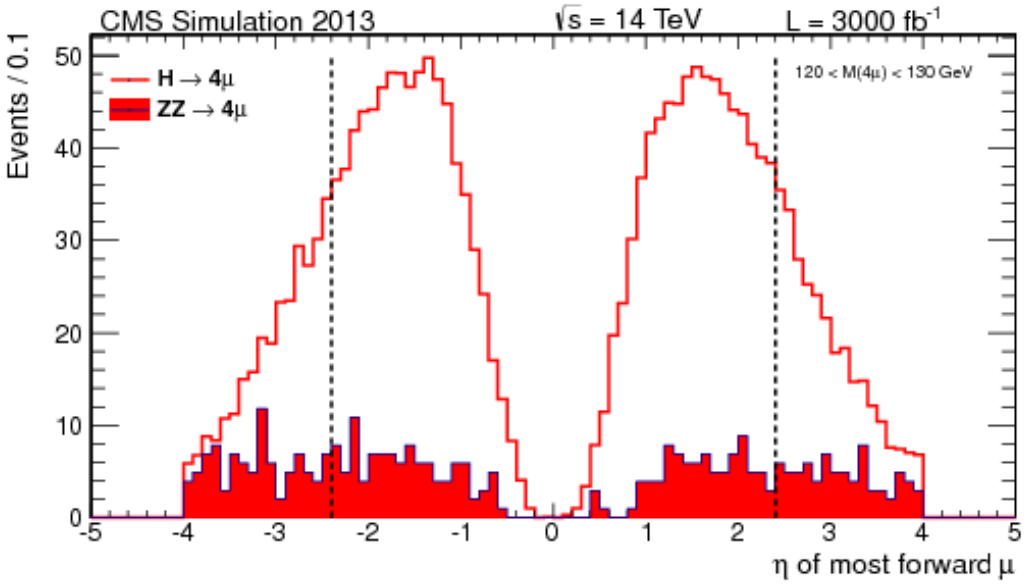

Figure 2.36: $H \rightarrow ZZ^* \rightarrow 4\mu$ channel: η distribution of the highest-$|\eta|$ muon among the 4 produced in the decay. The events represented in the distribution are given by a selection that was produced using a CMS geometry with tracking, calorimeter and muon systems extended to $|\eta| = 4.0$. The signal events $H \rightarrow ZZ^* \rightarrow 4\mu$ and the irreducible background events $ZZ \rightarrow 4\mu$ are respectively indicated with empty and solid red. The dashed lines correspond to the acceptance of CMS at the end of Run 1 [76].

Chapter 3

GE1/1 quality control and commissioning

In this chapter I will focus on the activities I have carried out during my PhD in the quality control of GE1/1 detector and in particular in the monitoring of the HV and LV systems, both at the assembly site and at the CMS experiment site.

3.1 Production and quality control of GE1/1 chambers

The schedule for the production of a GE1/1 Super-Chamber involves many steps and Quality Controls (QC). Since the total number of GE1/1 chambers is 144 and due to the fact that many checks are needed to produce a correctly operating detector, to speed up the production the effort is shared among many production sites in the world:

- National Center for Physics (Pakistan) - Pakistan;
- National Institute of Nuclear Physics (INFN), Section of Bari, and Bari University (Italy);
- INFN, Section of Frascati National Laboratories (Italy);
- Florida Institute of Technology (USA);
- Ghent University (Belgium);
- Bhabha Atomic Research Center, Delhi University and Panjab University (India);
- CERN GEM production site (France).

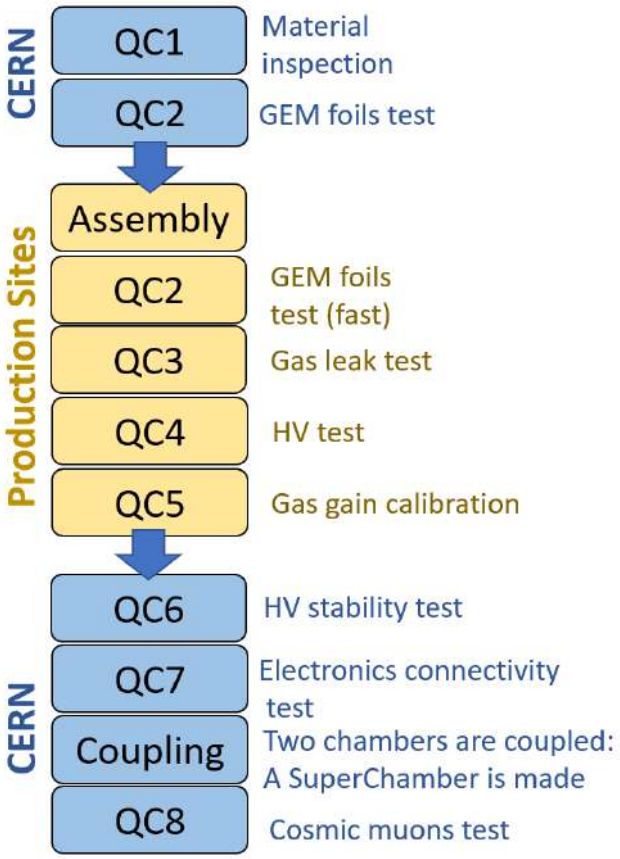

Figure 3.1: Schedule for the production of a GE1/1 Super-Chamber, from the material inspection to the final validation: the components and the GEM foils are firstly inspected at CERN and then shipped to the production sites, to ensure they use good quality components in the production. At the production sites, as well as at CERN, quality controls up to QC5 are performed, before shipping the detectors back to CERN, where the last quality controls are performed [77].

The procedure for the production of a GE1/1 Super-Chamber is sketched in Fig.3.1, and here briefly summarised. The single steps will be illustrated in more detail in the next paragraphs:

- QC1: material inspection;
- QC2: test of the GEM foils;
- assembly of a single chamber;
- QC2: new test on the GEM foils;
- QC3: gas leak test;
- QC4: HV test;

Process	Estimated time
QC1	2 days
QC2 + assembly	2 days
QC3	1 day
QC4	1 day
QC5	1-2 days
QC6	Performed until single chamber is coupled
QC7	2 days
Coupling	20 minutes
QC8	1-2 weeks

Table 3.1: Estimated time for each main step in the production of a GE1/1 Super-Chamber.

- QC5: Gas gain calibration;
- QC6: HV stability test
- QC7: Electronics connectivity test;
- coupling of 2 single chambers in a Super-Chamber;
- QC8: cosmic test;

In Tab. 3.1 an indicative time required by each of the steps in the production is pointed out.

3.1.1 QC1: the material inspection

The first operation to start the production of a GE1/1 chamber is the most fundamental one: the inspection of every component needed for its assembly. This operation is performed at CERN and is fundamental to save time that would be lost in substituting it after a defect has been spotted by some QC.

The QC1 procedure consists in:

- a visual inspection, to check for cracks or major defects in the components;
- cleaning of the components;
- measurement of the sizes of the components to ensure they respect the design requirements: for example is fundamental a correct size of the O-rings which ensure the chamber gas tightness;
- connectivity test of the strips of the readout board, used to check for shorts between the readout strips and the continuity of the strips.

3.1.2 QC2: the leakage current test

When a chamber is operated, a high voltage is applied to the top and bottom surfaces of the GEM foils. Inside of the GEM holes, the surface of the foil is exposed to the air (or gas mixture during the operation); this external surface can represent a lower resistance path, with a so-called *leakage current* flowing on it. Defects in the manufacturing of the foils (small drops of copper coming out of the foil and ending inside the hole, dust deposition or any kind of pollution) can ease the current flowing in this path, increasing the leakage current observed at a fixed voltage, as sketched in Fig. 3.2. Also, humidity and temperature can influence the measurement, requiring continuous monitoring of these quantities. The amount of the leakage current represents in this way an indicator of the quality and of the health of the GEM foil. Since the deposition of dust could happen at any moment and to be sure that the foils in a stack are not damaged, the QC2 test has so to be performed before installing the foils in a chamber and also after completing the chamber assembly. To avoid additional deposition of dust on the foils, this test must take place in a clean room.

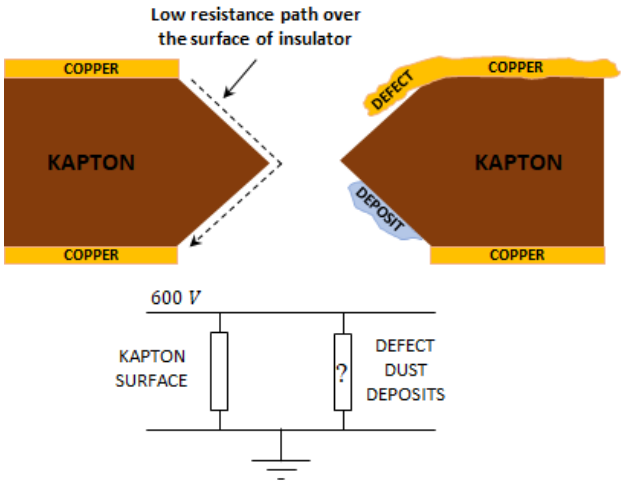

Figure 3.2: Scheme of a GEM foil, with defects and deposits which could increase its leakage current [19].

The QC2 can be performed in different ways and moments:

- QC2 fast test: a Multi Mega-ohmmeter, also called *MEGGER* is used to apply a potential difference of 550 V between the top and bottom surface, for 10 minutes. The leakage current, and so the impedance, and the number of sparks produced are measured. The test is performed in the air inside the clean room; it is considered passed if the impedance of the foil is higher than 10 GΩ and the number of sparks in the last three minutes of test is lower than 2. If the sparks created during the test,

produced any relevant damage to the foils this should indeed reflect on the impedance and in the spark rate.

- QC2 long test: the test is performed inside a clean room, with the foil placed inside a box filled with nitrogen, fluxing at 50 l/h, to lower the humidity level below 7%. As for the fast test, a high voltage is applied to the two foil faces, but in this case using a programmable power supply. The test is passed if, with an applied voltage of 600 V, a leakage current of ~ 3 nA and less than 3 sparks have been registered in the last 6 hours of operation.

- QC2 after assembly: this test is performed in air outside the clean room to ensure that potential amounts of dust produced during the assembly have not affected the operation of the foil. This test is similar to the QC2 fast test, but in this case 550 V are applied, one pair at a time, both to the two faces of a foil and to the electrodes creating an electric field in the gaps. The test is passed if the impedance of foils and gaps are respectively higher than 10 GΩ and 100 GΩ, and if the number of sparks counted in the last ten minutes of testing is zero. If the test is not passed, the chamber has to be opened in the clean room to identify and fix the problem.

- QC2 fast in dry gas: this test is performed before the mounting of the HV distribution circuit, but used also as the leading step of investigation for chambers with suspicious operating conditions. Before performing the test the chamber has to be flushed with pure CO_2 for at least 5 hours to evacuate any trace of humidity deposited on the foils. Performing the test in pure CO_2 is also fundamental to prevent damages on the readout plane from a propagating discharge; the CO_2 acts indeed as a quencher in the standard GEM gas mixture. After this preliminary phase the same procedure used for the QC2 fast post assembly test is performed and in this case the impedances of foils and gaps have to be higher than 20 GΩ and 100 GΩ.

3.1.3 The assembly

The assembly is performed at the production sites and at CERN. It has to take place in a clean room, to avoid the deposition of dust and other kinds of pollutants on the foils. In this phase the drift board, the three GEM foils and the readout board are fixed to the frames, providing a solid structure to the detector. At the end of the assembly procedure, the chamber can be kept outside of the clean room, paying attention to putting a plug on the gas inlet and outlet, to minimise the amount of pollution from the external environment.

3.1.4 QC3: the gas leak test

Once a chamber has been assembled and has passed the *QC2 test after assembly,* it is delivered to QC3, a test designed to spot and measure the amount of gas leakage on a GE1/1 chamber.

The test is performed by flushing pure CO_2 in the detector. An overpressure of 25 mBar inside the detector is provided by closing the gas output valve. Once this condition is reached, also the input valve is closed and a measurement of the internal overpressure starts. At the same time, the environmental conditions (pressure and temperature) are continuously monitored, to be sure to estimate correctly the internal overpressure.

The internal overpressure will decrease exponentially in time following the law

$$P(t) = P_0 e^{-t/\tau}, \tag{3.1}$$

where P_0 is the internal overpressure at time $t = 0$ and τ is a gas leak time constant, quantifying how fast is the overpressure decrease. The test is passed if the internal overpressure drop is lower than 7 mBar/hour.

3.1.5 QC4: HV test in CO_2

The QC4 test is performed flushing the detector with pure CO_2, with a flux rate of $5\,l/h$. The aim of the test is:

- identify any possible defect present in the HV circuit, measuring the I-V curve;
- measure the intrinsic noise rate.

During the test, the HV is distributed to the single electrodes, by a power supply with a resistive divider, illustrated in Fig. 3.3. To measure the I-V curve the voltage is varied from 0 V to 3.0 kV by 200 V steps and then up to 4.9 kV by 100 V steps. From the curve, the resistance $R_{measured}$ is then calculated and a comparison is made with the expected resistance $R_{expected}$. This first step of the test is passed if the percentage difference between the resistances is lower than 2%

$$\frac{|R_{measured} - R_{expected}|}{R_{expected}} < 0.02. \tag{3.2}$$

To determine the intrinsic noise rate a dedicated setup is used, sketched in Fig. 3.4. It receives the signal produced on the bottom of the third GEM foil and counts the number of signals registered in 1 minute of operation at a fixed HV value. This procedure is repeated for the same voltage values used in the I-V curve scan. The test is passed if the noise rate at 4.9 kV is below $0.02\,\mathrm{Hz/cm^2}$.

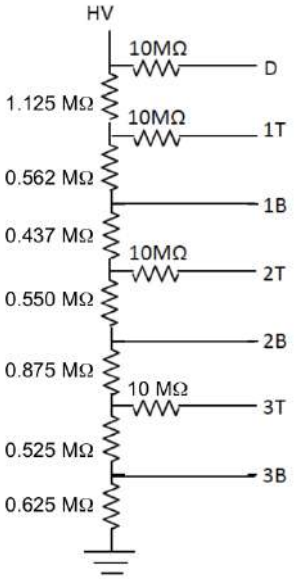

Figure 3.3: Scheme of the resistive divider used during the QC tests. On the right are indicated the channels corresponding to each connection: D for Drift, 1T, 2T and 3T for the top face of the three foils, 1B, 2B, 3B for the bottom face [19].

3.1.6 QC5: Gas gain and uniformity response measurement

The QC5 test consists of two steps:

- the measurement of the effective gas gain given by the detector at a fixed voltage applied through a resistive divider;
- the measurement of the response uniformity.

An X-ray gun emitting $22 - 25\,\text{keV}$ photons is used in this phase and the detector is placed inside a copper box for the containment of radiation and flushed with the nominal mixture Ar/CO_2 (70/30%) at $5\,l/h$. When the photons delivered by the X-ray gun hit the copper layer of the drift board, they are absorbed by the copper, which de-excites emitting 8.03 keV photons. This Cu fluorescence will be absorbed into the detector gas medium, emitting electrons. These electrons, called *primary electrons,* will be multiplied by the three GEM foils and produce a signal on the readout strips.

3.1.6.1 Effective gas gain measurement

The effective gas gain (G) of the detector is measured according to the relation

$$G = \frac{I_a}{R \cdot n_e \cdot e}, \tag{3.3}$$

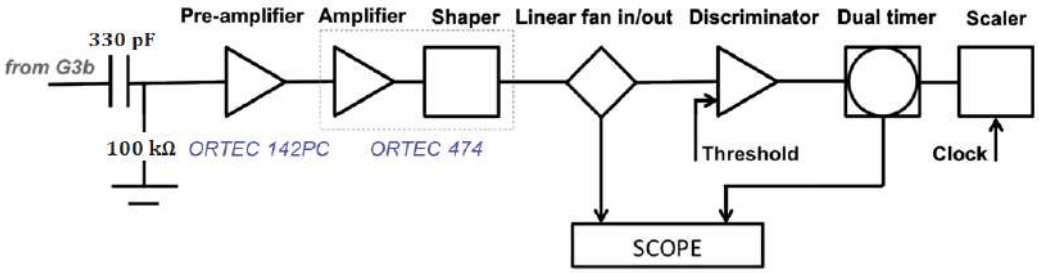

Figure 3.4: Scheme of the setup used for the noise rate measurement in QC4 [19].

where I_a is the current produced by the multiplication electrons on the anode, R the interaction rate of photons, n_e the number of primary electrons and e the charge of the electron. The gain measurement is performed always on the sector $(i\eta, i\phi) = (4, 2)$ (Fig. 2.30), applying in sequence voltage values equivalent to a divider current from 550 μA to 700 μA, in steps of 10 μA.

The number of primary electrons is estimated by the relation

$$n_e = E_\gamma \left(\frac{f_{Ar}}{W_i(Ar)} + \frac{f_{CO_2}}{W_i(CO_2)} \right), \tag{3.4}$$

where

- $E_\gamma = 8.03\,\text{keV}$ is the energy of photons converting inside of the gas medium;
- W_i are the work functions for Ar and CO_2 : $W_i(Ar) = 26\,\text{eV}$, $W_i(Ar) = 33\,\text{eV}$;
- on the fractions' numerators there are the concentrations of the gases in the mixture, respectively $f_{Ar} = 0.70$ and $f_{CO_2} = 0.30$.

The amplified current I_a produced on the strips of the readout sector is measured by a pico-ammeter, while the interaction rate of photons is measured using a dedicated experimental setup sketched in Fig. 3.5, which counts the number of signals produced on the readout strips in a time interval of 60 seconds. To perform a correct measurement of R and I_a, the counts and currents observed in the same time conditions, but with the X-ray gun off, are used to perform a background subtraction.

A typical value of gain for a GE1/1 detector at a divider current of 700 uA is $3.5 \cdot 10^4$, while in Fig. 3.6 are illustrated some results for a short chamber.

3.1.6.2 Gas gain uniformity

To have a complete vision of the gas gain all over the detector the procedure described before cannot be used, since it would be too time consuming.

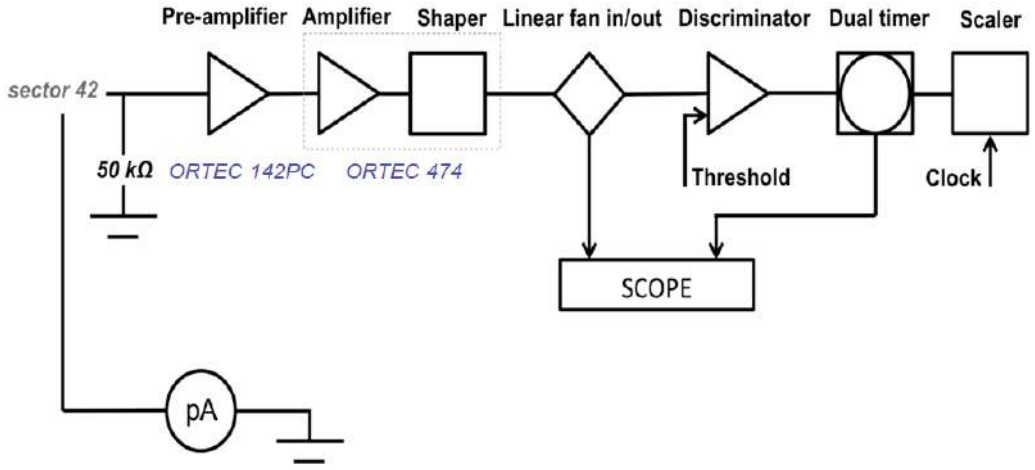

Figure 3.5: Scheme of the setup used for the effective gas gain measurement in QC5 [19].

The strategy adopted was then to irradiate the whole detector with an X-ray gun and reading the signals produced on every strip. Also in this case the test is performed inside the copper box, flushing the detector with the Ar/CO_2 (70/30%) gas mixture with a flux rate of $5\,l/h$, and the HV is still distributed through a resistive divider. To avoid saturating the electronics with readout signals, making it impossible to notice differences in gain between nearby regions in the detector, it has been chosen to operate the chamber at a low gain (~ 600).

During the analysis of the data, the collected charge of each cluster of strips producing a signal is used to create a uniformity map. This map is used to calculate the average effective gas gain over the whole detector and its standard deviation. More details can be found in [19].

3.1.7 QC6: HV stability test

After having passed the QC5 test, the chambers are delivered to CERN for the final validation steps; during the transport the chambers could get mechanically stressed and some dust could move inside. As previously said, the moving dust could affect the behaviour of the foils in terms of HV stability and thus a new quality control test is performed on the HV system, called QC6.

This test is performed in pure CO_2 and consists of several steps:

- measurement of the impedance of each foil with a MEGGER: the step is passed if the impedance in one minute is higher than $10\,G\Omega$ for each of them;
- measurement of the I-V curve for each of the HV electrodes (foils, trans-

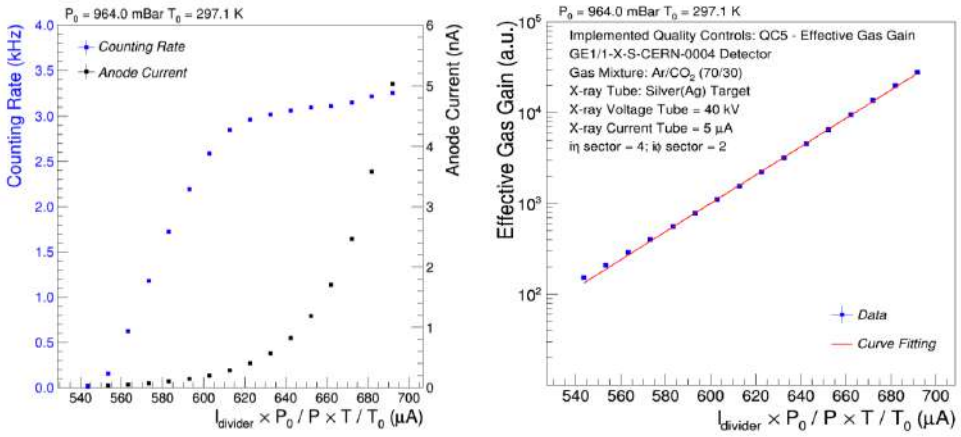

(a) (b)

Figure 3.6: (a) Anodic current I_a and photon interaction rate R; (b) effective gas gain as a function of the HV equivalent divider current $I_{divider}$, corrected by a normalisation factor, which contains the pressure and temperature of the production site P and T where QC5 has been performed, and the mean values of pressure and temperature present in the CMS experimental cavern P_0 and T_0. This provides a common reference for chambers tested in different production sites, with different environmental condition [78].

fer regions, induction and drift gaps) using a multichannel power supply with an A1515TG board, to spot any possible defect in the T-filter circuits or in the distribution from the filter box to the HV sectors, such as faulty soldering. In this procedure, the electrodes are ramped up together, from 200 V to 4600 V of equivalent-divider voltage;

- evaluate the stability of each of the foils.

To perform this last evaluation, a voltage of 580 V with a current threshold $I_0 = 2\,\mu$A is applied to one foil at a time. This limit defines the current at which the voltage is turned off to protect the detector. An event where the current exceeds the threshold of a channel, with a consequent turn off of its feeding voltage, is called a *trip*. This last step in the QC6 is passed if the trip rate is lower than 1 trip/hour. To obtain this result the test could last many hours, in order to evacuate all the contaminants that could deposit on the foils.

The contaminants indeed can create a conductive channel inside a GEM hole, which remains until these pollutants are not removed. In the case of dust, it can be vaporised (burned) applying a voltage difference for a long time or applying a potential difference with the MEGGER. In the worst case, the deposition, for example, a drop of copper melted during a discharge and deposited inside of the hole, can create a permanent short between the top and the bottom copper layer of the foil. In this case, the voltage applied to

the sector of the foil containing the short drops to 0, and so its gain. At the same time the channel of the power supply which feeds the foil starts to drain a higher current and the voltage applied to the other sectors decreases, since a fraction of the power supply voltage will fall on the filter resistors.

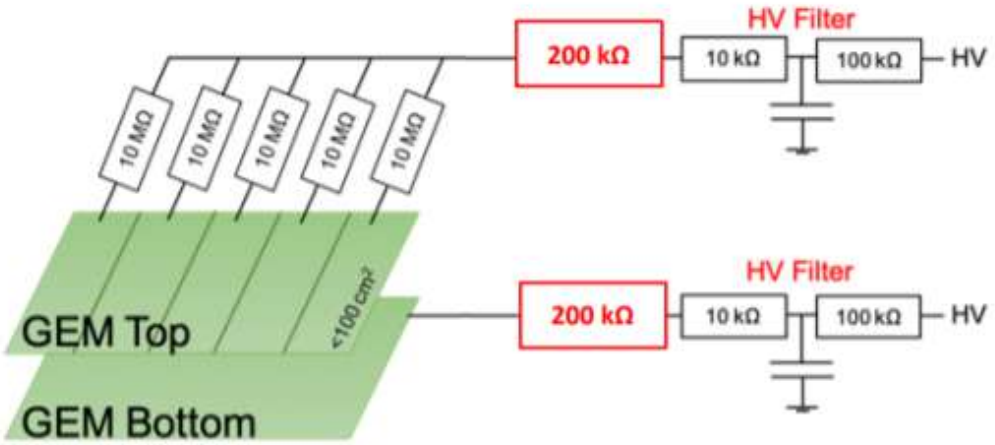

Figure 3.7: Scheme of the HV circuit used to power each GEM foil in a GE1/1 detector [80].

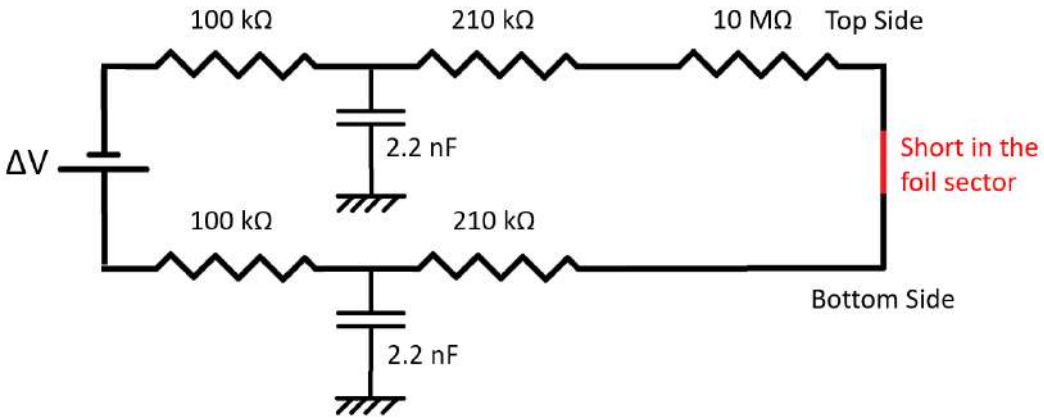

Figure 3.8: Equivalent circuit of a GEM foil with an HV sector with a short in a GE1/1 detector.

To better understand this, in Fig. 3.7 the scheme of the HV circuit powering a single GEM foil is represented, while Fig. 3.8 shows the equivalent circuit for a foil with a short. In case of no short the current drained by the channel of the power supply is ideally 0, practically $< 2\,\mu$A due to the leakage current across the foil. If a short is created in an HV sector, the current drained by the power supply, for example if the power supply provides a potential difference

$\Delta V = 400\,\mathrm{V}$, becomes

$$I_{mon} = \frac{\Delta V}{620\,\mathrm{k\Omega} + 10\,\mathrm{M\Omega}} = \frac{400\,\mathrm{V}}{10.62\,\mathrm{M\Omega}} = 37.7\,\mu\mathrm{A}. \tag{3.5}$$

In general for a number of sectors with a short in the same foil N_{short}, the current drained by the power supply will be

$$I_{mon} = \frac{\Delta V}{620\,\mathrm{k\Omega} + 10\,\mathrm{M\Omega}/N_{short}}. \tag{3.6}$$

The short will affect also the other HV sectors of the foil, showing a drop in the applied voltage. With the circuit closed on the short in an HV sector, a current I_{mon} starts to flow in the filter resistors and this translated in a potential difference falling on the top and bottom-side filters equal to

$$\Delta V_{filter} = 620\,\mathrm{k\Omega} \cdot \mathrm{I_{mon}}. \tag{3.7}$$

Still referring to the $\Delta V = 400\,\mathrm{V}$, the voltage applied on the foil, in case of one sector with a short, would be 24 V (6%) lower, translating in a drop in the gain provided by the whole foil. This can be restored by increasing the voltage provided by the power supply, with a consequent increase also in the monitored current I_{mon}.

This solution cannot be implemented anyway if the HV supply cable is feeding two chambers and only one of the two is problematic, since an increase in the provided voltage would translate in an increase of the voltage also for the non problematic one. Before applying this solution, the HV cable feeding the layer with the short should be decoupled by the healthy one and powered with a different HV board.

3.1.8 QC7: electronics test

After performing the QC6 test, the chambers are equipped with the electronic components: the GEB, 24 VFATs, 9 FEASTs and the OptoHybrid board. The task of verifying all their correct operation is assigned to the QC7 quality control, which is the main quality control I have been involved in during the validation of GE1/1 detectors.

The main objectives of QC7 are:

- determine the optimal configuration of the VFAT in terms of the global charge threshold level;
- determine if there is any issue with the electronics (dead channels, disconnections).

3.1.8.1 Two chamber equipment phases in QC7

The QC7 test is performed 2 times before declaring validated the chamber:

- without the cooling plate: in this phase, the chamber is equipped only with the electronics and the cooling of the electronics components is ensured applying heat sinks on each of them, coupled with the component thanks to a thermal pad with a drop of non-conductive thermal paste and by a fan placed above the chamber to evacuate the heat as fast as possible (Fig. 3.9);
- with the cooling plate and the chimney of the chamber, which has a foil of Kapton applied on its inner side to ensure the electrical insulation between the chimney and the cooling plate.

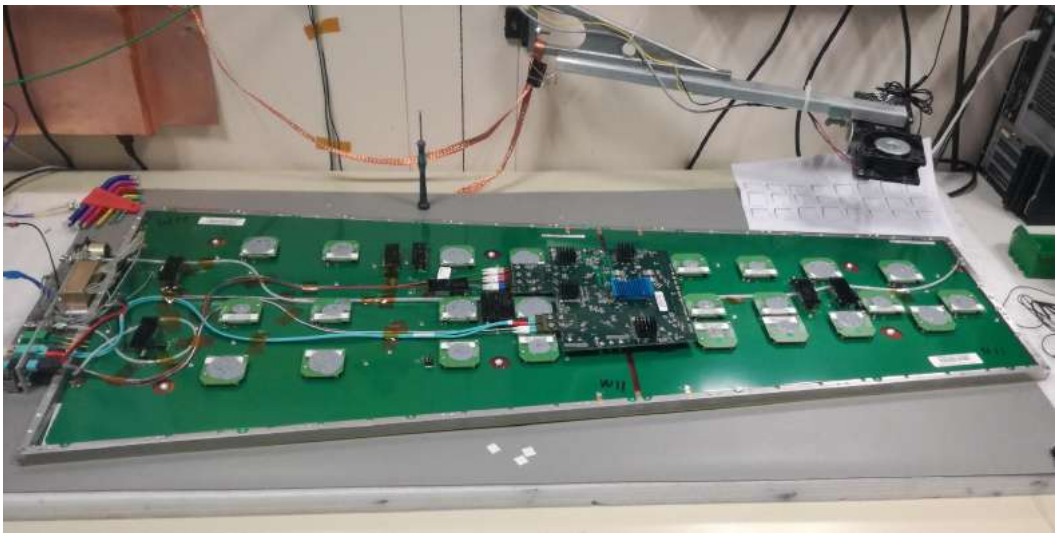

Figure 3.9: GE1/1 chamber on the QC7 stand, equipped only with the electronics. The evacuation of the heat from FEASTs and the OptoHybrid is granted by heat sinks and a fan placed above the chamber [81].

The adopted procedure is the same in both cases. The test is simply repeated to ensure that the electronics is working properly in both the chamber equipment configurations, verifying for example if the application of the cooling plate has altered the noise level of the VFATs or if any of them has been partially unplugged. In such a case the chimney and the cooling plate have to be removed and QC7 has to be repeated from scratch.

3.1.8.2 Procedure in QC7

As it will be illustrated in the following paragraphs, the procedure followed in QC7 is:

- connectivity test;

- first s-curve scan;
- s-bit scan;
- second s-curve scan;
- threshold scan.

This procedure is repeated in both of the chamber equipment configurations.

Preparation for the test. In this phase, the chamber is positioned on the stand where:

- the back-end fibers (trigger and data path) are connected on the chamber patch panel;
- the LV cable is connected and 8 V are provided with a portable power supply. If the chamber is properly working, the current drained by the power supply at the power up is ~ 1.75 A;
- if the cooling plate has not yet been installed, heat sinks are positioned on FEASTs, on Giga-Bit Transceivers (GBTs) and on the FPGA, and the fan over the chamber is activated. Otherwise, the flux of cooling water inside of the cooling pipe is activated.

Connectivity test. The procedure starts with the verification of the communication between the front-end electronics (VFAT chips and OpthoHybrid board), followed by the calibration of the VFAT Digital to Analogue Converters (ADCs), to determine the correspondence between a DAC threshold value and an applied bias voltage.

As previously illustrated a VFAT chip is basically a comparator returning a logic 1, if the input signal is higher than a certain threshold, and a logic 0 otherwise. This threshold, common to all the 128 channels of the VFAT, is written in a register called *CFG_THR_ARM* and is set by a DAC, with a resolution given by an 8-bit number (0-255 in decimal). Setting this threshold to a fixed value will determine in this way the amplitude required to the input signal to pass the selection performed by the VFAT and thus its noise rate.

Having this in mind, the QC7 procedure continues, performing two main tasks: to measure the noise rate of each VFAT installed on the chamber and to analyse the response efficiency of the VFAT to signals of different intensities.

First s-curve scan. Observing the response of the VFAT channels to fixed charge input signals is one of the most fundamental tasks that can be carried out on VFAT channels to understand their operation. This procedure is called s-curve scan and consists of sending 100 pulses for each charge value that can be delivered by the internal VFAT pulse generator. Ideally, if a threshold value

CFG_THR_ARM has been set on the VFAT all the channels should start to give a logical one over a certain charge value, resulting in a step response. In practice two uncertainty components are present in the system:

- the channel shows differences in manufacturing, due to variation in characteristics of the components connected to them (for example in the resistors and transistors);
- the contribution of the intrinsic noise of the circuital system, consisting in the noise collected by the strips, the noise sensed by the connections between the strips and the readout electronics and the noise given by the electronics itself (the VFAT chip).

This additional level of complexity smears the ideal step response in a sigmoid response: this shape is given by the convolution of the step with a Gaussian noise. Here the threshold charge value of the step is defined by searching the value of charge corresponding to a 50% efficiency response, while the standard deviation of the gaussian will give an indication of the importance of the contribution of the noise in the response. The standard deviation is called *Equivalent Noise Charge* (ENC), as illustrated in Fig. 3.10. Since the noise affects all the channels and cannot be eliminated, observing a too low ENC in some of the channels is the symptom that the channel is not correctly responding, maybe due to a disconnection from the readout strips, as illustrated in Fig. 3.11. In this figure also dead channels appear, represented as vertical white lines, meaning 0 efficiency for every charge of the input signal.

The first s-curve scan performed in QC7 is executed applying a value of $CFG\_THR\_ARM = 100$, to have a first indication on the response of the VFAT channels in terms of noise and to identify if the chamber has any dead or non-communicating channels in the VFATs. The test is passed if less than three dead/non-responding channels are identified in the same detector η-partition, otherwise, the test is not passed and it should be repeated after trying to fix the spotted issue. Usually, a first attempt consists in re-plugging the problematic VFAT after cleaning the connector with ethanol, to ensure that the bad connection is not due to some kind of deposition on the connector. If the s-curve still shows the same issue, the solution is to replace the VFAT with a healthy one. A typical s-curve taken at $CFG\_THR\_ARM = 100$ is shown in Fig. 3.12a, representing a VFAT behaviour of a particular chamber. This s-curve was in particular taken with the cooling and chimney already installed, in the last step of QC7 validation.

S-bit rate scan. This phase has the objective of fixing the global threshold of the VFAT to limit the noise signals accepted by the front-end electronics. Taking into account that during their operation in CMS in the HL-LHC phase, the GE1/1 detectors will experience a maximum total hit rate $\sim 1.5\,\mathrm{kHz/cm^2}$, a limit noise value of 100 Hz has been established for each of the VFAT.

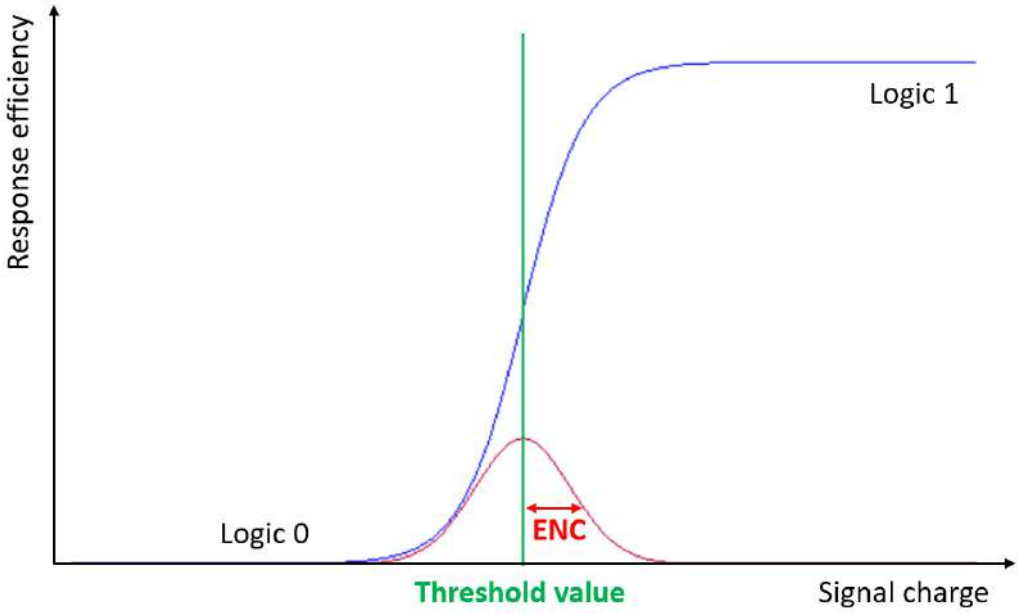

Figure 3.10: Scheme of the response efficiency of a VFAT channel to an input charge signal in presence of noise. In blue is represented the s-curve response, given by the step response smeared by the white noise and in green the charge threshold value of the response (50% efficiency). In red is represented the noise with its standard deviation, the ENC.

The procedure to determine for a given VFAT the CFG_THR_ARM value corresponding to the 100 Hz noise threshold, consists in counting for 1 second the number of trigger hits produced in the VFAT readout sector at a fixed CFG_THR_ARM value. The trigger hits are given by the logical OR among the 64 s-bits (VFAT half granularity datapath). This counting operation is repeated for each of the 256 values of CFG_THR_ARM register. From this information, the noise trigger hit rate vs VFAT threshold curve is built, illustrated in Fig. 3.13a.

From this curve the VFAT threshold is extracted, expressed in DAC units, corresponding to a noise hit rate equal to 100 Hz. This curve shows an initial plateau given by the saturation of the electronics for low values of DAC threshold, and then a gradual fall for increasing DAC threshold values. If the curve does not follow this behaviour is usually a symptom of an issue in the VFAT connection or of the presence of faulty channels. An example of this situation is represented in Fig. 3.13b, where the s-bit rate curve for the VFAT 5 of chamber GE11-X-S-FIT-0004 in July 2020 is reported, when already installed in the CMS detector. Due to this issue, GE11-X-S-FIT-0004 was extracted from CMS and returned to QC7 to fix the issue. The behaviour shown by VFAT 5 is called *broken s-bit line* and results usually from a faulty connection of the VFAT to the Panasonic connector on the readout board

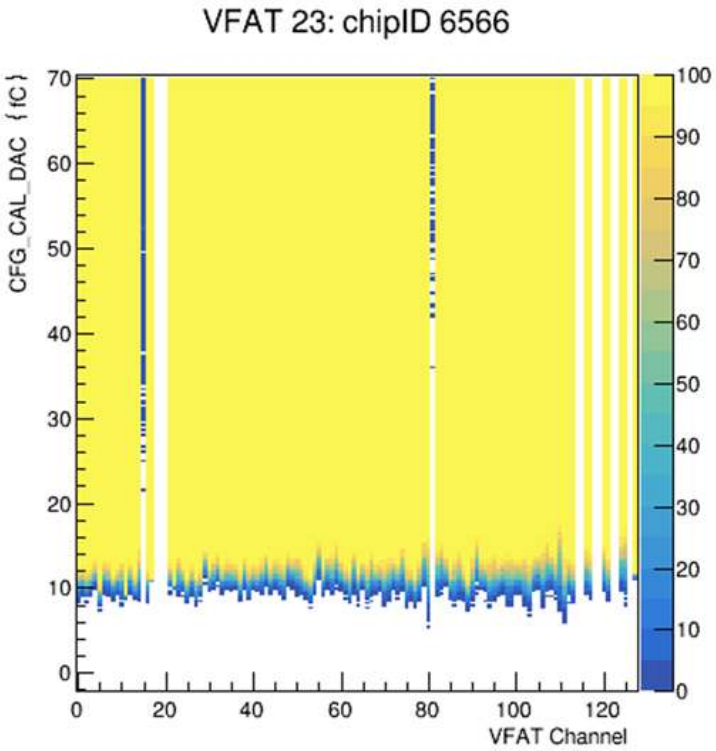

Figure 3.11: S-curve of chamber GE+1/1/09 of the positive endcap in the CMS experiment. This chamber shows dead channels in VFAT 23 (vertical white lines) and channels with a low ENC (too narrow colour change with respect to the other channels), for example near channel 17 or 128.

or of the OptoHybrid board to the SAMTEC connector on the GEB, and can usually be fixed by re-plugging the electronic components. Before the re-plugging of the VFAT, the Panasonic connector is cleaned with ethanol, to ensure that the problem is not caused by any kind of deposition on the connector. Instead, if the issue lays on the SAMTEC connector, for example a damage causing an unplugging of part of the OptoHybrid board, the main solution is the replacement of the GEB.

Second s-curve scan. After the threshold DAC value corresponding to 100 Hz noise has been determined for each VFAT installed on the chamber, these thresholds are used to configure the VFATs and then a new s-curve scan is performed.

This second scan produces new s-curve plots for each of the 24 VFATs and also in this case verification of the correct response from all the channels is performed, as well as the measure of their noise level. The requirements to pass this validation step are:

- the average value of the ENC of all the channels of a single VFAT has to be lower than 0.7 fC;

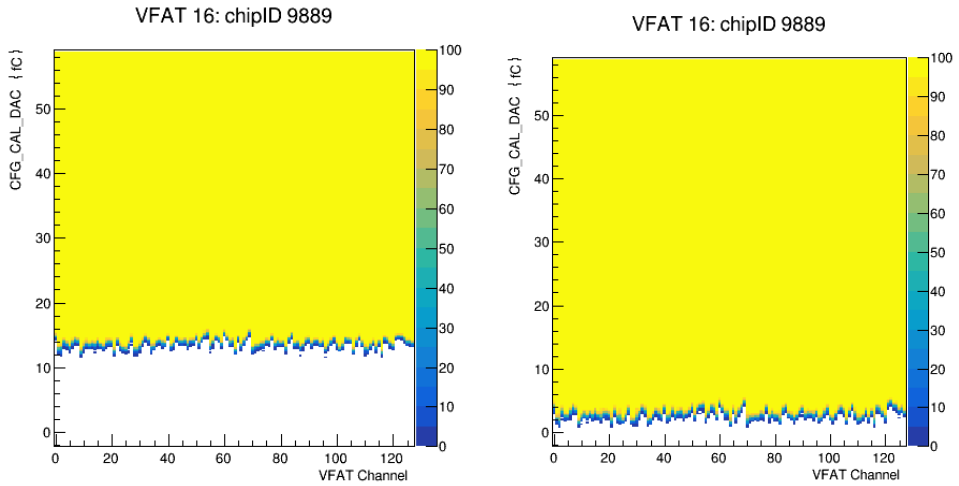

(a) (b)

Figure 3.12: S-curves of VFAT 16 of chamber GE11-X-L-CERN-0007, equipped with the cooling plate and the chimney. On the left the s-curve taken at $CFG\_THR\_ARM = 100$, while on the right that taken after applying the 100 Hz noise threshold value [82].

- the average ENC of single channels has to be lower than 1.5 fC, otherwise the channel is masked;
- no more than three masked channels are accepted in the same η-partition.

If these conditions are not satisfied, the QC7 test has to be repeated replacing the VFATs which don't fulfil the test requirements. An example of summary plot for ENC values is shown in Fig. 3.14b. The choice of these particular charge values to accept or refuse the test is dictated by the amplitude of the intrinsic noise and by the room offered by the bias voltage to adjust the global and per channel VFAT thresholds, and illustrated more in detail in [65].

Fig. 3.14a shows a summary of the charge threshold values obtained from the VFAT channels after applying the 100 Hz DAC threshold. It can be observed in particular as the threshold increases going from the narrow (VFAT 0, 8 and 16) to the wide side (VFAT 7, 15 and 23) of the chamber (VFAT numbering scheme in Fig. 2.30). This is due to the area covered by the strips, which have always the same radial angular spacing, reflecting thus in a greater area for the lower η readout sectors. The strip area indeed increases the strip intrinsic capacitance and this reflects in a higher noise collection.

Threshold scan. The final step in the QC7 validation consists in performing a scan of the VFAT threshold DAC value per each readout channel. This scan is designed to verify if all the VFAT channels are properly connected to the readout board. In case of a channel faulty connection, the VFAT chan-

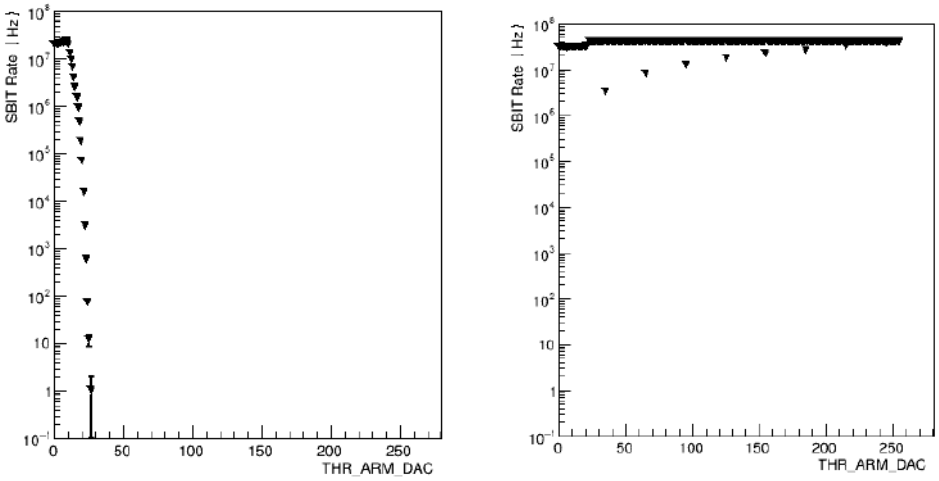

(a) (b)

Figure 3.13: S-bit rate curves: (a) curve taken for VFAT 16 of chamber GE11-X-L-CERN-0007, already equipped with the cooling plate and the chimney [82]; (b) broken s-bit curve for VFAT 5 of chamber GE11-X-S-FIT-0004. This chamber was already installed in the CMS experiment and was re-extracted and sent back to QC7 to fix this issue. The broken s-bit line in this chamber has been fixed by re-plugging the OptoHybrid board and the VFAT [83].

nel does not collect nor the noise signals coming, resulting in a low DAC threshold setting. To fix this issue it is enough to re-plug the VFAT, which requires removing the cooling plate and the chimney if the chamber is in its final equipment configuration. A VFAT showing this behaviour is illustrated in Fig. 3.15 in chamber GE11-X-L-CERN-0043.

Current monitoring during QC7. During QC7 all the performed operations require a different power consumption, and this in particular increases if there is an issue with some VFATs. In case of normal operation three main current levels can be highlighted, as illustrated in Fig. 3.16:

- VFATs standby mode at the chamber power up (1.75 A),
- VFATs toggled to run mode (2.85 A),
- scan mode (3.50 A).

After passing all these steps, and repeating the QC7 quality control both with and without the cooling plate and the chimney, the chamber can be released from the QC7 stand and moves to the final quality control step.

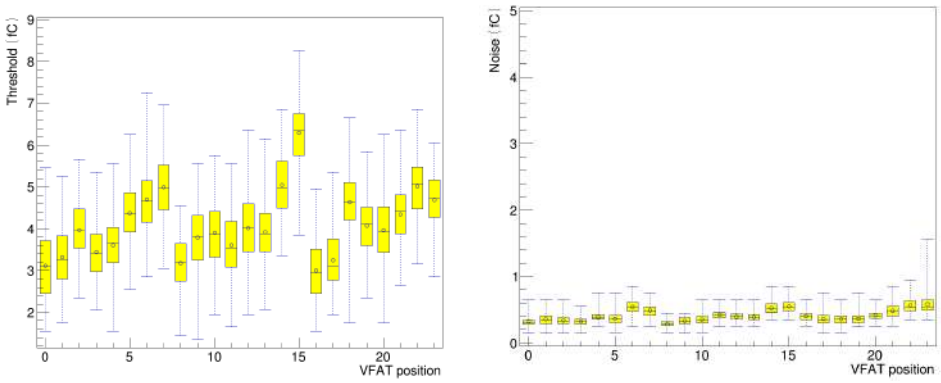

(a) (b)

Figure 3.14: Summary plots for VFATs in chamber GE11-X-L-CERN-0007: (a) the box plot of the charge threshold values of all the channels of the VFAT; (b) the ENC values [82]. The summary is made using a standard box plot, including in the yellow box a fraction of values from the first quartile to the third quartile (25%-75%); the median is represented by the central box horizontal line and the distribution mean with a small circle [84].

3.1.9 Chamber coupling

After passing QC7, two chambers with similar gain are parallelly coupled using aluminium holders. This choice is due to the design of the GEM HV system in CMS, feeding both the layers of a Super-Chamber with the same HV board channels. Since the voltage applied to the electrodes of both layers is the same, the chambers are required to have a similar gain, to provide similar behaviour.

3.1.10 QC8: cosmic test

The last step in chamber validation is performed in a cosmic ray stand, set up at the GEM lab at 904 building at CERN. This installation will be described in the next paragraphs and has the aim of

- check if all the chambers and their supplying services and components are operating correctly;
- study the detection efficiency of the chamber;
- study the tracking throughput offered by the chambers;
- study the mid-term stability of the chambers, regarding the HV system (GEM foils in particular) and the electronic components, supplied by the LV system ($O(2\,\text{weeks})$).

To pass the QC8 quality control, a Super-Chamber is required to show an average detection efficiency higher than 95% in both of its layers.

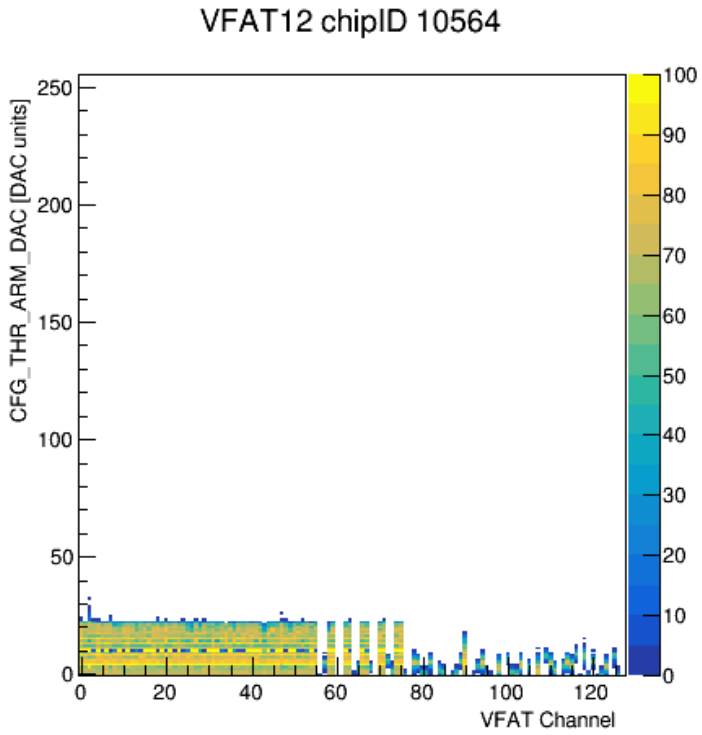

Figure 3.15: VFAT DAC threshold scan for VFAT 12 of chamber GE11-X-L-CERN-0043. The low threshold for channels in the right part of the plot is given by the partial unplugging of the VFAT: the absence of connection among the chip and the strips reduces the capacitance of the readout channel and in this way its collection of noise signals, resulting in a very low and unrealistic DAC threshold for the unplugged channels [85].

3.1.10.1 The experimental setup of the QC8 cosmic stand

The cosmic stand is a $200 \times 200 \times 200\,\mathrm{cm}^3$ installation, built with aluminium profiles. An illustration of its structure is provided in Fig. 3.17, while a picture of the stand equipped with some Super-Chambers is provided in Fig. 3.18.

The stand is composed of 7 shelves, with the top and bottom ones occupied by large area plastic scintillators used to trigger on the muons crossing the stand: the scintillators organised on the same shelf are put in a logic OR, while a logic AND is done between the scintillators placed on the roof and at the base of the stand. Due to the detection efficiencies and area of the scintillators, the global trigger rate provided by this logic AND is $96.42 \pm 0.05\,\mathrm{Hz}$; this last value is estimated from a typical run, lasting $\sim$ 9h. In the other five shelves the Super-Chambers are hosted, 3 per shelf in parallel columns, numbered as illustrated in Fig. 3.17: the naming convention adopted for Super-Chambers includes, the number of the shelf row and the number of the column. To identify a specific layer of the Super-Chamber, the suffix *Top* or *Bot* is added, identifying respectively the layer of the Super-Chamber placed in the higher

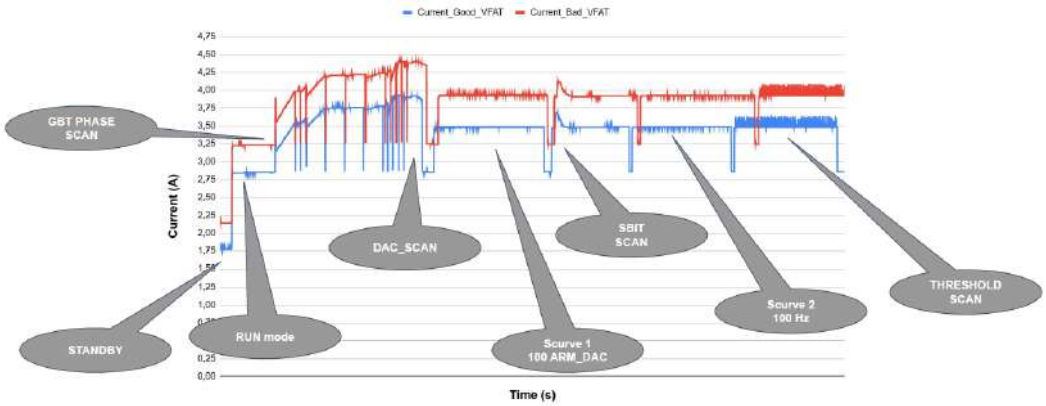

Figure 3.16: Current plot showing the current drained by the power supply at 8 V during the operation on the QC7 stand. [81].

or lower position in the stand.

The supply lines and controls of the services have been installed on the stand sides.

The cooling system. The cooling system supplies the stand with a cooling line for each Super-Chamber (15), while two other lines are dedicated to the cooling of the chambers installed on the QC7 stands. The pipes supply cool water at a temperature of 16 °C and with a pressure lower than the environmental one, differently from the CMS site, where pressurized water at 9 bar is supplied. This lower pressurization is used to avoid spreads of water in case of leaks in the cooling pipes connections: in such a case the water is simply sucked by the cooling system.

The gas system. The gas system in the QC8 stand supplies each Super-Chamber with a dedicated gas line, connecting the Super-Chamber layers with a plastic pipe. This differs from the configuration in P5 where six adjacent single chambers, each belonging to Layer 1 or Layer 2, are supplied in sequence by the same supply line. The gas flux is controlled by 15 flow controllers installed on a panel on the right side of the stand and their return flux is monitored on the same panel by as many rotameters. In addition, on each supply line a filter is installed, to prevent particles with a size larger than 5 μm to enter in the chambers. During the chambers operations, the flux is usually set to 3 L/h.

The main line supplies all the 15 Super-Chambers with the standard GE1/1 gas mixture, Ar/CO_2 (70/30%). A line apart can supply a single Super-Chamber pure CO_2, to dry out the chamber, or pure air, which contains oxygen O_2 and has proved to be effective to eliminate shorts in chambers. When a residual on a foil is burned, thanks to the oxygen, non-conductive metal oxides are created, interrupting the conduction between top and bottom

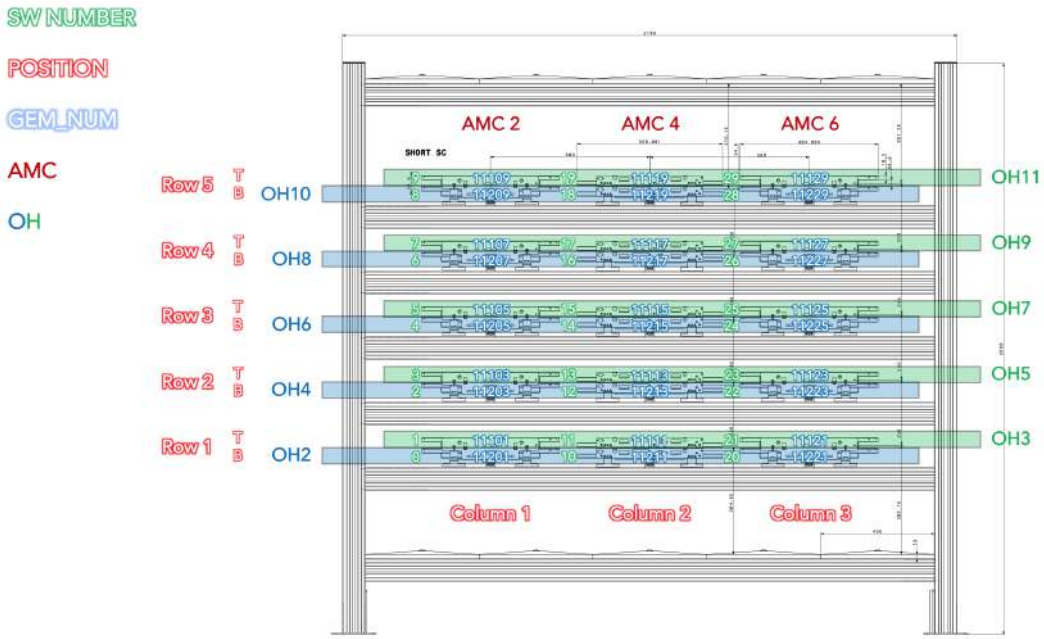

Figure 3.17: Structure of the QC8 stand with the naming conventions adopted to identify the chambers and the labels of the electronic modules connected to the corresponding positions [65].

sides of the foil and thus removing the short circuit; this obviously depends on the nature of the residual which created the short.

The High Voltage (HV) system. In the racks of the QC8 stand two CAEN A1526N boards powering the scintillators, and 15 CAEN A1515TG boards for the Super-Chambers are installed. In the QC8 stand, each board channel feeds only one electrode of one chamber, differently from the configuration adopted in the CMS detector site, where one channel feeds two electrodes belonging to the two layers of the same Super-Chamber. This offers much higher flexibility and allows also spotting directly from the DCS panel which is the problematic layer in a Super-Chamber (for example a layer with a short in a GEM foil).

The Low Voltage (LV) system. The LV system of the QC8 stand is structured in the same way as that used at P5, using in total 5 CAEN A3016 boards. Due to the availability in the laboratory, the boards belong to different models: 2 are *HP* and 3 belong to the previous standard model (the HP ones are those used at the CMS site). The only difference between these boards is that a non-HP board is not able to provide a voltage higher than 8 V : the chambers are usually operated at 8 V, so the board has to provide this voltage plus an additional one, to compensate for the voltage drop along the cable. It has been so established, to operate the chambers fed by the non-HP boards

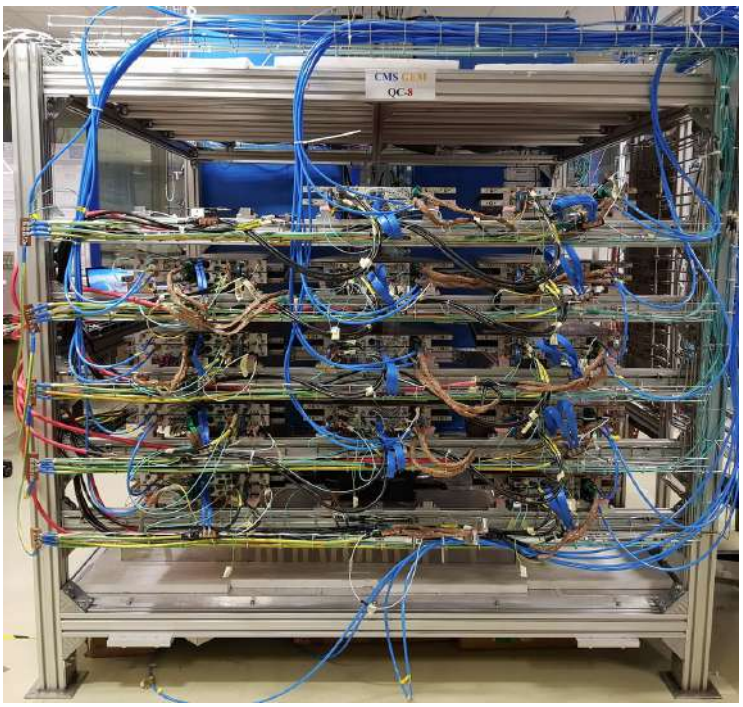

Figure 3.18: Picture of the QC8 cosmic stand at the GEM lab in the 904 building at CERN [86].

at 7 V : this results only in a higher current drained by the FEASTs (+12%) and not in a chamber performance variation.

Each LV board supplied power to the three Super-Chambers hosted on a single shelf, with a correspondence 1-1 between supply channel and LV cable (1 LV channel - 1 LV cable - 1 Super-Chamber layer).

The Detector Control System. The DCS for the QC8 stand has been designed with a style similar to that adopted for the CMS experiment site, only with the additional possibility to control the HV lines supplying the photo-multipliers for the scintillators placed on the roof and on the floor of the stand. The QC8 DCS monitors and controls the HV and LV systems, while only monitors the environmental (temperature, pressure, dew point and humidity) and gas mixing parameters and the electronics temperature, and stores them in a dedicated database.

In particular, for the HV and LV systems, the following parameters are stored:

- the monitored current *Imon* drained by each board channel;
- the monitored voltage *Vmon* provided by each board channel;
- the channel status.

The main parameters that the user can set in the HV panel are:

- the operation voltage V_0 of each HV channel of a single chamber;
- the current limit I_0 that can flow in a channel: if this limit is overcome the board switches off the channel (*trip event*) and the DCS raises an alarm;
- the ramp-up: the voltage derivative in time, which determines how fast the voltage is increased during a transition from a lower to a higher voltage value;
- the ramp-down: the voltage derivative in time, which determines how fast the voltage is decreased during a transition from a higher to a lower voltage value;
- the trip time: a maximum time interval during which a channel can overcome the I_0 limit. If the I_0 limit is overcome for a longer time, the channel trips and the DCS raises an alarm. The trip time is usually set to 1 s, because if set to 0 s also a minimal instability would lead to a power off of the chamber and to a dead time of operation, needed to recover the chamber;
- mode of powering: GEM mode or FREE mode.
  - In GEM mode, when a chamber is powered all the channels are activated and their ramp occurs in sequence (a channel ramps only after the previous channel has completed its ramp and reached the desired voltage). In case a channel trips, also all the other channels are turned off.
  - In FREE mode, the chambers can be ramped independently from each other. In this case when a channel trips, it is the only to be turned off.

In addition to these options, an automatic recovery macro has been introduced in the DCS, which takes action ~ 30 s after an HV trip to recover the chamber. The number of consecutive recoveries can be set from the panel and in case this number is reached and a new trip occurs, the chamber is no longer recovered and left in the OFF state. The introduction of the automatic recovery is intended to ensure the longest data taking as possible during a run, to avoid long periods of inactivity in case the operator is away from the panel (for example during the night).

Furthermore, a safety system, that turns off completely the HV in case the gas mixture is missing, has been implemented in the DCS.

On the other hand, the main parameters that the user can set in the LV panel are:

- the operation voltage V_0 of the LV channel feeding a single Super-Chamber layer;

Bit number	Meaning
0	0 = Off, 1 = On
1	Ramp Up (RUP)
2	Ramp Down (RDW)
3	Over Current (OVC)
4	Over Voltage (OVV)
5	Under Voltage (UVV)
6	External Trip
7	Maximum Voltage
8	External Disable
9	Internal Trip
10	Calibration Error
11	Unplugged

Table 3.2: Meaning of the status bits in the HV 12-bit status code for a CAEN A1515TG board.

- the current limit I_0 that can flow in a channel;
- the trip time.

To monitor the operating status of the channels of each board, both in the HV and in the LV case, a set of status codes has been defined by the producer (CAEN). Every time in the board a change of status occurs (for example the channel is ramping up) a corresponding status code is set and saved in a dedicated database, together with voltage and current data. In the case of HV status, a 12-bit code is used, while a 16-bit one for LV. Their meaning is illustrated in tables Tab. 3.2 and Tab. 3.3. The meaning of the status code is also shown on the DCS panel, which presents the last recorded status.

The DAQ system The back-end electronics used in the QC8 stand is the same as that used in the CMS experiment. It is organised in a μTCA shelf and consists of:

- one MicroTCA Carrier Hub (MCH);
- one AMC13, which distributes to the cards the trigger signal given by the scintillators. Every time a trigger signal comes, the data are collected from the front-end electronics, packed by the AMC13 and sent to a storage disk;
- 3 CTP7s, one per each column of Super-Chambers (Fig. 3.17), labelled as AMC2, AMC4 and AMC6.

The description of these components was illustrated in section 2.2.2.7.

Bit number	Meaning
0	0 = Off, 1 = On
1	Not assigned
2	Not assigned
3	Over Current (OVC)
4	Over Voltage (OVV)
5	Under Voltage (UVV)
6	Not assigned
7	Over HvMax
8	Not assigned
9	Internal Trip
10	Calibration Error
11	Unplugged
12	Not assigned
13	Over Voltage Protection
14	Power Fail
15	Temperature Error

Table 3.3: Meaning of the status bits in the LV 16-bit status code for a CAEN A3015/A3015HP board.

3.1.10.2 Procedure in QC8

The procedure in QC8 can be divided mainly into three phases:

- preparation for the run;
- data taking;
- data analysis.

Preparation for the run The first operation is the installation of the chamber inside the stand, connecting all the services (gas, cooling, HV, LV), the electronics fibres and the grounding.

After this phase, the chamber is configured, tuning the single channel VFAT thresholds by a procedure called trimming illustrated in detail in [65]. Thus a set of s-curves is produced, to determine the final optimal charge thresholds for each VFAT.

Data taking. In this phase, the cosmic muon data are collected. This phase consists of 5 data taking runs, performed setting the Super-Chamber at 5 different equivalent divider current HV configurations, from 700 μA to 660 μA, with 10 μA steps between a run and the previous one. Each run lasts for $\sim$ 12 hours, to accumulate high enough statistics.

The variation of the equivalent divider current among the five runs is meant to show how a variation in the applied HV (and so of the effective gas gain), impacts on the chamber detection efficiency.

The detection efficiency globally depends on many parameters, like the number of primary electrons produced during the ionisation, the effective gas gain, the number of strips involved in the signal collection, the signal time width, the signal amplification and VFAT operation, the channel readout threshold.

Data analysis. The analysis phase is structured in 4 main phases:

- *identification of dead and hot strips*;
- *event certification*: in this phase, only the events collected during a stable HV operation are accepted for the further steps. Indeed, if an HV trip occurred during the operation, the events recorded since the channel turn off till the time of recovery to the operating voltage condition, must be rejected, because these data have been collected in a gain configuration different from the desired one. The occurrence of HV trips occur mostly in the initial phases of HV operation, due to possible dust depositions which have not yet been completely burned by the HV prolonged application;
- *fast efficiency calculation*: this step calculates the efficiency of a layer using only the data produced by the Super-Chamber itself, and not using the information given by other detectors. This allows having a first picture of the efficiency of the detector, spotting eventually major inefficiency areas.
- *track-based efficiency calculation:* in this case, a tracking algorithm is used in the efficiency computation, which involves also the other detectors installed in the stand during the run.

At the end of this procedure, an averaged efficiency of the 24 VFAT readout sectors is computed and this parameter is used to consider a chamber validated or discarded in terms of efficiency.

3.1.10.3 Monitoring of HV and LV

During the chamber operation, it is useful to have a tool that can retrieve the operating parameters from the DCS database to perform an off-line analysis, or just to monitor if a single board is producing anomalous voltage value. In this context, a tool has been developed to monitor the LV and the HV systems used in the QC8 stand.

The monitoring tool needs three main information to retrieve the data in the correct way from the DCS database:

- a mapping which matches the board channels with the single chamber electrodes;
- the period of usage of each mapping, since the operating conditions in the stand evolve in time;
- the list of chambers that the user wants to monitor;
- the start and end of the period that the user wants to monitor, expressed as UTC time.

Once the environment is ready the monitoring tool deploys the following operations:

- read all the files with the channels mapping conditions used during the operations and recognise the correct usage period for each of them;
- read the file with the chambers that the user wants to monitor;
- connect to the DCS Oracle database;
- get with an SQL query the information to match the power channel, with an identification number (*ELEMENT_ID*) used internally in the database to label the sources of stored information. Together with the ELEMENT_ID, its period of validity is taken, in case the mapping changes;
- get with an SQL query all the data corresponding to the desired channel in the monitored period, and store this information in an output file.

An important aspect that must be underlined is that a voltage, current or status value is registered in the database only when there is an appreciable variation in their value (for example a variation of 0.02 V for an HV channel).

The information available in the output file are:

- current data, with a plot showing the time evolution of the monitored current drained by the power supply and a histogram showing the distribution of current values;
- voltage data, with a plot showing the time evolution of the voltage monitored on the power supply and a histogram showing the distribution of voltage values. It must be remembered that, in case of a short in an HV sector, the voltage applied on the foil is different from that observed on the power supply, due to the voltage drop on the filter resistors;
- status data: in this case both the status code in its decimal format, binary format and its meaning in string format are stored. To better visualise this information a time evolution plot and a histogram are used, showing the decimal status code, and in addition also a table

that summarises all this information and allows to follow in detail the evolution of the status (for example during a trip event).

The usage of histograms is useful in case we want to monitor how often values over a certain threshold show up, and spotting in this way any problem with a board.

HV channel labels. The same labelling convention adopted by the DCS has been used:

- *G1Top*, for the first GEM foil: in this way, ΔV_{G1Top} is the voltage difference created between the top and bottom face of the GEM foil. On the other hand, I_{G1Top} is the current drained by the power supply channel which creates the voltage difference on the foil.
- *G1Bot*, for the Transfer 1 gap, between the 1st and 2nd GEM foil;
- *G2Top*, for the second GEM foil;
- *G2Bot*, for the Transfer 2 gap, between the 2nd and 3rd GEM foil;
- *G3Top*, for the third GEM foil;
- *G3Bot*, for the Induction gap, between the 3rd GEM foil and the readout plane;
- *Drift*, for the Drift gap, between the drift plane and the 1st GEM foil.

HV monitoring plots. Some monitoring plots for the current, the voltage and the status of the HV system are shown in Fig. 3.19, Fig. 3.20 and Fig. 3.21.

From these plots it can be observed that during a channel ramp up the current drained by the power supply is positive, while, on the other hand, the power supply shows a negative current during a ramp down. During the ramp up in voltage, the current drained by the power supply can increase and the current threshold I_0 has to be raised (usually to $20\,\mu$A) to complete the ramp; once the ramp has been completed the current is reset to the operating value of $2\,\mu$A.

From Fig. 3.21, it can be noticed as the first voltage ramp down (2021-06-25 02:04 UTC) in the chamber operation was given by a trip of the channel (status ≥ 512). Looking to the current in Fig. 3.22, it can be noticed as the trip starts with a current spike of $16.6\,\mu$A, which overcomes the $I_0 = 2\,\mu$A threshold (coming for example by a trial of burning a dust deposition on the foil). This triggers a raise of the status and thus the channel is turned off and ramped down, to ensure detector safety.

The status plot allows understanding at a glance when a problem arises, but the full information on the status evolution remains a bit hidden. These information can be provided in detail by the table summarising all the status

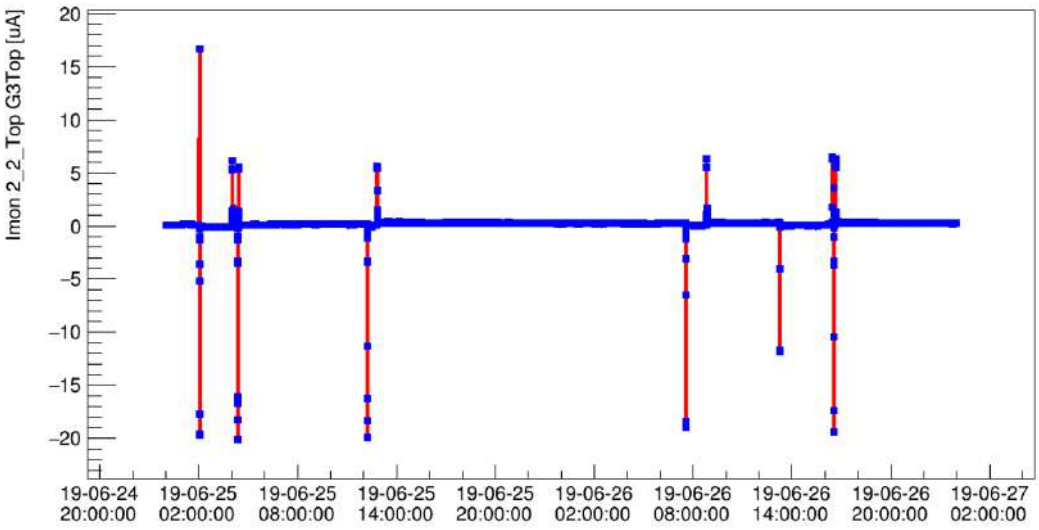

Figure 3.19: Current drained by the HV power supply on channel G3Top of chamber in position 2-2-Top in the QC8 stand from 2019-06-25-00:00:01 UTC to 2019-06-27-00:00:01 UTC.

information, illustrated in Fig. 3.23, providing to the user a more complete view on the process evolution.

LV monitoring plots. For the Low Voltage system, a similar monitoring tool has been developed, with current, voltage and status plots. The only variation consists in the fact that the status code is based on a 16-bit number and that for the voltage application a power gradual ramp is not needed, since only 7 V are applied to the chamber during the operation in the QC8 stand. This results in a higher current consumption with respect to what is observed on the QC7 stand (Fig. 3.16), but it does not affect the detector performances.

An example of the currents observed on the LV board A3016 during the operation in QC8 is represented in Fig. 3.24, where the characteristic three current levels of current operation for a chamber can be observed:

- the standby mode at the chamber power up (~ 1.96 A),
- the run mode (~ 3.10 A),
- the scan mode (~ 3.75 A).

3.2 Operation of chambers at P5

In this section, the main modes of operation of Super-Chamber at P5 will be illustrated. The most common issues encountered will be analysed, together with the tools developed for the monitoring of the chambers. The description

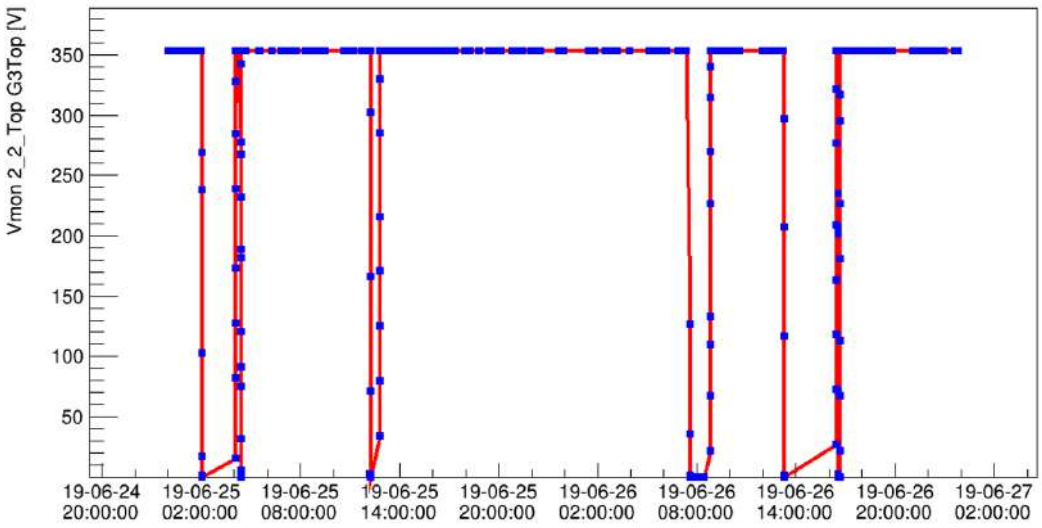

Figure 3.20: Voltage provided by the HV power supply on channel G3Top of chamber in position 2-2-Top in the QC8 stand from 2019-06-25-00:00:01 UTC to 2019-06-27-00:00:01 UTC.

of the operation will start with the most fundamental procedure executed to bring the Super-Chambers in their operation regime in P5: the HV training. In addition, it will be presented the first operation of GE1/1 station chambers in the CMS magnetic field and during LHC collisions: this first period of operation allowed us to gain expertise also in these conditions, spotting the main issues and suggesting strategies for their operation in Run-3.

HV training procedure The aim of this procedure is to clean the detector as much as possible, to reduce at the bare minimum the occurrence of trips in a chamber. The procedure consists in:

- a training of the foils one by one: the voltage of the foils is raised gradually hour by hour and then kept stable at a voltage of 430 V for G1Top and G2Top and 380 V for G3Top, cumulating a total time of operation of $\sim 12\,h$. The occurrence of trips in the first half an hour of operation is common since the dust accumulated on the foil, during its burning could induce a trip. This procedure is then repeated with all the three foils activated at the same time;

- the following step is to turn on half of the electrodes (Drift, G1Top, G1Bot and G2Top): in this configuration, the voltage of the stack is raised hour by hour from voltages given by an equivalent divider 660 μA to 710 μA, and then kept stable for at least 6 hours. The non-activation of the last foil and of the corresponding transfer electrodes prevent the propagation of discharges to the readout plane. If no discharge is observed, the procedure can move to the next step;

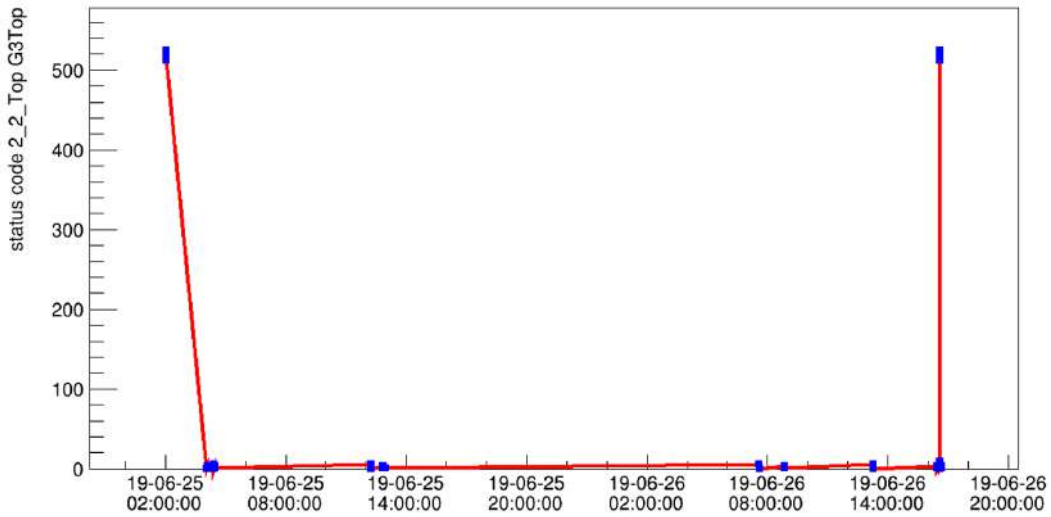

Figure 3.21: Status of HV G3Top channel of the chamber in position 2-2-Top in the QC8 stand from 2019-06-25-00:00:01 UTC to 2019-06-27-00:00:01 UTC.

- activation of all the electrodes apart from the induction gap (G3Bot) and activation of the transfer-2 (G2Bot) electrode at 50% of the voltage it should have at a fixed equivalent divider current. During this step, voltages for equivalent divider current from 660 μA to 710 μA are applied hour by hour, in steps of 10 μA. The 710 μA configuration is monitored for $\sim$ 6 h and if no discharge is observed, the procedure can move to the next step;

- activation of all the electrodes apart from the induction gap (G3Bot) and activation of the transfer-2 (G2Bot) electrode at 70% of the voltage it should have at a fixed equivalent divider current. The procedure is the same as the previous step, apart from that each equivalent divider current step is maintained for 30 min instead of 1 hour;

- activation of all the electrodes apart from the induction gap (G3Bot) and activation of the transfer-2 (G2Bot) electrode at its nominal value. In this case, each equivalent divider current step is maintained for 1 hour and the 710 μA configuration is monitored for $\sim$ 6 h. If no discharge is observed, the procedure can move to the next step;

- check the health of the front-end electronics taking s-curves. This is done to understand if any of the previous steps have induced any damage on the front-end electronics and to know its status before moving to the last step, where the propagation of discharges towards the readout plane is more probable;

- activation of all the electrodes at their nominal equivalent divider current values, from 660 μA to 710 μA in steps of 10 μA, maintained for 1 hour.

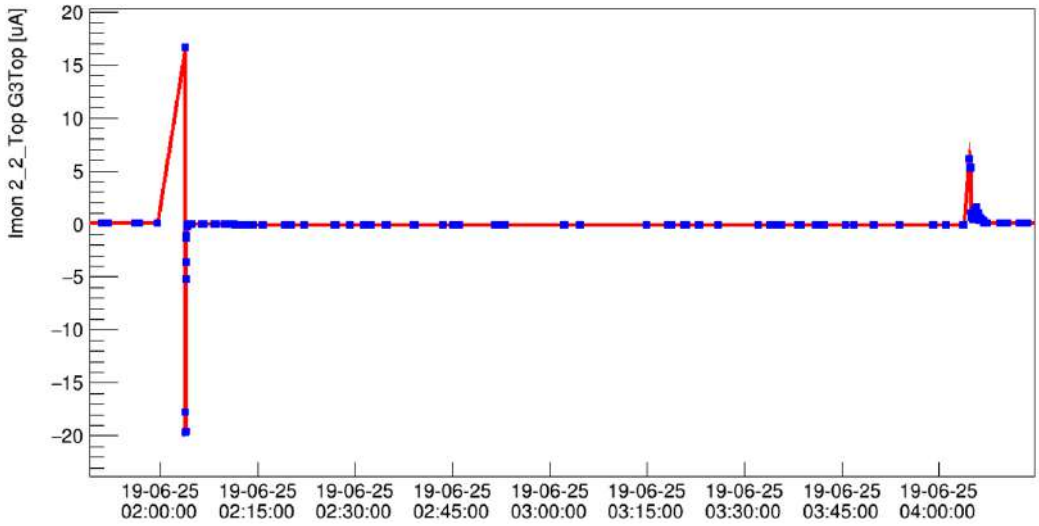

Figure 3.22: Current values for the G3Top channel of the chamber in position 2-2-Top: zoom on the time region when the trip occurred. The positive current which triggered the trip of the channel (02:04 UTC), the negative current of the ramp down and the positive current corresponding to the new channel ramp up (04:04 UTC) can be observed.

The 710 μA is finally monitored for 12 hours.

Once this procedure is completed the detectors can be fully operated for the data taking and a trip rate of around 1 trip per day per Super-Chamber is expected.

3.2.1 HV on-line monitor

Following the activity done for the monitoring of the HV and LV system on the QC8 stand, once the GE1/1 Super-Chambers started to be installed inside of the CMS detector, the need for similar tools also for the P5 site emerged. In this view, two similar tools have been developed: one for the off-line monitoring of the chamber and one for the on-line monitoring.

The on-line monitoring tool has been developed to have an HV monitor independent from the DCS, in case a user wants to see how a Super-Chamber is operating in real-time, without accessing the DCS panel.

The main operations performed by the tool are:

- download data from the DCS database every 10 seconds;
- visualize them in a browser interface.

Get the data. The data are retrieved from the DCS database with a SQL query. The operations performed in this phase are:

Instance	TS	DecimalStat	BinaryStat	MeaningStat
0	2019-06-25 02:03:48.869000	525.0	0b001000001101	ON RDW OVC Int Trip
1	2019-06-25 02:03:50.838000	517.0	0b001000000101	ON RDW Int Trip
2	2019-06-25 02:03:56.816000	513.0	0b001000000001	ON Int Trip
3	2019-06-25 02:04:00.859000	512.0	0b001000000000	OFF Int Trip
4	2019-06-25 04:03:01.190000	0.0	0b000000000000	OFF
5	2019-06-25 04:04:45.443000	3.0	0b000000000011	ON RUP
6	2019-06-25 04:04:59.454000	1.0	0b000000000001	ON
7	2019-06-25 04:25:32.222000	5.0	0b000000000101	ON RDW
8	2019-06-25 04:25:38.157000	1.0	0b000000000001	ON
9	2019-06-25 04:25:42.269000	0.0	0b000000000000	OFF

Figure 3.23: Detailed evolution of the status of channel G3Top for chamber in position 2-2-Top in the QC8 stand during the trip occurred at 2019-06-25 02:04. In the table are reported the Time Stamp (TS) of a status value, the status in decimal and binary format and its complete meaning.

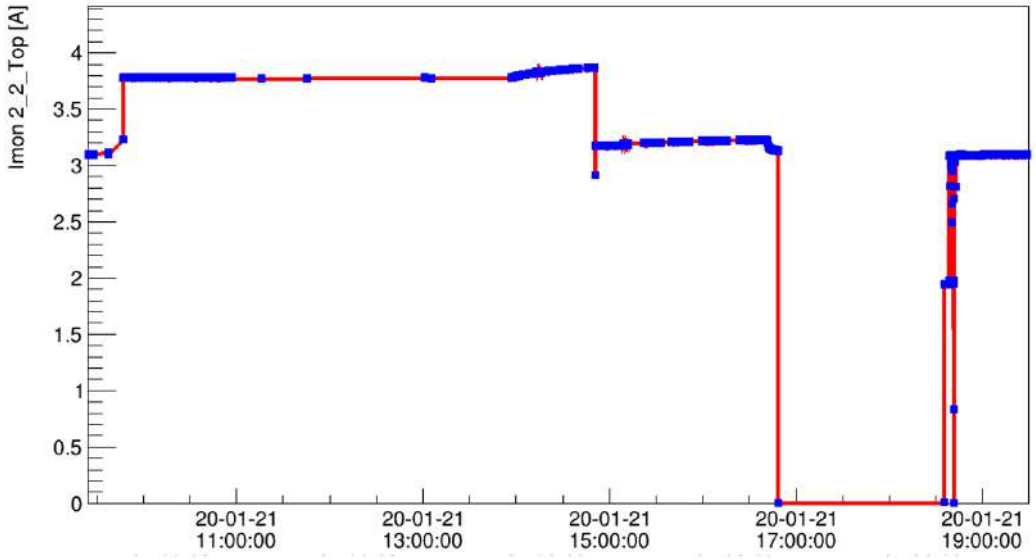

Figure 3.24: LV current drained by the A3016 board during the operation in the QC8 stand by chamber in position 4-2-Bot.

- write in a file the Super-Chambers that the user wants to monitor;
- connect to the DCS database;
- match each Super-Chamber channel with its DataPoint ID (DPID). In the DCS database each channel is labelled with an identification code;
- identify the last current, voltage and status recorded information;
- retrieve every 10 seconds the newly saved data.

Visualize the data. For the data visualization, the Bokeh Python package has been chosen, which offers a simple data visualization in a web browser. The chosen visualization is illustrated in Fig. 3.25 and consists of:

- one tab for each Super-Chamber in the top-left part of the panel;

- in each tab a set of plots for each HV channel is stored, with:
  - in the first column (blue) a plot representing the current monitored on the power supply I_{mon};
  - in the second column (red) a plot representing the voltage monitored on the power supply V_{mon};
  - in the third column (green) a plot representing the status code of the channel. The meaning of the status code for HV channels is explained in Tab. 3.2.

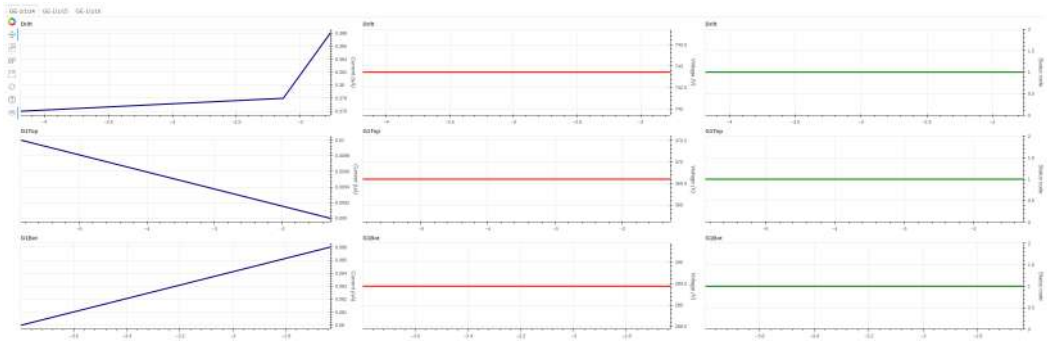

Figure 3.25: Panel of the online HV monitor: in the top-left corner of the browser the desired Super-Chamber can be selected by a tab, while in each tab is created a 7×3 grid, with on each line three plots for each HV channel of the Super-Chamber. In each line, from left to right there are current, voltage and status code plots.

The Bokeh package offers in particular some functionalities very useful for the user. The plots in the browser are indeed interactive and allow in particular:

- to zoom and drag a plot to visualize it better in any time region of interest;
- to save the visualization in a file;
- to visualize the precise information about a single data point, just hovering the cursor on it.

3.2.2 HV and LV off-line monitor

This tool has been structured in a fashion similar to that made for the QC8 stand, but with some additional features:

- the possibility to have a full view of all the electrodes at the same time on the same plot;

- the production of a file containing a history of the trips undergone by each Super-Chamber.

The visualization of all the electrodes on the same plot allows having a more complete view regarding the evolution of phenomena inside of a single chamber, since in the P5 site the Super-Chamber operation can depend on many external factors and on the operation of other sub-systems (for example the activation of the CMS magnet).

Some example plots representing the HV and LV systems are provided in the following sections, in the description of the various phenomena occurring during the Super-Chambers operation. From these plots many information not saved in the database can be derived, mainly regarding the HV system, such as:

- the ramp-up and ramp-down parameters;
- the power mode (FREE or GEM);
- the operation mode (STANDBY or READY FOR PHYSICS) and the equivalent divider current used in these modes.

Still, some useful parameters have to be implemented in this tool since were not yet available in the DCS database at the time of the tool development, such as:

- the current threshold I_0 for each of the electrodes;
- the temperature measured inside of the chamber.

In addition, it must be remembered that in the P5 site one HV cable feeds both layers of a Super-Chamber. From this, the user cannot understand exclusively from the HV data what is happening in the Super-Chamber and he has to combine his information with those given by the operator reports; for example, he cannot understand:

- in which layer of a chamber there is an issue, but only on which electrode;
- if one layer has been disconnected from the power system. To notice this from the data the status have to be raised to the unplugged level (status = 2048), and this happens only if both layers are disconnected. If this does not happen, he only sees the HV data given by the connected layer.

3.2.2.1 Main features of the HV monitoring

Power mode: GEM or FREE. As previously explained, the HV system feeding the Super-Chamber can be set in two modes:

- FREE mode, where all the electrodes can be operated independently and if one of them overcomes the I_0 threshold for a time longer than the trip time, only this channel is turned off;
- GEM mode, all the electrodes are operated in concert and if one of them trips all the electrodes are turned off simultaneously.

In addition, in GEM mode the ramp up of the electrodes occurs in sequence (one electrode starts its ramp only when the previous one has ended its ramp and reached the set voltage value), while in FREE mode more electrodes can be ramped simultaneously, as illustrated in Fig. 3.26. In particular, the sequence used for the ramp up in GEM mode is: 1st foil (G1Top), 2nd foil (G2Top), 3rd foil (G3Top), Drift gap (Drift), 1st transfer gap (G1Bot), 2nd transfer gap (G2Bot) and induction gap (G3Bot).

On the other hand, when a ramp down command is sent, it is applied simultaneously to each of the interested electrodes in FREE mode and to all the electrodes in GEM mode. The ramp down is usually set to 20 V/s.

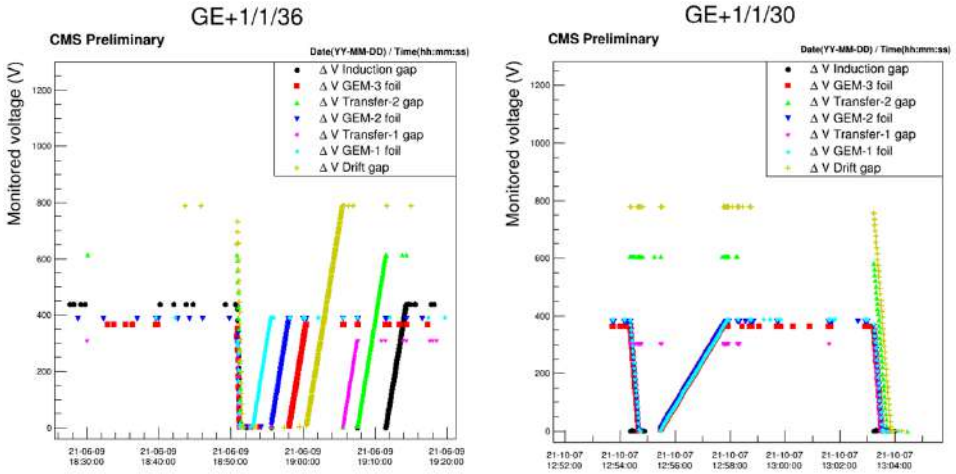

(a) (b)

Figure 3.26: (a) Super-Chamber GE+1/1/36 operated in GEM mode: here all the electrodes are operated in concert and the ramp-up occurs in sequence ($\text{ramp} - \text{up} = 3\,\text{V/s}$). (b) Super-Chamber GE+1/1/30 operated in FREE mode: here the three foils trip, they are turned off and then recovered, while all the other electrodes stay stable.

Automatic recovery. As in the QC8 DCS, also in the P5 GEM DCS an automatic recovery macro has been implemented, to restore the chamber voltage after a trip when the operator is away from the DCS panel. This is done to reduce at the minimum the inactivity period of the detector, for example during the data taking or during an HV training. The automatic recovery

procedure stops when the number of consecutive recoveries is hit before clearing the generated alarms: in this case, the chamber remains off and action on the DCS panel by the operator is required, as shown in Fig. 3.27. In this case, the maximum number of consecutive recoveries was set to 6.

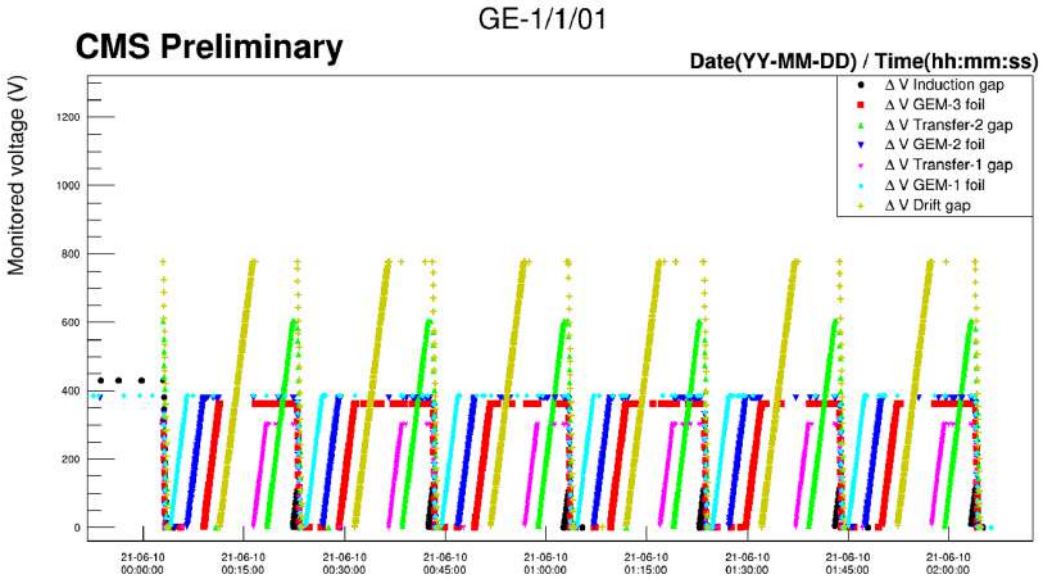

Figure 3.27: Six consecutive recoveries on the HV of chamber GE-1/1/01. In this case, when the chamber started the ramp of the last electrode the chamber tripped, the channels are all turned off and the recovery procedure restarts from scratch. When the limit of six recoveries is reached, the channels are left off.

Super-Chamber operation mode. During their operation in the CMS detector, GE1/1 chambers are not always kept at the equivalent divider current voltage values used for the data taking (700 μA), which is also called *READY FOR PHYSICS mode*, but at the lower level of 580 μA, also known as *STANDBY mode*. This mode is used to keep the detector in a safe status to protect it from any damage since the electric field inside the holes becomes low enough to prevent the formation of discharges. This mode is used for example before the LHC beam injection, to ensure the safety of the detector in case of any problem with the beam. In addition, in this way, it is ensured that the detectors are always ready to be ramped quickly to the READY FOR PHYSICS mode, when a data taking is incoming: the complete ramp-up from the 0 V level would indeed require few minutes, while from the STANDBY level less than one minute. Indeed, the ramp to the READY FOR PHYSICS mode configuration is performed using a ramp up value of 10 V/s. Finally, it is discouraged to keep off the detectors until the moment just before the collision, since an absence of voltage for a long period could cause HV trips

due to the deposition of dust on the foils. Thus the time needed to recover the chambers would induce an additional data taking time loss.

The transition process occurs usually during the LHC handshake, operation that precedes the delivery of collisions in the CMS detector and the detectors stay in this status until the beam injection is finished (precisely when the beam is at the end of the *FLAT TOP* status) [87]. During the LHC handshake, the systems of the CMS experiment are asked to prepare themselves to collisions, reaching as quickly as possible a configuration to detect particles efficiently. Once CMS declares itself ready to receive collisions, the LHC beams are injected in the cavern and collisions begin. The transition between the two GE1/1 HV states is executed for all the Super-Chambers in concert and consists in a procedure that ramps in sequence the seven electrodes.

During the first collisions delivered by the LHC, in week 43 of 2021 (end of November), on 2021-10-27 an issue that interrupted the transition from the READY FOR PHYSICS mode to the STANDBY mode, was observed. The detectors were operating in the GEM power mode. At 19:21 UTC an LHC injection handshake started and the detector protection system reacted, starting to move the detectors to the STANDBY mode. When such an operation is performed, the system is required to answer to the handshake confirming that the transition was completed. In this particular case, the transition started, ramping down the three GEM foils and the Drift electrode to the STANDBY designed value. The transition then stopped (Fig. 3.28), leaving the other electrodes (G1Bot, G2Bot and G3Bot) in the READY FOR PHYSICS mode configuration; this happened to all the detectors since they were operated in concert. This was due to the fact that during the transition one chamber was being recovered after the occurrence of a trip (precisely chamber GE+1/1/09, which tripped at 19:20 UTC), and this prevented the answer of the system to the LHC handshake. After this investigation a new version of the GEM DCS was deployed, fixing this issue.

3.2.2.2 LV monitoring

While the HV monitors at the same time the voltage provided to both layers of a Super-Chamber, the LV has an independent supply line for each of them. An example plot of the LV current drained by the two layers is illustrated in Fig. 3.29, where the characterising operation levels can be observed, using the same 8.0 V configuration used in the QC7 stand.

Study of current levels and front-end channel damage. The identification of current levels can be useful to detect increases in current consumption, which can be a symptom of damages in the front-end electronics. A study on this subject has been performed, to correlate with the occurrence of trips the change in current consumption in one Super-Chamber layer.

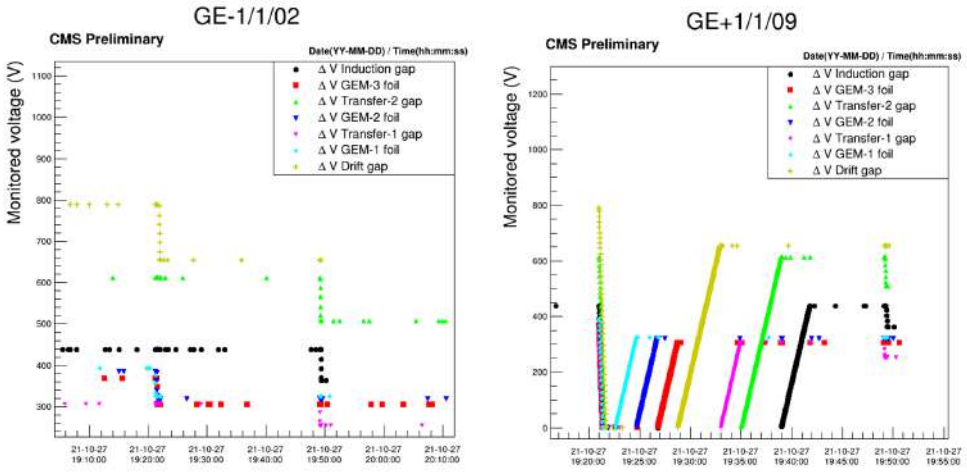

(a) (b)

Figure 3.28: Transition from READY FOR PHYSICS mode (700 μA) to STANDBY mode (580 μA) interrupted from the occurrence of a trip and its recovery, while the transition procedure was being executed. (a) The interruption of the transition in Super-Chamber GE-1/1/02; (b) the trip in Super-Chamber GE+1/1/09 which triggered the interruption.

If the layers are completely healthy or have the same amount of damage, they should drain the same current from the power supply when operated, otherwise, they should show two distinct but constant levels of current. Since, during the operations, the layers of a Super-Chamber are operated together, their operation mode changes simultaneously, and in this way also their current consumption move simultaneously from a level to another.

If during the operation a trip occurs and if the discharge propagates to the readout plane, it could induce a damage in the front-end electronics and thus cause a change in the LV current consumption of one of the two layers. It must be remembered that the damage given by a propagating discharge can happen mainly when the induction gap field is activated.

To detect a damage from a trip are so required three main things:

- the occurrence of a trip;
- the change of current level of one of the two layers;
- the appearance of new dead channels or channels with a low ENC on the S-curve.

This strategy has proved to be effective and it allowed to understand the reason of unexpected current consumption in many chambers. A particularly significant example is given for layer 1 of Super-Chamber GE+1/1/30. In this case a trip occurred at 2021-07-18 18:06:20 UTC, when the induction gap was active as illustrated in Fig. 3.30.

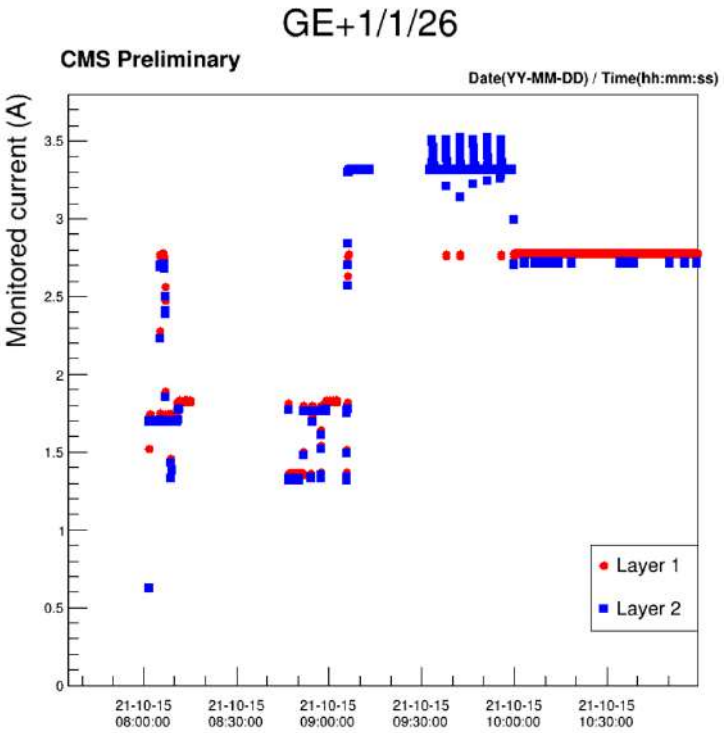

Figure 3.29: LV current for both layers of Super-Chamber GE+1/1/26, operated at 8 V. The main levels present also in QC7 operation can be spotted: the STANDBY mode at the power up (1.75 A), the run mode (2.8 A) and the scan mode (with a mean current level over 3.3 A). Layer 1 was excluded from the scan in this case.

Looking to the LV current plot in Fig. 3.31 it can be noticed as:

- before the trip event the currents of the two layers showed a difference of ~ 0.05 A on the highest current operation level;
- since the trip occurrence time, a distancing among the levels of the two layers appears (~ 0.27 A at the highest current operation level) and this difference is maintained in forever.

This distancing is a symptom of a damage created in the front-end electronics and is indeed confirmed by comparing the s-curves collected before and after the occurrence of the event, illustrated in Fig. 3.32. Comparing them, it can be observed as after the trip occurrence, 8 new dead channels appeared on VFAT 16, which was completely healthy before that moment.

It was also observed as the displacement in current sometimes manifests after a few minutes from the trip, or in other cases it starts simultaneously with the trip and it gradually reaches the final displacement, as if the damage reaches gradually its final stadium.

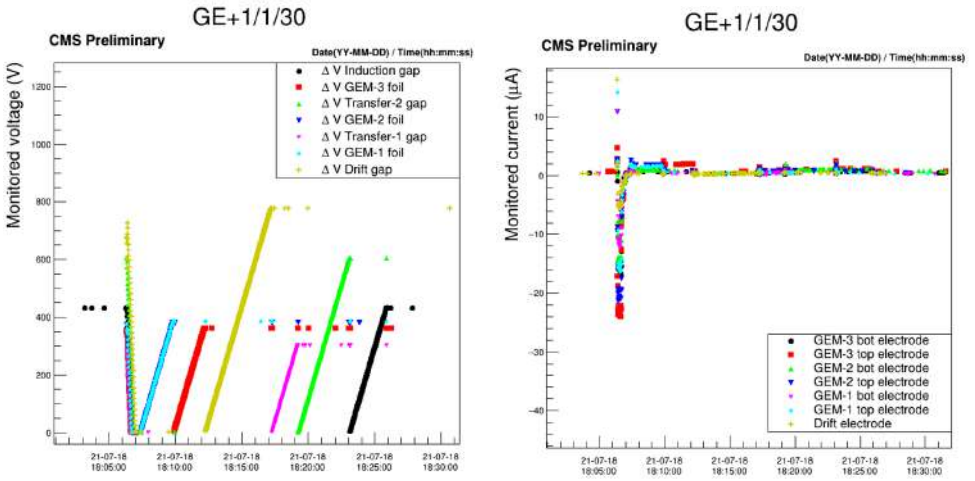

(a) (b)

Figure 3.30: Trip on Super-Chamber GE+1/1/30: (a) the voltage plot, (b) the current plot. During this event a discharge propagated to the readout plane and damaged the front-end electronics.

3.2.2.3 Study of HV trip rates

To determine the behaviour of Super-Chambers in terms of HV trips, a routine, which identifies the HV trips, has been inserted in the HV monitoring tool. The HV trips can occur in many situations:

1. when all the electrodes are active and stable at a fixed voltage;
2. when only part of the electrodes are active and stable;
3. during the ramp of one of the electrodes.

Since the front-end damage from a propagating discharge occurs mainly when all the electrodes are active, it was decided to count only the trips occurring in the 1st configuration. From this, all the trips occurring for example during the recovery of the chamber or during an HV training procedure involving only some electrodes, are not counted, as illustrated in Fig. 3.33.

After scanning the HV data and identifying all the trips occurring in stable operating conditions with all the electrodes activated, the monitoring tool produces a file summarising this kind of HV trip, reporting the Time Stamp, the status code and the name of the channel which triggered the trip (the first in time having a status code ≥ 512). At the same time, the total time the chamber stays with its 7 electrodes stables at the nominal operating voltage is computed. This information is thus used to calculate the Super-Chamber trip rate, in terms of trips per day.

To better estimate the trip rate of a detector, it is thus required a long time of operation, since the observation of a small number of trips on a limited

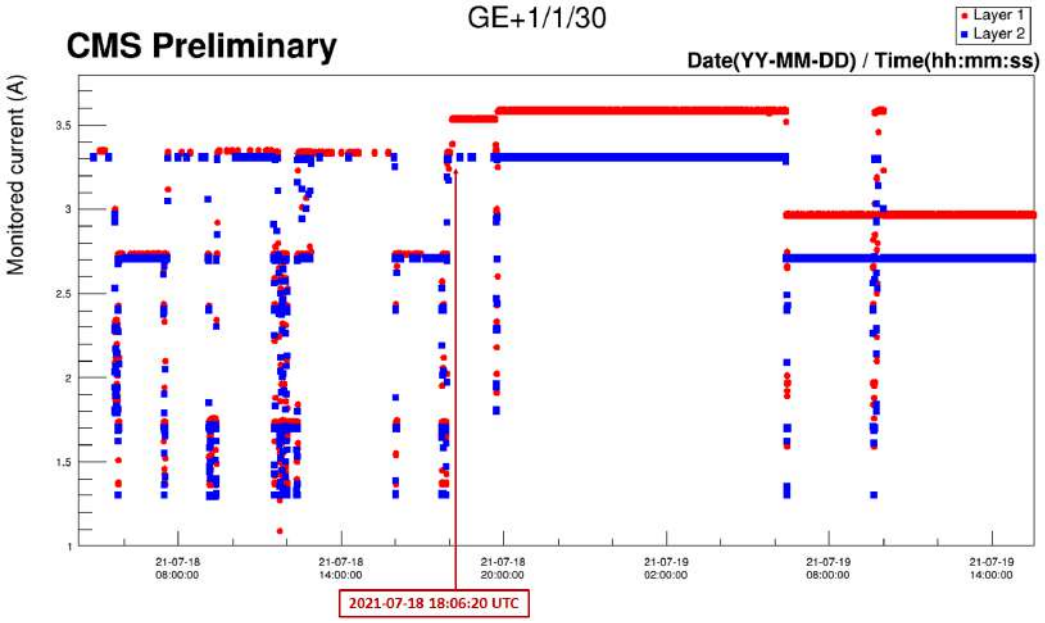

Figure 3.31: LV current plot of Super-Chamber GE+1/1/30: since the occurrence of a trip in the HV system at 2021-07-18 18:06:20 UTC, a distancing of the current levels shows up. This is symptom of damage created in the front-end electronics.

time range would give an unrealistic estimation of the trip rate. From this, it was decided to produce a weekly estimation of the trip rate for each of the Super-Chambers. In particular, this monitoring collected the data starting from the 18th week of 2021.

In the top plot of Fig. 3.34 the trip rate per day for Super-Chamber GE+1/1/03 is shown, given by the ratio between the number of trips counted during the week (mid plot) and the operation time with all the electrodes active and stable (bottom plot). The period illustrated goes from the 18th to the 39th week of 2021 (3rd May - 3rd October). This illustration is particularly useful to understand if a high trip rate in a fixed week depends really on the number of trips, or if it is only caused by a small operation time.

A summary of the trip rate for all the Super-Chambers in the same period (week 18-39) is provided in Fig. 3.35. Here the trip rate is calculated over the entire operation period from week 18 to 39, showing clearly as the trip rate of all the chambers stays below 1 trip per day, apart from Super-Chambers GE-1/1/01, GE-1/1/11 and GE+1/1/03, which at the same time show a lower operation time with respect to the other Super-Chambers.

This plot reports in particular monitoring until week 39, because in week 40 the commissioning of the CMS magnet started and it is interesting to illustrate that part of the operation separately.

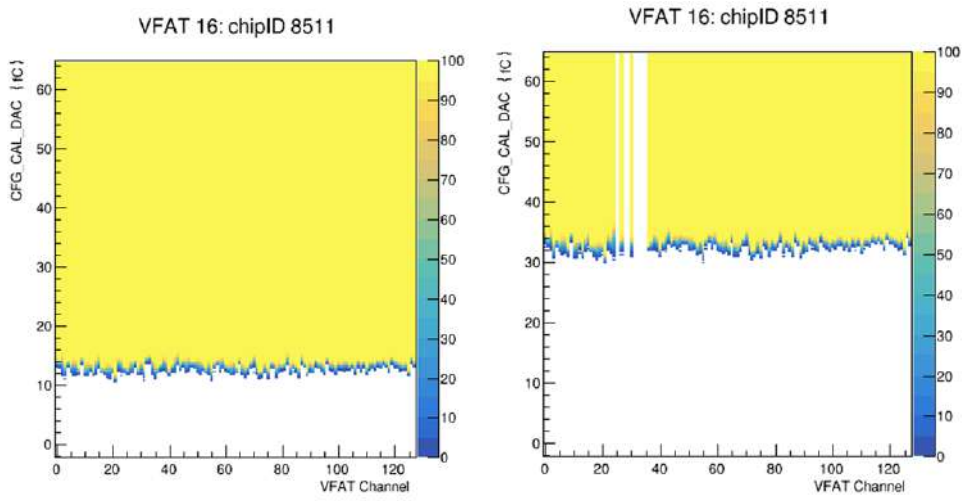

(a) (b)

Figure 3.32: S-curves of Layer 1 of Super-Chamber GE+1/1/30 for VFAT 16: on the left the s-curve collected at the end of June 2021, while on the right that collected on 22 July 2021. The first s-curve was collected applying the $THR\_ARM\_DAC = 100$ threshold, while the second was collected at a higher value because of an issue in the VFAT calibration. It can be noticed anyway as after the trip occurrence, 8 new dead channels appeared on VFAT 16.

3.2.2.4 Operation during the CMS magnet commissioning.

On 7th October 2021, the first operation of the CMS magnet since the beginning of LS2 started.

The operation of detectors during a variation of the magnetic field is a delicate matter, since during the magnet ramp mechanic vibrations are induced on the structure supporting the CMS detector and, in addition, it could produce movement of dust inside of the detector. During this process, instabilities in the HV and so discharges could occur: for this reason, it was chosen to keep off the last electrode (G3Bot).

First magnet ramp up. The operation of the CMS magnet started at 14:52 CET (12:52 UTC) with a ramp up: this operation lasted 11 minutes and reached a value of 0.20 T at 15:03 CET.

During the ramp indeed a large number of detectors experienced instability in the HV (60 Super-Chambers over a total of 72), with a positive current spike which triggered the trip status in the detectors, turning them off. During this phase, the detectors were powered with the FREE mode, to allow to keep off the G3Bot electrode. Because of this, only the tripping channels were turned off, while the others stayed stable. After this, the automatic recovery took

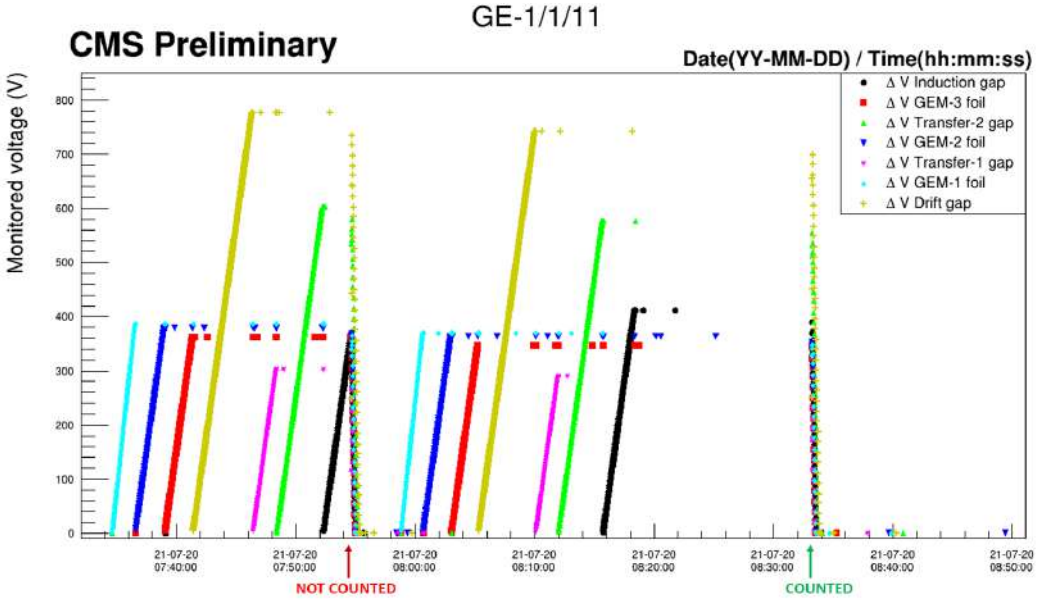

Figure 3.33: Example of valid and non valid trips: the first trip is not counted since happens when the ramp is ongoing and the stability of the last electrode has not yet been reached, the second trip is counted, since it happened with all the electrodes active and stable.

action to recover the detectors.

Due to the high number of tripping chambers, the operator decided to turn off all the detectors, to perform a deep investigation and to preserve the detector safety. After this phase, an HV training procedure started, to clean the foils one by one. The procedure was performed in absence of a magnetic field until October 14th and then with the magnetic field constant at 3.8 T, as illustrated in Fig. 3.36.

Effects of the 7th October trips. Observing the HV data, it can be noticed that some dust was deposited on the foils and it was burned by the HV ramp up during the recovery of the foils. In this case, problems of current thresholds I_0 show up, since the dust creates a short circuit between the two faces of the foil and this manifests as an increase of the current during the channel recovery ramp up. The current increase can indeed induce a trip if the I_0 threshold is overcome.

But it can also happen that a short circuit becomes permanent and the only way to operate the chamber is by increasing the current threshold. This is the case of Super-Chamber GE-1/1/31, in which during the HV training procedure a short was spotted on the third foil (G3Top), as illustrated in Fig. 3.37. It can be observed that the short drains a current of 42.1 μA, when the G3Top channel is set at 430.2 V. In particular, it was verified that the short is localised on the G3Top foil of Layer 2 of the Super-Chamber.

The first track of a short-like behaviour (a linear increase of the current given by the voltage ramp up) in the G3Top channel has been identified during a ramp up recovery after the trip which occurred during the magnet ramp, at 12:55 UTC on the G3Top channel, as illustrated in Fig. 3.38. While performing the ramp, it can be observed as at 12:57 UTC the channel trips again, because the current flowing in the channel has overcome the 20 μA limit used during the channel ramps.

The second effect that was observed in some chambers after the 7th October event is a distancing among the LV current levels, as was observed in case of front-end damage, but, in this case, it should be remembered as the induction gap electrode was kept off, to minimize the propagation of discharges towards the readout plane.

In this context, three single chamber layers experienced an increase of current consumption higher than 0.1 A. In this case, unfortunately, it was not possible to check for a VFAT channel damage on the s-curves, because the system producing the s-curves was performing an upgrade program. Anyway, as soon as this service will be restored, it should be checked.

Transitions between operation modes. As illustrated previously in section 3.2.2.1, the detector can operate in STANDBY and READY FOR PHYSICS modes, which correspond to two different equivalent divider current levels, and this is done to reach the data taking configuration quickly, instead of powering the detectors from scratch.

On 27th October, GEM participated in the LHC collisions in CMS in concert with the other CMS subsystems and this operation lasted until the 31st October. During this period, the detectors were operated accordingly to the LHC operations: in this restart phase, the LHC made some tests, and changes of mode every few hours were observed, while the mode change foreseen during the data taking is around one or two times per day. Indeed, during data taking periods, beams are kept circulating in the LHC and colliding in experiments for many hours, before degrading enough to require a beam dump and the following preparation of a new LHC beam.

This frequent change of mode created some issues in the detector operation, since the period immediately after a ramp (30 minutes) could be characterised by the occurrence of trips in HV channels. In addition, the detectors tripping in these situations will be recovered with the same ramps used for the transitions (ramp up 10 V/s and ramp down 20 V/s), producing a total inactive time of ~ 6 min.

Due to the occurrence of trips near to the change mode ramps, an investigation has been performed, to understand if a different equivalent divider current voltage configuration in the STANDBY mode would help to improve the trip rate. Two different configurations have been defined:

- STANDBY mode at $I_{eq} = 580\,\mu$A and READY FOR PHYSICS mode at $I_{eq} = 700\,\mu$A (27th-28th October);

- STANDBY mode at $I_{eq} = 620\,\mu$A and READY FOR PHYSICS mode at $I_{eq} = 700\,\mu$A (29th-31st October).

In this context, four different disjoint categories of trips have been defined:

- trip occurring during the STANDBY mode (later than 30 minutes from a mode transition);
- trip occurring within a window of 30 minutes from a transition from STANDBY to READY FOR PHYSICS mode ($SB \rightarrow RD$);
- trip occurring during the READY FOR PHYSICS mode (later than 30 minutes from a mode transition);
- trip occurring within a window of 30 minutes from a transition from READY FOR PHYSICS to STANDBY mode ($RD \rightarrow SB$).

The hours of operation available, in the $580 - 700\,\mu$A and $620 - 700\,\mu$A configurations, are limited and only a rough estimation of trip rates can be done. To calculate the trip rate occurring in a stable operation period (in STANDBY or READY FOR PHYSICS mode), the number of trips is normalised to the hours operating in that state, while to calculate the trip rate relative to a transition, the number of trips occurring near a transition is normalised to the number of transitions of that type.

The results obtained for each trip category are reported in Fig. 3.39-3.42, showing the trip rate per each Super-Chamber, while a global category summary is reported in Fig. 3.43.

As can be observed from Fig. 3.39 and from Fig. 3.43, the trip rates of the READY FOR PHYSICS mode ($700\,\mu$A), obtained after moving from STANDBY levels of $580\,\mu$A and $620\,\mu$A, are compatible. This means that a transition does not affect the trip rate after 30 minutes from a transition ramp up. As expected, the trip rate in this state is higher than that observed at the STANDBY level, since the electric field in the holes increases. On the other hand, small differences in the global trip rate can be observed for the other categories.

A first difference can be observed in the $SB \rightarrow RD$ category (Fig. 3.40), which results to be globally 63% higher for transitions starting from a $580\,\mu$A level than from a $620\,\mu$A level, as illustrated in Fig. 3.43. This is due to the fact that making a transition from a lower working point requires a higher charge to be accumulated on the foils, increasing the probability of occurrence of an HV instability. It has to be remembered as anyway is a rare occurrence and a low number of transitions has been performed, requiring a higher statistics for confirmation.

On the other hand, an opposite behaviour can be observed for the global trip rate of the STANDBY category, where the trip rate for the $580\,\mu$A level is half of that occurring in the $620\,\mu$A STANDBY level (Fig. 3.43). These

trips are sometimes correlated with chambers which usually showed a higher trip rate during operation time at 700 μA. Also in this case the rarity of the event has to be remembered, which does not provide a strong reason to prefer an equivalent divider current level respect to the other.

Regarding the last category, $RD \rightarrow SB$ (Fig. 3.42), also in this case the occurrence of trips is rare and correlated sometimes to chambers which showed a higher trip rate during the operation at 700 μA.

These results suggest as a choice of the level of the STANDBY mode cannot be chosen on the basis of the trip rate, since the differences are too small. A solid criteria to prefer 580 μA for the STANDBY state is otherwise the fact that the detector is in a safer state (lower electric field in the holes), respect to the 620 μA configuration, and this would protect it in case, for example, of beam loss, where heavy ionising particles like protons could arrive on the detector.

The shorter ramp time needed for the 620 μA to reach the READY FOR PHYSICS state is not relevant enough to prefer it to the 580 μA, since there is a difference of only $\sim$ 20 seconds.

Magnet ramp down: 1st November. After 24 days of operation, on the 1st of November the CMS magnet was turned off, with a ramp down starting at $9:42\,CET$ at a field $B = 3.8\,\mathrm{T}$ and ended at $14:13\,CET$ at a field $B = 0\,\mathrm{T}$. During this period all the HV and LV electrodes of all the chambers were kept off.

When the electrodes were powered again, six new shorts showed up. This is due probably to some dust movement induced by the variation of the magnetic field, which deposited on the foils and that turned into a short once the HV was powered.

Study on HV shorts circuits. The creation of a short circuit in an HV foil sector is a major problem for the Super-Chamber operation. As previously mentioned, a short circuit in one foil sector leads to a drop to zero of the high voltage applied on the sector, and to a lower voltage applied to each HV sector of the same foil (-6%), due to the potential difference falling of the filter resistors. The main consequence of this is a reduction of the gain provided by the whole foil, with a null gain for the sector where the short circuit lives.

To have a clear picture of the system, a scheme of the HV circuit without any short circuit is provided in Fig. 3.44.

When a short circuit is created, the HV sector on the foil top face is connected with the bottom face. The connection could be purely conductive or with a low resistance, depending on the nature of the deposition which created the short circuit. The equivalent circuit given by the connection in one sector of one foil is provided in Fig. 3.8 and its equivalent resistance is 10.62 MΩ.

If the number of short circuits increases, the configuration can become more complex: we could have for example two shorts in the same foil of the same Super-Chamber layer (Fig.3.45a) or two shorts in the same foil type of a Super-Chamber but in distinct Super-Chamber layers (Fig.3.45b). In these cases, parallels of resistors are created and the equivalent resistances for these two configurations are respectively

- 2 short circuits in 1 foil in the same Super-Chamber layer: $R_{eq} = 5.62\,\mathrm{M\Omega}$;
- 2 short circuits in the same foil type but in distinct Super-Chamber layers: $R_{eq} = 5.31\,\mathrm{M\Omega}$.

Obviously, the effective value of the resistance can fluctuate, since the resistance of each resistor could be a bit different from the nominal value.

Up to 18th November 2021, 15 short circuits and 1 big current leak have been observed in GE1/1 Super-Chambers. For each of them the resistance corresponding to the voltage and current values provided by the power supply has been computed. This value can differ from the expected resistance due to two main factors:

- the resistors could differ from their nominal value due to the production tolerance;
- the short circuit created could be partially resistive instead of being purely conductive.

The summary of observed resistances is illustrated in Fig. 3.46a, where the resistances of short circuits for each Super-Chamber are illustrated. In Super-Chamber GE+1/1/36 there are two shorts and one big current leak, distributed in the following way:

- one short circuit on 1st foil of Layer 1, with an observed resistance of $10.9\,\mathrm{M\Omega}$, compatible with the scenario of one short;
- one current leak on the 2nd foil of Layer 2, with an observed resistance of $37.7\,\mathrm{M\Omega}$. It has not yet turned into a short circuit but is a significant current leak;
- one short circuit on the 3rd foil of Layer 2, with an observed resistance of $7.3\,\mathrm{M\Omega}$. This is could be due to the presence of two short circuits, with at least one of them resistive, or it could be due to the contribution of many resistive shorts created on the foil. The only way to verify is unfortunately opening the chamber.

A different resistance summary is provided by Fig. 3.46b, which shows the frequency of resistance values. Most of them fall in the scenario compatible with a single short circuit, the highest resistance in the plot is the current

leak on G2Top of Layer 2 of GE+1/1/36, and the lowest resistances have a resistance approaching the scenario with two short circuits in the same foil of the same chamber.

To contextualize more deeply the origin of short circuits, two additional information have been investigated:

- the foil where the short circuit is created: the most subject to the formation of the short circuit has shown to be the 1st and 3rd foils (Fig. 3.47a), probably because they are the external ones and so more subject to the deposition of dust;
- the operation context when the short circuit manifested for the first time: it can be observed that the variation of magnetic field and the HV training procedures are the major actors playing in their formation (Fig. 3.47b).

Up to now, the only solution available to restore the correct gain on the sectors without the short circuit is by increasing the voltage provided by the power supply. To perform this operation, the layers of the Super-Chambers have to be powered separately: increasing the voltage on the power supply with the two layers still powered by the same cable, would increase the voltage both on the layer with the short circuit and on the healthy one, leading to potential damage on this last one.

3.2.2.5 Conclusion

This period of operation was useful for the GEM group as it gave the possibility to gain expertise in the operation of chambers in the magnetic field and during LHC collisions, allowing to start adopting solutions to grant a smooth as possible operation. In addition, this study led to the investigation of the creation of shorts in a controlled environment with a magnetic field, trying to create and heal short circuits only operating the detector from the DCS or acting on the cables from the patch panel $\sim 40\,\text{m}$ far from the detector [89]. Finally, this study led to the development of strategies to operate chambers with shorts in the CMS experiment, reorganising the HV distribution to include slots dedicated to the healing of chambers with shorts [90] and following the expertise gained by the ALICE experiment about the HV training of GEM detectors and their operation during the ramp of the magnetic field.

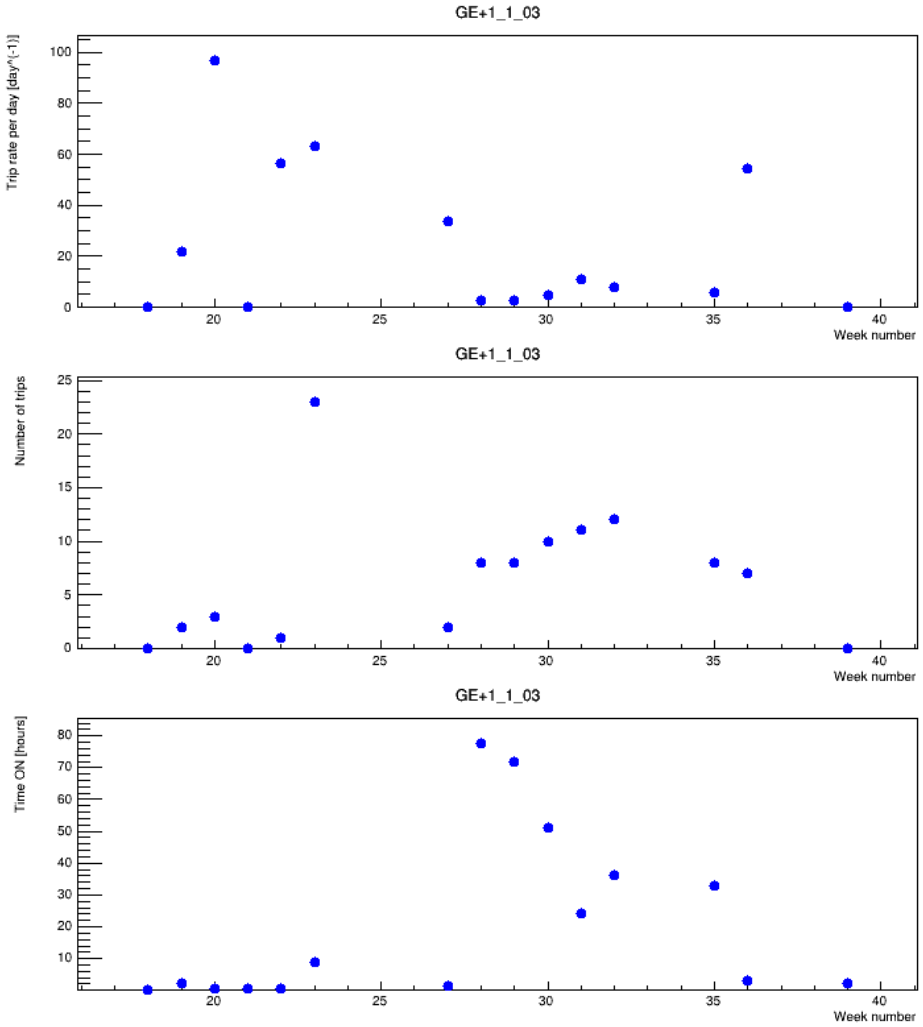

Figure 3.34: Weekly trip report for Super-Chamber GE+1/1/03 from week 18 to week 39 of 2021 (3rd May - 3rd October): in the top plot is reported the trip rate per day for this chamber, given by the ratio between the number of trips counted during the week (mid plot) and the operation time with all the electrodes active and stable (bottom plot).

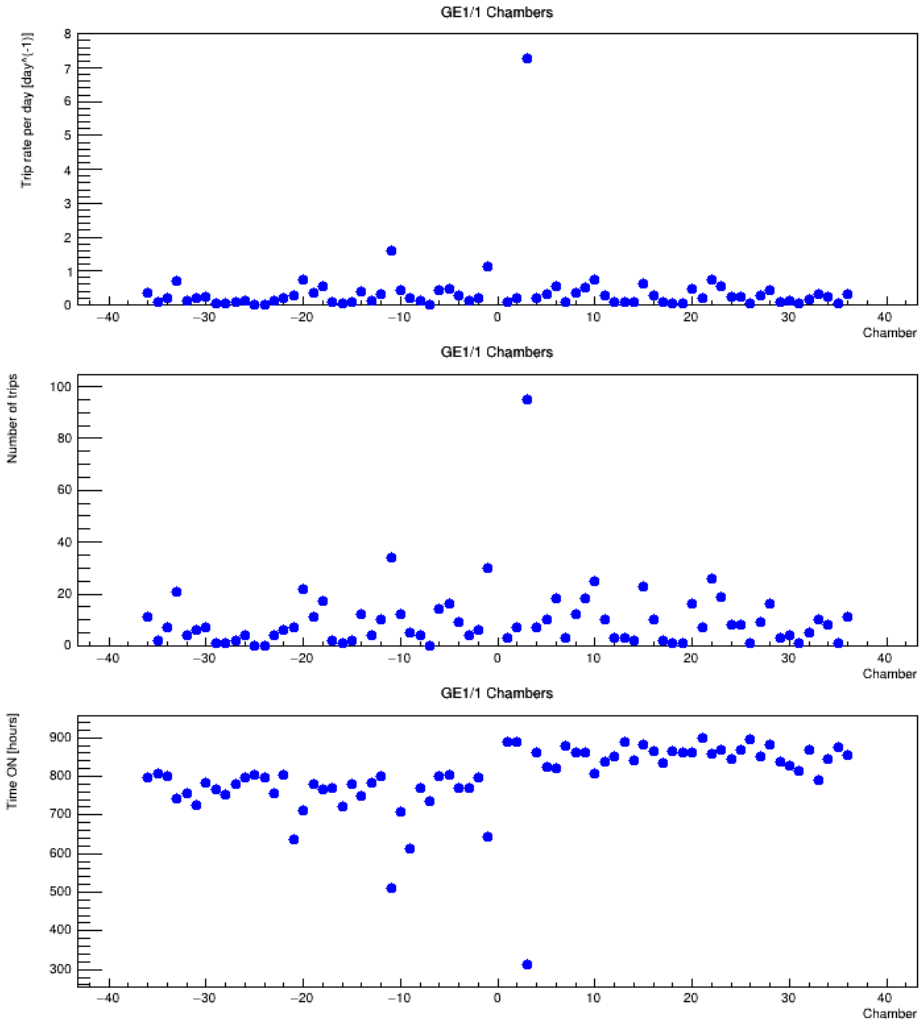

Figure 3.35: Trip report for all Super-Chambers from week 18 to week 39 of 2021 (3rd May - 3rd October): in the top plot is reported the trip rate per day per Super-Chamber, given by the ratio between the number of trips counted during the week (mid plot) and the operation time with all the electrodes active and stable (bottom plot). It can be noticed that the outlier Super-Chambers in the trip rate plot correspond to those with a lower operation time.

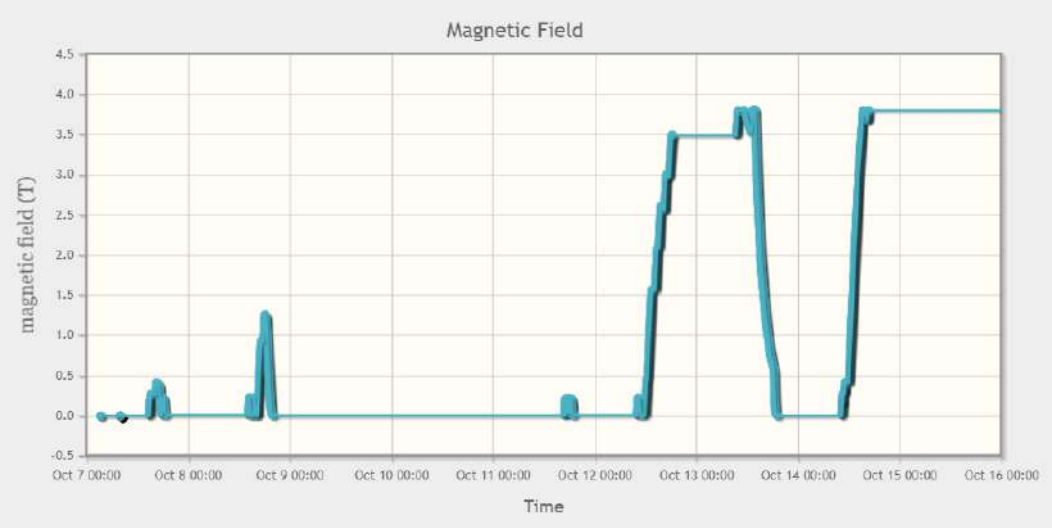

Figure 3.36: Operation of the CMS magnetic field from 7th to 16th October 2021.

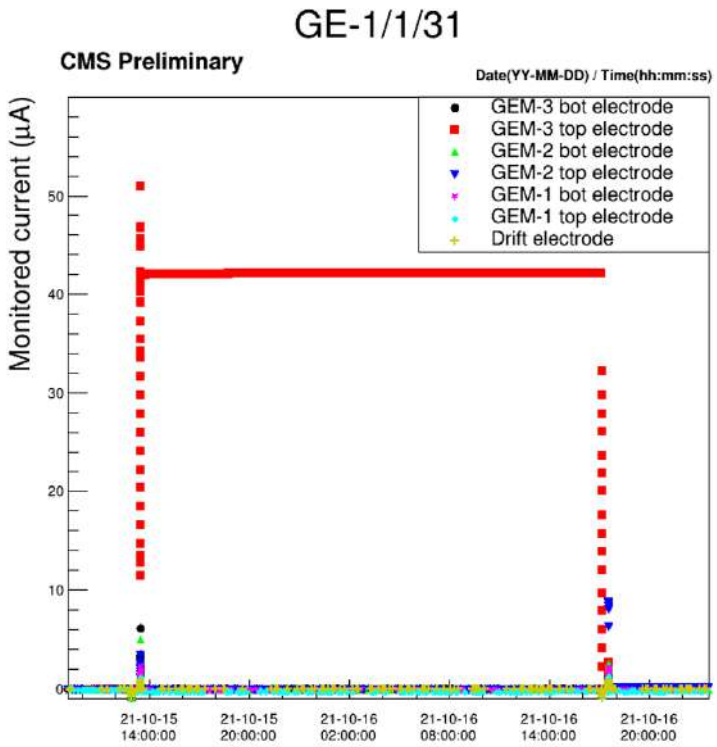

Figure 3.37: Short in the GE-1/1/31 Super-Chamber ($I_{G3Top} = 42.1\,\mu$A, at $\Delta V_{G3Top} = 430.2\,$V). This short has been identified to be on the 3rd foil in Layer 2.

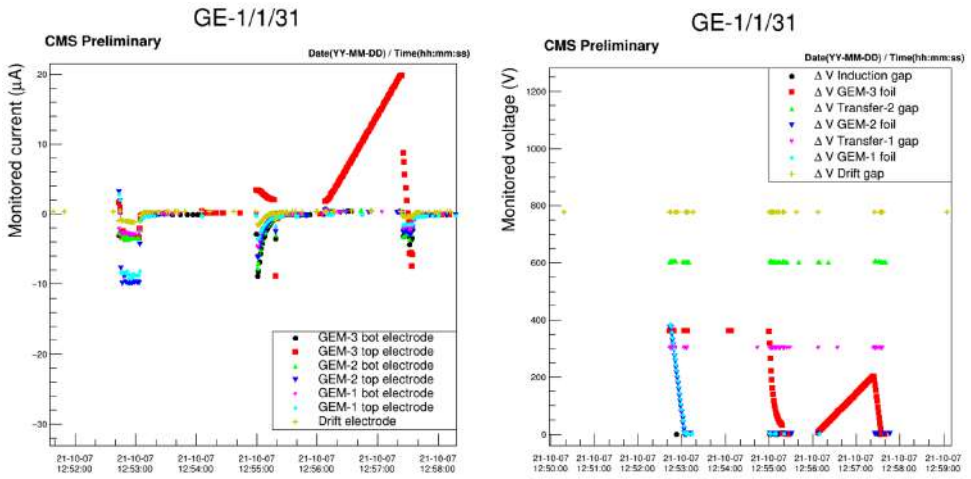

(a) (b)

Figure 3.38: Super-Chamber GE-1/1/31: first occurrence of a linear increase of the current of channel G3Top, during a recovery ramp. This happens after a trip involving G1Top and G2Top (12:53 UTC) and in particular after the trip on G3Top (12:55 UTC). From left to right are reported respectively the HV current and voltage plots.

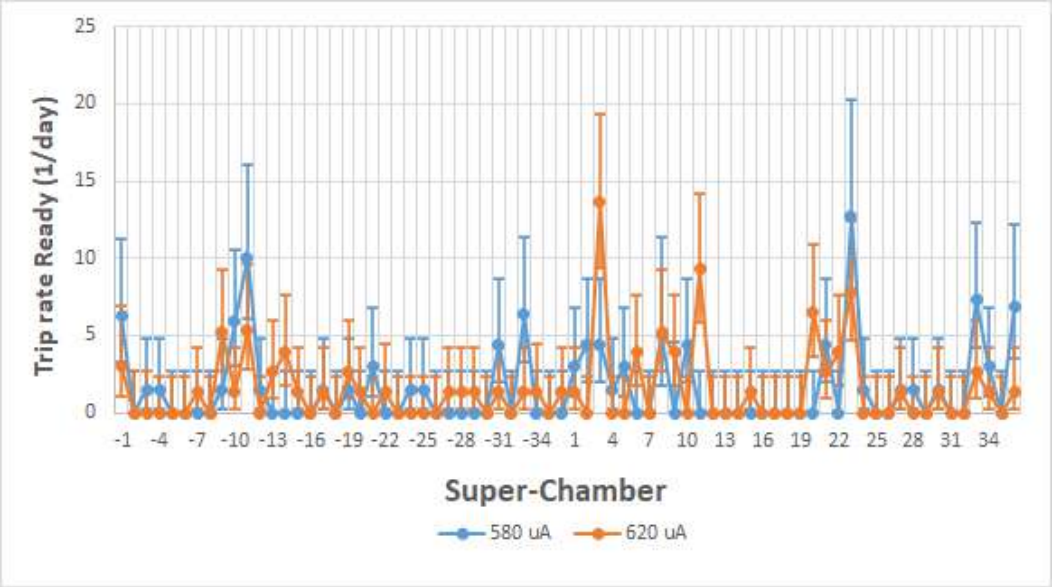

Figure 3.39: Trip rate calculated during the READY FOR PHYSICS mode, using 580 μA and 620 μA equivalent divider current voltages for the STANDBY mode, for each Super-Chamber.

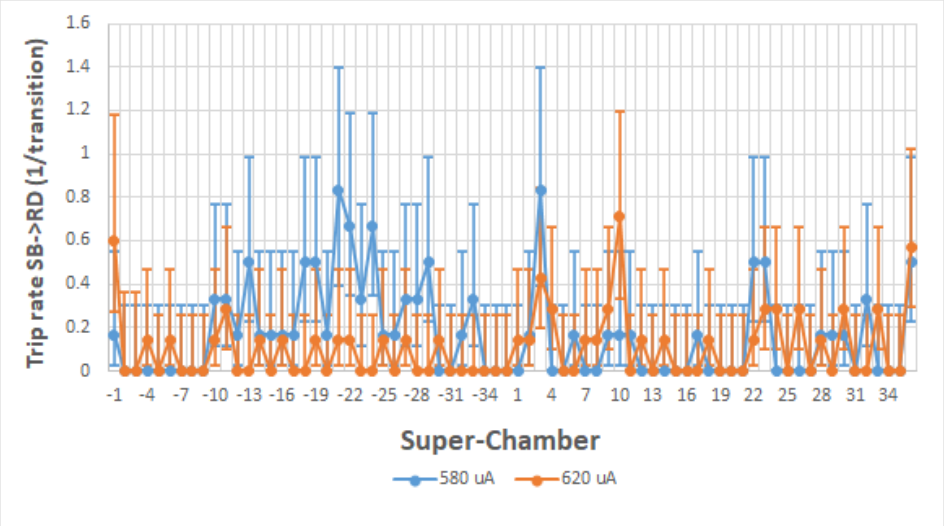

Figure 3.40: Trip rate calculated for the transitions from STANDBY to READY FOR PHYSICS mode, using 580 μA and 620 μA equivalent divider current voltages for the STANDBY mode, for each Super-Chamber.

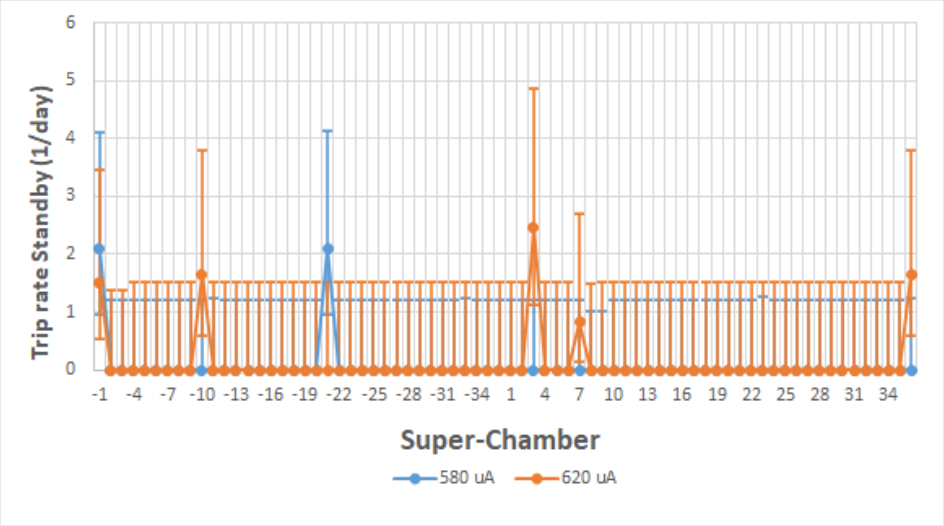

Figure 3.41: Trip rate calculated for trips occurring in the STANDBY mode, using 580 μA and 620 μA equivalent divider current voltages for the STANDBY mode, for each Super-Chamber.

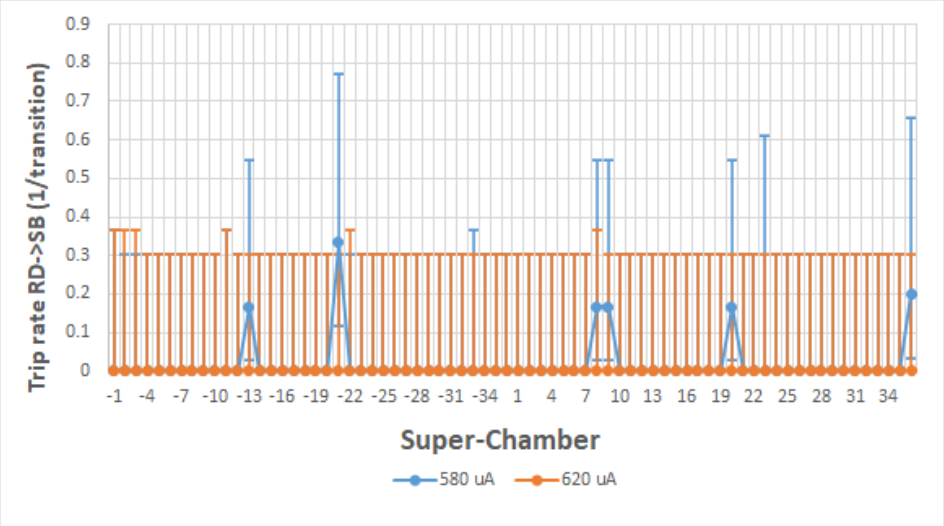

Figure 3.42: Trip rate calculated for the transitions from READY FOR PHYSICS to STANDBY mode, using 580 μA and 620 μA equivalent divider current voltages for the STANDBY mode, for each Super-Chamber.

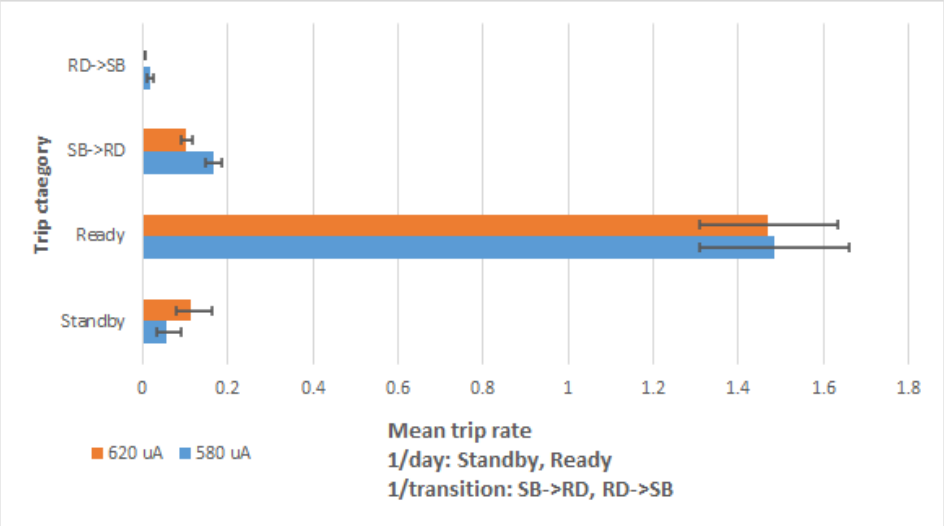

Figure 3.43: Summary of the mean trip rate for the 72 GE1/1 Super-Chambers, occurring in the STANDBY (SB) and READY FOR PHYSICS (RD) modes and during the transitions between these two states: $SB \rightarrow RD$ and $RD \rightarrow SB$. Two different sets of equivalent divider current voltages have been used for the STANDBY mode, 580 μA and 620 μA, while in the READY FOR PHYSICS mode the Super-Chambers were always set to 700 μA equivalent divider current voltages. The trip rate relative to the trips occurring during the READY FOR PHYSICS and STANDBY mode is normalised over the days of operation. On the other hand, for trips occurring during the transitions, the rate is normalised over the number of transitions performed.

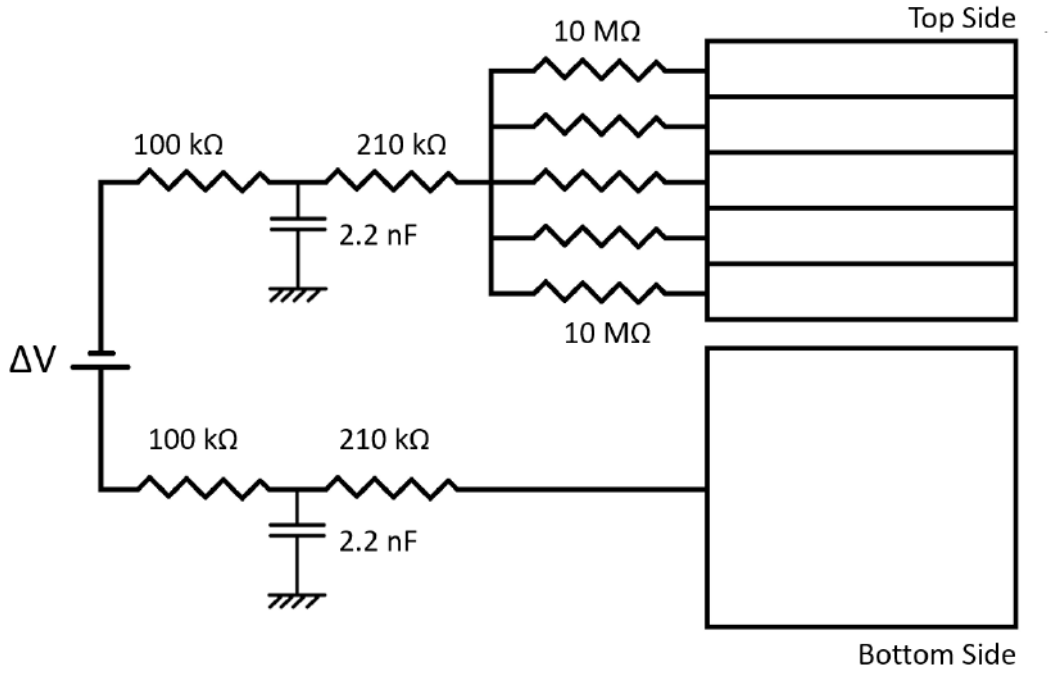

Figure 3.44: Scheme of the HV circuit which powers one GEM foil. The foil top face is segmented into sectors (40 for short chambers and 47 for the long ones), while the bottom face is not segmented.

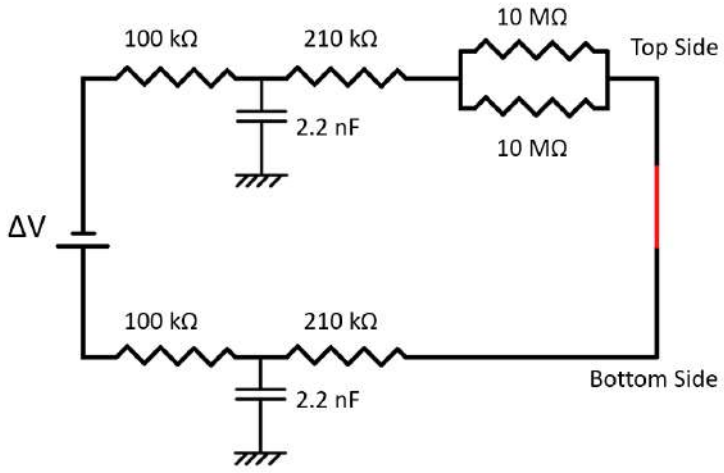

(a)

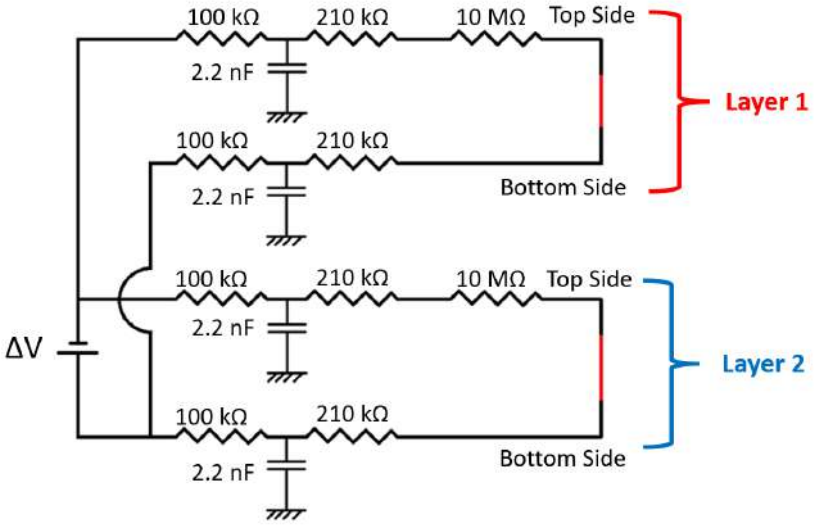

(b)

Figure 3.45: (a) Scheme of the equivalent circuit given by the creation of a short circuit in two HV sectors of the same foil in the same Super-Chamber layer. (b) Scheme of the equivalent circuit given by the creation of a short circuit in two HV sectors of the same foil type but in distinct Super-Chamber layers.

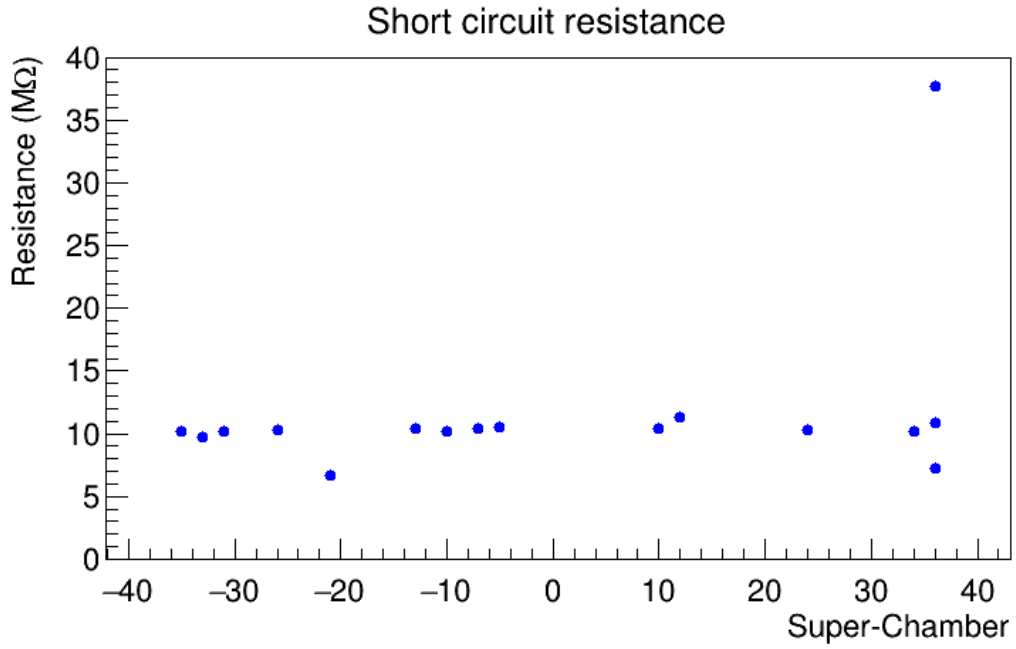

(a)

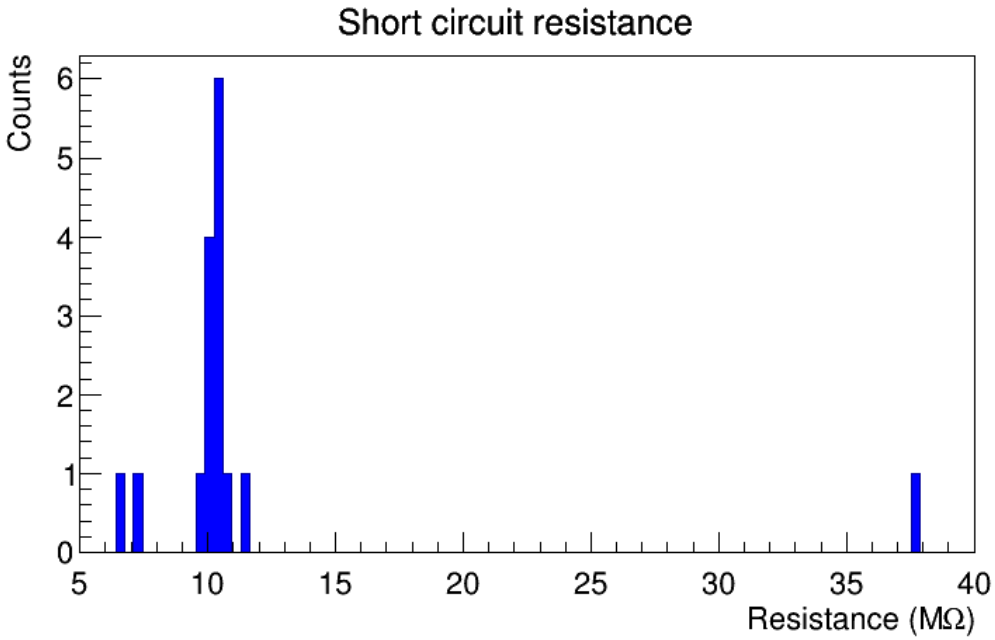

(b)

Figure 3.46: (a) Resistance of short circuits per each Super-Chamber involved; (b) distribution of resistance values

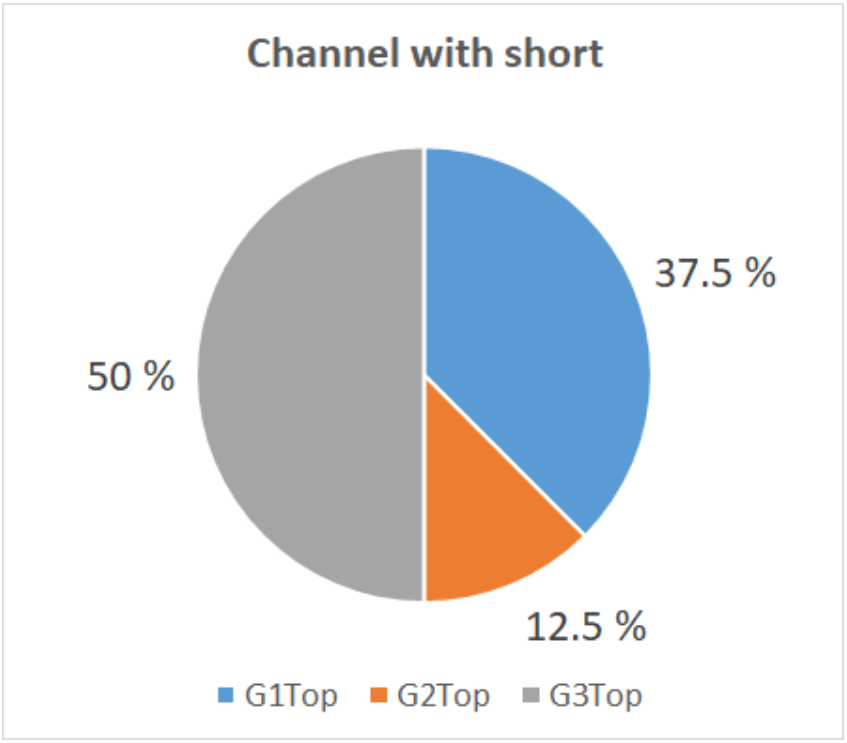

(a)

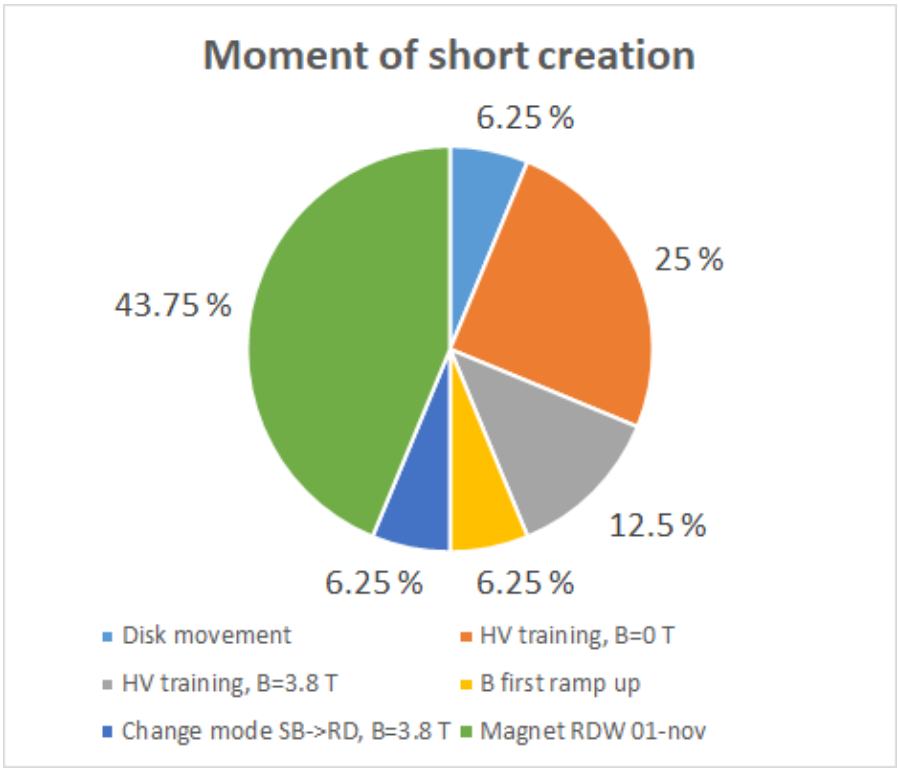

(b)

Figure 3.47: (a) Foil with the short circuit; (b) context when the short circuit manifested for the first time. The labels on the external side of the pie chart are the frequency percentages.

Chapter 4

A trigger study on $\tau \to 3\mu$ channel for the Phase 2 upgrade

In this chapter, a trigger study dedicated to the $\tau \to 3\mu$ decay is presented, exploiting the possibilities offered by the newly installed GEM chambers and the upgrade of the detectors foreseen in Phase 2. In particular, at first the possibilities offered by the single GEM stations are analysed, then finally the analysis will involve the objects provided by more complex infrastructures, such as the Endcap Muon Track Finder (EMTF) and Tracker Muons (Tk-Muons).

The conclusion consists of the performance evaluation, in terms of signal efficiency and trigger rate, of triggers using the above mentioned objects.

4.1 The $\tau \to 3\mu$ decay

The $\tau \to 3\mu$ decay is a process allowed in the Standard Model with an incredibly small branching ratio, in the order of $\mathcal{B}(\tau \to 3\mu) \sim 10^{-40}$, as it involves processes of neutrino oscillation, as illustrated in the example of Fig. 4.1.

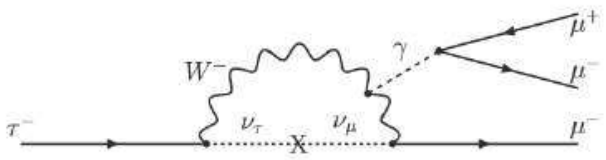

Figure 4.1: Example diagram of the decay of τ in three muons in the final state, with neutrino oscillation [91].

The hope to observe such decay is placed in exotic models that foresee branching ratios in the range $10^{-11} - 10^{-8}$ [92] [93] [94] [95] [96]. These models involve for example technicolor models, seesaw mechanism as the expla-

Particle	Mass (GeV)	Contribution to the total tau yield
D_s	1.97	72%
D^+	1.87	3%
B^+	5.28	11%
B^0	5.28	11%
B_s	5.37	3%
W	80.4	10^{-4}
Z	91.2	$2 \cdot 10^{-5}$

Table 4.1: Channels contributing to the production of tau leptons at the LHC. The charge conjugate states are included in the estimation [91]

nation of neutrino oscillation data and a scenario with minimal supergravity (mSUGRA).

All of them give a branching ratio estimation below the upper limit set by the Belle experiment $\mathcal{B}(\tau \to 3\mu) < 2.1 \cdot 10^{-8}$, with a 90 % confidence level [97].

The main reason motivating the search of the $\tau \to 3\mu$ decay is the fact that this decay is a Lepton Flavour Violation (LFV) decay channel, and furthermore it is one of the cleanest decays contained in the LFV class. Observing such a decay would indeed suggest the existence of new physics beyond the Standard Model, pushing the particle physics research in this direction.

4.2 Production at the LHC

During the whole duration of the LHC Phase 2, with a foreseen integrated luminosity of 3000 fb^{-1}, a production of $\sim 5{\cdot}10^{14}$ tau leptons can be estimated. The main channels leading to the production of a tau lepton are summarised in Tab. 4.1, and involve the decay of mesons and vector bosons.

The main actor in the production of tau leptons is the D_s meson, that decays in a tau lepton with a branching ratio $\mathcal{B}(D_s \to \tau\nu_\tau) = 0.055$. Using PYTHIA to estimate the production cross section of D_s mesons and using the upper limit provided by the Belle experiment as branching ratio for the $\tau \to 3\mu$ decay, a total number of $1.22 \cdot 10^5 \pm 0.07 \cdot 10^5$ events containing the $\tau \to 3\mu$ decay has been estimated from the $D_s \to \tau\nu_\tau$, for a total integrated luminosity $\int \mathcal{L}\, dt = 3000\,\text{fb}^{-1}$. This is calculated using the following relationship:

$$N(\tau \to 3\mu) = \int \mathcal{L}\, dt \cdot \sigma(pp \to D_s) \cdot \mathcal{B}(D_s \to \tau\nu_\tau) \cdot \mathcal{B}(\tau \to 3\mu), \qquad (4.1)$$

where $\sigma(pp \to D_s) = 3.52 \cdot 10^{10} \pm 0.94 \cdot 10^{10}$ fb is the production cross section of the D_s meson in proton proton collisions with 14 TeV center of mass

energy. The production cross section was estimated from an officially produced sample containing the decay chain $D_s \to \tau\nu_\tau$, $\tau \to 3\mu$ decays, using the *GenXSecAnalyzer* tool available in the CMSSW simulation environment [98]. The details on the samples used will be illustrated in more detail in the next sections.

4.3 Simulation environment

The study has been performed in the CMSSW environment [99], using official samples produced by the Trigger Study Group (TSG). CMSSW is the software framework used to simulate collision events in CMS, from the collision of protons, to the interaction of particles within the detectors, to their final reconstruction and determination of physical parameters.

In CMSSW the simulation starts from the generation of particles produced during the proton-proton collisions with two main properties:

- the energy of colliding protons,
- the pileup conditions (PU).

In our case, the collisions occur with a center of mass energy 14 TeV, while pileup conditions 0, 140 and 200 are analysed, each with its own dedicated dataset. Once the collisions have been simulated, the primary particles produced are generated and propagated inside of the detector until they decay. The propagation is performed accordingly to the interaction of the particle with the magnetic field of the CMS detector. When a particle decays, the daughter particles are generated and these are as well propagated till the final state is reached (the particle is absorbed or it exits from the detector volume, like a high energy muon). This gives a complete view of the decay chain of particles, from their generation to the final state.

The samples considered in this study contain D_s particles and each of these mesons is forced to undertake the decay chain $D_s \to \tau\nu_\tau$, $\tau \to 3\mu$. Events not satisfying this condition are discarded.

Once the particles have been generated and propagated in the CMS detector, their interaction with the single detector components has to be simulated, to determine where the particles released part of their energy. These points are called *hits*. The first thing to be set in this context is the geometry foreseen for the CMS detector for the considered period: in this study, the geometry *Extended2026D49* has been adopted, which includes new detectors not yet installed as the endcap calorimeter HGCal or the muon stations GE2/1 and ME0. A more detailed description of the geometry is available here [100].

The energy depositions in the single detectors are then digitised according to the detector granularity and to the response of the detector electronics. These digitalised interactions are called *digis*. For example, in the case of a GEM station, digis correspond to the strips that detected a signal.

Digis are then used to produce objects of interest for the reconstruction of particles, depending on the type of detector station:

- for the ME0 station the signals of the single pads are employed by a dedicated algorithm to build a reconstructed hit (RecHit). In turn the RecHits of each of the six layers of the ME0 station are used to build a *ME0 segment*, which will represent a first step in the reconstruction of the muon trajectory;
- for the GE1/1 and GE2/1 stations, the information produced by the strips are used to return the hit pad number. This information is then combined with those provided by stations ME1/1 and ME2/1, respectively for GE1/1 and GE2/1 stations, in building a so-called *CSCCorrelatedLCTDigi* object, where LCT stands for Local Charged Track.

After the production of the so called Trigger Primitives by each subdetector, their information is combined to build more complex and refined objects. In this study, in addition to ME0 segments and CSCCorrelatedLCTDigis for stations GE1/1-ME1/1 and GE2/1-ME2/1, the following objects will be considered:

- EMTF tracks, produced by the Endcap Muon Track Finder system;
- TkMuons, produced by the central CMS tracker.

All the objects mentioned above will be discussed in the following sections.

4.3.1 Used samples

The samples used in the study can be divided into two main kinds: *signal* samples and *minimum bias (MinBias)* samples.

The signal samples contain events with the decay of D_s meson with the complete chain $D_s \to \tau\nu_\tau$, $\tau \to 3\mu$. Three centrally produced samples have been used, to investigate different pileup conditions: $PU = 0$ ($1.52{\cdot}10^5$ events), $PU = 140$ ($1.52 \cdot 10^5$ events) and $PU = 200$ ($1.45 \cdot 10^5$ events).

To have higher statistics to analyse in a better way the signal, a private sample was produced, starting from the same code fragment used for the centrally produced ones. This sample has $PU = 0$ and a total number of events of $8.51 \cdot 10^5$.

On the other hand, the minimum bias sample is a collection of proton-proton collision events where a loose trigger is used in the collection of events to select a large fraction of the inelastic scattering. This should give a good and general representation of collision events of any kind, without the introduction of significant biases.

The MinBias samples used in this case are characterised by $PU = 140$ ($4.98{\cdot}10^5$ events) and $PU = 200$ ($5.00{\cdot}10^5$ events). Both of them are centrally produced.

The complete names of the datasets are provided in Appendix A.1.

4.4 Features of the signal sample

Observing the signal sample it can be noticed that tau leptons have been produced within all the CMS acceptance, both in ϕ and η (Fig. 4.2a). In Fig. 4.2b is represented the generated τ p_t distribution, which has a mode $\sim 7.5\,\text{GeV}$ (in the whole description $c = 1$ is used).

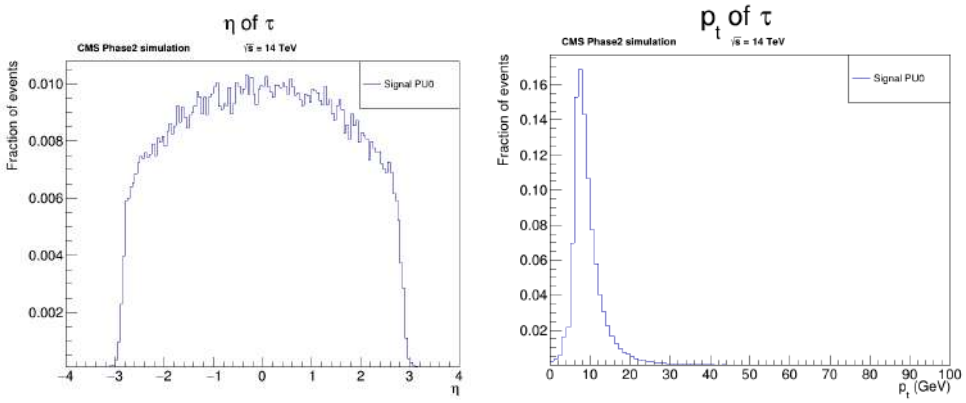

(a) (b)

Figure 4.2: (a) η distribution of generated tau leptons; (b) p_t distribution of generated tau leptons.

As pointed out in Fig. 4.3a, the distribution of the generated muons mimics the distribution of the generated τ leptons. On the other hand in Fig. 4.3b the p_t distribution of the muons produced by the decay of the tau lepton is represented.

Since a minimum momentum is required for the muons to reach the detector components, the detection efficiency of all the three muons is small, due to the low p_t of the trailing one and has been shown to be most probable in the CMS endcaps. The η distribution of τ leptons which produced muons with a high enough p_t to be reconstructed in CMS is shown in Fig. 4.4a, while the η distribution of TkMuons is plotted in Fig. 4.4b: it reflects well the concentration of reconstructable muons in the endcap region.

Other general useful features of the signal concern the mutual distance among the muons, as illustrated in Fig. 4.5. From these mutual distances in $\Delta\eta$ and $\Delta\phi$ can be understood how the muons produced by the τ decay live in a narrow cone. In particular, it can be noticed how the medium and maximum p_t muons lie close to each other, while the farther one is the minimum p_t muon.

The distance among muons is well represented also calculating their $\Delta R = \sqrt{(\Delta\eta)^2 + (\Delta\phi)^2}$. Since we are working with three objects, three different ΔR can be computed, one per pair of muons. The strategy adopted to summarise in a unique parameter the mutual distance among the muons was to build a triangle with the three ΔR, given by the pairs, and then determine the radius of the smallest circumference which contains the triangle. This radius will

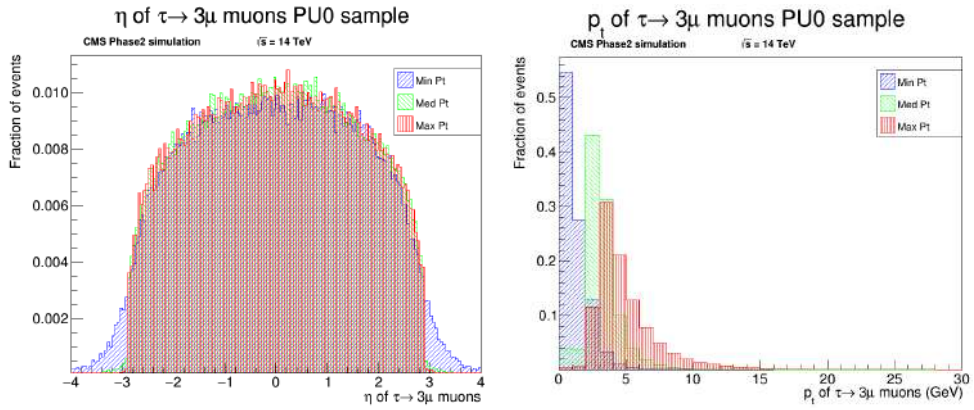

(a) (b)

Figure 4.3: (a) η distribution of generated muons coming from the decay of tau leptons; (b) p_t distribution of generated muons coming from the decay of tau leptons. In blue, green and red are respectively shown the distributions corresponding to the trailing, medium and leading-p_t muons.

represent so the smallest cone which can contain the three muons: the plot with its distribution for the generated muons is illustrated in Fig. 4.6a.

When the triangle is built, three situations can be obtained:

- an acute triangle, where the radius of the smallest circumference (the circumscribed one) is given by the formula $R = \frac{abc}{4A}$, where a, b and c are the sides of the triangle and A its area (top illustration in Fig. 4.6b);
- an obtuse triangle, where the radius of the smallest circumference which contains the triangle is given by half of the longest triangle side, as illustrated in the bottom right part of Fig. 4.6b;
- a rectangle triangle, where the radius of the smallest circumference containing the triangle is given by the circumscribed circumference radius. This is due to the fact that this is the limit case between the acute and obtuse triangle, where the smallest circumference is circumscribed to the triangle and the longest side (the hypotenuse) is its diameter.

4.5 Objects used in the study

As previously mentioned the study will concentrate on 5 different CMSSW objects in total: the ME0 segments, ME1/1 and ME2/1 CSCCorrelatedLCT, the EMTF tracks and the TkMuons. The main objective is to study the performances of trigger paths exploiting these objects. The discussion will now concentrate on the description of each object used and of the cuts implemented for each of them.

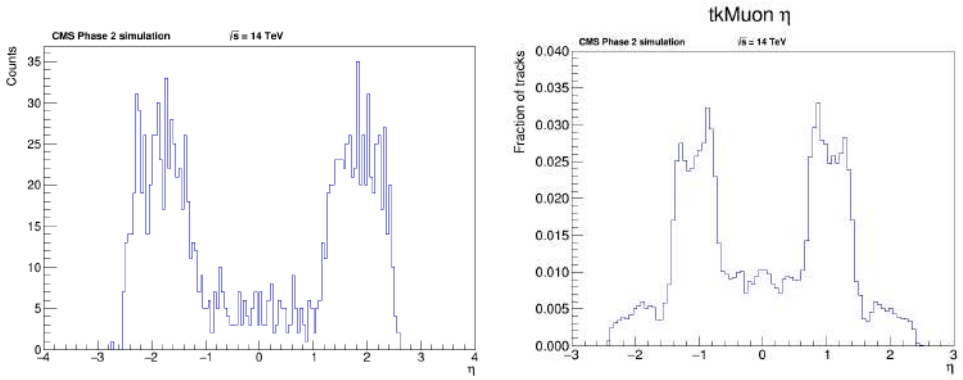

(a) (b)

Figure 4.4: (a) η distribution of generated tau leptons (GEN_PARTICLES [99]) which decayed into muons with a high enough p_t to produce a global muon in the reconstruction: the cuts applied to the muons GEN_PARTICLES are $p_t > 3.5\,\text{GeV}$ in the barrel ($|\eta| < 1.2$) and $p_t > 2.0\,\text{GeV}$ in the endcap ($|\eta| > 1.2$); (b) η distribution of TkMuons. Both plots have been produced using the PU0 signal sample.

4.5.1 ME0 segments

The ME0 segments are built by the ME0 station, exploiting all the six layers of the station. In particular, it is useful to remember that each of the layers is segmented in 284 strips in the ϕ direction (the pitch of each strip covers 0.455 mrad in ϕ) and with 8 partitions in the η direction (each η-partition covers ~ 0.1 in η). As for the other GEM stations, this coarse segmentation in η results in a coarse measurement of the position of the hits in the η direction. Taking this into account, in the building process of a ME0 segment the hits laying in a region of $\Delta\phi \times \Delta\eta = 0.02 \times 0.05$ for each layer are used to build a reconstructed hit (RecHit) and then the RecHits are fitted with a straight segment. In particular, the number of RecHits used to build the segment is not always the same, but it can vary from a minimum of 4 to a maximum of 6 RecHits (1 per layer).

4.5.1.1 Cut on the $\Delta\phi$ bending angle

When a muon is produced in CMS, during its travel it modifies trajectory according to the magnetic field: this happens most inside the CMS Tracker, where the magnetic field is more intense. On the other hand, when the muon arrives in the first layer of the ME0 station it moves in a region with a lower but pretty uniform magnetic field ($\sim 3\,\text{T}$). The muon bending occurs in the ϕ direction and can be quantified inside of the ME0 station, by measuring the displacement in ϕ between the origin and the end of the ME0 segment. This brought to the idea of performing a cut on the muon bending angle $\Delta\phi$.

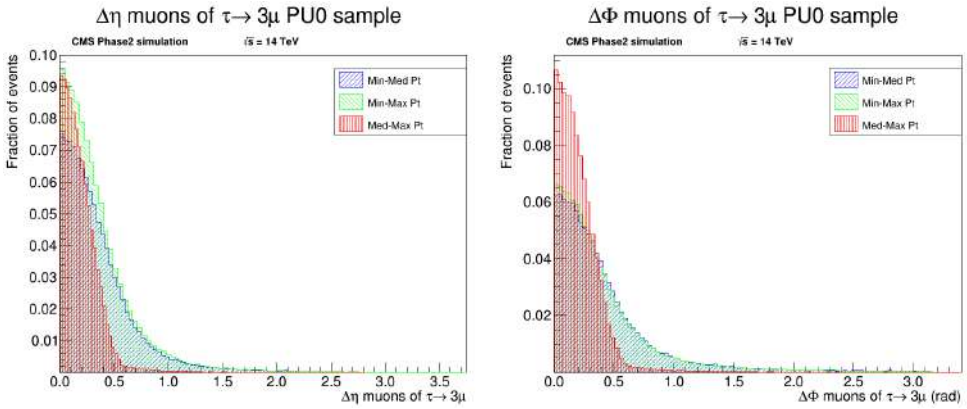

(a) (b)

Figure 4.5: (a) $\Delta\eta$ mutual distance among generated muons produced by the τ decay; (b) $\Delta\phi$ mutual distance among generated muons produced by the τ decay. In blue are represented the distribution of mutual distances between the trailing and the medium-p_t muons, in green between the trailing and leading ones, and in red between the medium and leading ones.

p_t (GeV)	Cut flag	$\Delta\phi_{thr}$ (rad)
2	1	0.0182
3	2	0.0126
5	3	0.0070
10	4	0.0037
20	5	0.0026
50	6	0.0021

Table 4.2: $\Delta\phi$ threshold values designed to select 95% of muons with a fixed p_t.

In particular, the muon bending depends on the muon p_t, with the bending angle $|\Delta\phi|$ which increases with decreasing muon p_t. From this, $\Delta\phi$ thresholds for different p_t has been defined to discriminate between different p_t muons. In this way, if we want to select a muon with $p_t > p_{t_{thr}}$, this selection can be performed accepting the muon with $|\Delta\phi| < \Delta\phi_{thr}$.

The $\Delta\phi_{thr}$ have been determined for 6 different p_t values (2, 3, 5, 10, 20 and 50 GeV) generating event samples containing single muons with fixed p_t. For a fixed p_t, the threshold has been designed to have a selection efficiency of 95% of muons with that p_t.

Since the distributions for the different p_t overlap a lot, only a coarse estimation can be done, as illustrated in Fig. 4.7, while the thresholds defined for each p_t value are reported in Tab. 4.2.

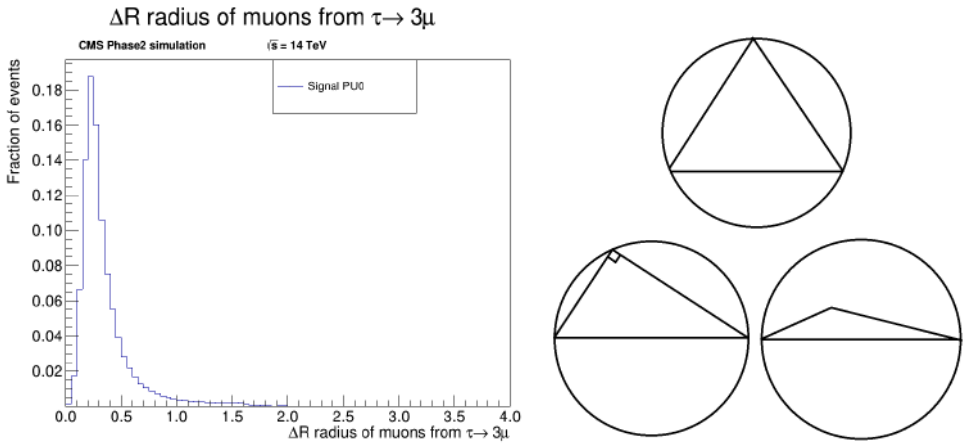

(a) (b)

Figure 4.6: (a) ΔR radius calculated for the three generated muons produced by the $\tau \rightarrow 3\mu$ decay. This parameter is the radius of the smallest circle containing the triangle built using the three muon pairs ΔR as sides; (b) illustration of the three different triangles which can be obtained in the triangle construction: acute on the middle top, rectangle on the left bottom and obtuse on the right bottom.

Asymmetric bending cuts. Choosing how many segments to involve in a selection is the first element to fix in the building process of a trigger selection, and from this derives how many segments would have to satisfy a fixed cut on the bending angle $\Delta\phi$. From this, three categories have been designed:

- single ME0 segment, requiring that at least one ME0 segment satisfies the $\Delta\phi$ cut;
- double ME0 segment, requiring that at least two segments satisfy the $\Delta\phi$ cut;
- triple ME0 segment, requiring that at least three segments satisfy the $\Delta\phi$ cut.

For the single muon selection, 6 $\Delta\phi$ cuts have been designed (Tab. 4.2). For double and triple segment selections a more refined structure has been set, to scan all the possible combinations of $\Delta\phi$ cuts. If more than one segment is involved in the selection it is indeed possible to design an asymmetric $\Delta\phi$ cut, requiring for example that in a pair of segments, the lowest bending segment has to pass a certain threshold, while that with the highest bending has to overcome a different threshold.

For example, for a double segment selection, it can be requested that the highest bending muon satisfies the selection done by the 2 GeV $\Delta\phi$ threshold ($|\Delta\phi| < \Delta\phi_{2\,GeV}$), while the lowest bending muon satisfies the 5 GeV $\Delta\phi$ selection ($|\Delta\phi| < \Delta\phi_{5\,GeV}$).

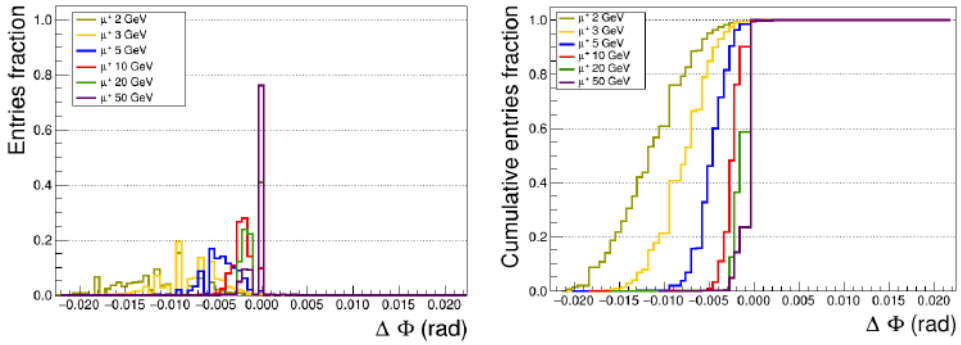

(a) (b)

Figure 4.7: (a) distribution of $\Delta\phi$ bending angle for different p_t positive muons in the positive endcap of CMS; (b) cumulative distribution of $\Delta\phi$ bending angle for different p_t positive muons in the positive endcap of CMS.

This selection allows improving the cut efficiency, keeping good events that could be otherwise rejected, in case the cut was performed requiring the same bending threshold on all the segments.

In particular, the description of the selection illustrated in the previous example is *doubleME0_2GeV_5GeV*, where the *2GeV* flag is the bending angle cut applied to the highest bending segment (lower p_t), while the last flag refers to the bending angle cut applied to the lowest bending segment (higher p_t). Similarly, for a triple segment selection, the description will be *tripleME0_2GeV_3GeV_5GeV*, where the middle one is the selection applied to the medium bending segment (medium p_t).

In this way, 21 and 56 cuts have been designed respectively for double and triple segment selections, from the number of combinations available.

4.5.1.2 Cut on quality

This cut has been designed to filter the ME0 segments available in an event, keeping those characterised by high quality and discarding the poor quality ones. This selection looks at the number of RecHits used to build the ME0 segment. Three threshold values have been set:

- *Quality 0*: segment built with ≥ 4 RecHits (the minimum to build the segment);
- *Quality 1*: segment built with ≥ 5 RecHits;
- *Quality 2*: segment built with ≥ 6 RecHits.

As illustrated in Fig. 4.8a, rejecting low quality segments allows rejecting a great part of ME0 segments produced by the background.

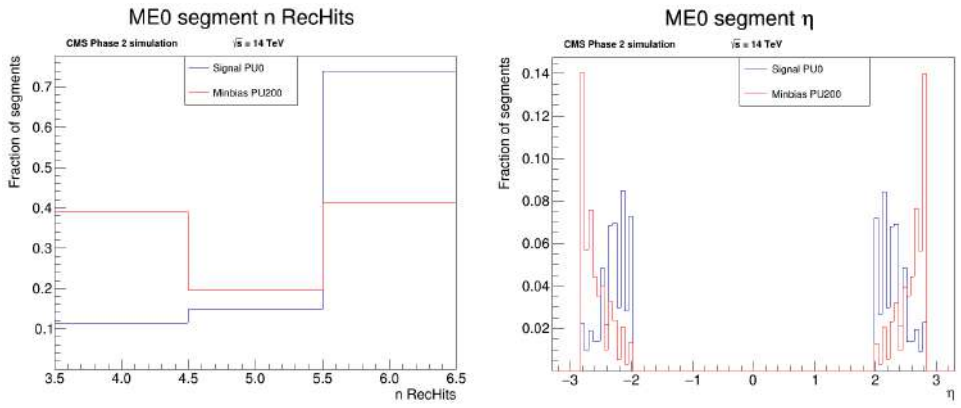

(a) (b)

Figure 4.8: (a) Number of RecHits used to build ME0 segments in signal and background samples; (b) ME0 segments η position in signal and background samples.

4.5.1.3 Cut on η position

A cut on the η position assigned to each segment has been designed to reduce the trigger rate, discarding the ME0 partitions placed in the highest η region, subjected to the highest flux of background particles (Fig. 4.8b). The selection is based on the segment origin point in the first ME0 layer and 4 thresholds have been set:

- *Veto 0*: accepts ME0 segments at every η;
- *Veto 1*: discards ME0 segments starting in the 8th η-partition;
- *Veto 2*: discards ME0 segments starting in the 7th and 8th η-partitions;
- *Veto 3*: discards ME0 segments starting in the 6th, 7th and 8th η-partitions;

The segmentation of ME0 η-partitions has been done such that each of them has a $\Delta\eta \sim 0.1$ coverage. The specific values of coverage for each η-partition is summarised in Tab. 4.3.

4.5.1.4 Cut on $\Delta\eta - \Delta\phi$ separation

This cut has been designed to provide a separation on ME0 segments, without grouping the information in the unique ΔR radius parameter illustrated in section 4.4.

To design this selection, the muons generated in the $\tau \to 3\mu$ decay have been matched to the corresponding ME0 segments, looking to the muon triplets which all lie in the ME0 acceptance. The information saved per each

η-partition	$\Delta\eta$ (rad)
1	0.100
2	0.113
3	0.100
4	0.112
5	0.100
6	0.112
7	0.103
8	0.115

Table 4.3: $\Delta\eta$ coverage of each ME0 η-partition.

of these events is the maximum $\Delta\eta$ separation among the segments and their maximum $\Delta\phi$ separation. From this, two plots have been built:

- the first representing the separation of the segments given by the position of the segments' point on the 1st ME0 layer (Fig. 4.9a);
- the second with the separation looking to the position of the segments' point on the 6th ME0 layer (Fig. 4.9b).

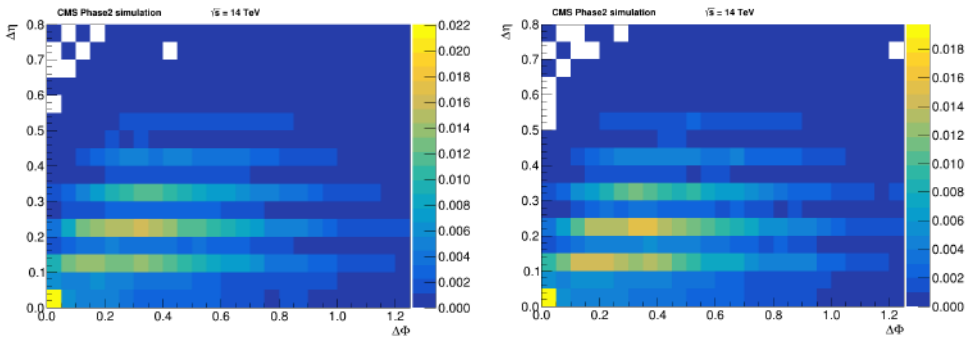

(a) (b)

Figure 4.9: Maximum $\Delta\eta - \Delta\phi$ separation among ME0 segments matched with $\tau \to 3\mu$ muons. The events plotted are those where all the three muons lied within the ME0 acceptance. In (a) and (b), the separations built looking to the ME0 segments points in the 1st and 6th layer are respectively represented.

On the other hand, the distributions of maximum $\Delta\eta - \Delta\phi$ separation for each triplet of ME0 segments for background events are reported, respectively for the 1st and 6th layers, in Fig. 4.10a and Fig. 4.10b, characterised by high $\Delta\phi$ values.

To select the area where most of the signal events concentrate, first of all, a bi-gaussian fit is performed on the signal plots, to determine the μ_x, μ_y, σ_x, σ_y and ρ. These parameters are the means and standard deviations along the

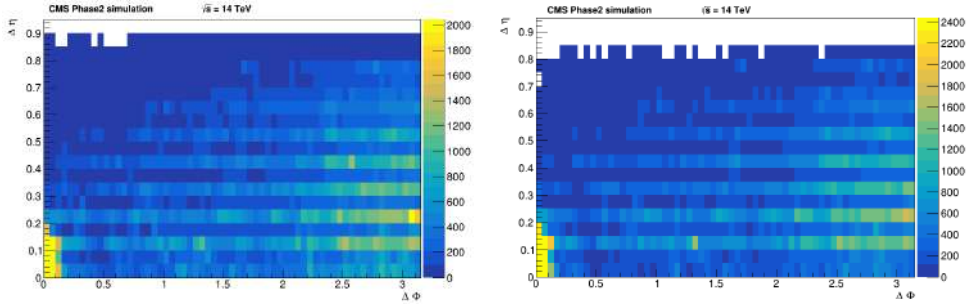

(a) (b)

Figure 4.10: Maximum $\Delta\eta - \Delta\phi$ separation for each triplet of ME0 segments for background events. The angular separations are determined looking to the η and ϕ positions of ME0 segments points in the 1st (a) and 6th ME0 layers (b).

Parameter	1st layer	6th layer
μ_x	0.295	0.307
μ_y	0.116	0.105
σ_x	0.343	0.352
σ_y	0.203	0.202
ρ	0.392	0.415

Table 4.4: Bi-gaussian fit parameters for $\Delta\eta - \Delta\phi$ segments separations seen in the 1st and 6th ME0 layer.

x-axis ($\Delta\phi$ separation) and y-axis ($\Delta\eta$ separation), while ρ is the correlation coefficient. The parameters obtained are reported in Tab. 4.4.

After this operation, the $\Delta\eta - \Delta\phi$ area of interest is enclosed in a concentration ellipses, which is defined by the points with coordinates (x,y) satisfying the following equation for a fixed Q value:

$$Q = \frac{1}{1-\rho^2}\left(\frac{(x-\mu_x)^2}{\sigma_x^2} - 2\rho\frac{(x-\mu_x)(y-\mu_y)}{\sigma_x\sigma_y} + \frac{(y-\mu_y)^2}{\sigma_y^2}\right), \tag{4.2}$$

where Q defines the percentage of events which are contained inside of the ellipses for bi-gaussian distributed random variables [101]. In this way, an event is accepted if its Q value is higher than the Q value which defines the concentration ellipses. In particular, 8 different Q values have been defined and their features are summarised in Tab. 4.5: the flag identifying this kind of cut is *ChiXX*, where XX is the percentage of events enclosed in the concentration ellipses for bi-gaussian distributed random variables. In Tab. 4.5 is also presented the flag *Chi100*, which represents the case where the separation cut is not activated to keep all the events.

Since a concentration ellipse has been produced both for separations given on the 1st and 6th ME0 layers, an event to be accepted has to be enclosed in

Cut flag	Q	Fraction
Chi100	-	100%
Chi95	6.16	95.4%
Chi68	2.30	68.3%
Chi39	1.00	39.0%
Chi20	0.446	20.0%
Chi10	0.211	10.0%
Chi05	0.103	5.0%
Chi02	0.0404	2.0%

Table 4.5: Features of the Q values which define the concentration ellipses, with the relative fraction of events enclosed inside of the ellipses for bi-gaussian distributed random variables.

both the ellipses.

4.5.1.5 Cut on ΔR radius

A different approach to determine the separation among muons is to calculate the angular radius ΔR illustrated in 4.4. In this case, 8 different ΔR radius ranges have been determined, according to the ratio between signal and background events accepted in a fixed ΔR radius range.

To optimise the determination of these ranges, the following scan operation has been performed:

- set the lower (ΔR_1) and upper (ΔR_2) bound to define a ΔR radius range;
- calculate the ratio S between the fraction of triplets of segments contained in the ΔR window $(\Delta R_1, \Delta R_2)$ for signal and background events

$$S = \frac{\int_{\Delta R_1}^{\Delta R_2} f_{sig}(x)\, dx}{\int_{\Delta R_1}^{\Delta R_2} f_{bkg}(x)\, dx}, \tag{4.3}$$

  where f_{sig} and f_{bkg} are the histograms describing the fraction of triplets contained in a certain ΔR radius interval, illustrated respectively in Fig. 4.11a and Fig. 4.11b. To define f_{sig} is indeed used the histogram which contains just one triplet for each event, provided by the match of segments with muons of the $\tau \to 3\mu$ decay. For the background case all the triplets combinations are considered;
- repeat the calculation varying the lower bound of the window and its width;
- select the ranges which obtained the highest ratio score S.

Cut flag	Lower edge (ΔR radius)	Upper edge (ΔR radius)
DeltaR0	-	-
DeltaR1	0.1	0.35
DeltaR2	0.2	0.45
DeltaR3	0.1	0.55
DeltaR4	0.2	0.65
DeltaR5	0.1	0.75
DeltaR6	0.3	0.55
DeltaR7	0.2	0.85

Table 4.6: ΔR radius cuts for the ME0 segments. The *DeltaR0* flag indicates the setting where the ΔR radius cut is not applied.

The ΔR radius distribution given by ME0 segments matched to muons produced by the $\tau \to 3\mu$ is illustrated in Fig. 4.11a, while the distributions obtained for each triplet of ME0 segments for signal and background events is illustrated in Fig. 4.11b : using the procedure illustrated above, the 7 ΔR radius ranges which obtained the highest ratio score S have been selected and their details are reported in Tab. 4.6.

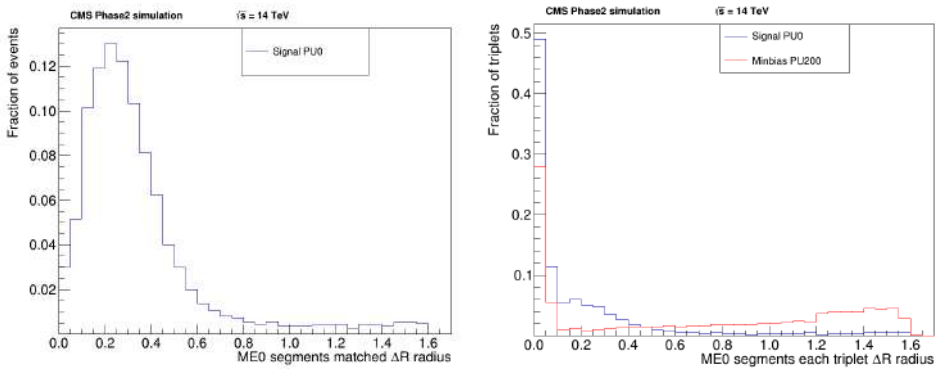

(a) (b)

Figure 4.11: (a) ΔR radius distribution for ME0 segments matched with muons produced by the $\tau \to 3\mu$ decay. (b) ΔR radius distribution for each triplet of ME0 segments for signal and background events.

4.5.2 CSCCorrelatedLCT of ME1/1 and ME2/1

The ME1/1 and ME2/1 cooperate respectively with GE1/1 and GE2/1 stations in building an object called *CSCCorrelatedLCT*, that uses the tracking informations given by the strips and wires of the 6 layers of CSC chambers and the information given by the two layers of GEM detectors used to return the hit GEM pad number. In particular, the information given by the

CSC chambers are produced in form of two Local Charged Tracks (LCTs), one for the cathode strips called CLCT (Cathode LCT) and one for the anode wires called ALCT (Anode LCT). This information is then joined in a Correlated LCT, which includes the GEM tracking information. The CSCCorrelatedLCT building algorithm assigns in particular two parameters used to define its position: the "key strip" and "key wire", both belonging to the 3rd CSC layer.

4.5.2.1 Cut on the $\Delta\phi$ bending angle

The cut on the $\Delta\phi$ bending angle for GE1/1 and GE2/1 is calculated making the difference between the ϕ positions of:

- the pad hit in the first GEM layer;
- the position of the key point of the LCT, placed in the 3rd CSC layer and given by the intersection between the "key wire" and "key strip".

In this case, it was not possible to put an indicative flag on the p_t of the muon which generated the LCT because the bending distributions for different muon p_t values showed a too high overlapping. In this case, the cuts were extracted directly from the bending distribution of CSCCorrelatedLCTs for ME1/1 and ME2/1 stations obtained from the signal sample, which are illustrated in Fig. 4.12. The $\Delta\phi$ threshold values are illustrated in Tab. 4.7.

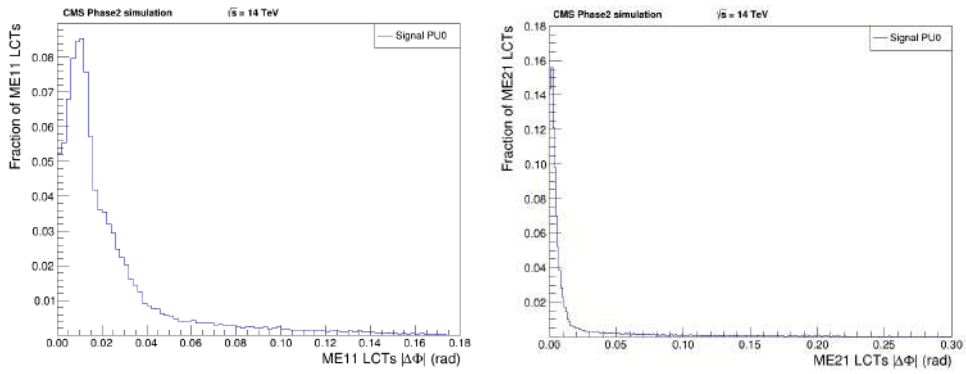

(a) (b)

Figure 4.12: $|\Delta\phi|$ bending angle calculated for ME1/1 (a) and ME2/1 (b) CSCCorrelatedLCTs. The tails at high bending angles comes from an erroneous assignment of the GEM pad by the reconstruction algorithm.

Similarly to what was done for ME0 segments, also for ME1/1 and ME2/1 CSCCorrelatedLCTs an asymmetric bending angle cut structure has been set, with single, double and triple LCTs selections, each with respectively 6, 21 and 56 cut options on the bending angle. Also in this case, the LCT with the highest bending is put in the first position of the selection description, followed by the medium and lowest bending $|\Delta\phi|$.

Cut flag	ME1/1 $\Delta\phi_{thr}$ (rad)	ME2/1 $\Delta\phi_{thr}$ (rad)
PhiCut_1	0.062	0.115
PhiCut_2	0.038	0.012
PhiCut_3	0.022	0.006
PhiCut_4	0.016	0.0036
PhiCut_5	0.012	0.0024
PhiCut_6	0.008	0.0012

Table 4.7: $\Delta\phi$ bending thresholds set for ME1/1 and ME2/1 CSCCorrelatedLCTs.

4.5.2.2 Cut on quality

Similarly to what was done for ME0, also for ME1/1 and ME2/1 CSCCorrelatedLCTs a cut on the object quality has been set. The quality thresholds have been set looking to the quality distributions, trying to reduce the contribution of the background, consisting mainly of objects with lower quality with respect to those defining the signal, as illustrated in Fig. 4.13a. The quality thresholds are summarised in Tab. 4.8.

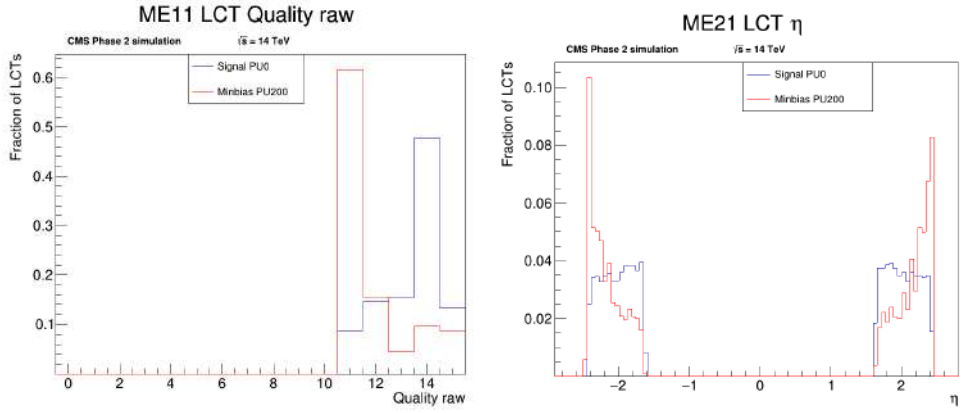

(a) (b)

Figure 4.13: (a) quality of CSCCorrelatedLCTs from ME1/1 station; (b) η position of CSCCorrelatedLCTs from ME2/1 station.

4.5.2.3 Cut on η position

For ME1/1 and ME2/1 CSCCorrelatedLCTs, five different cuts on the η position of the object have been defined: the position taken to perform the selection is that given by the intersection of "key strip" and "key wire" in the 3rd CSC layer. As for ME0 segments, the strategy of rejecting segments formed in the highest η covered by the detector allows rejecting a good num-

Cut flag	Quality threshold
Quality0	-
Quality1	≥ 7
Quality2	≥ 12

Table 4.8: Quality thresholds adopted for ME1/1 and ME2/1 CSCCorrelatedLCTs. *Quality0* is the flag when no quality cut is applied. *Quality1* gives only a minimal contribution, but it has been defined anyway to try to keep the highest possible fraction of signal events. The specific description of the meaning of the different quality codes is reported in [102].

Cut flag	LCTs rejected η
Veto0	-
Veto1	≥ 2.2875
Veto2	≥ 2.1750
Veto3	≥ 2.0625
Veto4	≥ 1.9500

Table 4.9: Cuts applied on LCT η position: the table reports the values which are rejected by each selection. The *Veto0* is the flag when no selection is applied.

ber of LCTs generated by background events (Fig. 4.13b), contributing in this way to a reduction of the trigger rate. The details on cuts are illustrated in Tab. 4.9.

4.5.2.4 Cut on $\Delta\eta - \Delta\phi$ separation

As for ME0 segments (section 4.5.1.4), concentration ellipses have been defined also for ME1/1 and ME2/1 LCTs. The distributions of $\Delta\eta - \Delta\phi$ separations are illustrated in Fig. 4.14, while the bi-gaussian fit parameters are reported in Tab. 4.10. On the other hand, the separation distributions given by the background are reported in Fig. 4.15, showing a clear difference respect to the signal ones.

Parameter	ME1/1 LCTs	ME2/1 LCTs
μ_x	0.213	0.551
μ_y	-0.013	0.429
σ_x	0.513	0.077
σ_y	0.213	0.185
ρ	0.426	0.411

Table 4.10: Bi-gaussian fit parameters for $\Delta\eta - \Delta\phi$ LCTs separations seen in the ME1/1 and ME2/1 stations.

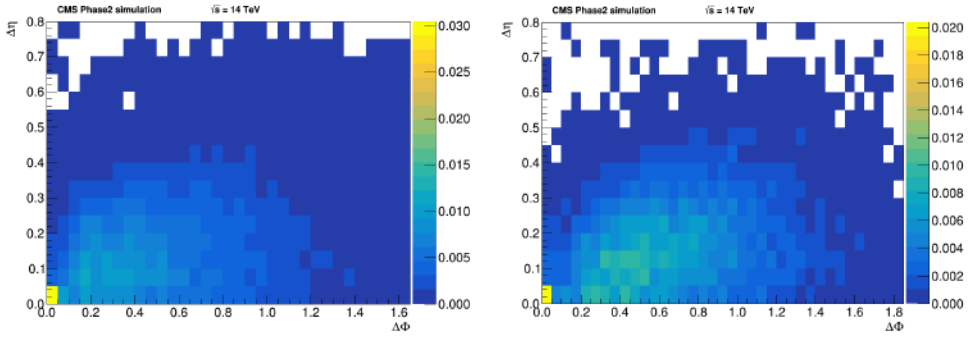

(a) (b)

Figure 4.14: Maximum $\Delta\eta - \Delta\phi$ separation among ME1/1 (a) and ME2/1 (b) CSCCorrelatedLCTs matched with $\tau \rightarrow 3\mu$ muons. The events plotted are those where all the three muons lied in the stations acceptance. The angular separations are determined looking to the η and ϕ positions of points given by the intersection of key LCT strips and wires in the 3rd CSC layer.

The Q values used to set the concentration ellipses are the same illustrated in Tab. 4.5, but, in this case, only one ellipse per station is built, using the position of LCTs in the 3rd CSC layer. This is due to the fact that the η position of the LCT in a GEM layer is not available, since only the azimuthal pad number is provided.

4.5.2.5 Cut on ΔR radius

The window method illustrated in section 4.5.1.5 has been used also to determine the ΔR radius ranges for cuts on ME1/1 and ME2/1 LCTs. In this case, the parameters used are reported in Tab. 4.11 and Tab. 4.12, while the ΔR radius distributions for ME1/1 and ME2/1 LCTs are illustrated in Fig. 4.16. On the other hand, the distributions of ΔR radius for each triplet of objects for signal and background events are reported in Fig. 4.17, showing their clear separation.

4.5.2.6 Cut on diffDR

An additional parameter has been introduced for ME1/1 and ME2/1 LCTs to be sure to get rid of possible LCT duplicates, called *diffDR*. In the version of CMSSW used indeed it was possible to check for ME0 segment duplicates, checking the position of the RecHits used to build the segment, but this possibility was not yet available for ME1/1 and ME2/1 LCTs. It was so chosen to get rid of duplicates dropping LCTs closer than a fixed ΔR : the *diffDR* investigated values have been 0.001, 0.01, 0.04, 0.07 and 0.10.

Cut flag	Lower edge (ΔR radius)	Upper edge (ΔR radius)
DeltaR0	-	-
DeltaR1	0.0	0.25
DeltaR2	0.1	0.35
DeltaR3	0.0	0.45
DeltaR4	0.1	0.55
DeltaR5	0.2	0.45
DeltaR6	0.0	0.65
DeltaR7	0.1	0.75

Table 4.11: ΔR radius cuts for the ME11 LCTs. The *DeltaR0* flag indicates the setting where the ΔR radius cut is not applied.

Cut flag	Lower edge (ΔR radius)	Upper edge (ΔR radius)
DeltaR0	-	-
DeltaR1	0.0	0.25
DeltaR2	0.1	0.35
DeltaR3	0.0	0.45
DeltaR4	0.2	0.45
DeltaR5	0.1	0.55
DeltaR6	0.0	0.65
DeltaR7	0.3	0.55

Table 4.12: ΔR radius cuts for the ME21 LCTs. The *DeltaR0* flag indicates the setting where the ΔR radius cut is not applied.

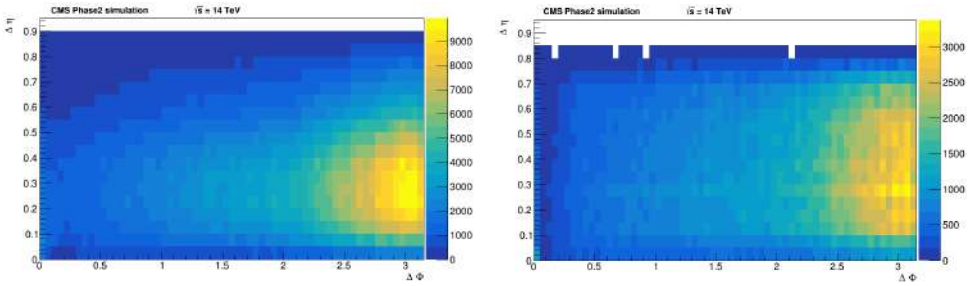

(a) (b)

Figure 4.15: Maximum $\Delta\eta - \Delta\phi$ separation for each triplet of ME1/1 (a) and ME2/1 (b) CSCCorrelatedLCTs for background events. The angular separations are determined looking to the η and ϕ positions of points given by the intersection of key LCT strips and wires in the 3rd CSC layer.

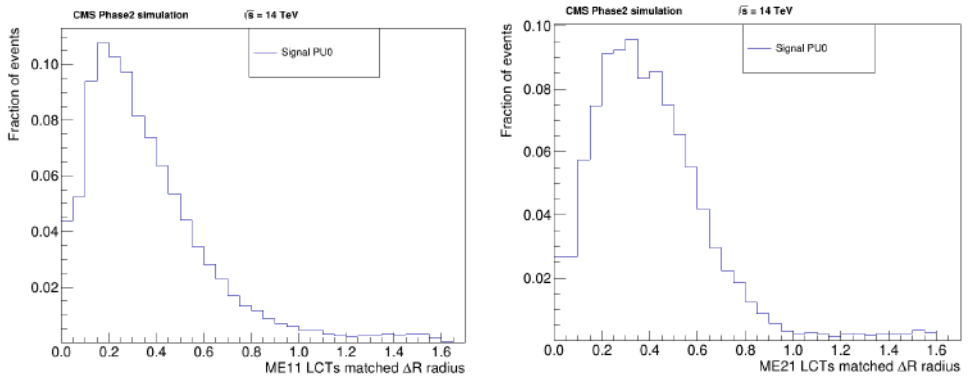

(a) (b)

Figure 4.16: ΔR radius distribution for ME1/1 (a) and ME2/1 (b) LCTs matched with muons produced by the tau decay.

4.5.3 EMTF tracks

The Endcap Muon Track Finder (EMTF) builds tracks joining the information coming from the different muon stations installed in the CMS endcap. This large amount of information allows reconstructing a complete muon track in the endcap of the muon spectrometer and from its curvature provides a measurement of its p_t and its charge. The EMTF track parameters used in this study, and described in the next sections, are the track p_t, charge, quality and separation.

4.5.3.1 Cut on p_t

A representation of the EMTF track p_t distribution, for the signal sample and the minimum bias one, is provided in Fig. 4.18a, where it can be noticed that the greatest part of background contribution is in the low p_t region. In this

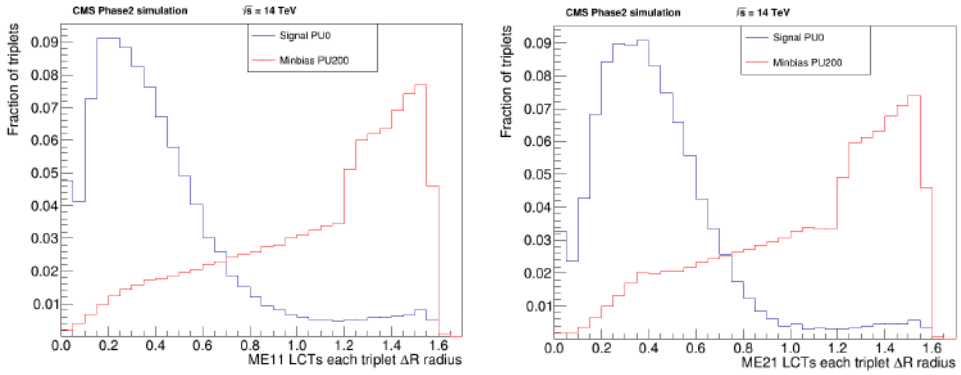

(a) (b)

Figure 4.17: ΔR radius distribution for each triplet of ME1/1 (a) and ME2/1 (b) LCTs for signal and background events.

study the structure for the cut on EMTF track p_t has been modelled using the structure made for the ME0 segments $\Delta\phi$ bending angle cut (section 4.5.1.1) and, for this reason, the chosen p_t thresholds are 2, 3, 5, 10, 20 and 50 GeV.

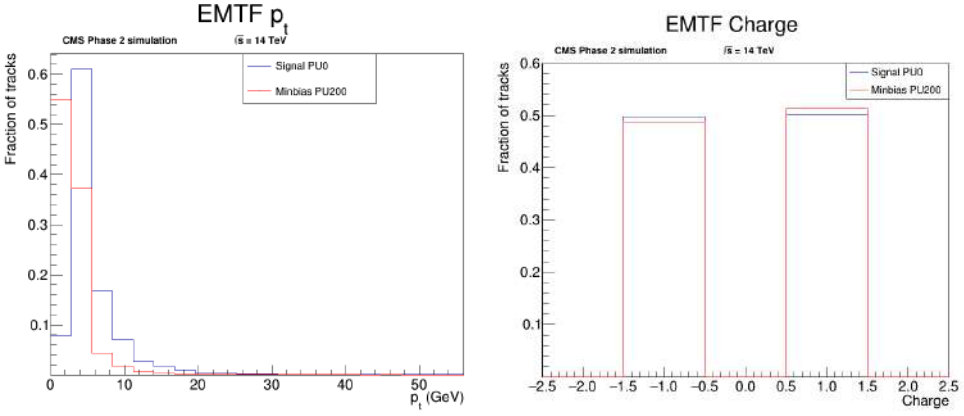

(a) (b)

Figure 4.18: (a) p_t distribution of EMTF tracks; (b) Charge distribution of EMTF tracks.

In this way, a path describing a selection on a triplet of EMTF tracks puts three different p_t thresholds on the leading, medium and trailing p_t tracks. To pass the selection an event must have at least one triplet of tracks overcoming at the same time all the three p_t thresholds. For example, if the p_t cut description is *2GeV_3GeV_5GeV*, an event must have at least one triplet of tracks with the trailing p_t track with $p_t > 2\,GeV$, the medium-p_t one with $p_t > 3\,GeV$ and the leading-p_t one with $p_t > 5\,GeV$.

4.5.3.2 Cut on charge

From the bending of the track, the EMTF assigns a charge value to the tracks. In this study, a selection on charge has been designed to identify if in an event there is at least one triplet of tracks which ensures the charge conservation to belong to a $\tau \to 3\mu$ decay event. Here are listed the name of the charge cuts applied to a triplet of EMTF tracks, with the requirement asked to pass the selection and be accepted:

- *Charge 0*: no selection on charge;
- *Charge 1*: at least 2 tracks with an opposite sign;
- *Charge 2*: $|\sum_{i=1}^{3} Q_i| = 1$, where the Q_i is the charge of the i-th track. This ensures that the triplet conserves the charge in τ^+ or τ^- decay;
- *Charge 3*: 2 tracks with charge $Q = -1$ and 1 track with charge $Q = +1$, compatible with the decay of a τ^- lepton;
- *Charge 4*: 1 track with charge $Q = -1$ and 2 tracks with charge $Q = +1$, compatible with the decay of a τ^+ lepton.

A different charge selection has been designed in case only one or two EMTF tracks are involved. In this case, the cut cannot be used for a check on the charge conservation, but just to try to identify a suitable charge selection with a low enough trigger rate. The charge cuts implemented for selections involving two EMTF tracks are:

- *Charge 0*: no selection on charge;
- *Charge 1*: 2 tracks with charge $Q = +1$;
- *Charge 2*: 1 track with charge $Q = +1$ and 1 track with charge $Q = -1$;
- *Charge 3*: 2 tracks with charge $Q = -1$;

Finally in case of selections containing just one EMTF track, the designed cuts are:

- *Charge 0*: no selection on charge;
- *Charge 1*: 1 track with charge $Q = +1$;
- *Charge 2*: 1 track with charge $Q = -1$;

Cut flag	Quality threshold
Quality0	-
Quality1	≥ 9
Quality2	≥ 14

Table 4.13: Features of quality cuts used for EMTF tracks. The *Quality0* flag indicates the setting where the quality cut is not applied.

4.5.3.3 Cut on quality

The reconstruction algorithm assigns to each track a score from 0 to 15, defining a track quality in an increasing way. From this, three different quality thresholds have been defined, trying to minimize the contribution of background tracks, and their definition is reported in Tab. 4.13, while in Fig. 4.19a a comparison between the quality of tracks observed in signal and background is shown.

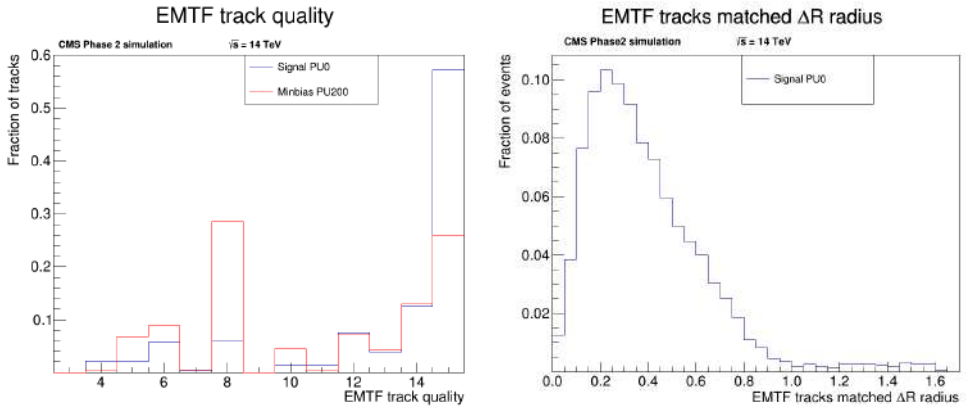

(a) (b)

Figure 4.19: (a) Quality of EMTF tracks for signal and background events; (b) ΔR radius distribution for EMTF tracks matched with muons produced by the tau decay.

4.5.3.4 Cut on ΔR radius

A cut on the mutual distance of EMTF tracks has been made only using the ΔR radius method (Fig. 4.19b): 8 ΔR ranges have been identified using the same strategy illustrated in section 4.5.1.5, by identifying the ΔR ranges with the highest contribution from signal and the lowest from background events. The distributions of ΔR radius for each triplet of EMTF tracks for signal and background events are reported in Fig. 4.20, showing their clear separation, while detailed description of the parameters of each selected ΔR radius range is illustrated in Tab. 4.14.

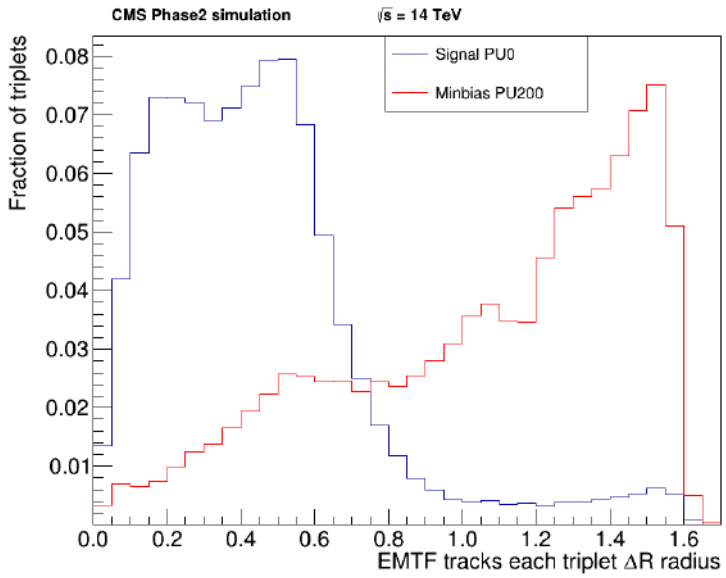

Figure 4.20: ΔR radius distribution for each triplet of EMTF tracks for signal and background events.

4.5.3.5 Selection categories involving EMTF tracks

In the case of selections involving at least one EMTF track, several categories of selections were investigated, all based on objects triplets. The triplets in the different categories involved EMTF tracks, ME0 segments and CSCCorrelatedLCTs from stations ME1/1 and ME2/1. The description of these categories is reported in detail in Tab. 4.15.

When different objects are used it must be taken into account that they could have been used in the track building or that two segments could be generated by the same particle. To avoid double counting cases, a check on the ΔR separation among the objects has been introduced: similarly to what

Cut flag	Lower edge (ΔR radius)	Upper edge (ΔR radius)
DeltaR0	-	-
DeltaR1	0.0	0.25
DeltaR2	0.1	0.35
DeltaR3	0.0	0.45
DeltaR4	0.2	0.45
DeltaR5	0.1	0.55
DeltaR6	0.0	0.65
DeltaR7	0.2	0.65

Table 4.14: ΔR radius cuts for the EMTF tracks. The *DeltaR0* flag indicates the setting where the ΔR radius cut is not applied.

Category name	Objects used
tripleEMTF	3 EMTF tracks
doubleEMTFsingleME11	2 EMTF tracks, 1 ME1/1 CSCCorrelatedLCT
doubleEMTFsingleME21	2 EMTF tracks, 1 ME2/1 CSCCorrelatedLCT
doubleEMTFsingleME0	2 EMTF tracks, 1 ME0 segment
doubleEMTFsingleStub	2 EMTF tracks and 1 other object (1 ME0 segment OR 1 ME1/1 CSCCorrelatedLCT OR 1 ME2/1 CSCCorrelatedLCT)
singleEMTFdoubleME11	1 EMTF track, 2 ME1/1 CSCCorrelatedLCTs
singleEMTFdoubleME21	1 EMTF track, 2 ME2/1 CSCCorrelatedLCTs
singleEMTFdoubleME0	1 EMTF track, 2 ME0 segments
singleEMTFsingleME0singleME11	1 EMTF track, 1 ME0 segment, 1 ME1/1 CSCCorrelatedLCT
singleEMTFsingleME0singleME21	1 EMTF track, 1 ME0 segment, 1 ME2/1 CSCCorrelatedLCT
singleEMTFsingleME11singleME21	1 EMTF track, 2 CSCCorrelatedLCTs (1 from ME1/1, 1 from ME2/1)

Table 4.15: Categories involving EMTF tracks. All of them require three input objects and their description is provided in the second column.

illustrated in section 4.5.2.6, the variable used is called *diffDR* and the same logic is applied. This check was not implemented for ME0 objects, since at the development and samples production time, ME0 was not yet fully integrated into EMTF.

4.5.4 TkMuons

The tracker muons (TkMuons) are objects produced by the CMS tracker: they are produced by an algorithm that checks for Tracker Tracks which have a compatible signature in the calorimeters and in the muon system. This kind of object is particularly useful for low p_t muons (in the order of few GeV), which could leave a too low number of hits in the muon system for a standalone muon reconstruction.

4.5.4.1 Cut on p_t

For TkMuons a selection based on p_t has been built with the same structure adopted for EMTF tracks and using the same p_t thresholds: 2 GeV, 3 GeV, 5 GeV, 10 GeV, 20 GeV and 50 GeV. As in the EMTF track description, also in this case in the labelling convention the first label states the p_t cut used on the trailing muon, the second for the medium p_t muon and the last one for the leading p_t muon. Fig. 4.21a shows the p_t of tracker muons observed in a signal and in a background sample: as expected the background muons

Cut flag	Lower edge (Reduced χ^2)	Upper edge (Reduced χ^2)	Fraction signal tracks (%)
Quality0	-	-	100%
Quality1	0.0	2.64	94.0%
Quality2	0.24	1.20	67.6%

Table 4.16: Reduced χ^2 cuts used for the TkMuons. The *Quality0* flag indicates the setting where the reduced χ^2 cut is not applied. In the last column, the fraction of TkMuons included in the selection range is reported.

concentrate in the low p_t region, near to the signal p_t muons.

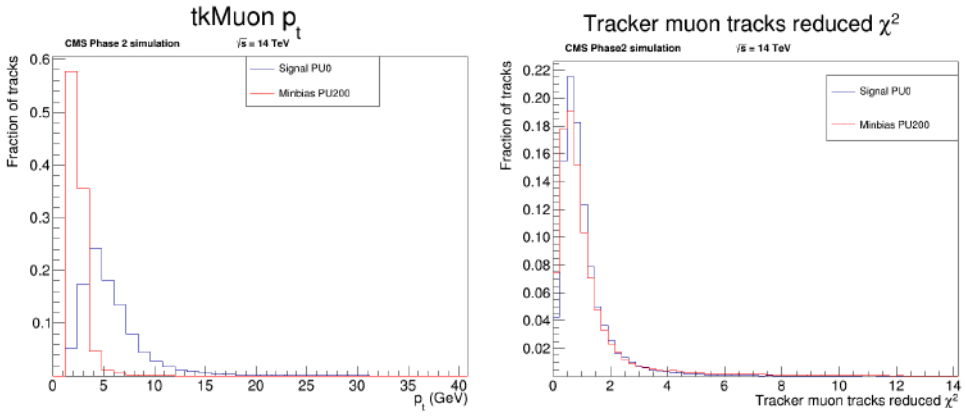

(a) (b)

Figure 4.21: (a) p_t distribution of TkMuons; (b) Reduced χ^2 distribution of TkMuons.

As in the previous cases, an accepted event has to show at least three TkMuons which overcome the p_t thresholds set for the trailing, medium and leading p_t muons.

4.5.4.2 Cut on reduced χ^2

To provide a quality-like selection also for TkMuons, it has been chosen to look at their reduced χ^2, (Fig. 4.21b). The distribution, in this case, is not very discriminating between signal and background, but three flags have been set anyway, as shown in Tab. 4.16: the fraction of TkMuons accepted is reported in the 3rd column of the table.

4.5.4.3 Cut on charge

Similarly to what has been done for EMTF tracks, a check on the charge conservation has been designed also for selections involving triplets of TkMuons.

Cut flag	Description
Charge0	No curvature selection applied
Charge1	Triplets containing 2 TkMuons with opposite sign
Charge2	TkMuons triplets with 2 positive and 1 negative curvatures $1/r$ OR with 1 positive and 2 negative curvatures $1/r$
Charge3	TkMuons triplets with 2 negative and 1 positive curvatures $1/r$
Charge4	TkMuons triplets with 2 positive and 1 negative curvatures $1/r$

Table 4.17: Features of cuts on curvature $1/r$ used for TkMuons. The *Charge0* flag indicates the setting where the cut is not applied.

Cut flag	Threshold on z-POCA (cm)	Fraction signal tracks (%)
Vtx0	-	100%
Vtx1	0.30	95.4%
Vtx2	1.75	68.3%

Table 4.18: Cuts on the z-coordinate of POCA of TkMuons. To be used, a TkMuon has to present a POCA with $|z|$ higher than the threshold illustrated in the second column ($|z_{POCA}| > z_{threshold}$).

In this case, the charge is not directly accessible, so the sign of the track curvature (called $1/r$) has been exploited, this last being linked to the sign of the particle. From this, 5 different selection flags have been defined, and their description is provided in Tab. 4.17.

4.5.4.4 Cut on POCA (Point Of Closest Approach) position

In each TkMuon track, its closest point to the interaction point, called Point Of Closest Approach (POCA), can be identified. In the available samples, only its z coordinate was available, while the x and y coordinates were not yet filled. From this, a comparison between the position of POCA z coordinate for signal and background events has been made, as illustrated in Fig. 4.22a. The distributions are not really discriminant between signal and background, but they can anyway be used to scale down the number of selected events. As illustrated in Tab. 4.18, these cuts have been designed to reject the central part of the distribution, where the highest variation among signal and background can be observed. In this way, only the TkMuons with $|z_{POCA}| > z_{threshold}$ are selected.

4.5.4.5 Cut on ΔR radius

As for the objects illustrated in the previous sections, also for TkMuons a selection on their mutual distance has been set, identifying 7 different ranges of ΔR radius values which maximize the contribution of signal TkMuons and

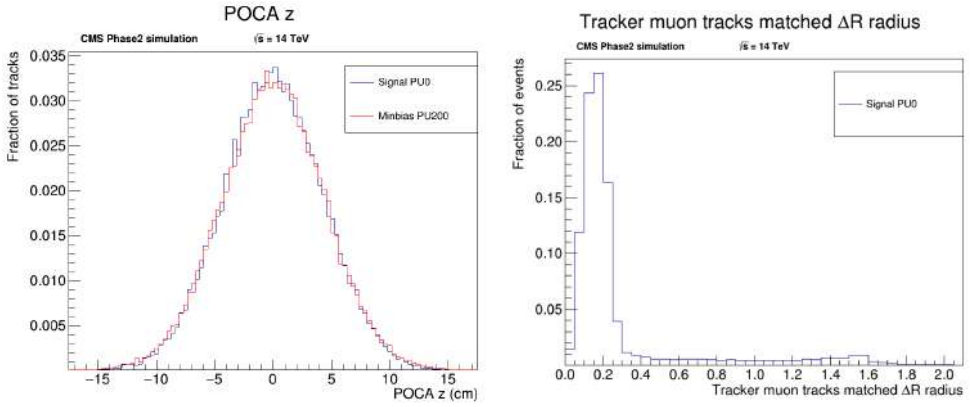

(a) (b)

Figure 4.22: (a) Distribution of POCA z coordinate for TkMuons; (b) ΔR radius distribution for TkMuons matched with muons produced by the τ decay.

Cut flag	Lower edge (ΔR radius)	Upper edge (ΔR radius)
DeltaR0	-	-
DeltaR1	0.0	0.25
DeltaR2	0.1	0.35
DeltaR3	0.0	0.45
DeltaR4	0.1	0.55
DeltaR5	0.0	0.65
DeltaR6	0.2	0.45
DeltaR7	0.1	0.75

Table 4.19: ΔR radius cuts used for the TkMuons. The *DeltaR0* flag indicates the setting where the ΔR radius cut is not applied.

minimize the contribution of background ones. The thresholds are reported in Tab. 4.19, while the distribution of signal radii is illustrated in Fig. 4.22b. Finally, the distributions of ΔR radius for each triplet of TkMuons for signal and background events are reported in Fig. 4.23, showing the clear separation among them.

4.5.4.6 Cut on invariant mass

The last cut implemented on TkMuons is that on the invariant mass of a triplet of muons: in this context, the objective is to select events that contain a triplet of TkMuons forming an invariant mass compatible with that of the τ lepton (1.776 GeV). The invariant mass $m_{\mu\mu\mu}$ is computed summing the

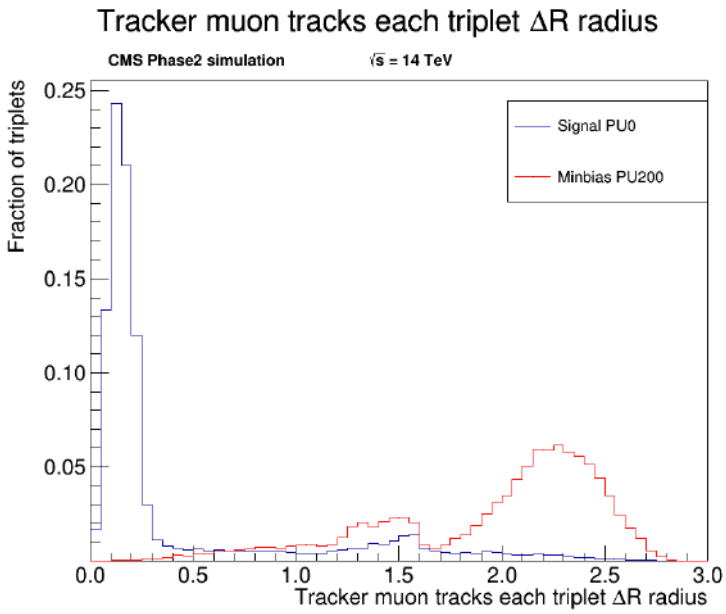

Figure 4.23: ΔR radius distribution for each triplet of TkMuons for signal and background events.

Cut flag	Lower $m_{\mu\mu\mu}$ edge (GeV)	Upper $m_{\mu\mu\mu}$ edge (GeV)
Mass0	-	-
Mass1	1.67	1.83
Mass2	1.20	1.90

Table 4.20: Invariant mass $m_{\mu\mu\mu}$ cuts used for the TkMuons. The *Mass0* flag indicates the setting where the cut is not applied.

Lorentz vectors defined for the three TkMuons:

$$m_{\mu\mu\mu} = \sqrt{\left(\sum_{i=1}^{3} E_i\right)^2 - \|\sum_{i=1}^{3} \mathbf{p}_i\|^2}, \tag{4.4}$$

where all E_i and $\mathbf{p}_i$ are respectively the i-th muon energy and momentum expressed in GeV.

Two mass cuts have been set, identifying two invariant mass ranges which maximize the contribution of signal events and minimize the contribution of background ones. To choose the best mass ranges, the same method used to identify the ΔR radius ranges has been used (section 4.5.1.5), computing the ratio of the fraction of triplets accepted in each mass range. The chosen mass ranges are reported in Tab. 4.20.

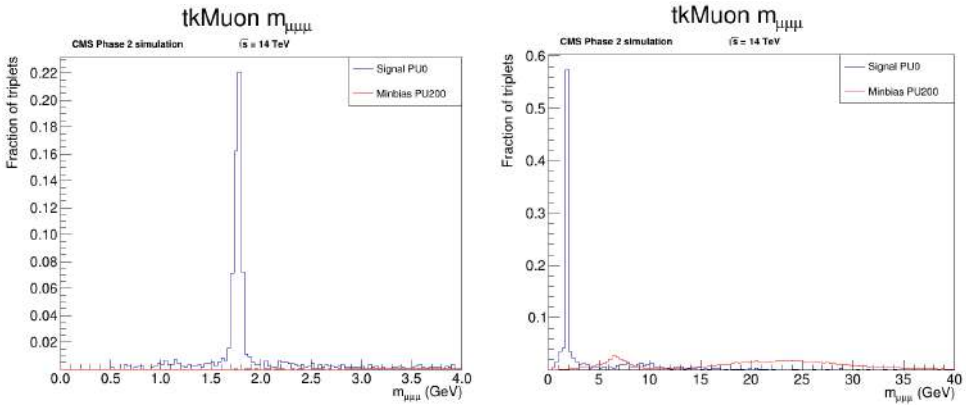

(a) (b)

Figure 4.24: TkMuon invariant mass obtained from signal and background TkMuon triplets, zooming on the τ mass range (a) and looking the whole mass range (b). As can be noticed, in the background distribution, the peak typical of the $\tau \to 3\mu$ decay is absent and the distribution is well separated from it. The shape of the background is determined by the combinatorics of TkMuon objects.

4.6 Efficiency and rate results

For each selection presented in the previous sections trigger efficiency and rate have been computed, to understand if they represent a potentially interesting selection path. The environment used to produce this result is that provided by the CMSSW_11_1_3 version, reprocessing the samples according to the recipe presented in [103].

The trigger signal efficiency has been calculated running on a fixed PU signal sample, using the Wilson formula [101],

$$\epsilon = \frac{f + \frac{t^2}{2n}}{\frac{t^2}{n} + 1} \pm \frac{t\sqrt{\frac{t^2}{4n^2} + \frac{f(1-f)}{n}}}{\frac{t^2}{n} + 1}, \tag{4.5}$$

with $t = 1$ indicating the parameter to define the 1σ distribution quantile, which for $n >> 1$ converge to the gaussian ones. In this equation $f = x/n$, where x is the number of events accepted by a fixed trigger selection and n is the total number of events considered (in this case the number of events in the dataset with one $\tau \to 3\mu$ decay).

On the other hand, the trigger rate of a selection has been calculated running on a minimum bias dataset which has the same pileup condition found in the signal sample, used to determine the signal efficiency of the considered selection. The trigger rate and its error are again calculated using the Wilson formula to determine the fraction of accepted events and multiplying it by 31.039 MHz. This last value is indeed the average collision rate that is obtained

multiplying the number of bunches used in the filling scheme of the LHC (2760), by the LHC orbit rate 11.246 kHz.

The numerous combinations of cuts investigated, involving different object combinations, range from a few hundred Hz to several MHz, In Fig. 4.25 is illustrated the span in efficiency and rate, for implemented selections involving 3 TkMuons, where each point represents the trigger rate and efficiency obtained for a different selection.

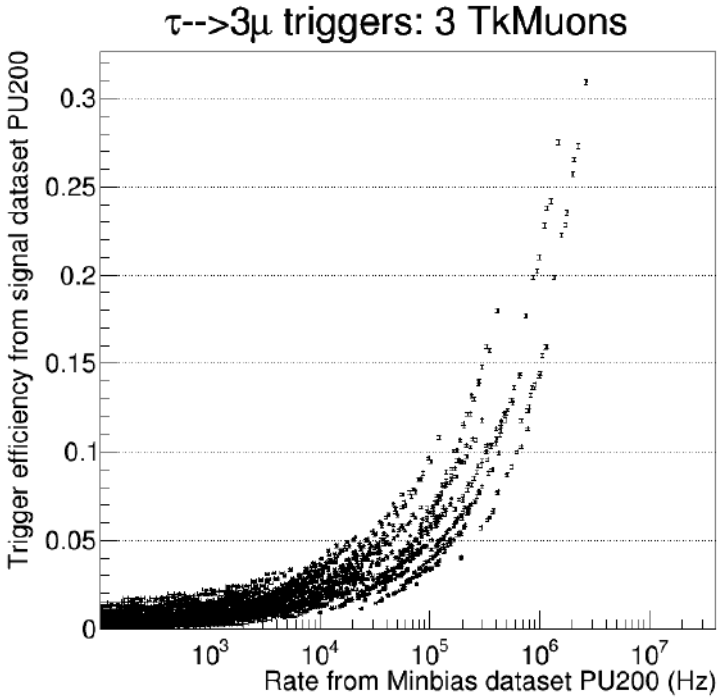

Figure 4.25: Trigger rate and efficiency obtained for selections using 3 TkMuons at $PU = 200$. Each point represents the trigger rate and efficiency for a different selection.

Since a single trigger path is not authorised to use too much bandwidth of the trigger system, to allow the implementation of many algorithms in the menu, it is common practice to develop triggers whose rate is of the order of few kHz (< 10 kHz). In this optic, in the following sections only this kind of results will be illustrated, being the most profitable ones.

4.6.1 Visualization of results

The most handful way to visualize data is to display the variation of cuts one by one, looking at the corresponding obtained rate and efficiency. For example, this strategy is illustrated in Fig. 4.26, where the selections involving 3 EMTF tracks with a fixed cut on ΔR radius range and varying p_t, quality and charge cuts are reported.

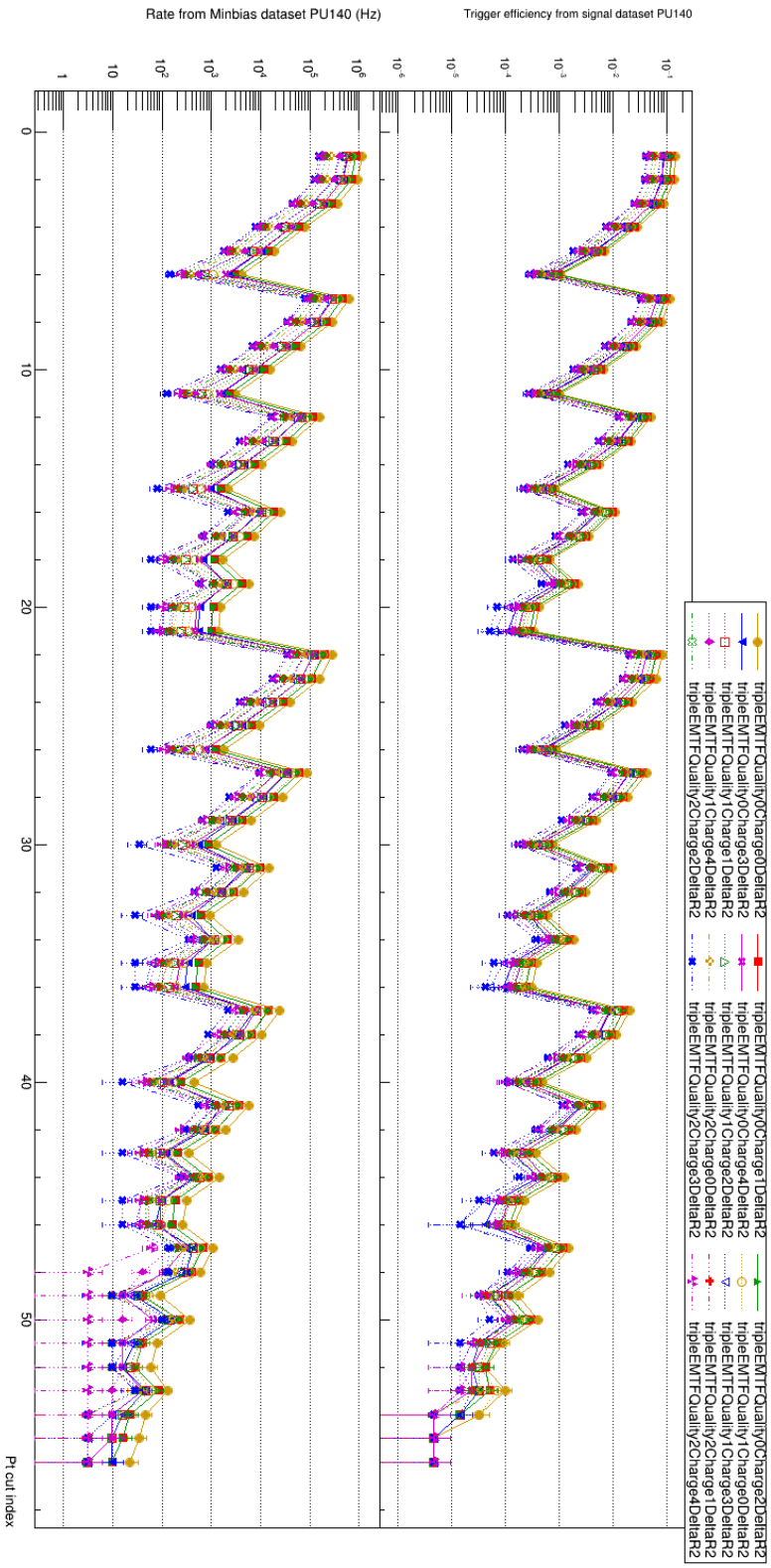

Figure 4.26: Triple EMTF selections with fixed ΔR radius flag *DeltaR2,* and different p_t, quality and charge cuts. On the x-axis is reported an index which corresponds to a particular combination of p_t cuts, explained in Tab. A.1.

This kind of visualization is effective to scan the variation of parameters one by one but allows to show only a limited amount of results. For this reason, it has been chosen to have visualizations providing only the maximum efficiency selection in a fixed trigger rate range. In particular, the following results will be presented:

- a summary of the results for each of the analysed categories, in the rate region $R < 10\,\text{kHz}$;
- a summary of the results obtained for the three selection categories with the highest efficiency in the rate region $R < 10\,\text{kHz}$;
- a summary of the results obtained in general in the rate region $R < 10\,\text{kHz}$.

4.6.2 Summary of results for each category

For each category two different kinds of data can be presented:

- the results obtained in a fixed PU condition for different *diffDR* values (the *diffDR* parameter was implemented not for all the categories);
- the results obtained with a fixed *diffDR* parameter value varying the PU condition.

In the following plots are reported in particular the maximum number of triggerable signal events for each category in the rate region $R < 10\,\text{kHz}$, with their respective trigger rate. This number is obtained by multiplying the signal efficiency for the number of events expected in an integrated luminosity $\int \mathcal{L}\,dt = 3000\,\text{fb}^{-1}$ for $\mathcal{B}(\tau \to 3\mu) = 2.1 \cdot 10^{-8}$, which is equal to $1.22 \cdot 10^5$, as explained in section 4.2.

Fixed PU condition, variation of *diffDR* parameter. Fig. 4.27 shows the results obtained for $PU = 200$ varying the *diffDR* parameter, that has been implemented not for all the categories reported in the plot. The categories where this parameter does not act are *tripleME0* (using 3 ME0 segments), *tripleEMTF* (3 EMTF tracks), *tripleTK* (3 TkMuons), *doubleEMTFsingleME0* (2 EMTF tracks and 1 ME0 segment) and *singleEMTFdoubleME0* (1 EMTF track and 2 ME0 segments) (section 4.5.3.5). In particular, it can be observed that the categories collecting the highest number of events are *tripleTK*, *doubleEMTFsingleME0* and *singleEMTFdoubleME0*. The presence of ME0 in these three categories is indeed significant, since ME0 is the most forward installed station, pointing out as the extension of the CMS acceptance offered by ME0 plays a significant role in the detection of the $\tau \to 3\mu$ channel. In particular, for these three categories, the *diffDR* has not been implemented, but indeed this parameter has not a very big impact in terms of signal efficiency neither in the other categories.

Fixed *diffDR* parameter, variation of PU condition. Fig. 4.28 shows the results obtained for each category for pileup conditions $PU = 140$ and $PU = 200$, and with *diffDR* set to 0.001. Also in this case, it can be noticed as the most profiting categories are *tripleTK*, *doubleEMTFsingleME0* and *singleEMTFdoubleME0*.

4.6.3 Summary of results for three most profitable categories

As mentioned before, the categories able to collect the highest number of events in the trigger rate region $R < 10\,\text{kHz}$ are *tripleTK*, *doubleEMTFsingleME0* and *singleEMTFdoubleME0*. In this section, the results obtained for these three categories will be illustrated, dividing the 10 kHz rate region in 500 Hz slices and reporting for each of them the selection with the highest signal efficiency (highest number of triggerable signal events).

- **Results for category singleEMTFdoubleME0:** in Fig. 4.29 the signal efficiency and number of triggerable signal events obtained for the selections belonging to the category *singleEMTFdoubleME0*, for each 500 Hz slice in the trigger rate region $R < 10\,\text{kHz}$ are respectively reported. All the details on selections are illustrated in Tab. A.2 for $PU = 140$ and in Tab. A.3 for $PU = 200$.

- **Results for category doubleEMTFsingleME0:** in Fig. 4.30 the signal efficiency and number of triggerable signal events obtained for the selections belonging to the category *doubleEMTFsingleME0*, for each 500 Hz slice in the trigger rate region $R < 10\,\text{kHz}$ are respectively reported. All the details on selections are illustrated in Tab. A.4 for $PU = 140$ and in Tab. A.5 for $PU = 200$.

- **Results for category tripleTK:** in Fig. 4.31 the signal efficiency and the number of triggerable signal events obtained for the selections belonging to the category *tripleTK* (using triplets of TkMuons), for each 500 Hz slice in the trigger rate region $R < 10\,\text{kHz}$ are respectively reported. All the details on selections are illustrated in Tab. A.6 for $PU = 140$ and in Tab. A.7 for $PU = 200$.

  It can be noticed as the maximum efficiency selection at low rate involve the invariant mass cut (*Mass* flag in the path), while for the other 500 Hz slices the maximum profitable selections involve the ΔR radius cut (*DeltaR* flag in the path).

  This category is also the one providing the maximum number of triggerable events in each 500 Hz slice in the rate region $R < 10\,\text{kHz}$. The maximum efficiency values reached respectively for $PU = 140$ and $PU = 200$ are $\epsilon_{PU=140} = 4.75 \pm 0.07\%$ and $\epsilon_{PU=200} = 3.71 \pm 0.06\%$. On the other

hand the triggerable events are respectively $N_{PU=140} = 5780 \pm 330$ and $N_{PU=200} = 4520 \pm 260$. Finally, the corresponding rates for these trigger paths are $R_{PU=140} = 9.70 \pm 0.25\,\text{kHz}$ and $R_{PU=200} = 8.80 \pm 0.23\,\text{kHz}$.

4.6.4 Comparison between similar cuts

In this section a comparison between cuts that are used alternatively (when one is used the other is deactivated) will be presented. These are:

- the cuts on the objects mutual distance performed on ΔR radius (section 4.5.1.5) and on the $\Delta\eta - \Delta\phi$ separation (section 4.5.1.4), identified respectively with *DeltaR* and *Chi* flags. These are used alternatively in categories *tripleME0*, *tripleME11* and *tripleME21*.
- the cuts on the ΔR radius and invariant mass for TkMuons in the tripleTK category, identified respectively by the flags *DeltaR* and *Mass*.

Comparison between ΔR radius and $\Delta\eta - \Delta\phi$ cuts. A representation of the selection which collected the maximum number of events in the rate region $R < 10\,\text{kHz}$ for the category *tripleME0* (using triplets of ME0 segments) is reported in Fig. 4.32a. Here it can be observed as, for $PU = 140$, the number of triggerable events obtained from the *DeltaR*-flagged cuts reaches higher values than those obtained from the selections using *Chi*-flagged cuts: the number of triggerable events remains anyway pretty low, ~ 470 events, with respect to the number of triggerable events offered by the other categories.

On the other hand, for $PU = 200$ the two classes of cuts achieve almost the same results, with a number of triggerable events always below ~ 360 events.

This kind of investigation has been performed also for the *tripleME11* and *tripleME21* categories:

- for category *tripleME11* no selection was found in the rate region $R < 10\,\text{kHz}$;
- for category *tripleME21* only selections involving the *Chi*-flagged cuts have been found in the rate region $R < 10\,\text{kHz}$, and not selections involving the *DeltaR* cut. The number of events remains anyway below 100 events (Fig. 4.32b).

Comparison between ΔR radius and invariant mass cuts. Only for the *tripleTK* category a comparison is available between the performance offered by the selections involving, in alternative ways, cuts on the separation given by the ΔR radius and on the invariant mass of triplets of TkMuons, since the invariant mass cut has been implemented only for TkMuons. The

comparison among them is illustrated in Fig. 4.33, where it can be observed as, both for $PU = 140$ and $PU = 200$, the *DeltaR*-flagged cuts can select a higher number of signal events, apart from the low rate region, where the *Mass*-flagged cuts show a better result.

4.6.5 Logical OR among the three best categories

The maximum efficiency paths identified for the three best performing categories, reported

- in Tab. A.2 and Tab. A.3 for *singleEMTFdoubleME0*,
- in Tab. A.4 and Tab. A.5 for *doubleEMTFsingleME0*,
- in Tab. A.6 and Tab. A.7 for *tripleTK*,

are used as input of a logical OR procedure between 2 trigger paths at a time of these categories, to see if a higher number of events could be obtained, keeping the trigger rate below 10 kHz. The results obtained from the logical OR are illustrated in Fig. 4.34, while the details of each selection in the plot are reported in Tab. A.8 and Tab. A.9, respectively for $PU = 140$ and $PU = 200$ conditions. In these tables, the trigger efficiency, the trigger rate and the number of triggerable events are respectively indicated with ϵ, R and N.

To give a final overall vision, a summary of the best results with rate $R < 10$ kHz is reported in Tab. 4.21. In the first three lines, the highest efficiencies performance offered by the three single categories are reported, while in the last line the results obtained with the logical OR are shown. In this context, it must be remembered that when an OR between two different trigger paths is performed, both the efficiency and the rate increase, since both the signal and background events collected by the two paths are joined. In this way, the highest efficiency path with $R < 10$ kHz, will be formed by paths with a lower trigger rate. For example:

- for $PU = 140$, the OR path with the highest number of triggerable events is characterised by $N_{PU=140} = 6660 \pm 380$, $\epsilon_{PU=140} = 5.47 \pm 0.07\%$ and $R_{PU=140} = 9.85 \pm 0.25$ kHz, and is composed by two trigger paths which are characterised by:
  - 1st path in OR: $N_1 = 4790 \pm 280$, $\epsilon_1 = 3.93 \pm 0.06\%$, $R_1 = 4.04 \pm 0.16$ kHz,
  - 2nd path in OR: $N_2 = 2140 \pm 130$, $\epsilon_2 = 1.75 \pm 0.04\%$, $R_2 = 5.84 \pm 0.19$ kHz,
- for $PU = 200$, the OR path with the highest number of triggerable events is characterised by $N_{PU=200} = 5630 \pm 320$, $\epsilon_{PU=200} = 4.62 \pm 0.07\%$ and $R_{PU=200} = 9.90 \pm 0.25$ kHz, and is composed by two trigger paths which are characterised by:

- 1st path in OR: $N_1 = 3730 \pm 220$, $\epsilon_1 = 3.06 \pm 0.05\%$, $R_1 = 3.27 \pm 0.14\,\text{kHz}$,
- 2nd path in OR: $N_2 = 4090 \pm 240$, $\epsilon_2 = 3.35 \pm 0.06\%$, $R_2 = 7.48 \pm 0.21\,\text{kHz}$.

The results reported in Tab. 4.21, as well as in Fig. 4.34, show a significant increase in the number of triggerable events, with respect to what was obtained with the single categories (section 4.6.3).

In addition, also a summary of the best results for the rate region $R < 1\,\text{kHz}$ is provided, in Tab. 4.22. This is indeed more interesting for potential implementation since the required trigger rate bandwidth would be much lower. It can be observed that the number of triggerable events for the trigger OR at $PU = 200$ is lower than that obtained by the *tripleTK* category: this result is expected, since, as previously mentioned, performing the logical OR of two different trigger paths increases both the efficiency and the rate, moving the particular trigger path in a higher rate region. Furthermore, to produce the 1 kHz OR result, only 2 paths per category were used, due to the used 500 Hz rate granularity. Using a lower granularity on a fixed 10 kHz range for all the three best categories was indeed too computationally time consuming in terms of combination of trigger paths that had to be elaborated. In this way only the $0.0 - 0.5\,\text{kHz}$ and $0.5 - 1.0\,\text{kHz}$ maximum efficiency trigger paths were used in the OR evaluation, limiting a lot the room for action. Depending on the future bandwidth availability, a rate region of particular interest will be analysed with a smaller granularity (for example the region $R < 1\,\text{kHz}$), to provide a more refined vision.

The trigger paths used to compose the $PU = 200$ $R < 1\,\text{kHz}$ trigger OR, reported in the first line of Tab. A.9, have indeed separately the following performances:

- 1st path in the OR: $\epsilon_1 = 1.93 \pm 0.04\%$, $R_1 = 0.47 \pm 0.05\,\text{kHz}$, $N_1 = 2350 \pm 140$ (first line of Tab. A.7);
- 2nd path in the OR: $\epsilon_2 = 0.13 \pm 0.01\%$, $R_2 = 0.43 \pm 0.05\,\text{kHz}$, $N_2 = 154 \pm 16$ (first line of Tab. A.3).

4.6.6 Conclusion and future outlook

The results obtained from this study are only a first step in the direction of implementing trigger algorithms exploiting the upgrades foreseen for Phase 2 and the installation of the GE1/1 and GE2/1 stations (increasing the redundancy of the muon system), as well as ME0 (in addition extending also the coverage of the muon system up to $|\eta| < 2.8$).

To deploy the trigger algorithms and include them in a future trigger menu, I plan to study their practical implementation using the most updated version

Category	PU = 140			PU = 200		
	ϵ (%)	R (kHz)	N	ϵ (%)	R (kHz)	N
singleEMTFdoubleME0	2.41	9.61	2930	1.27	8.87	1550
doubleEMTFsingleME0	2.28	9.91	2770	1.40	9.18	1710
tripleTK	4.75	9.70	5780	3.71	9.92	4520
3 best categories OR	5.47	9.85	6660	4.62	9.90	5630

Table 4.21: Summary of highest efficiency results obtained by categories *singleEMTFdoubleME0*, *doubleEMTFsingleME0* and *tripleTK* and by their logical OR, in the rate region $R < 10\,\text{kHz}$. In the table are reported the trigger efficiency (ϵ), the trigger rate (R) and the number of triggerable events (N) referred to $3000\,\text{fb}^{-1}$ integrated luminosity.

Category	PU = 140			PU = 200		
	ϵ (%)	R (kHz)	N	ϵ (%)	R (kHz)	N
singleEMTFdoubleME0	0.47	0.92	574	0.25	0.96	301
doubleEMTFsingleME0	0.60	0.84	735	0.26	0.71	314
tripleTK	2.89	0.91	3520	2.19	0.93	2660
3 best categories OR	2.90	0.94	3530	2.05	0.90	2490

Table 4.22: Summary of highest efficiency results obtained by categories *singleEMTFdoubleME0*, *doubleEMTFsingleME0* and *tripleTK* and by their logical OR, in the rate region $R < 1\,\text{kHz}$. In the table are reported the trigger efficiency (ϵ), the trigger rate (R) and the number of triggerable events (N) referred to $3000\,\text{fb}^{-1}$ integrated luminosity.

of the L1 trigger emulators, to build new trigger cuts, such as those involving the muon separation.

The $\tau \to 3\mu$ channel is indeed an interesting case study for future deployment of trigger algorithms involving physics channels with many muons in their final states. Furthermore, its interest lies in the fact that it involves objects concentrated mostly in the endcaps, where the background plays a significant role in the signal selection, and finally the signal muons are characterised by a low p_t.

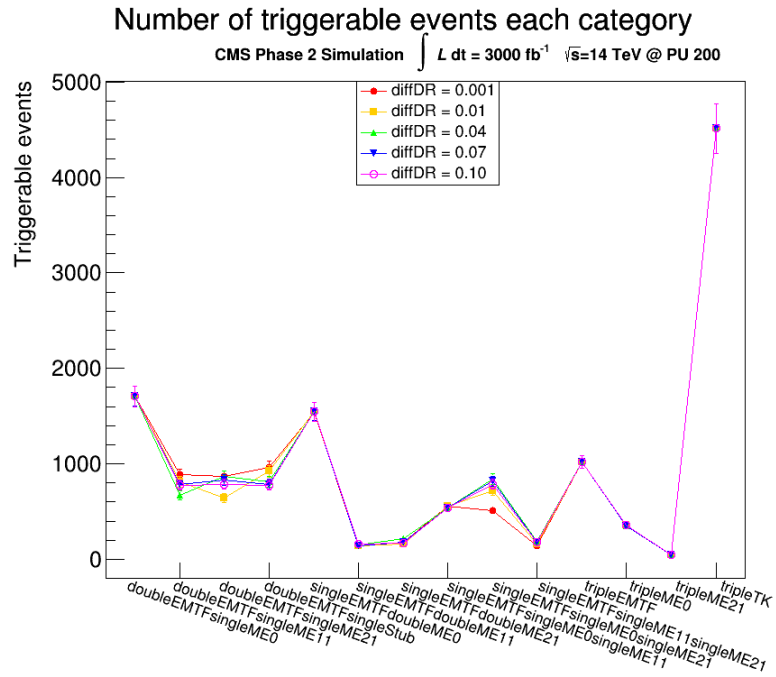

(a)

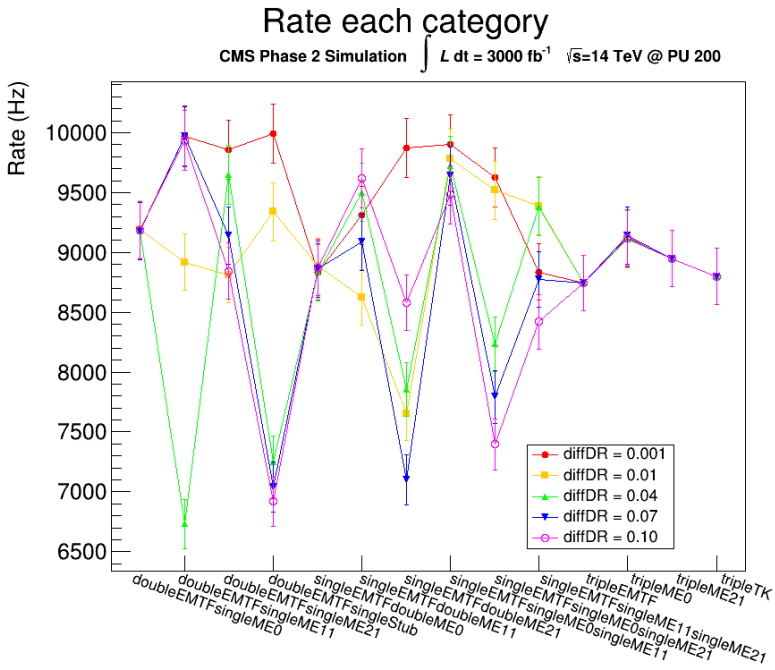

(b)

Figure 4.27: Maximum number of triggerable signal events (a) for selections with a trigger rate $R < 10\,\text{kHz}$. Their corresponding trigger rate is reported in the plot (b). The total integrated luminosity considered is $\int \mathcal{L}\,dt = 3000\,\text{fb}^{-1}$, and the pileup condition is $PU = 200$. In the plots the results for different values of the *diffDR* parameter are shown. This parameter does not act on the categories where it was not implemented: tripleME0, tripleTK, tripleEMTF, doubleEMTFsingleME0 and singleEMTFdoubleME0.

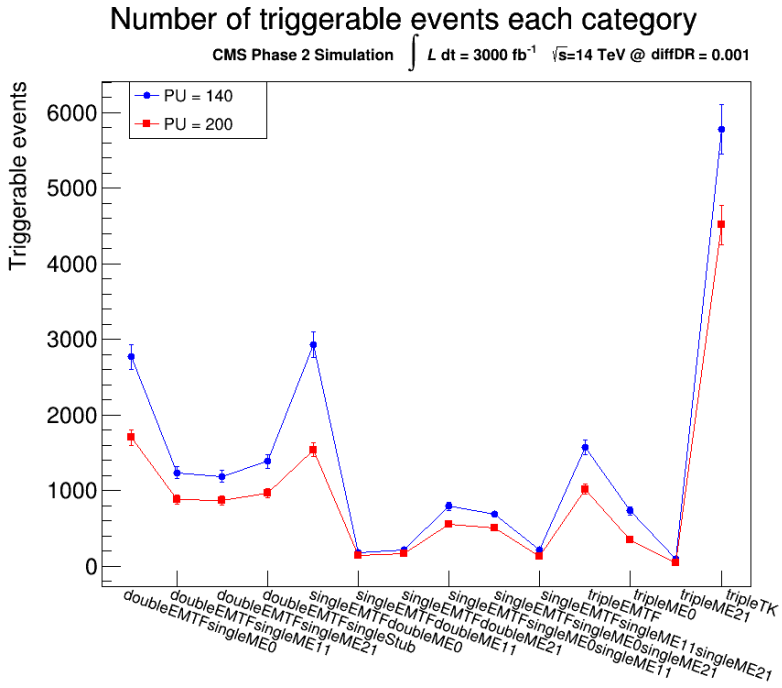

(a)

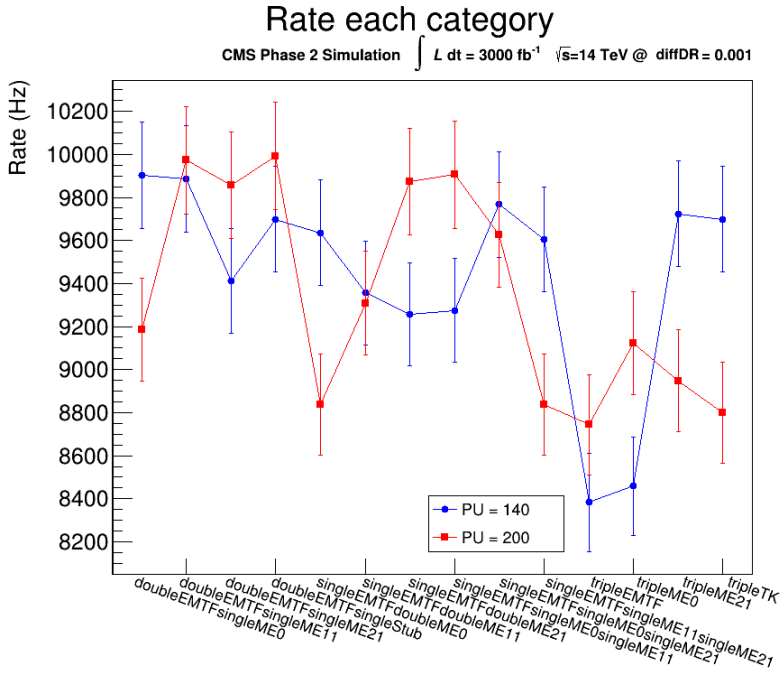

(b)

Figure 4.28: Maximum number of triggerable signal events (a) for selections with a trigger rate $R < 10\,\text{kHz}$. Their corresponding trigger rate is reported in plot (b). The total integrated luminosity considered is $\int \mathcal{L}\, dt = 3000\,\text{fb}^{-1}$, and the *diffDR* parameter is set to 0.001. In the plots the pileup condition are $PU = 140$ and $PU = 200$.

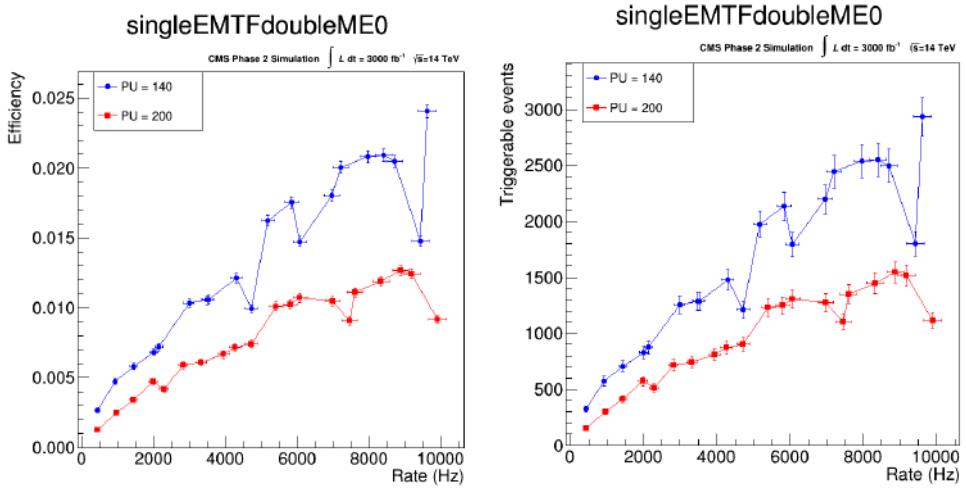

(a) (b)

Figure 4.29: Category *singleEMTFdoubleME0*: maximum signal efficiency (a) and number of triggerable signal events (b) in each 500 Hz slice for rate $R < 10\,\text{kHz}$. The total integrated luminosity considered is $\int \mathcal{L}\,dt = 3000\,\text{fb}^{-1}$. The details on each point are reported in Tab. A.2 for $PU = 140$ and in Tab. A.3 for $PU = 200$.

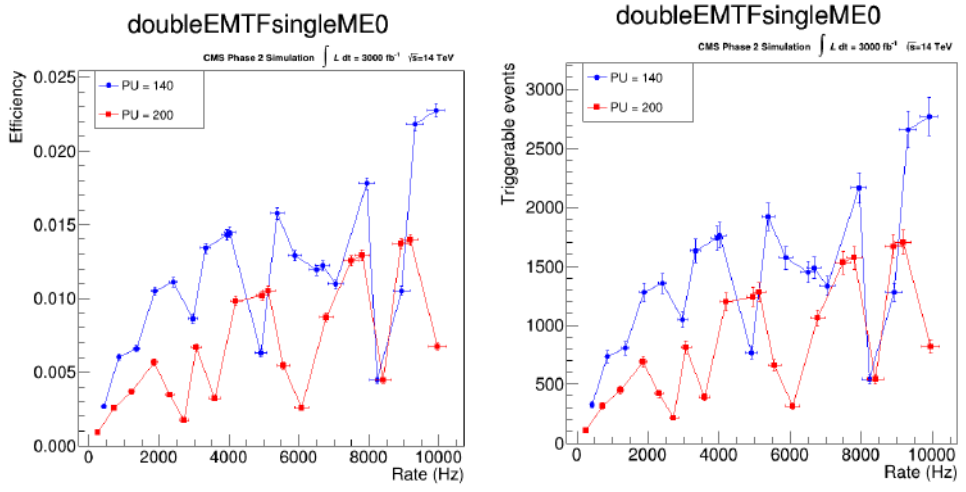

(a) (b)

Figure 4.30: Category *doubleEMTFsingleME0*: maximum signal efficiency (a) and number of triggerable signal events (b) in each 500 Hz slice for rate $R < 10\,\text{kHz}$. The total integrated luminosity considered is $\int \mathcal{L}\,dt = 3000\,\text{fb}^{-1}$. The details on each point are reported in Tab. A.4 for $PU = 140$ and in Tab. A.5 for $PU = 200$.

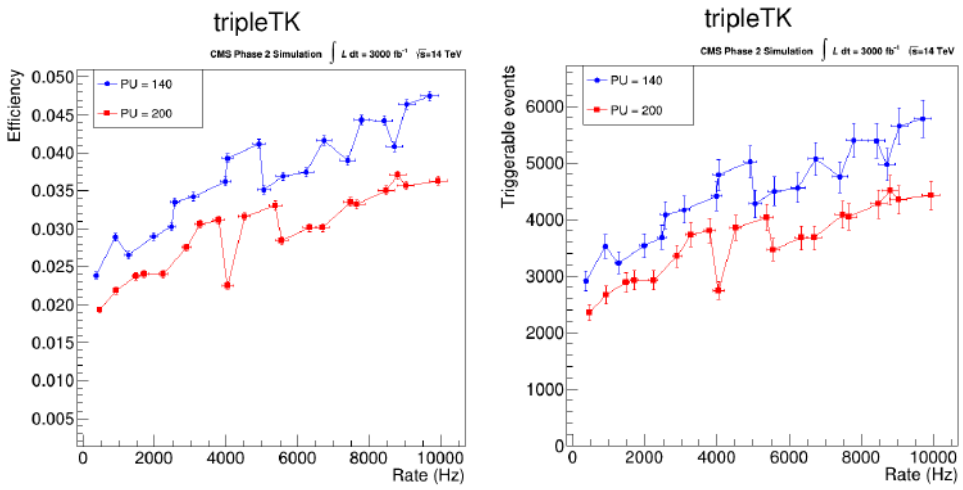

(a) (b)

Figure 4.31: Category *tripleTK*: maximum signal efficiency (a) and number of triggerable signal events (b) in each 500 Hz slice for rate $R < 10\,\text{kHz}$. The total integrated luminosity considered is $\int \mathcal{L}\,dt = 3000\,\text{fb}^{-1}$. The details on each point are reported in Tab. A.6 for $PU = 140$ and in Tab. A.7 for $PU = 200$.

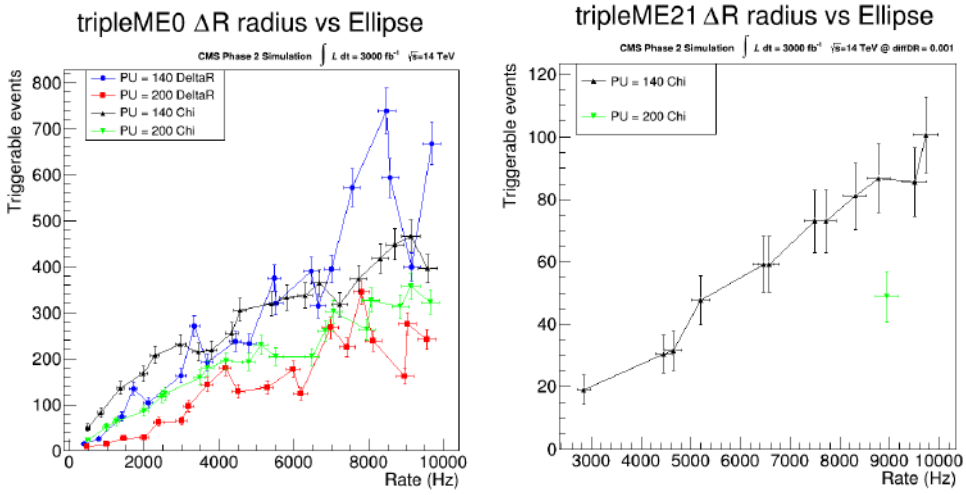

(a) (b)

Figure 4.32: (a) Category *tripleME0*: comparison between the maximum number of triggerable events per 500 Hz slice offered by the cuts on ΔR radius and on $\Delta\eta-\Delta\phi$ separation (identified with the flags *DeltaR* and *Chi*); (b) Category *tripleME21*: comparison between the maximum number of triggerable events per 500 Hz slice offered by the cuts on ΔR radius and on $\Delta\eta-\Delta\phi$ separation with *diffDR* parameter set to 0.001, (indicated in the top right part of the plot). The same result has been obtained also for the other *diffDR* investigated values (0.01, 0.04, 0.07 and 0.10). In this case, only for the *Chi*-flagged cuts results were found in the rate region $R < 10$ kHz. In both figures, both $PU = 140$ and $PU = 200$ pileup scenarios are reported.

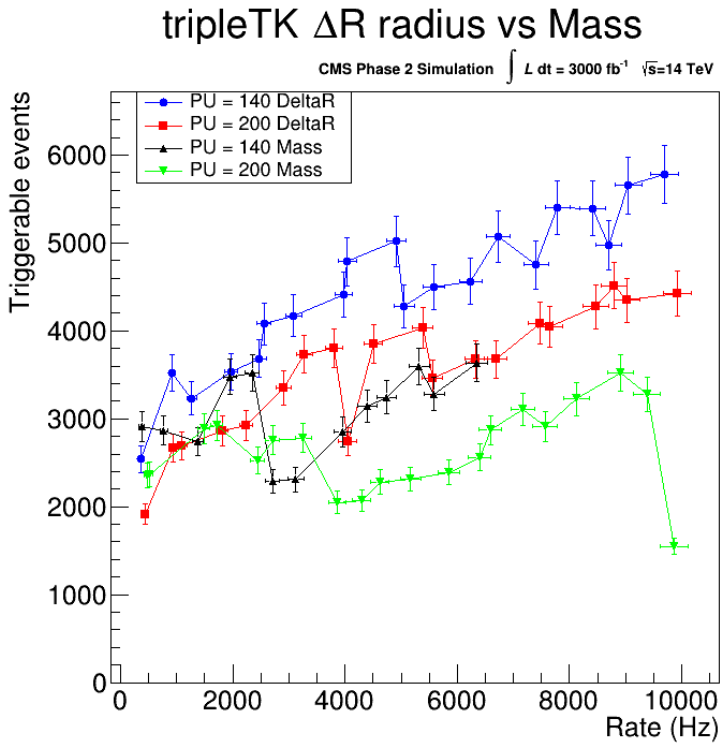

Figure 4.33: Category *tripleTK*: comparison between the maximum number of triggerable events offered by the cuts on ΔR radius and on the invariant mass of the TkMuon triplet (identified respectively with the flags *DeltaR* and *Mass*).

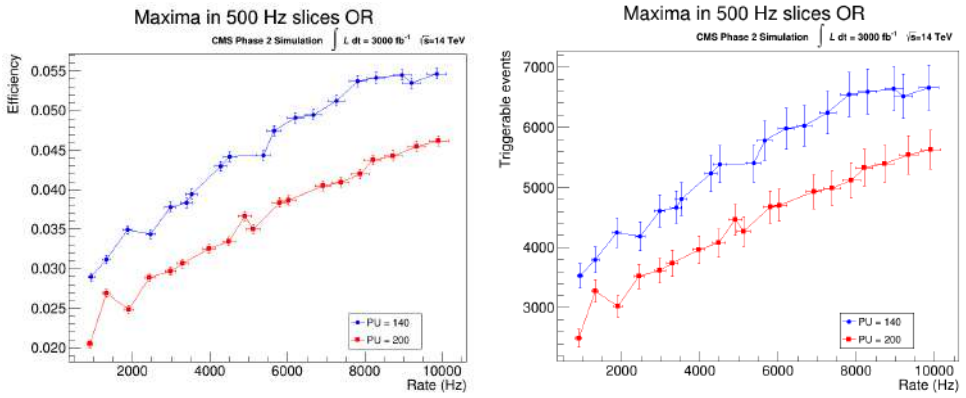

(a) (b)

Figure 4.34: Summary of results obtained performing a logical OR between the most proficient trigger paths for $PU = 140$ (reported in Tab. A.4, Tab. A.2 and Tab. A.6) and for $PU = 200$ (reported in Tab. A.5, Tab. A.3 and Tab. A.7). On the left is reported the signal efficiency, while on the right the number of triggerable events, for a total integrated luminosity of $3000\,\mathrm{fb}^{-1}$.

Chapter 5

Conclusion

This thesis work concentrated mainly on three different aspects concerning the upgrades for Phase 2 of the CMS muon system: the production and installation of the first muon station using the GEM detector technology in the CMS experiment (GE1/1), its commissioning and the study of trigger algorithms for the Phase 2 upgrade, exploiting the installation of the new GEM detector stations (GE1/1, GE2/1 and ME0).

The first topic described in the thesis is the production and validation of the GE1/1 detectors: this activity was supported by a wide variety of quality control tests, designed to ensure the correct operation of the detectors before their delivery to the CMS experiment site. In particular, the work performed on the electronics quality control (QC7) and on the cosmic stand (QC8) is presented; these protocols are the last quality controls performed at the CERN assembly site before the shipment of Super-Chambers to the experimental site.

The installation of the GE1/1 chambers in the CMS experiment took place since July 2019 and it was completed in September 2020. After this period, the Super-Chambers commissioning inside the CMS experiment started, integrating the chambers in the systems deputed to ensure its correct and smooth operation in concert with the other CMS sub-systems. In this context, an extensive study on the HV trips has been performed, to understand at best the causes of occurrence of such phenomena and to adopt operation procedures that reduce them as much as possible, such as the particular power on ordering of the electrodes (HV training).

At the end of October 2021, CMS started the magnet commissioning and the first test collisions of LHC took place: this provided new expertise to the operation of the GE1/1 chambers in the magnetic field. In this context, I have performed a study on the generation of short circuits in the GEM foil HV sectors, highlighting their main context of creation: the variation of the magnetic field. In December 2021 a campaign has started to understand in a controlled B-field environment how to heal a short circuit only operating on the HV supply line. Un-installing a detector is indeed not the correct

choice, since it will not be feasible during the data taking runs. In addition, a program of remapping of HV supply lines is ongoing, to operate the detectors with shorts in case the healing procedure has not yet taken place.

Finally, in the last chapter, a study on trigger paths dedicated to the $\tau \to 3\mu$ decay channel is presented. This decay is of particular interest since it is a Lepton Flavour Violating decay, representing a search for new physics in the HL-LHC phase. In addition, it involves many low p_t muons in the final state. Most of them are reconstructed in the endcap region, where the background plays an important role in signal selection. The work carried out on the $\tau \to 3\mu$ channel could so become profiting also for other channels with similar features.

The study has involved different objects, trying to profit from the CMS Phase 2 detector upgrades, in particular the extension in η coverage of the muon system ($|\eta| < 2.8$) and of the tracker ($|\eta| < 4$). Many potentially interesting trigger paths have been identified, involving objects reconstructed in the tracker and in the muon stations, with a particular role of the new GEM stations, leading to a significant increase in the selection potential, maintaining a contained trigger rate.

Appendices

Appendix A

Additional information about the trigger study

A.1 Samples used in the trigger study

Here are listed the full names of the samples used in the study, which can be found on CMS Data Aggregation Service (DAS).

$D_s \to \tau\nu_\tau$, $\tau \to 3\mu$ **signal samples.**

- Centrally produced samples:
  - PU0 ($1.52{\cdot}10^5$ events): */DsToTauTo3Mu_TuneCP5_14TeV-pythia8 /Phase2HLTTDRSummer20ReRECOMiniAOD-NoPU_111X_mcRun4_realistic _T15_v1_ext1-v1/FEVT*;
  - PU140 ($1.52 \cdot 10^5$ events): */DsToTauTo3Mu_TuneCP5_14TeV-pythia8 /Phase2HLTTDRSummer20ReRECOMiniAOD-PU140_withNewMB_111X _mcRun4_realistic_T15_v1_ext1-v1/FEVT*;
  - PU200 ($1.45 \cdot 10^5$ events): */DsToTauTo3Mu_TuneCP5_14TeV-pythia8 /Phase2HLTTDRSummer20ReRECOMiniAOD-PU200_withNewMB_111X _mcRun4_realistic_T15_v1_ext1-v1/FEVT.*
- Private sample: PU0 ($8.51 \cdot 10^5$ events): */DsTau3Mu_Phase2_GEN-SIM/caruta-DsToTauTo3Mu_Phase2_112X_mcRun4_realistic_v4_GEN-SIM-DIGI-RAW-9683d33334181502dc70ae4e79574322/USER*

Minimum bias samples.

- PU140 ($4.98 \cdot 10^5$ events): */MinBias_TuneCP5_14TeV-pythia8 /Phase2HLTTDRSummer20ReRECOMiniAOD-PU140_withNewMB_111X _mcRun4_realistic_T15_v1_ext1-v2/FEVT*;

p_t index	Meaning	p_t index	Meaning
1	2_2_2_GeV	29	3_5_20_GeV
2	2_2_3_GeV	30	3_5_50_GeV
3	2_2_5_GeV	31	3_10_10_GeV
4	2_2_10_GeV	32	3_10_20_GeV
5	2_2_20_GeV	33	3_10_50_GeV
6	2_2_50_GeV	34	3_20_20_GeV
7	2_3_3_GeV	35	3_20_50_GeV
8	2_3_5_GeV	36	3_50_50_GeV
9	2_3_10_GeV	37	5_5_5_GeV
10	2_3_20_GeV	38	5_5_10_GeV
11	2_3_50_GeV	39	5_5_20_GeV
12	2_5_5_GeV	40	5_5_50_GeV
13	2_5_10_GeV	41	5_10_10_GeV
14	2_5_20_GeV	42	5_10_20_GeV
15	2_5_50_GeV	43	5_10_50_GeV
16	2_10_10_GeV	44	5_20_20_GeV
17	2_10_20_GeV	45	5_20_50_GeV
18	2_10_50_GeV	46	5_50_50_GeV
19	2_20_20_GeV	47	10_10_10_GeV
20	2_20_50_GeV	48	10_10_20_GeV
21	2_50_50_GeV	49	10_10_50_GeV
22	3_3_3_GeV	50	10_20_20_GeV
23	3_3_5_GeV	51	10_20_50_GeV
24	3_3_10_GeV	52	10_50_50_GeV
25	3_3_20_GeV	53	20_20_20_GeV
26	3_3_50_GeV	54	20_20_50_GeV
27	3_5_5_GeV	55	20_50_50_GeV
28	3_5_10_GeV	56	50_50_50_GeV

Table A.1: Meaning of each p_t index for triple selections with a cut on p_t.

- PU200 ($5.00 \cdot 10^5$ events): */MinBias_TuneCP5_14TeV-pythia8 /Phase2HLTTDRSummer20ReRECOMiniAOD-PU200_withNewMB_111X _mcRun4_realistic_T15_v1_ext1-v2/FEVT.*

A.2 Main labels of p_t cuts

In this study when in a selection involving three objects a cut on p_t is designed, an index is attached to the combination of p_t thresholds acting on each object: the first label corresponds to the threshold applied to the trailing p_t object, followed by the medium p_t and then by the leading p_t one. This convention is fully explained in Tab. A.1.

A.3 Details on trigger best categories

A.3.1 Details on singleEMTFdoubleME0 category

In Tab. A.2 for $PU = 140$ and in Tab. A.3 for $PU = 200$, all the details about the selections which produced the results illustrated in Fig. 4.29 are reported.

A.3.2 Details on doubleEMTFsingleME0 category

In Tab. A.4 for $PU = 140$ and in Tab. A.5 for $PU = 200$, all the details about the selections which produced the results illustrated in Fig. 4.30 are reported.

A.3.3 Details on tripleTK category

In Tab. A.6 for $PU = 140$ and in Tab. A.7 for $PU = 200$, all the details about the selections which produced the results illustrated in Fig. 4.31 are reported.

A.4 Details on trigger OR results

In Tab. A.8 for $PU = 140$ and in Tab. A.9 for $PU = 200$, all the details about the selections which produced the results illustrated in Fig. 4.34 are reported.

Trigger path	Efficiency	Rate (Hz)	N events ($3000\,\mathrm{fb}^{-1}$)
Quality2Charge1DeltaR1[SegmME0GeV_3_5_TkGeV_10]	0.0027	421	326
Quality2Charge0DeltaR1[SegmME0GeV_3_5_TkGeV_10]	0.0047	925	574
Quality2Charge2DeltaR1[SegmME0GeV_2_50_TkGeV_2]	0.0058	1430	707
Quality2Charge2DeltaR1[SegmME0GeV_2_20_TkGeV_20]	0.0068	2000	829
Quality2Charge2DeltaR1[SegmME0GeV_2_20_TkGeV_10]	0.0072	2140	876
Quality2Charge2DeltaR1[SegmME0GeV_2_10_TkGeV_20]	0.0103	2980	1260
Quality2Charge1DeltaR1[SegmME0GeV_2_10_TkGeV_10]	0.0106	3480	1290
Quality2Charge2DeltaR1[SegmME0GeV_2_10_TkGeV_10]	0.0106	3520	1290
Quality2Charge0DeltaR1[SegmME0GeV_2_20_TkGeV_10]	0.0121	4300	1480
Quality1Charge0DeltaR1[SegmME0GeV_3_3_TkGeV_20]	0.0099	4730	1210
Quality2Charge0DeltaR1[SegmME0GeV_2_20_TkGeV_2]	0.0162	5180	1980
Quality2Charge0DeltaR1[SegmME0GeV_2_10_TkGeV_20]	0.0175	5840	2140
Quality1Charge1DeltaR1[SegmME0GeV_2_20_TkGeV_2]	0.0147	6070	1790
Quality2Charge0DeltaR1[SegmME0GeV_2_10_TkGeV_10]	0.0180	6950	2200
Quality2Charge1DeltaR1[SegmME0GeV_2_5_TkGeV_5]	0.0201	7210	2440
Quality2Charge1DeltaR1[SegmME0GeV_2_5_TkGeV_2]	0.0208	7970	2540
Quality2Charge2DeltaR1[SegmME0GeV_2_5_TkGeV_2]	0.0209	8400	2550
Quality2Charge0DeltaR1[SegmME0GeV_2_10_TkGeV_2]	0.0205	8700	2500
Quality2Charge0DeltaR2[SegmME0GeV_2_20_TkGeV_2]	0.0148	9430	1800
Quality2Charge1DeltaR1[SegmME0GeV_2_3_TkGeV_50]	0.0241	9610	2930

Table A.2: Category *singleEMTFdoubleME0*: details on the selections that, in $PU = 140$ conditions, achieved the maximum efficiency in 500 Hz slices with trigger rate $R < 10\,\mathrm{kHz}$. Inside the square brackets, the description of the p_t cut is reported, with the last number indicating the p_t threshold for the EMTF track involved in the selection, and the first and second numbers indicating the p_t ($\Delta\phi$ bending) threshold required on the ME0 segments pair. The first flag is applied to the segment with the highest bending in the pair (lowest p_t), while the second flag is applied to the segment with the lowest bending in the pair (highest p_t). The details on ME0 $\Delta\phi$ thresholds are provided in section 4.5.1.1. In the last three columns the signal efficiency, the trigger rate and the number of triggerable events in an integrated luminosity of $3000\,\mathrm{fb}^{-1}$ are reported.

Trigger path	Efficiency	Rate (Hz)	N events ($3000\,\text{fb}^{-1}$)
Quality2Charge0DeltaR1[SegmME0GeV_5_10_TkGeV_2]	0.0013	432	154
Quality2Charge2DeltaR1[SegmME0GeV_3_5_TkGeV_10]	0.0025	960	301
Quality2Charge0DeltaR1[SegmME0GeV_3_20_TkGeV_2]	0.0034	1430	413
Quality2Charge0DeltaR1[SegmME0GeV_3_5_TkGeV_10]	0.0047	1980	572
Quality2Charge1DeltaR1[SegmME0GeV_3_3_TkGeV_2]	0.0042	2280	510
Quality2Charge1DeltaR1[SegmME0GeV_2_50_TkGeV_10]	0.0059	2810	715
Quality2Charge0DeltaR1[SegmME0GeV_3_5_TkGeV_2]	0.0061	3320	741
Quality2Charge0DeltaR1[SegmME0GeV_3_3_TkGeV_20]	0.0066	3950	810
Quality2Charge2DeltaR1[SegmME0GeV_2_20_TkGeV_10]	0.0072	4260	871
Quality2Charge1DeltaR1[SegmME0GeV_2_20_TkGeV_10]	0.0074	4720	902
Quality2Charge0DeltaR1[SegmME0GeV_2_50_TkGeV_10]	0.0101	5410	1230
Quality2Charge2DeltaR1[SegmME0GeV_2_10_TkGeV_20]	0.0102	5810	1250
Quality2Charge1DeltaR1[SegmME0GeV_2_10_TkGeV_20]	0.0107	6070	1310
Quality2Charge2DeltaR1[SegmME0GeV_2_10_TkGeV_10]	0.0105	6980	1280
Quality1Charge2DeltaR1[SegmME0GeV_2_50_TkGeV_50]	0.0090	7450	1100
Quality2Charge1DeltaR1[SegmME0GeV_2_10_TkGeV_10]	0.0111	7590	1350
Quality2Charge0DeltaR1[SegmME0GeV_2_20_TkGeV_20]	0.0119	8330	1450
Quality2Charge0DeltaR1[SegmME0GeV_2_20_TkGeV_10]	0.0127	8870	1550
Quality2Charge1DeltaR1[SegmME0GeV_2_10_TkGeV_2]	0.0124	9180	1520
Quality2Charge2DeltaR2[SegmME0GeV_2_20_TkGeV_2]	0.0091	9900	1110

Table A.3: Category *singleEMTFdoubleME0*: details on the selections that, in $PU = 200$ conditions, achieved the maximum efficiency in 500 Hz slices with trigger rate $R < 10\,\text{kHz}$. Inside the square brackets, the description of the p_t cut is reported, with the last number indicating the p_t threshold for the EMTF track involved in the selection, and the first and second numbers indicating the p_t ($\Delta\phi$ bending) threshold required on the ME0 segments pair. The first flag is applied to the segment with the highest bending in the pair (lowest p_t), while the second flag is applied to the segment with the lowest bending in the pair (highest p_t). The details on ME0 $\Delta\phi$ thresholds are provided in section 4.5.1.1. In the last three columns the signal efficiency, the trigger rate and the number of triggerable events in an integrated luminosity of $3000\,\text{fb}^{-1}$ are reported.

Trigger path	Efficiency	Rate (Hz)	N events ($3000\,\mathrm{fb}^{-1}$)
Quality2Charge2DeltaR1[TkGeV_3_5_SegmME0GeV_2]	0.0027	414	326
Quality2Charge2DeltaR1[TkGeV_2_50_SegmME0GeV_2]	0.0060	844	735
Quality2Charge2DeltaR2[TkGeV_2_50_SegmME0GeV_2]	0.0066	1360	803
Quality2Charge2DeltaR1[TkGeV_2_20_SegmME0GeV_2]	0.0105	1870	1280
Quality2Charge2DeltaR1[TkGeV_2_10_SegmME0GeV_2]	0.0111	2400	1360
Quality2Charge2DeltaR3[TkGeV_2_50_SegmME0GeV_2]	0.0086	2970	1050
Quality2Charge2DeltaR2[TkGeV_2_20_SegmME0GeV_2]	0.0134	3330	1630
Quality2Charge2DeltaR2[TkGeV_2_10_SegmME0GeV_5]	0.0143	3930	1740
Quality2Charge2DeltaR2[TkGeV_2_10_SegmME0GeV_2]	0.0145	4020	1760
Quality0Charge2DeltaR1[TkGeV_3_5_SegmME0GeV_10]	0.0063	4910	767
Quality2Charge2DeltaR1[TkGeV_2_5_SegmME0GeV_2]	0.0158	5380	1920
Quality1Charge2DeltaR2[TkGeV_2_50_SegmME0GeV_2]	0.0129	5870	1570
Quality2Charge2DeltaR4[TkGeV_2_20_SegmME0GeV_20]	0.0119	6500	1450
Quality2Charge2DeltaR4[TkGeV_2_20_SegmME0GeV_2]	0.0122	6670	1490
Quality2Charge2DeltaR6[TkGeV_2_50_SegmME0GeV_2]	0.0111	7040	1330
Quality2Charge2DeltaR3[TkGeV_2_20_SegmME0GeV_2]	0.0178	7940	2170
Quality1Charge3DeltaR1[TkGeV_3_3_SegmME0GeV_20]	0.0045	8230	543
Quality1Charge2DeltaR3[TkGeV_3_3_SegmME0GeV_2]	0.0105	8930	1280
Quality2Charge2DeltaR2[TkGeV_2_5_SegmME0GeV_10]	0.0218	9310	2660
Quality2Charge2DeltaR2[TkGeV_2_5_SegmME0GeV_5]	0.0228	9910	2770

Table A.4: Category *doubleEMTFsingleME0*: details on the selections that, in $PU = 140$ conditions, achieved the maximum efficiency in 500 Hz slices with trigger rate $R < 10\,\mathrm{kHz}$. Inside the square brackets the description of the p_t cut is reported, with the first and second numbers indicating the p_t threshold applied respectively on the trailing and leading p_t tracks in the pair of EMTF tracks involved in the selection, and the last number indicating the p_t ($\Delta\phi$ bending) threshold required on the ME0 segment. The details on ME0 $\Delta\phi$ thresholds are provided in section 4.5.1.1. In the last three columns the signal efficiency, the trigger rate and the number of triggerable events in an integrated luminosity of $3000\,\mathrm{fb}^{-1}$ are reported.

Trigger path	Efficiency	Rate (Hz)	N events ($3000\,\text{fb}^{-1}$)
Quality2Charge2DeltaR1[TkGeV_3_20_SegmME0GeV_2]	0.0009	245	109
Quality2Charge2DeltaR1[TkGeV_3_5_SegmME0GeV_2]	0.0026	705	314
Quality2Charge2DeltaR1[TkGeV_3_3_SegmME0GeV_2]	0.0037	1210	448
Quality2Charge2DeltaR1[TkGeV_2_50_SegmME0GeV_2]	0.0057	1860	691
Quality2Charge2DeltaR3[TkGeV_3_5_SegmME0GeV_2]	0.0034	2300	418
Quality1Charge2DeltaR3[TkGeV_5_5_SegmME0GeV_2]	0.0017	2720	212
Quality2Charge2DeltaR2[TkGeV_2_50_SegmME0GeV_2]	0.0067	3070	811
Quality2Charge2DeltaR4[TkGeV_3_3_SegmME0GeV_2]	0.0032	3590	390
Quality2Charge2DeltaR1[TkGeV_2_20_SegmME0GeV_2]	0.0098	4200	1200
Quality2Charge2DeltaR1[TkGeV_2_10_SegmME0GeV_10]	0.0102	4940	1240
Quality2Charge2DeltaR1[TkGeV_2_10_SegmME0GeV_2]	0.0105	5130	1280
Quality2Charge2DeltaR4[TkGeV_2_50_SegmME0GeV_2]	0.0054	5560	662
Quality2Charge1DeltaR1[TkGeV_3_3_SegmME0GeV_2]	0.0026	6070	313
Quality2Charge2DeltaR3[TkGeV_2_50_SegmME0GeV_2]	0.0087	6770	1060
Quality2Charge2DeltaR2[TkGeV_2_20_SegmME0GeV_20]	0.0126	7490	1530
Quality2Charge2DeltaR2[TkGeV_2_20_SegmME0GeV_2]	0.0129	7800	1570
Quality1Charge2DeltaR4[TkGeV_3_5_SegmME0GeV_2]	0.0044	8400	541
Quality2Charge2DeltaR2[TkGeV_2_10_SegmME0GeV_10]	0.0137	8920	1670
Quality2Charge2DeltaR2[TkGeV_2_10_SegmME0GeV_2]	0.0140	9180	1710
Quality0Charge2DeltaR1[TkGeV_3_5_SegmME0GeV_10]	0.0067	9960	820

Table A.5: Category *doubleEMTFsingleME0*: details on the selections that, in $PU = 200$ conditions, achieved the maximum efficiency in 500 Hz slices with trigger rate $R < 10\,\text{kHz}$. Inside the square brackets the description of the p_t cut is reported, with the first and second numbers indicating the p_t threshold applied respectively on the trailing and leading p_t tracks in the pair of EMTF tracks involved in the selection, and the last number indicating the p_t ($\Delta\phi$ bending) threshold required on the ME0 segment. The details on ME0 $\Delta\phi$ thresholds are provided in section 4.5.1.1. In the last three columns the signal efficiency, the trigger rate and the number of triggerable events in an integrated luminosity of $3000\,\text{fb}^{-1}$ are reported.

Trigger path	Efficiency	Rate (Hz)	N events ($3000\,\mathrm{fb}^{-1}$)
Quality0Charge0Mass2VtxZ0[2_3_3GeV]	0.0239	377	2910
Quality0Charge0DeltaR1VtxZ0[2_3_3GeV]	0.0289	913	3520
Quality0Charge1DeltaR3VtxZ0[2_3_5GeV]	0.0265	1270	3230
Quality1Charge1DeltaR1VtxZ0[2_2_3GeV]	0.0290	1970	3530
Quality0Charge0DeltaR2VtxZ0[2_3_3GeV]	0.0302	2470	3680
Quality0Charge1DeltaR1VtxZ0[2_2_3GeV]	0.0335	2560	4080
Quality0Charge0DeltaR1VtxZ0[2_2_3GeV]	0.0343	3090	4170
Quality0Charge0DeltaR5VtxZ0[2_3_5GeV]	0.0362	3980	4420
Quality0Charge1DeltaR3VtxZ0[2_3_3GeV]	0.0393	4040	4790
Quality0Charge0DeltaR3VtxZ0[2_3_3GeV]	0.0412	4920	5020
Quality1Charge1DeltaR4VtxZ0[2_3_3GeV]	0.0351	5060	4280
Quality0Charge0DeltaR7VtxZ0[2_3_5GeV]	0.0369	5580	4500
Quality1Charge0DeltaR4VtxZ0[2_3_3GeV]	0.0375	6240	4560
Quality0Charge1DeltaR4VtxZ0[2_3_3GeV]	0.0416	6730	5070
Quality0Charge0DeltaR4VtxZ1[2_3_3GeV]	0.0390	7410	4750
Quality1Charge1DeltaR5VtxZ0[2_3_3GeV]	0.0444	7780	5400
Quality0Charge0DeltaR4VtxZ0[2_3_3GeV]	0.0443	8420	5390
Quality0Charge0DeltaR5VtxZ0[2_2_5GeV]	0.0408	8690	4970
Quality0Charge1DeltaR5VtxZ1[2_3_3GeV]	0.0464	9050	5650
Quality1Charge0DeltaR5VtxZ0[2_3_3GeV]	0.0475	9700	5780

Table A.6: Category *tripleTK*: details on the selections that, in $PU = 140$ conditions, achieved the maximum efficiency in 500 Hz slices with trigger rate $R < 10\,\mathrm{kHz}$. Inside the square brackets the description of the p_t cut is reported, with the first, second and third number indicating the p_t threshold applied respectively on the trailing, medium and leading p_t tracks in the triplet of TkMuons involved in the selection. In the last three columns the signal efficiency, the trigger rate and the number of triggerable events in an integrated luminosity of $3000\,\mathrm{fb}^{-1}$ are reported.

Trigger path	Efficiency	Rate (Hz)	N events ($3000\,\text{fb}^{-1}$)
Quality0Charge1Mass1VtxZ0[2_3_3GeV]	0.0193	469	2350
Quality0Charge1DeltaR1VtxZ0[2_3_5GeV]	0.0219	929	2660
Quality0Charge1Mass2VtxZ0[2_3_3GeV]	0.0237	1480	2890
Quality0Charge0Mass2VtxZ0[2_3_3GeV]	0.0240	1710	2920
Quality1Charge1DeltaR1VtxZ1[2_3_3GeV]	0.0240	2230	2920
Quality0Charge1DeltaR1VtxZ1[2_3_3GeV]	0.0275	2900	3350
Quality0Charge1DeltaR1VtxZ0[2_3_3GeV]	0.0306	3270	3730
Quality0Charge0DeltaR1VtxZ0[2_3_3GeV]	0.0312	3800	3800
Quality0Charge1DeltaR2VtxZ1[2_2_5GeV]	0.0225	4050	2740
Quality0Charge1DeltaR3VtxZ0[2_3_5GeV]	0.0316	4510	3850
Quality0Charge0DeltaR3VtxZ0[2_3_5GeV]	0.0331	5380	4030
Quality1Charge1DeltaR4VtxZ0[2_3_5GeV]	0.0284	5560	3470
Quality1Charge1DeltaR2VtxZ0[2_3_3GeV]	0.0302	6330	3680
Quality1Charge0DeltaR4VtxZ0[2_3_5GeV]	0.0302	6690	3680
Quality0Charge1DeltaR4VtxZ0[2_3_5GeV]	0.0335	7480	4090
Quality1Charge1DeltaR5VtxZ1[2_3_5GeV]	0.0332	7660	4050
Quality0Charge1DeltaR2VtxZ0[2_3_3GeV]	0.0351	8470	4270
Quality1Charge1DeltaR5VtxZ0[2_3_5GeV]	0.0371	8800	4520
Quality0Charge0DeltaR4VtxZ0[2_3_5GeV]	0.0357	9020	4350
Quality0Charge0DeltaR2VtxZ0[2_3_3GeV]	0.0363	9920	4430

Table A.7: Category *tripleTK*: details on the selections that, in $PU = 200$ conditions, achieved the maximum efficiency in 500 Hz slices with trigger rate $R < 10\,\text{kHz}$. Inside the square brackets the description of the p_t cut is reported, with the first, second and third number indicating the p_t threshold applied respectively on the trailing, medium and leading p_t tracks in the triplet of TkMuons involved in the selection. In the last three columns the signal efficiency, the trigger rate and the number of triggerable events in an integrated luminosity of $3000\,\text{fb}^{-1}$ are reported.

Trigger path	$\epsilon(\%)$	R (Hz)	N
tripleTK_Q0C0M2V0:2_3_3GeV_OR_tripleTK_Q0C0DR1V0:2_3_3GeV	2.90	938	3530
tripleTK_Q0C0DR1V0:2_3_3GeV_OR_singleEMTFdoubleME0Q2C1DR1:SegmME0GeV_3_5_TkGeV_10	3.12	1330	3800
tripleTK_Q0C0DR1V0:2_3_3GeV_OR_tripleTK_Q0C1DR3V0:2_3_5GeV	3.49	1870	4250
tripleTK_Q0C0M2V0:2_3_3GeV_OR_tripleTK_Q0C0DR2V0:2_3_3GeV	3.44	2470	4190
tripleTK_Q0C1DR3V0:2_3_5GeV_OR_tripleTK_Q1C1DR1V0:2_2_3GeV	3.78	2970	4610
tripleTK_Q0C1DR1V0:2_2_3GeV_OR_doubleEMTFsingleME0Q2C2DR1:TkGeV_2_50_SegmME0GeV_2	3.83	3400	4670
tripleTK_Q0C1DR1V0:2_2_3GeV_OR_tripleTK_Q0C1DR3V0:2_3_5GeV	3.94	3520	4800
tripleTK_Q0C0M2V0:2_3_3GeV_OR_tripleTK_Q0C0DR5V0:2_3_5GeV	4.30	4280	5230
tripleTK_Q0C0DR1V0:2_3_3GeV_OR_tripleTK_Q0C0DR5V0:2_3_5GeV	4.42	4500	5380
tripleTK_Q0C1DR3V0:2_3_3GeV_OR_doubleEMTFsingleME0Q2C2DR2:TkGeV_2_50_SegmME0GeV_2	4.43	5370	5400
tripleTK_Q0C0DR5V0:2_3_5GeV_OR_tripleTK_Q1C1DR1V0:2_2_3GeV	4.75	5650	5780
tripleTK_Q0C0DR5V0:2_3_5GeV_OR_tripleTK_Q0C1DR1V0:2_2_3GeV	4.91	6200	5980
tripleTK_Q0C0DR1V0:2_2_3GeV_OR_tripleTK_Q0C0DR5V0:2_3_5GeV	4.95	6670	6030
tripleTK_Q0C0DR7V0:2_3_5GeV_OR_tripleTK_Q1C1DR1V0:2_2_3GeV	5.13	7260	6250
tripleTK_Q0C0DR7V0:2_3_5GeV_OR_tripleTK_Q0C1DR1V0:2_2_3GeV	5.37	7810	6540
tripleTK_Q0C0DR1V0:2_2_3GeV_OR_tripleTK_Q0C0DR7V0:2_3_5GeV	5.42	8280	6600
tripleTK_Q0C0DR3V0:2_3_3GeV_OR_tripleTK_Q0C0DR7V0:2_3_5GeV	5.46	8960	6640
tripleTK_Q0C1DR3V0:2_3_3GeV_OR_singleEMTFdoubleME0Q2C0DR1:SegmME0GeV_2_20_TkGeV_2	5.35	9190	6520
tripleTK_Q0C1DR3V0:2_3_3GeV_OR_singleEMTFdoubleME0Q2C0DR1:SegmME0GeV_2_10_TkGeV_20	5.47	9850	6660

Table A.8: Details on trigger path OR for $PU = 140$, performed using the most proficient trigger paths indicated in Tab. A.2 Tab. A.4 and Tab. A.6. In the path description, Q stands for *Quality*, C for *Charge*, V for *VtxZ*, DR for *DeltaR* and M for *Mass*. In the right columns are reported in order the signal efficiency ϵ, the trigger rate R and the number of triggerable events N, for a total integrated luminosity of $3000\,\text{fb}^{-1}$.

Trigger path	$\epsilon(\%)$	R (Hz)	N
tripleTK_Q0C1M1V0:2_3_3GeV_OR_is_singleEMTFdoubleME0Q2C0DR1:SegmME0GeV_5_10_TkGeV_2	2.05	898	2490
tripleTK_Q0C1M1V0:2_3_3GeV_OR_is_tripleTK_Q0C1DR1V0:2_3_5GeV	2.69	1330	3280
tripleTK_Q0C1M2V0:2_3_3GeV_OR_is_singleEMTFdoubleME0Q2C0DR1:SegmME0GeV_5_10_TkGeV_2	2.48	1910	3020
tripleTK_Q0C0M2V0:2_3_3GeV_OR_is_tripleTK_Q0C1DR1V0:2_3_5GeV	2.89	2440	3520
tripleTK_Q0C1DR1V0:2_3_5GeV_OR_is_tripleTK_Q0C1DR1V1:2_3_3GeV	2.97	2980	3610
tripleTK_Q0C1M1V0:2_3_3GeV_OR_is_tripleTK_Q0C1DR1V0:2_3_3GeV	3.07	3290	3740
tripleTK_Q0C1DR1V0:2_3_3GeV_OR_is_doubleEMTFsingleME0Q2C2DR1:TkGeV_3_5_SegmME0GeV_2	3.25	3970	3960
tripleTK_Q0C1DR1V0:2_3_3GeV_OR_is_doubleEMTFsingleME0Q2C2DR1:TkGeV_3_3_SegmME0GeV_2	3.35	4480	4080
tripleTK_Q0C1M1V0:2_3_3GeV_OR_is_tripleTK_Q0C1DR3V0:2_3_5GeV	3.66	4900	4460
tripleTK_Q0C1DR1V0:2_3_3GeV_OR_is_doubleEMTFsingleME0Q2C2DR1:TkGeV_2_50_SegmME0GeV_2	3.50	5120	4260
tripleTK_Q0C1M2V0:2_3_3GeV_OR_is_tripleTK_Q0C1DR3V0:2_3_5GeV	3.84	5790	4670
tripleTK_Q0C0M2V0:2_3_3GeV_OR_is_tripleTK_Q0C1DR3V0:2_3_5GeV	3.86	6020	4710
tripleTK_Q0C1M2V0:2_3_3GeV_OR_is_tripleTK_Q1C1DR4V0:2_3_5GeV	4.05	6910	4930
tripleTK_Q0C0DR1V0:2_3_3GeV_OR_is_tripleTK_Q0C1DR3V0:2_3_5GeV	4.09	7380	4990
tripleTK_Q0C1DR1V1:2_3_3GeV_OR_is_tripleTK_Q1C1DR4V0:2_3_5GeV	4.20	7870	5120
tripleTK_Q0C1DR1V0:2_3_3GeV_OR_is_tripleTK_Q1C1DR4V0:2_3_5GeV	4.38	8200	5330
tripleTK_Q0C0DR1V0:2_3_3GeV_OR_is_tripleTK_Q1C1DR4V0:2_3_5GeV	4.43	8720	5400
tripleTK_Q0C1DR1V0:2_3_3GeV_OR_is_tripleTK_Q1C0DR4V0:2_3_5GeV	4.55	9330	5540
tripleTK_Q0C1DR1V0:2_3_3GeV_OR_is_tripleTK_Q0C1DR4V0:2_3_5GeV	4.62	9900	5630

Table A.9: Details on trigger path OR for $PU = 200$, performed using the most proficient trigger paths indicated in Tab. A.3, Tab. A.5 and Tab. A.7. In the path description, Q stands for *Quality*, C for *Charge*, V for *VtxZ*, DR for *DeltaR* and M for *Mass*. In the right columns are reported in order the signal efficiency ϵ, the trigger rate R and the number of triggerable events N, for a total integrated luminosity of $3000\,\text{fb}^{-1}$.

Bibliography

[1] LHC/LC Study Group Collaboration. *Physics Interplay of the LHC and the ILC*. Phys. Rep., 426(hep-ph/0410364. ANL-HEP-PR-2004-108. CERN-PH-TH-2004-214. DCPT-2004-134. DESY-04-206. DESY-2004-206. IFIC-2004-59. IISc-CHEP-2004-13. IPPP-2004-67. SLAC-PUB-10764. UB-ECM-PF-2004-31. UCD-2004-28. UCI-TR-2004-37. 2-6):47–358. 472 p, Oct 2004. URL: https://cds.cern.ch/record/800650.

[2] ATLAS Collaboration, *The ATLAS Experiment at the CERN Large Hadron Collider*, JINST 3 (2008).

[3] CMS Collaboration, *The CMS experiment at the CERN LHC*, JINST 3 (2008).

[4] ALICE Collaboration, *The ALICE experiment at the CERN LHC*, JINST 3 (2008).

[5] LHCb Collaboration, *The LHCb Detector at the LHC*, JINST 3 (2008).

[6] Lyndon Evans and Philip Bryant. LHC Machine. JINST, 3:S08001, 2008.

[7] CMS Collaboration, *Observation of a new boson at a mass of 125 GeV with the CMS experiment at the LHC*, Phys. Lett. B 716 (2012) 30.

[8] ATLAS Collaboration, *Observation of a new particle in the search for the Standard Model Higgs boson with the ATLAS detector at the LHC*, Phys. Lett. B 716 (2012) 1.

[9] *Combination of standard model Higgs boson searches and measurements of the properties of the new boson with a mass near 125 GeV*. Technical Report CMS-PAS-HIG-13-005, CERN, Geneva, 2013. URL: https://cds.cern.ch/record/1542387.

[10] CERN, *CMS measures Higgs boson's mass with unprecedented precision*, URL: https://home.cern/news/news/physics/cms-measures-higgs-bosons-mass-unprecedented-precision.

[11] The LHC Study Group, *The Large Hadron Collider Conceptual Design Report*. CERN/AC 95-05, 1995.

[12] Brüning, Oliver Sim et al., *LHC Design Report*, v.1 : the LHC Main Ring, CERN-2004-003-V-1, URL: https://cds.cern.ch/record/782076, CERN, 2004.

[13] R. W. Assmann , *LEP operation and performance with electron-positron collisions at 209 GeV*. CERN, 2001.

[14] LHC/LC Study Group Collaboration. Physics Interplay of the LHC and the ILC. Phys. Rep., 426(hep-ph/0410364. ANL-HEP-PR-2004- 108. CERN-PH-TH-2004-214. DCPT-2004-134. DESY-04-206. DESY- 2004-206. IFIC-2004-59. IISc-CHEP-2004-13. IPPP-2004-67. SLACPUB- 10764. UB-ECM-PF-2004-31. UCD-2004-28. UCI-TR-2004-37. 2- 6):47–358. 472 p, Oct 2004. URL: https://cds.cern.ch/record/800650.

[15] S. Dittmaier et al. Handbook of LHC Higgs Cross Sections: 1. Inclusive Observables. CERN, Geneva, 2011. URL: https://cds.cern.ch/record/1318996. Comments: 153 pages, 43 figures, to be submitted to CERN Report. Working Group web page, URL: https://twiki.cern.ch/twiki/bin/view/LHCPhysics/CrossSections.

[16] A. Gaz, *SUSY searches at CMS*, URL: https://cds.cern.ch/record/1968317/plots.

[17] M.Kramer, A.Kulesza, R.van der Leeuw, M.Mangano, S.Padhi, T.Plehn, X.Portell, Supersymmetry production cross sections in pp collisions at $\sqrt{s} = 7\,TeV$, CERN-PH-TH/2012-163, 2012.

[18] Sakuma Tai, *Cutaway diagrams of CMS detector*, J. Phys.: Conf. Ser. 513 022032, URL: https://cds.cern.ch/record/2665537/, 2019.

[19] F. Fallavollita, *Triple-Gas Electron Multiplier technology for future upgrades of the CMS experiment: construction and certification of the CMS GE1/1 detectors and longevity studies*, URL: http://www.infn.it/thesis/thesis_dettaglio.php?tid=12848, 2019.

[20] M. Vretenar et al., *Linac4 design report*, CERN-2020-006, URL: https://cds.cern.ch/record/2736208, 2020.

[21] CERN, Home page, URL: https://home.cern/.

[22] M. Tanabashi et al. (Particle Data Group), *Accelerator Physics of Colliders*, Phys. Rev. D 98, 030001 (2018) and 2019 update, URL: https://pdg.lbl.gov/rev2019/2019/reviews/rpp2019-rev-accel-phys-colliders.pdf, 6th December, 2019.

[23] CMS Collaboration, *The Magnet Project Technical Design Report*, CERN/LHCC 97-10 CMS TDR 1, 2 May 1997, URL: https://cds.cern.ch/record/331056?ln=it.

[24] CERN Document Server, *The CMS solenoid descends to 100 Kelvin*, URL: http://cdsweb.cern.ch/record/930268.

[25] CMS Collaboration, *Precise Mapping of the Magnetic Field in the CMS Barrel Yoke using Cosmic Rays*, JINST 5 (2010) T03021, arXiv:0910.5530. CMS-CFT-09-015. URL: http://cdsweb.cern.ch/record/1215500.

[26] V. Karimäki et al., *The CMS tracker system project: Technical Design Report*, Technical Design Report CMS, CERN, Geneva, 1997, URL: https://cds.cern.ch/record/368412?ln=it.

[27] *The CMS electromagnetic calorimeter project: Technical Design Report.* Technical Design Report CMS, CERN, Geneva, 1997, URL: https://cds.cern.ch/record/349375?ln=it.

[28] *The CMS hadron calorimeter project: Technical Design Report.* Technical Design Report CMS, CERN-LHCC-97-031, CERN, Geneva, 1997, URL: https://cds.cern.ch/record/357153?ln=it.

[29] *Calibration of the CMS hadron calorimeters using proton-proton collision data at* $\sqrt{s} = 13\,TeV$, CMS Collaboration, JINST 15 (2020) P05002, URL: https://cds.cern.ch/record/2691403?ln=it.

[30] *The CMS Outer Hadron Calorimeter*, CMS Collaboration, CMS-NOTE-2006-127, 2006, URL: https://cds.cern.ch/record/973131.

[31] *Design, Performance, and Calibration of CMS Hadron-Barrel Calorimeter Wedges*, CMS HCAL Collaboration, CMS-NOTE-2006-138, 2007, URL: https://cds.cern.ch/record/1049915?ln=it.

[32] *The CMS muon project: Technical Design Report.* Technical Design Report CMS, CERN-LHCC-97-032. CERN, Geneva, 1997, URL: https://cds.cern.ch/record/343814?ln=it.

[33] CMS Collaboration, *The CMS experiment at LHC*, JINST 08 (2008) 03, URL: https://cds.cern.ch/record/1129810?ln=it.

[34] V. Khachatryan et al., *The CMS trigger system*, JINST 12 P01020, 2017, URL: https://iopscience.iop.org/article/10.1088/1748-0221/12/01/P01020/pdf.

[35] CMS Collaboration, *Commissioning of the CMS High-Level Trigger with cosmic rays*, JINST 5 T03005, 2010, URL: https://iopscience.iop.org/article/10.1088/1748-0221/5/03/T03005.

[36] *CMS TriDAS project : Technical Design Report, Volume 1: The Trigger Systems*. Technical Design Report CMS, CMS-TDR-6-1, 15 December 2000, URL: https://cds.cern.ch/record/706847?ln=it.

[37] *CMS The TriDAS Project : Technical Design Report, Volume 2: Data Acquisition and High-Level Trigger*. Technical Design Report CMS, CMS-TDR-6, 15 December 2002, URL: https://cds.cern.ch/record/578006?ln=it.

[38] A.M. Sirunyan et al., *Performance of the CMS Level-1 trigger in proton-proton collisions at* $\sqrt{s} = 13\,TeV$, JINST 15 P10017, 2020, URL: https://iopscience.iop.org/article/10.1088/1748-0221/15/10/P10017.

[39] S. Donato, *CMS trigger performance*. EPJ Web of Conferences 182, 02037 (2018), URL: https://doi.org/10.1051/epjconf/201818202037.

[40] A. Afaq et al., *The CMS High Level Trigger System*. IEEE Transactions on Nuclear Science (Volume: 55, Issue: 1, Feb. 2008), URL: https://ieeexplore.ieee.org/document/4448533.

[41] *LHC Performance Workshop 2022*, 24-27 January 2022, URL: https://indico.cern.ch/event/1097716/.

[42] HL-LHC project, *Project schedule*, September 2021, URL: https://project-hl-lhc-industry.web.cern.ch/content/project-schedule.

[43] D. Contardo et al., *Technical Proposal for the Phase-II Upgrade of the CMS Detector*, CERN-LHCC-2015-010, June 2015, URL: http://cds.cern.ch/record/2020886.

[44] C. Ochando, *HGCAL: A High-Granularity Calorimeter for the Endcaps of CMS at HL-LHC*, J. Phys.: Conf. Ser. 928 (2017) 012025, URL: https://cds.cern.ch/record/2311394.

[45] CMS Collaboration, *The Phase-2 Upgrade of the CMS Endcap Calorimeter*, CMS-TDR-019, URL: https://cds.cern.ch/record/2293646?ln=it.

[46] A. Ball et al., *The Phase-2 Upgrade of the CMS Muon Detectors*, CERN-LHCC-2017-012, CMS-TDR-016, 12 September 2017, URL: https://cds.cern.ch/record/2283189?ln=it.

[47] D. Contardo et al., *Technical Proposal for the Phase-II Upgrade of the CMS Detector*, CMS-TDR-15-02, URL: https://cds.cern.ch/record/2020886?ln=it.

[48] W. R. Leo, *Techniques for nuclear and particle physics experiments*, Springer, 1987.

[49] G. F. Knoll, *Radiation detection and measurement*, John Wiley & Sons, Inc., 2000.

[50] F. Sauli, *Principles of operation of multiwire proportional and drift chambers*, CERN 77-09, 3 May 1977, URL: https://cds.cern.ch/record/117989?ln=it.

[51] Gas Detectors Development Group, CERN, 22 Sep. 2021, URL: https://gdd.web.cern.ch/others-msgc.

[52] F. Sauli et al., *Micropattern Gaseous Detectors*, Annu. Rev. Nucl. Part. Sci. 1999. 49:341–88, URL: https://www.annualreviews.org/doi/pdf/10.1146/annurev.nucl.49.1.341.

[53] E. Garutti, *Gaseous detectors measurement of ionization position determination*, DESY, URL: https://www.desy.de/~garutti/LECTURES/ParticleDetectorSS12/L4_gasDetectors.pdf.

[54] R. Bouelier et al., *Ageing of microstrip gas chambers: problems and solutions*, Nuclear Instruments and Methods in Physics Research A 381 (1996) 289-319 , URL: https://www.sciencedirect.com/science/article/pii/S0168900296002689.

[55] J. Manjarrés et al., *Performances of anode-resistive Micromegas for HL-LHC*, Journal of Instrumentation, Volume 7, March 2012, URL: https://iopscience.iop.org/article/10.1088/1748-0221/7/03/C03040/meta.

[56] F. Sauli, *The gas electron multiplier (GEM): Operating principles and applications*, Nuclear Instruments and Methods in Physics Research Section A: Accelerators, Spectrometers, Detectors and Associated Equipment, Volume 805, 1 January 2016, URL: https://www.sciencedirect.com/science/article/pii/S0168900215008980.

[57] S. Bachmann et al., *Charge amplification and transfer processes in the gas electron multiplier*, Nuclear Instruments and Methods in Physics Research A 438 (1999) 376-408, URL: https://www.physi.uni-heidelberg.de/~glassel/journalclub19/bachmann.pdf.

[58] J. A. Merlin, *Study of long-term sustained operation of gaseous detectors for the high rate environment in CMS,* CERN-THESIS-2016-041, 2016, URL: https://cds.cern.ch/record/2155685?ln=it.

[59] G. Bencivenni et al., *A triple GEM detector with pad readout for high rate charged particle triggering,* Nuclear Instruments and Methods in Physics

Research Section A: Accelerators, Spectrometers, Detectors and Associated Equipment, Volume 488, Issue 3, 11 August 2002, Pages 493-502, URL: https://www.sciencedirect.com/science/article/pii/S0168900202005156.

[60] G. Bencivenni et al., *Performance of a triple-GEM detector for high rate charged particle triggering,* Nuclear Instruments and Methods in Physics Research Section A: Accelerators, Spectrometers, Detectors and Associated Equipment, Volume 494, Issues 1–3, 21 November 2002, Pages 156-162, URL: https://www.sciencedirect.com/science/article/pii/S0168900202014602?via%3Dihub.

[61] J. A. Merlin, *Single-hole discharges in GEMs,* 20 June 2018, URL: https://indico.cern.ch/event/709670/contributions/3008626/attachments/1672294/2683230/JMERLIN_RD51ColMeeting_GEM_DischargeEffects_24052018.pdf.

[62] J. A. Merlin, *Discharge propagation study and foil double segmentation,* 26 February 2019, URL: https://indico.cern.ch/event/801581/contributions/3331709/attachments/1802038/2939582/JMerlin_PhaseII_Discharge_Propagation_26022019.pdf.

[63] D. Fiorina, *GEM Spark Protection Studies,* Muon UpgradeWorkshop, 7-9 Oct 2019, URL: https://indico.cern.ch/event/850576/contributions/3580313/attachments/1921830/3179456/Muon_Upgrade_Workshop_DFiorina_GEMSparkProtectionStudies.pdf.

[64] A. Colaleo et al., *CMS Technical Design Report for the Muon Endcap GEM Upgrade,* CERN-LHCC-2015-012, CMS-TDR-013, 30 September 2015, URL: https://cds.cern.ch/record/2021453.

[65] G. Mocellin, *Performance of the GE1/1 detectors for the upgrade of the CMS muon forward system*, RWTH Aachen University, 2021, URL: https://publications.rwth-aachen.de/record/822893

[66] CAEN website, *SY4527 Universal Multichannel Power Supply System,* URL: caen.it/products/sy4527/.

[67] CAEN website, *A1515B 16/14 Channel 1-1.3kV (1 - 3 mA) Individual Floating Channel Dual Range Boards for Quadruple and Triple GEM detectors,* URL: https://www.caen.it/products/a1515b/.

[68] CAEN website, *A1676A EASY Branch Controller,* URL: https://www.caen.it/products/a1676a/.

[69] CAEN website, *A3486 3-phase 220/400 Vac . 48 Vdc (2 ch x 2 kW/1 ch x 4 kW) Converter,* URL: https://www.caen.it/products/a3486/.

[70] CAEN website, *A3016 6 Channel 8 V / 16 A / 90 W Power Supply Board,* URL: https://www.caen.it/products/a3016/.

[71] E.R. Starling, *Status of the Readout Electronics for the Triple-GEM Detectors of the CMS GE1/1 System and Performance of the Slice Test in the 2017-18 LHC Run,* PoS(TWEPP2018)132, 2018, URL: https://inspirehep.net/files/0300a9fa105a1c8724f76cd1666bbb3b.

[72] PICMG, *MicroTCA Overview,* URL: https://www.picmg.org/openstandards/microtca.

[73] A. Svetek et al., *The Calorimeter Trigger Processor Card: the next generation of high speed algorithmic data processing at CMS,* JINST 11 02 C02011, 2016, URL: https://iopscience.iop.org/article/10.1088/1748-0221/11/02/C02011.

[74] D. Contardo et al., *Technical Proposal for the Phase-II Upgrade of the CMS Detector,* CERN-LHCC-2015-010, LHCC-P-008, CMS-TDR-15-02, 2015, URL: https://cds.cern.ch/record/2020886.

[75] M. Bianco, *Update on GE21 and ME0 projects,* Internal Meeting, URL: https://indico.cern.ch/event/702782/contributions/2896600/attachments/1603169/2542339/RD51_GE21-ME0_Summary_MBianco.pdf.

[76] I. Vai, *Development and performance of Micropattern Gaseous Detectors for the CMS muon system upgrade,* URL: https://cds.cern.ch/record/2316790?ln=it, 2017.

[77] S. Calzaferri, *Production and installation of first GEM station in CMS,* Journal of Instrumentation, The International Conference Instrumentation for Colliding Beam Physics (INSTR2020), 24–28 February 2020, Novosibirsk, Russia, URL: https://doi.org/10.1088/1748-0221/15/09/c09040.

[78] F. Fallavollita, *Upgrade of the CMS Muon System with GEM Detectors,* 15th Vienna Conference on Instrumentation, 18-22 February 2019.

[79] L. Felipe Ramirez G., *Construction and certification of the CMS GE1/1 detectors for the upgrade of the CMS experiment,* Posters at LHCC: Students' Poster Session at the 2020 Winter LHCC meeting, 19 Feb 2020, CERN, Geneva (Switzerland).

[80] D. Fiorina, *ME0 Rate Capability and Spark Protection,* Muon Upgrade Workshop, 2 September 2021, URL: https://indico.cern.ch/event/1067949/#21-me0-rate-capabilities-and-s.

[81] J. A. Jaramillo Gallego et al., *QC7 report,* GE-1/1 workshop, 12 June 2020, CERN.

[82] S. Calzaferri, *GE1/1-X-L-CERN-0007, with cooling, approved with cooling and chimney,* Internal report on the QC7 test of chamber GE1/1-X-L-CERN-0007, URL: http://cmsonline.cern.ch/cms-elog/1107564.

[83] C. Aime, *GE1/1-X-S-FIT-0004 with cooling, returned from P5 due to VFAT5 broken sbit line,* Internal report on the QC7 test of chamber GE1/1-X-S-FIT-0004, URL: http://cmsonline.cern.ch/cms-elog/1107370.

[84] Root website, *THistPainter Class Reference, the candle option,* URL: https://root.cern.ch/doc/v608/classTHistPainter.html#HP140.

[85] S. Calzaferri, *GE11-X-L-CERN-0043, no cooling, returned from QC8,* Internal report on the QC7 test of chamber GE1/1-X-L-CERN-0043, URL: http://cmsonline.cern.ch/cms-elog/1107566.

[86] F. Simone et al., *Prestazioni dei rivelatori a tripla GEM per la prima stazione del sistema a muoni dell'esperimento CMS misurate da raggi cosmici,* 106° SIF National Congress, 14-18 October 2020, URL: https://agenda.infn.it/event/23656/contributions/.

[87] CMS Online webpage, *DCS Automation*, URL: https://cmsonline.cern.ch/webcenter/portal/cmsonline/pages_common/dcs/automation.

[88] Bokeh website, *The Bokeh Visualization Library,* URL: https://bokeh.org/.

[89] D. Fiorina and F. Fallavollita, *Goliath magnet test*, 30th GEM Workshop, CERN, URL: https://indico.cern.ch/event/1096104/contributions/4611048/.

[90] M. Bianco, *GE1/1 HV Hospital*, 30th GEM Workshop, CERN, URL: https://indico.cern.ch/event/1096104/contributions/4631911/.

[91] M. Ressegotti, *Micropattern Gas Detectors for the CMS Experiment's Muon System Upgrade: Performance Studies and Commissioning of the first GEM Detectors*, URL: http://www.infn.it/thesis/thesis_dettaglio.php?tid=13762, 2019.

[92] M. Raidal et al., *Flavour physics of leptons and dipole moments,* Eur.Phys.J. C57 (2008) 13-182, URL: https://arxiv.org/abs/0801.1826.

[93] A. Abada et al., *Lepton flavour violation in low-scale seesaw models: SUSY and non-SUSY contributions,* JHEP 1411 (2014) 048, URL: https://arxiv.org/abs/1408.0138.

[94] E. Arganda et al., *Testing supersymmetry with lepton flavour violating τ and μ decays*, Phys.Rev. D 73 (2006) 055003, URL: https://journals.aps.org/prd/abstract/10.1103/PhysRevD.73.055003

[95] G. Cvetic et al., *On Lepton Flavor Violation in Tau Decays,* Phys.Rev. D 66 (2002) 034008; Erratum-ibid. D 68 (2003) 059901, URL: https://arxiv.org/abs/hep-ph/0202212.

[96] C. Yue et al., *Non-universal gauge bosons Z' and lepton flavour-violation tau decays,* Phys.Lett. B 547, 252 (2002), URL: https://arxiv.org/abs/hep-ph/0209291.

[97] Belle Collaboration, *Search for Lepton Flavor Violating τ Decays into Three Leptons with 719 Million Produced $\tau^+\tau^-$ Pairs,* Phys. Lett. B 687 (2010) 139, URL: https://arxiv.org/abs/1001.3221.

[98] CMS Twiki, *How to Compute Cross Sections with the GenXSecAnalyzer,* URL: https://twiki.cern.ch/twiki/bin/viewauth/CMS/HowToGenXSecAnalyzer.

[99] *CMSSW Application Framework,* URL: https://twiki.cern.ch/twiki/bin/view/CMSPublic/WorkBookCMSSWFramework.

[100] CMSSW Github web page *Phase 2 Geometries,* URL: https://github.com/cms-sw/cmssw/tree/master/Configuration/Geometry.

[101] A. Rotondi, P. Pedroni and A. Pievatolo, *Probabilità statistica e simulazione: programmi applicativi scritti con Scilab,* Springer, 2006.

[102] CMS internal web page, *Trigger MotherBoard (TMB)*, URL: https://cmsdoc.cern.ch/cms/MUON/cscTrigger/html/CERN/striplct.html.

[103] CMS Twiki, *L1 Trigger Emulator Phase-2 Upgrade Instructions*, URL: https://twiki.cern.ch/twiki/bin/view/CMSPublic/SWGuideL1TPhase2Instructions.